Geavanceerde voorwaartse modellen voor EEG-bronanalyse

Advanced Forward Models for EEG Source Imaging

Gregor Strobbe

Promotoren: prof. dr. S. Vandenberghe, dr. ir. P. van Mierlo
Proefschrift ingediend tot het behalen van de graad van
Doctor in de Ingenieurswetenschappen: Biomedische Ingenieurstechnieken

Vakgroep Elektronica en Informatiesystemen
Voorzitter: prof. dr. ir. R. Van de Walle
Faculteit Ingenieurswetenschappen en Architectuur
Academiejaar 2014 - 2015

UNIVERSITEIT
GENT

ISBN 978-90-8578-785-3
NUR 954
Wettelijk depot: D/2015/10.500/31

Department of Electronics and Information Systems
Medical Image and Signal Processing Group
Faculty of Engineering and Architecture
Ghent University

MEDISIP
IBiTech - iMinds
Campus Heymans, Blok B
De Pintelaan 185
9000 Ghent
Belgium

Promotors
Prof. dr. Stefaan Vandenberghe
Dr. ir. Pieter van Mierlo

Board of examiners
Prof. dr. ir. Patrick De Baets, chairman
Prof. dr. ir. Guillaume Crevecoeur , Ghent University, secretary
Dr. Geertjan Huiskamp, University Medical Center Utrecht
Prof. dr. Christoph Michel, University of Geneva
Prof. dr. Christophe Phillips, University of Liège
Prof. dr. Gilles Pourtois, Ghent University
Prof. dr. ir. Bart Vanrumste, University of Leuven
Prof. dr. ir. Sabine Van Huffel, University of Leuven
Dr. ir. Pieter van Mierlo, Ghent University
Prof. dr. Stefaan Vandenberghe, Ghent University

Prolog - Acknowledgements

"Between the click of the light and the start of the dream"
The Arcade Fire - No Cars Go

When I just started my studies engineering at Ghent University, I was already fascinated by the bridge that could be made between the engineering world and the medical field. Doing the master Biomedical Engineering really opened my eyes to the endless number of possibilities of applying the engineering skills that I had learned during my bachelor, to signals coming from the human body. After my master thesis, on brain computer interfaces, I was convinced I wanted to do brain research. The complexity of the brain and the broad spectrum of opportunities for research triggered me right from the start.

Writing this PhD thesis was a great adventure, with many challenges, opportunities and periods of stress. On paper, you're a doctor the day you graduate from the PhD program. In reality, I suppose, it happens somewhere along the way. This is not only due to the fact that you need to digest a lot of knowledge but also because of the many people you meet. The work performed in this PhD thesis is the result from many collaborations. Without the help of many great people I could not have written this thesis. I am really happy I can take the time to thank all of them here.

First of all I want to thank my promotor **prof. dr. Stefaan Vandenberghe**. Stefaan, thanks for giving me the opportunity to carry out this work at MEDISIP. The freedom that you gave me during my research really allowed me to discover several research directions. The atmosphere at MEDISIP is something special, stimulating initiative, creativity and ideas. Thanks for providing the supportive and open environment. We're living in exciting times for doing research, especially in the neuroscience field. I hope MEDISIP can be part of the whole neuroscience revolution that is to come! Thanks for the cycling trips and parties we had,

especially near the end of my PhD. I really enjoyed these!

Secondly, I want to thank my promotor **dr. ir. Pieter van Mierlo**. Strange to see the official term promotor before your name because I can think of many others. Your guidance and influence during my PhD were indispensable. You more than once lifted the quality of my research to a higher level, for which I am very grateful. Thanks a lot for the many, fruitful discussions we already had. I think our ideas and way of working are often very complementary. I am sure that it can lead to many more successful projects in the future. Also the trips to Banff, Beijing, Paris, Seattle, Geneva and many others were always fantastic and such a pleasure. It was and is really fun working with you. Something to cherish!

I also want to thank **Jose David López**. I am so happy we met through the SPM forum and immediately started working closely together. You deserve a very big thank you for all the advice you provided, the documents and technical reports you shared, the reviewing of all my papers and much more. The couple of days we worked together in London were great fun! I hope we can continue working together in the future and I hope I can come to Colombia, one day!

I further want to thank **prof. dr. ir. Roel Van Holen**. You really supported me in the beginning of my PhD after the IWT defenses, which I very much appreciated. Also the many parties we had with MEDISIP ending in the Video or Charlatan were always legendary when you were around. Hope there will be many more to come soon. Also thanks to **prof. dr. ir. Christian Van Hove** for always begin helpful with advice and being the smartest looking professor of the university.

A special thank you goes to **Ewout**. Thanks a lot for the advice and support you continuously gave me for the spin-off projects I wrote during the last summer. These were quite stressful moments and because of you I kept believing in the idea. Also the many dj-booth moments were amazing. Let's hit it at the next party. I furthermore want to thank **Vincent**. I really enjoy(ed) talking to you about my research and research in general. Always enlightening to hear your thoughts and ideas. The trip to Beijing was also so much fun.

I furthermore want to thank all the other colleagues at MEDISIP. **Bert** for the great times during lunch. Always fun to hear you talking about your training plans on your bike trainer. Everything analyzed to the smallest details. Don't forget the road though. **Karen** for the many discussions, great conversations and fun times we already had. Especially

at the Gentse Feesten, when I just submitted my PhD and the many Video nights! **Nathalie** for the great trip to Seattle. **Willeke** for your enthusiasm, your flexibility and the great trip to Geneva. You were one of my first thesis students and I am very happy you joined MEDISIP. I wish you all the best with your PhD and I am always happy to help you. **Thibault aka Does** for joining MEDISIP and your interest in the world of epilepsy. It was great getting to know you better the last couple of months. **Margo** for your keen interest in EEG and EEG source imaging. **Karel** for sharing your IWT innovation mandate document. **Pieter Mollet** for being funny. **Carmen** for your dancing moves. **Lara** for your organizational skills. **Radek** for the polish vodkas. **Stijn**, **Esther**, **Tiziana** and **Ekaterina** for joining the MEDISIP team.

I also want to thank **prof. dr. ir. Patrick Seghers**, **prof. dr. ir Pascal Verdonck**, **prof. dr. ir. Abigail Swillens**, **dr. ir. Matthieu De Beule** and all the colleagues from **BioMMeda**. Some special thanks to **Mathias** for being the PC guardian. I furthermore want to thank **Saskia** and **Inge** for the really nice support!

Some special thanks also go to **dr. ir. Hans Hallez**. Thank you for introducing me to the field of EEG signal processing, providing me with your code and the many great suggestions you gave me in the beginning of my PhD. **Victoria** for the amazing trip to Banff and sharing your head models. **Prof. dr. Daniele Marinazzo** for the great trips to Beijing and Seattle and the really nice training school you organized last year. **Margarita** for your enthusiasm, the great trip to Geneva and the many interesting conversations we already had. **Juan David Martinez Vargas** and **David Cárdenas** for your stays at MEDISIP. It was really fun working with you guys. **Tony** for the many funny moments at the beginning of my PhD.

I also want to thank the colleagues of Leuven, **Prof. dr. ir Sabine Van Huffel**, **Prof. dr. ir. Maarten De Vos**, **dr. ir. Bogdan Mijović** and **dr. ir. Katrien Vanderperren** for providing me the ERP data and the fruitful discussions.

A very special thanks goes to **iMinds** for organizing the iBootcamp in London. Especially to **Lisa** who stimulated me to continue with the spin-off idea and always pushed me to continue. Thanks **Lisa**, it is a pleasure working with you. I also want to thank **Steven** and **Devy** for the great times we had in London.

I want to thank the staff of the Department of Neurology of the University Hospital. Especially **Dr. Evelien Carrette** for your continuous

help collecting the patient data, reviewing my documents and getting the approval of the Ethics Committee. **Prof. dr. Paul Boon** for your interest in and support of the spin-off project and **Prof. dr. Kristl Vonck** for the critical reviews of the last chapter. It is a honor working with you and I hope we can collaborate more in the future. I also want to thank **Prof. dr. Patrick Santens**, **dr. Miet De Letter**, **Sarah** and **Annelies** for the successful collaboration. We're always there to help so I hope we can continue working together in the future.

Verder verdienen mijn **ouders**, **Marc** en **An** een speciale plaats in dit dankwoord. Bedankt om er steeds te zijn voor me en me de kans te geven om aan dit verhaal te kunnen beginnen. Bedankt **Mama** en **Marc** voor het inrichten van de verschillende plaatsen waar ik kon studeren, het op kot gaan, de 1000 en 1 fietsen, jullie geduld met alle kiertjes en open kasten! Bedankt **Papa** en **An** voor de steun en alle gezellige momenten. De ritjes op de fiets, de trip naar Sierra Nevada, de skireizen en etentjes! Ook mijn broer **Ilja** en zussen **Marit** en **Jade** wil ik bedanken om er altijd te zijn voor me. Mijn **Bobonne** en **Pepe** verdienen ook een hele erg grote dankuwel. Jullie aandeel in mijn studies is van onschatbare waarde. Bedankt dat ik me maanden bij jullie kon opsluiten om te studeren en ik me van niks anders iets moest aantrekken.

Verder wil ik ook mijn vrienden heel erg bedanken aka **The homesters** voor de topmomenten en ontspanning naast mijn onderzoek. En natuurlijk wil ik als laatste **Lotte** bedanken, mijn steun en toeverlaat. Bedankt om mijn leven mee te kleuren, voor je liefde en onuitputtelijke positieve instelling. Zonder jou had ik dit niet gekund! Bedankt om meermaals naar me te luisteren, me te steunen in het spin-off verhaal en oplossingen te zoeken als ik vast zat in mijn onderzoek!

A prolog is usually followed by an epilog. I hope I can bundle all the knowledge I acquired during these four years and a half of research into a successful spin-off of Ghent University. I am very happy I'm getting the chance to develop our technology to a commercial level and I am very motivated and excited to do everything I can to launch the **EPILOG** project in the coming years.

Gregor Strobbe, 21 March 2015.

"From small beginnings come ... "
Fink - Pilgrim

Table of Contents

List of Figures

List of Tables

Notation

x	real number
$\mathbf{x}$	vector
$\mathbf{X}$	matrix or tensor
$\mathbf{x}_i$	i-th element of vector $\mathbf{x}$
$\mathbf{X}_i$	i-th vector column of $\mathbf{X}$
$\mathbf{X}_{ij}$	the scalar element of the i-th column and j-th row of $\mathbf{X}$
$\|\mathbf{x}\|$	L_2-norm of $\mathbf{x}$
$\mathbf{X}^T$	transpose of $\mathbf{X}$
$tr(\mathbf{X})$	the trace of $\mathbf{X}$
$\|\mathbf{X}\|$	determinant of $\mathbf{X}$
$cov(\mathbf{X})$	covariance of $\mathbf{X}$
$\mathbf{I}_n$	$n \times n$ identity matrix
$\mathbf{1}_n$	$n \times 1$ vector of ones
$\mathbf{0}_n$	$n \times 1$ null vector
$Diag(\mathbf{x})$	$n \times n$ diagonal matrix whose diagonal is $\mathbf{x}$
$diag(\mathbf{X})$	$n \times 1$ vector containing the diagonal of matrix $\mathbf{X}$
$\mathbf{x}\|\mathbf{y}$	stands for "$\mathbf{x}$ given $\mathbf{y}$"
$p(\mathbf{x})$	the probability of $\mathbf{x}$
$\langle\mathbf{x}\rangle$	expectation of $\mathbf{x}$
$N(\mathbf{m}, \mathbf{C})$	Gaussian distribution, mean $\mathbf{m}$, covariance $\mathbf{C}$
∇	the nabla operator
$\nabla\cdot$	the divergence operator
$\nabla\times$	the curl operator

List of Acronyms

A

ARD	Automatic Relevance Detection

B

BEM	Boundary Element Method
BF	Bayes Factor

C

CSF	CerebroSpinal fluid
CT	Computed Tomography

D

d_R	Distance to the resected zone

E

EEG	Electroencephalography
ERP	Event Related Potential
ESI	EEG source imaging
ECD	Equivalent Current Dipole
EM	Expectation Maximixation
EIT	Electrical Impedance Tomography
EPSP	Excitatory Post-Synaptic Potential

F

FEM	Finite Element Method
FDM	Finite Difference Method
FDRM	Finite Difference Reciprocity Method
FFA	Fusiform Face Area

G

GS	Greedy Search
GABA	Gamma-Aminobutyric Acid
GBF	Group Bayes Factor

I

IED	Interictal epileptic discharges
IPSP	Inhibitory Post-Synaptic Potential

L

LORETA	Low Resolution Electrical Tomography

M

MSP	Multiple Sparse Priors
MRI	Magnetic Resonance Imaging
MREIT	Magnetic Resonance Electrical Impedance Tomography
MSVP	Multiple Sparse Volumetric Priors
MF	Mid Fusiform gyrus

P

PEB	Parametric Empirical Bayes
PPA	Parahippocampal Place Areas

R

RRE	Relative Residual Energy
ReML	Restricted Maximum Likelihood

S

SPM	Statistical Parametric Mapping
SNR	Signal to Noise Ratio

W

WMN	Weighted Minimum Norm

English summary

Nederlandstalige samenvatting

English summary

This dissertation is situated within the research field of ElectroEncephaloGraphy (EEG), which is a non-invasive technique to record the electrical activity of the brain. By placing electrodes on the scalp, the technique allows to measure the electrical potentials generated by electrically active areas in the brain. This allows to characterize brain activity with a milliseconds time resolution in a very straightforward and cheap way. Despite the simple nature of the recording technique, the analysis of EEG signals provides several challenges in an engineering context. EEG signals are often contaminated by noise, because any source of electrical activity is recorded through the electrodes, i.e. electrical activity from the muscles, eye blinks, the power net, etc. To solve this problem, several measuring and signal processing techniques have been developed that allow to record signals with lower noise contamination and allow to extract the 'relevant' information from the signals.

The measured EEG signals indirectly provide spatial information about the electrically active areas in the brain. This means that it is possible to determine the location of the active areas in the brain based on the recorded activity on the scalp. Therefore an inverse problem has to be solved. This is a process termed EEG source imaging (ESI) and is very challenging because only a limited number of electrodes, ranging from 20 to 256, are available to characterize the activity of the whole brain. The ESI process can be subdivided into 2 parts. The fist part consists of a generative model or forward model of the measured EEG data. The forward model includes the characterization and parameterization of the sources that are generating the EEG, commonly modeled as electrical current dipoles. It contains the geometry and electromagnetic properties of the head to calculate the field propagation of the sources that are assumed inside the head to the electrodes. Based on the forward model, the second part of ESI is an inverse technique that allows to determine the parameters of the forward model in function of the measured

EEG data.

The work presented in this dissertation is related to the forward model corresponding with ESI. There exist several forward modeling approaches depending on how the sources are modeled, how the head is modeled and which technique is chosen to model the field propagation of the sources. An analytical solution of the forward model is only possible for a highly symmetrical geometry, such as spherical approximations of the head, and homogeneous isotropic electrical conductivity in the head model. The use of high resolution anatomical MR images of a subject or a patient allows to construct a realistic model characterizing the properties of the head in detail. This is done by processing the MR image with segmentation techniques to extract the different tissues in the head and by assigning a certain conductivity to each tissue. Numerical methods that allow to construct such realistic forward models are the Finite Element Method (FEM), the Finite Difference Method (FDM) and the Boundary Element Method (BEM). The FEM and the FDM are volumetric forward modeling techniques that make no assumptions about the shape of the head model and allow the estimation of the electrical potentials at any location in the volume. The BEM is a surface based forward modeling technique that is based on the hypothesis that the volume is divided into subvolumes of homogeneous and isotropic conductivity and the potentials are estimated only on the surfaces separating these subvolumes. As a consequence the FEM and the FDM offer a more general solution of the forward model. They have many advantages over surface based BEM approximations of the head. First of all, the head models are constructed using 3D volumetric MR images so it is straightforward to construct 3D volumetric head models from it. Secondly, the volumetric forward modeling techniques allow to easily include different volumetric layers in the head model, including the highly conductivity cerebrospinal fluid (CSF). In a BEM model this is a difficult task due to the complex geometrical structure of the CSF, demanding a strongly increased computational effort.

The premise in this dissertation is that more accurate and realistic forward models will lead to more accurate EEG source imaging results. This was shown in several previous studies based on simulated data from an assumed true forward model. In contrast to these studies, we made use of realistic data recorded in subjects and patients in this dissertation to compare different forward models. Therefore we used the Parametric Empirical Bayesian (PEB) framework implemented in the Statistical Parametric Mapping Software (SPM). This is a MATLAB (The Math-

works. Inc., Natick, USA) to analyze EEG signals, MagnetoEncephalograpgy (MEG), Positron Emission Tomography (PET), Single Photon Emission Tomography (SPECT) and functional Magnetic Resonance Imaging (fMRI) data, that is widely used in the neuroimaging community. The PEB framework offers a natural way to introduce multiple constraints, or priors, in order to obtain a unique solution for ESI. It provides an alternative way of testing forward models, using real data, based on the estimated model evidence corresponding with a certain forward model.

The implementation of the PEB framework in the SPM software did however not allow to use volumetric forward models based on the FEM or FDM. By default a three-layered BEM model including a scalp, skull and brain compartment was used. We extended the PEB framework so it could be used with more realistic volumetric forward models, with specific focus on the inclusion of FDM models. Based on this extension we were able to compare different FDM forward models using real EEG data.

As a first step we introduced volumetric template head models based on an anatomical MRI template. We constructed a FDM head model equivalent to the BEM model used by default in the SPM software and extended the FDM model by including CSF. These models were compared within the context of three different types of source priors related to the type of inversion used in the PEB framework: independent and identically distributed (IID) sources, equivalent to classical minimum norm approaches, coherence (COH) priors similar to methods such as LORETA, and multiple sparse priors (MSP). The resulting models were compared based on EEG data recorded in 20 subjects. In brief, twenty healthy individuals performed trials of faces, houses, inverted faces and words stimuli resulting in 4 types of Event Related Potentials (ERP) for each subject. The different models were evaluated using Bayesian model selection for group studies and the reconstructed activity was also compared with the findings of previous studies using functional magnetic resonance imaging. We found strong evidence in favor of the extended FDM head model with CSF and assuming MSP.

In a second step, we revisited the multiple sparse priors (MSP) algorithm implemented in the PEB framework. In the current implementation, multiple cortical patches are introduced as source priors based on a dipole source space restricted to a cortical surface mesh. We presented a technique to construct volumetric cortical regions as source

priors by restricting the dipole source space to a segmented gray matter layer and using a region growing approach. This extension allowed us to reconstruct brain structures besides the cortical surface and facilitated the use of more realistic volumetric head models including more layers, such as a CSF layer, compared to the default 3-layered scalp-skull-brain head models in the SPM software. We called this technique the Multiple Sparse Volumetric Priors (MSVP) approach and illustrated the technique with EEG data recorded in 12 subjects, and the anatomical MR images of the subjects. In brief, the subjects performed 80 trials of circular black-and-white checkerboard stimuli presented to one of the four quadrants of the visual field resulting in 4 types of ERPs for each subject. Based on the segmented gray matter for each of the subjects, cortical regions were created and introduced as source priors for MSP-inversion assuming two types of head models. The standard 3-layered scalp-skull-brain head models and extended 4-layered head models including CSF. We compared with the current implementation by assessing the model evidence corresponding with each of the reconstructions using Bayesian model selection for group studies. Strong evidence was found in favor of the MSVP approach compared to the MSP approach based on cortical patches for both types of head models. Overall, the strongest evidence was found in favor of the MSVP reconstructions based on the extended head models including CSF. These results were verified by comparing the reconstructed activity.

Based on the MSP algorithm and the extensions to volumetric forward models in the previous step, we finally compared different sets of source priors to localize the generating sources of interictal spikes observed in EEG recordings of patients with refractory focal epilepsy. We introduced an EEG source imaging technique to estimate the activity of multiple distributed sources corresponding with the full time course of the spikes, and suggested to identify the origin of the activity based on the dipole source with the maximum energy during the rising phase of the spike. We introduced multiple sets of sparse volumetric priors in the PEB framework and illustrated the technique using averaged interictal epileptic spikes in 6 patients with refractory epilepsy that were successfully treated with surgery. Based on pre-surgical anatomical MR images and the electrode positions that were available for each patient, patient specific 5-layered head model were constructed. We modeled 100 different sets of 256 volumetric regions with locations that were maximally spread inside the gray matter of the patient. Each set of regions was introduced as priors for inversion, and we obtained the most likely set of priors using Bayesian

model selection. The resected zone in each of the patients, extracted from post-operative MR images, was used to evaluate the proposed approach. We compared with a LORETA approach implemented in the CARTOOL software and an equivalent current dipole (ECD) approach at the spike peaks and at 50% of the peaks during the rising phase of the spike. We found equally good or smaller distances to the border of resection, i.e. < 15 mm, with robust results for all the patients. The results we obtained are promising because the approach allows to identify the spatial spread of the sources, and allows incorporating prior knowledge from other clinical investigations such as Positron Emission Tomography (PET) and functional Magnetic Resonance Imaging (fMRI).

As an overall conclusion, we compared forward models based on realistic data in 32 subjects and 6 patients in this dissertation. The results we obtained in this work suggest that the use of realistic volumetric forward models improve EEG source imaging. We showed that the use of volumetric cortical regions as source priors is a useful complement to the present implementation in the PEB framework as it allows to introduce more complex head models and volumetric source priors in future studies. We introduced a new ESI technique to localize interictal spike activity based on patient specific head models by introducing multiple sparse regions in the Bayesian frameworks. The findings suggest that our approach is potentially useful to delineate the zone where the epileptic spikes originate in addition to the CARTOOL software and the currently used ECD modeling techniques. The resultt need verification in a larger patient group and need to be compared with the gold standard, being intracranial recordings.

Nederlandstalige samenvatting

Het onderzoek dat in dit proefschrift wordt beschreven is gesitueerd binnen het onderzoeksveld van ElektroEncefaloGrafie (EEG). Dit is een niet-invasieve techniek om de elektrische activiteit in de hersenen te registreren door het plaatsen van elektroden op de hoofdhuid. Elektrische potentialen worden opgemeten via de elektroden, die worden gegenereerd door elektrisch actieve gebieden in de hersenen. Dit maakt het mogelijk om de hersenactiviteit te karakteriseren met een milliseconden temporele resolutie op een rechtstreekse, eenvoudige en goedkope manier. Ondanks de eenvoud van de techniek biedt de analyse van EEG signalen verschillende technische uitdagingen. EEG signalen zijn bijvoorbeeld vaak verstoord door ruis omdat elke bron van elektrische activiteit wordt opgenomen via de elektrodes. Dit kunnen oogknipperingen zijn, activiteit van de spieren, het elektricititeitsnetwerk, enz. Verscheidene opname- en signaalverwerkingstechnieken zijn reeds ontwikkeld om signalen op te nemen die minder ruis bevatten en om de 'relevante' informatie uit te signalen te kunnen extraheren.

De opgenomen EEG signalen bevatten impliciet ook spatiële informatie omtrent de actieve gebieden in de hersenen. Dit betekent dat het mogelijk is om de locatie van de actieve gebieden in de hersenen te bepalen gebaseerd op de signalen die worden opgemeten op de hoofdhuid. Om dit mogelijk te maken moet een invers probleem worden opgelost. Dit is een proces dat EEG bronanalyse wordt genoemd (of EEG source imaging (ESI) in het Engels) en is uitdagend omdat slechts op een beperkt aantal elektroden kan beroep gedaan worden om de activiteit te karakteriseren van de volledige hersenen. Het proces van EEG bronanalyse kan worden opgedeeld in 2 componenten. De eerste component omvat een generatief of voorwaarts model van de gemeten EEG data. Het voorwaartse mo-

del omvat de karakterisering en parameterisatie van de bronnen die de opgemeten EEG signalen genereren, typisch gemodelleerd als elektrische stroomdipolen. Het omvat een beschrijving van de geometrie en de elektromagnetische eigenschappen van het hoofd. Ook een numerieke techniek om de propagatie te modelleren van de bronnen in het hoofdmodel naar de elektroden is noodzakelijk. De tweede component is een inverse techniek die het mogelijk maakt om de paramaters van het voorwaartse model te bepalen in functie van de opgemeten EEG data. Het onderzoek dat is beschreven in dit proefschrift is gericht op het voorwaartse model voor EEG bronanalyse. Er bestaan verschillende opties voor de voorwaartse modellering afhankelijk van de bronnen die worden verondersteld de activiteit te genereren, hoe het hoofd wordt gemodelleerd en welke techniek wordt gekozen om de propagatie te modelleren.

Een analytische oplossing bestaat alleen voor symmetrische geometrieën van het hoofd, zoals bolvormige benaderingen, en homogene en isotrope elektrische conductiviteiten in het hoofdmodel. Voor andere meer algemene gevallen maakt de opname van een hoge resolutie anatomisch MR-beeld van de proefpersoon of de patiënt het mogelijk om meer realistische modellen van het hoofd te bekomen waarbij de eigenschappen in detail worden gekarakteriseerd. Door het MR-beeld te segmenteren kunnen verschillende types weefsel en lagen in het hoofd worden geëxtraheerd en kan aan elk van deze lagen een specifieke conductiviteit worden toegekend. Numerieke technieken die dit mogelijk maken zijn de eindige-elementen-methode (of Finite Element Method (FEM) in het Engels), de eindige-differentie-methode (of Finite Difference Method (FDM) in het Engels) en de rand-elementen-methode (of Boundary Element Method (BEM) in het Engels). De FEM en FDM zijn volumetrische voorwaartse modelleringstechnieken die geen veronderstellingen maken over de vorm van het hoofdmodel en het mogelijk maken om de elektrische potentialen te berekenen op elke locatie in het volume van het hoofdmodel. De BEM maakt gebruik van oppervlakken en is gebaseerd op de hypothese dat het hoofdvolume kan worden opgesplitst in subvolumes met een homogene en isotrope conductiviteit, waarbij de potentialen enkel worden berekend op de oppervlakken die deze subvolumes scheiden. Bijgevolg bieden de FEM en FDM een meer generieke oplossing voor het voorwaartse model. Ze hebben verscheidene voordelen tegenover de BEM benadering van het hoofd. Eerst en vooral worden realistische hoofdmodellen geconstrueerd op basis van 3D volumetrische MR-beelden waardoor het voor de hand ligt om hieruit 3D volumetrische hoofdmodellen te construeren. Ten tweede maken volumetrische technieken het mogelijk om verschil-

lende lagen in het hoofdmodel te modelleren, zoals het sterk geleidende cerebrospinaal vocht (of CerebroSpinal Fluid (CSF) in het Engels). Dit is erg moeilijk in een BEM model door de complexe structuur van het CSF wat kan zorgen voor een erg lange berekeningstijd.

Het uitgangspunt in dit proefschrift is dat meer accurate en realistische voorwaartse modellen leiden tot meer accurate ESI resultaten. Dit is reeds aangetoond in verschillende studies in het verleden gebaseerd op gesimuleerde data waarbij een aangenomen "waar" voorwaartse model als referentie werd gekozen. In tegenstelling tot deze studies maakten we in dit proefschrift gebruik van realistische EEG data opgenomen in proefpersonen en patiënten, en een statistisch raamwerk om verschillende modellen met elkaar te vergelijken. We maakten gebruik van een Parametrisch Empirisch Bayesiaans (PEB) raamwerk dat is geïmplementeerd in de Statistical Parametric Mapping Software (SPM). Dit is een MATLAB (The Mathworks. Inc., Natick, USA) toolbox voor de analyse van EEG signalen, Magnetoencephalografie (MEG), Positron EmissieTomografie (PET), enkelvoudige foton-emissie computationele tomografie (of Single Photon Emission Computed Tomography (SPECT) in het Engels) en functionele Magnetische Resonantie Beeldvorming (fMRI) data. Dit software-pakket wordt wereldwijd veel gebruikt voor de beeldvorming van de hersenen. Het PEB raamwerk biedt een elegante manier om verschillende restricties op te leggen voor het oplossen van het invers probleem, en maakt het mogelijk om voorkennis te incorporeren om een unieke oplossing te bekomen. Het raamwerk biedt verder de mogelijkheid om verschillende voorwaartse modellen te testen op basis van realistische data via de geschatte model-evidentie die correspondeert met een bepaald voorwaarts model.

De implementatie van het PEB raamwerk in de SPM-software liet het echter niet toe om volumetrische voorwaartse modellen te vergelijken gebaseerd op FEM of FDM. Standaard werd er een BEM model gebruikt waarbij een 3-lagig hoofdmodel werd verondersteld met een hoofdhuid-, schedel- en hersencompartiment. Om meer realistische modellen te kunnen gebruiken hebben we in dit proefschrift het PEB raamwerk uitgebreid zodat ook volumetrische technieken konden gebruikt worden voor meer realistische voorwaartse modellen. Hierbij hebben we ons specifiek gefocust op de FDM. Op basis van deze uitbreiding werd het mogelijk om verscheidene voorwaartse modellen te vergelijken geconstrueerd met verschillende veronderstellingen.

In een eerste stap introduceerden we volumetrische sjabloon hoofdmo-

dellen gebaseerd op een sjabloon anatomisch MR-beeld. We construeerden een FDM hoofdmodel equivalent aan het BEM model standaard gebruikt in de SPM software en een uitgebreid FDM model met CSF. Deze modellen werden vergeleken in de context van 3 verschillende restricties opgelegd aan de bronnen die typisch worden gebruikt in het PEB raamwerk: onafhankelijk en gelijk gedistribueerde bronnen (Independent and Idencentically Distributed (IID) in het Engels) equivalent aan de klassieke minimum norm benaderingen, coherentie (COH) priors gelijkaardig aan methodes zoals LORETA, en meerdere ijle priors (Multiple Sparse Priors (MSP) in het Engels). De resulterende modellen werden vergeleken gebaseerd op stimulus gerelateerde potentialen (Event Related Potentials (ERP) in het Engels) van 20 proefpersonen. Kortweg gezegd werd het EEG geregistreerd in 20 gezonde proefpersonen waaraan stimuli van gezichten, huizen, omgekeerde gezichten en woorden werden gepresenteerd. Dit resulteerde in 4 verschillende ERP types per proefpersoon. Op basis van Bayesiaanse modelselectie voor groepstudies werden de verschillende modellen vervolgens vergeleken. Ook werd de gereconstrueerde activiteit vergeleken met de bevindingen van eerdere studies gebruik makende van fMRI. De bevindingen wijzen op betere resultaten op basis van het uitgebreide FDM hoofdmodel met CSF en in de veronderstelling van MSP.

In een tweede stap, reviseerden we het MSP algoritme in het PEB raamwerk. In de standaard implementatie werden verscheidene corticaal actieve zones geïntroduceerd als bronvoorkennis gebaseerd op een bronruimte beperkt tot een corticaal oppervlak. We stelden een nieuwe techniek voor om verscheidene corticale regio's te introduceren als bronvoorkennis door de bronruimte te beperken tot de gesegmenteerde grijze materie en op basis van een techniek om regio's te groeien. Deze uitbreiding biedt de mogelijkheid om hersenregio's te reconstrueren naast het corticaal oppervlak en maakte het mogelijk om meer realistische volumetrische hoofdmodellen te gebruiken met meerdere lagen in het hoofdmodel zoals CSF, in tegenstelling tot de 3-lagige hoofdmodellen die standaard werden gebruikt in de SPM software. Deze uitbreiding werd kort benoemd als MSVP of Multiple Sparse Volumetric Priors in het Engels. We illustreerden de technieken op basis van ERP data en anatomische MR-beelden in 12 proefpersonen. Kortweg gezegd werd het EEG opgenomen bij 12 gezonde proefpersonen waaraan schaakbordvormige stimuli werden gepresenteerd in één van de kwadraten van het gezichtsveld. Dit resulteerde in 4 verschillende ERP types per proefpersoon. Gebaseerd op de gesegmenteerde grijze materie voor elk van de

proefpersonen werden corticale regio's geconstrueerd en geïntroduceerd als bronvoorkennis voor MSP inversie in de veronderstelling van 2 types hoofdmodellen. Het standaard 3-lagige hoofdmodel gebruikt in de SPM software en een hoofdmodel uitgebreid met CSF. We vergeleken de huidige implementatie met de nieuwe technieken door de geschatte model-evidentie te vergelijken corresponderend met elk van de modellen en op basis van Bayesiaanse modelselectie voor groepstudies. De bevindingen wijzen op betere resultaten op basis van de MSVP benadering in tegenstelling tot de MSP benadering gebaseerd op het corticale oppervlak voor beide types hoofdmodellen. Globaal gezien tonen de resultaten dat de MSVP reconstructies gebaseerd op het hoofdmodel uitgebreid met CSF leidt tot betere reconstructies. De resultaten werden ook geverifieerd door de gereconstrueerde activiteit te vergelijken.

Gebaseerd op het MSP algoritme en de uitbreidingen die we deden in de vorige stap, vergeleken we vervolgens verschillende verzamelingen van bronvoorkennis, voor het lokaliseren van de bronnen die interictale spikes genereren in patiënten met refractaire epilepsie. We stelden een ESI techniek voor om de activiteit te schatten van meerdere bronnen in overeenstemming met het volledige tijdsverloop van de spike, en suggereerden om de oorsprong van de activiteit aan te duiden gebaseerd op de bron met de maximale energie gedurende de stijgingsfase van de spike. De EEG activiteit achter de piek van de spike correspondeert immers met propagatie van de activiteit. We introduceerden verschillende verzamelingen van bronvoorkennis in het PEB raamwerk en illustreerden de techniek op basis van uitgemiddelde interictale spikes in 6 patiënten met refractaire epilepsie die werden behandeld met chirurgie. Gebaseerd op de pre-chirurgische anatomische MR-beelden en de elektrodenposities die beschikbaar waren voor elke patiënt, construeerden we patiënt specifieke 5-lagige hoofdmodellen. We modelleerden 100 verzamelingen van 256 regio's met locaties die maximaal verspreid waren in de grijze materie van de patiënt. Elke verzameling van bronnen werd geïntroduceerd als bronvoorkennis voor inversie, en de verzameling met de hoogste model-evidentie werd aangeduid als de meest waarschijnlijke verzameling bronnen corresponderend met de spike. Om de techniek te vergelijken, gebruikten we de CARTOOL software. Dit is de referentie, vrij te verkrijgen, software voor spike-lokalisatie. Op basis van deze software lokaliseerden we de activiteit corresponderend met de spike pieken en op 50% van de spike pieken gedurende de stijgingsfase van de spike. Ook werd vergeleken met equivalente stroomdipolen (of Equivalent Current Dipole (ECD) in het Engels) corresponderend met de spike pieken en op 50%

van de spike pieken gedurende de stijgingsfase van de spike. ECD oplossingen worden namelijk typisch gebruikt in een klinische context. We extraheerden vervolgens de zone in elk van de patiënten die chirurgisch werd verwijderd. Dit is de resectie die we vervolgens gebruikten als verificatiebasis om de verschillende methodes mee te evalueren. We vonden gelijkaardige of kleinere afstanden tot de rand van de resectie, d.w.z. $<$ 15 mm, met robuste resultaten voor alle patiënten. De resultaten die we verkregen zijn veelbelovend omdat de de voorgestelde techniek toelaat om de spreiding van de bronnen te modelleren. Ook is het mogelijke om diverse types voorkennis te integreren van andere klinische onderzoeken zoals PET of fMRI.

In dit proefschrift werden verscheidene voorwaartse modellen vergeleken op basis van realistische EEG data in 32 proefpersonen en 6 patiënten. De resultaten die we bekwamen in dit proefschrift tonen aan dat het gebruik van realistische volumetrische voorwaartse modellen ESI kan bevorderen. We toonden aan dat het gebruik van volumetrische corticale regio's als bronvoorkennis een nuttige uitbreiding is op de bestaande implementatie in het PEB raamwerk omdat het de mogelijkheid biedt om meer complexe volumetrische voorwaartse modellen en bronruimtes te gebruiken in toekomstige studies. We introduceerden ook een nieuwe ESI techniek om interictale spike activiteit te lokaliseren gebaseerd op patiënt specifieke hoofdmodellen en door het introduceren van meerdere verzamelingen bronvoorkennis in het PEB raamwerk. De bevindingen suggereren dat de techniek waardevol is voor het aflijnen van de zone in de hersenen waar de epileptische spikes ontstaan bovenop de typisch gebruikte technieken. De resultaten vereisen nog verificatie in grotere groepen patiënten en met intracraniële EEG opnames.

Chapter 1

Introduction

"The path we're on is the path we chose"
Deus - Keep you close

1.1 Context

Electroencephalography (EEG) is a non-invasive technique to characterize the electrical activity of the brain. By placing electrodes on the scalp, the technique measures the electrical potentials generated by electrically active areas in the brain. This allows to characterize brain activity with a milliseconds time resolution in a very straight forward and cheap way.

Despite the simple nature of the recording technique, the analysis of EEG signals provides several challenges in an engineering context. EEG signals are often contaminated by noise, because any source of electrical activity is recorded through the electrodes, i.e. electrical activity from the muscles, eye blinks, the power net, etc. To solve this problem, several measuring and signal processing techniques have been developed that allow to record signals with lower noise contamination and allow to extract the 'relevant' information from the signals. The EEG signals indirectly provide spatial information about the electrical active sources in the brain. This means that it is possible to determine the location and activity of the sources in the brain based on the recorded activity on the scalp. Therefore an inverse problem has to be solved. This is a process termed EEG source imaging and is very challenging because only a small number of electrodes, ranging from 20 to 250, are available to characterize the activity of a whole brain.

Briefly stated, EEG source imaging consist of 2 parts: (i) a generative model or forward model of the measured EEG data characterized by a number of parameters and (ii) an inverse technique that allows to determine the parameters of the forward model in function of the measured EEG data. A forward model can be subdivided into 3 main components: (i) the characterization and parameterization of the generating sources of the measured EEG data, (ii) the characterization of the geometry and electromagnetic properties of the head and (iii) a method to calculate the field propagation of the sources through the head. The first EEG source imaging techniques were developed in the beginning of the 90's and the field experienced a slow progress since then due to computational limitations. Because of the fast progress in computation power and the development of new brain imaging techniques like Magnetic Resonance Imaging (MRI) to characterize the anatomy of the brain, new advances in the field of EEG source imaging became recently possible.

This dissertation is situated within the field of EEG source imaging with the focus on the forward model of the EEG data. There exist several different forward modeling approaches depending on how the head is modeled and which source modeling approach is chosen. An analytical solution is only possible for a highly symmetrical geometry and homogeneous isotropic electrical conductivity. For other more general cases, numerical methods are required which allow to make no assumptions about the shape of the head model and allow the estimation of the electrical potentials at any location in the volume. The recording of high resolution anatomical MR images of a subject or a patient allows to construct a realistic forward model characterizing the properties of the head in detail. This is done by processing the MR image with segmentation techniques to extract the different tissues in the head and by assigning a certain conductivity to each tissue. In absence of a high resolution MR image, often template MR images are used to construct a template model of the head.

The premise in this work is that more accurate and realistic forward models will lead to more accurate EEG source imaging results. This is shown in this dissertation for several forward models, by testing them using real data, rather than the more traditional simulated data from an assumed true forward model shown in various previous studies. We made use of a Bayesian framework to invert the forward model based on a distributed source model. In distributed models, the solution space typically contains a large number of sources at discrete points within the brain, which leads to a largely underdetermined EEG inverse prob-

lem. Bayesian approaches offer a natural way to introduce multiple constraints, or priors, to "regularize" the solution. In addition, and most importantly for the work performed in this dissertation, they provide an alternative way of testing forward models, using real data, based on the model evidence corresponding with a certain forward model. Based on the model evidence, we evaluated forward modeling choices both with and without the presence of an anatomical MR image using realistic data in about 32 subjects and 6 patients.

1.2 Outline

In what follows we describe the organization of this dissertation divided in 7 more chapters. This dissertation can be read as shown in Fig. 1.1. In **chapter 2**, we give a general introduction to electroencephalography. We start by describing the early history of EEG followed by the modern principles of recording EEG signals. The anatomy and physiology of the brain is subsequently briefly described. Next, we discuss the generators of the electrical potentials we measure on the scalp. Therefore, the electrical brain activity at different spatial scales is discussed and we describe the characteristics of the measurable sources with EEG. The chapter continues by describing the recording principles of EEG signals and how to visualize the signals. We continue with the types of activity that can be observed in an EEG recording, discuss the artifacts that are often present and explain some techniques to remove them. To conclude, some applications of EEG are presented starting with the clinical applications such as in epilepsy and sleep research. We briefly describe the role of EEG in cognitive neuroscience and recent applications for brain computer interfaces and neuromarketing.

In **chapter 3**, the background and recent developments in EEG source imaging are given in order to put the work in this dissertation in perspective. We start by describing the principles of EEG forward modeling. Therefore, we first introduce the current dipole and describe how an electromagnetic model of the head is subsequently constructed. After introducing the algebraic representation of the forward model, we discuss the techniques to model the propagation of the sources through the different tissues the head. Subsequently a general overview is given of the different inverse techniques that are developed for source imaging. Some application are presented and we discuss the position of EEG source imaging within other neuroimaging techniques in terms of spa-

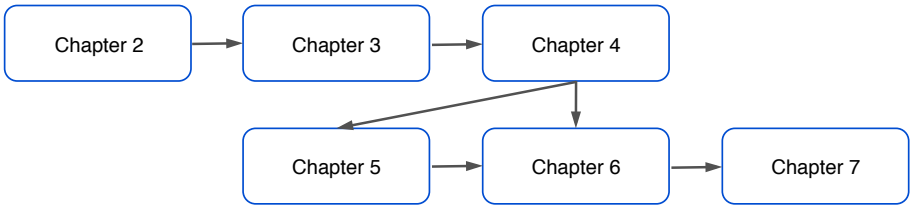

Figure 1.1: This dissertation can be read following this suggested diagram.

tial and temporal resolution. To conclude, the concept of multimodal neuroimaging is described and illustrated with an example.

In **chapter 4**, the Bayesian framework for EEG source imaging, which is the backbone in this dissertation, is described in detail. We start by describing Bayes' theorem. Next, the hierarchical Bayesian formulation of the EEG inverse problem is introduced. We subsequently describe the approach to introduce multiple priors in terms of covariance components and how a unique solution can be obtained by optimizing the free energy cost function using a restricted maximum likelihood technique. We explain that the free energy is an approximation of the model evidence and can be used to compare different forward models based on realistic EEG data.

In **chapter 5**, we present the results of a comparison study of template forward models in absence of an anatomical MR image, for EEG source imaging based on EEG data of 20 subjects. Using the Bayesian framework presented in chapter 4, we compared the typically used 3-layered scalp-skull-brain head models with head models including the highly conductive cerebrospinal fluid. Using EEG data of 20 subjects evidence is provided that it is worthwhile to model the CSF in a template head model.

In **chapter 6**, we go a step further and compare subject specific forward models constructed based on high resolution anatomical MR images. Based on EEG data of 12 subjects the effect of modeling the CSF is evaluated and the concept of using volumetric regions as source priors for inversion is introduced.

In **chapter 7**, we describe an application of the Bayesian framework and the techniques developed in chapter 6, using patient specific forward models, for EEG source imaging of epileptic activity. Using the high resolution anatomical MR images of 6 patients with epilepsy that were

treated with surgery, we compare the results of a classical approaches to localize the activity to a new approach presented in this chapter. The different techniques are compared based on the area in the brain that was removed during surgery and served as our verification basis.

A summary of the results that are described in this thesis, along with the conclusions that can be drawn from them is given in **chapter 8**. Some possibilities for future research and a final conclusion is also presented there.

Chapter 2

Electroencephalography

"We are electronics"
Air - Electronic Performers

2.1 Introduction

In this chapter, the principles of electroencephalography (EEG) are explained. The chapter starts off with a brief history of the first EEG recordings. These measured brain activity over time using metal strips pasted on top of the scalp. To understand the origin of the measured EEG activity, the subsequent section describes the anatomy and function of the brain with the focus on the mechanisms of neural activity. This allows us to elaborate on the origin of electrical brain activity at different spatial scales, going from electrical signals measurable at the microscopic level to signals that are measurable on top of the scalp. Next, we look at the modern EEG recording techniques and describe methods to visualize the recorded data. The chapter continues with a description of the various types of brain activity that can be observed in an EEG recording. The different types of artifacts often present in the recordings, and some techniques to remove them are described subsequently. To finish the chapter, we present a number of applications.

2.2 Early History

The first human EEG recordings were carried out by Hans Berger in 1924. He used metal strips pasted on top of the scalps of his subjects to record

their brain activity using a sensitive galvanometer. This is an instrument to measure electrical currents based on a moving electromagnetic coil. To visualize the measured activity over time, Berger plotted the successive positions of the moving coil of the galvanometer on a continuous roll of paper [1]. As such, he was able to measure irregular, relatively small electrical potentials (in the range of 50 μV to 100 μV) coming from the brain. In his report of 1929, Berger describes oscillating brain activity at 10 Hz. He used chlorinated silver needle electrodes, platinum wires, and zinc-plated steel needles to record the activity of his son [2], see Fig. 2.1. The lower line is a 10 cycles/sec sine wave for use as a time marker. The upper line is the recording from Berger's son.

Berger is the founder of the present applications of electroencephalography. He started using the word electroencephalogram to denote the EEG recorded signals themselves. The word is derived from the Greek word $\epsilon\gamma\kappa\epsilon\phi\alpha\lambda o\zeta$ or enkephalos which literally means "with brain". Nowadays the terms electroencephalography and electroencephalogram are both used in literature and are both abbreviated as EEG.

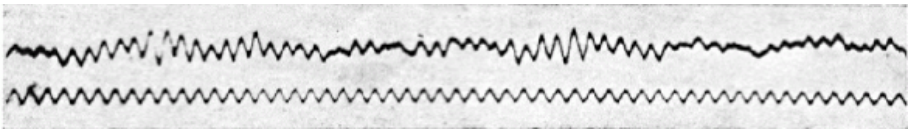

Figure 2.1: The first recorded electroencephalogram of a human. Figure adapted from [2] with permission from Springer.

2.3 The human brain

It is critical for the use of EEG as a brain activity recording technique to understand the nature of the sources generating the measured activity. For this purpose, the following section introduces the brain's anatomy and function allowing for a clear understanding of the used terminology.

2.3.1 The neuron

2.3.1.1 Anatomy

The basic building block of the human brain is the neuronal cell or the neuron. A brain contains approximately 86 billion neurons, all intercon-

nected to form a complex network [3]. Neuron cells are the information carriers and signal processing units of the human body. Each neuron connects with 5.000-200.000 other neurons and the complexity of the network increases from birth to the infant years, resulting in a full grown brain at the age of 30.

The anatomy of the neuron is shown in Fig. 2.2. A neuron consists of a cell body or soma, dendrites and an axon. Dendrites transmit information to the cell body, the cell body regulates the information coming from several dendrites and the axon sends information away from the cell body. Dendrites are very thin (≈ 1 μm) and the length of a single dendrite is typically several 100μm. Dendrites brach multiple times and can therefore reach several centimeters in total. We distinguish dendrites that are close to the cell body or basal dendrites and dendrites that are distant to the cell body or apical dendrites. The axon is much thicker ($\approx$ 25 μm) than the dendrites, and can transmit information over distances up to meters. In order to prevent the signals from loss in signal strength, the axon is covered with myelin sheaths. The area in the cell body where the signal transmission to the axon originates is the axon hillock. The ends of the axon reaching another neuron cell are the axon terminals. Between connecting neurons there is a gap, called the synapse. The neuron that transmits its information to another neuron is termed as the pre-synaptic neuron. The neuron that receives information from another neuron is termed as the post-synaptic neuron. The pre-synaptic neuron transmits its information along its axon to the post-synaptic dendrite.

There are many different types of neurons in the human brain that can be classified based on their function or morphology. We distinguish afferent, efferent and interneurons. Afferent neurons are also called sensory neurons that transmit information from tissues and organs to the brain. Efferent neurons are also called motor neurons and convey signals from the brain to the to the muscles, glands and organs in the body. Interneurons connect neurons between specific regions in the brain. The most important type of neuron we consider in this dissertation is the pyramidal neuron cell, which has a triangular shaped cell body. Pyramidal cells have an axon, a large apical dendrite and multiple basal dendrites, as can be seen in Fig. 2.3.

2.3.1.2 Function

The communication between neurons is based on chemical and electrical conduction. Signals are transmitted electrically along the neuron.

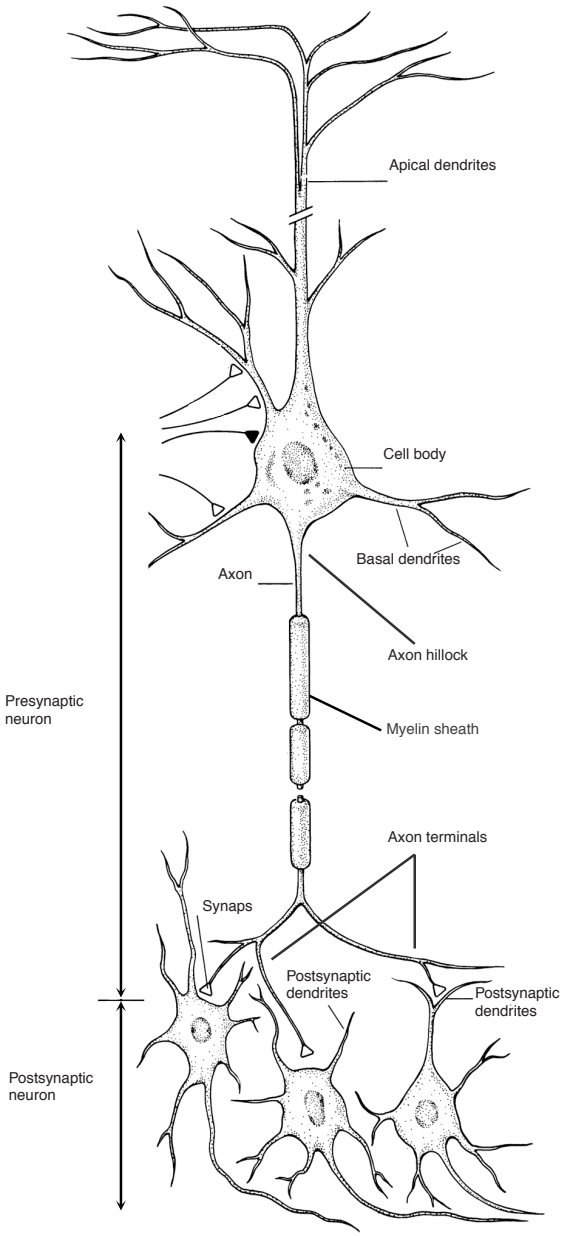

Figure 2.2: The anatomy of the neuron. Figure adapted from [4].

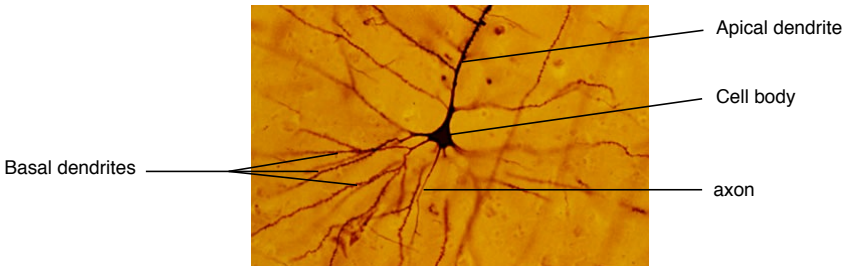

Figure 2.3: Example of a pyramidal neuron neuron stained via the Golgi technique. (Image obtained from `http://en.wikipedia.org/wiki/Pyramidal_cell/mediaviewer/File:GolgiStainedPyramidalCell.jpg`, used under a Creative Commons Attribution-ShareAlike license: `http://creativecommons.org/licenses/by-sa/3.0/`)

Based on the synapse structure the electrical signal can be transmitted chemically to another connecting neuron. A schematic overview is given in Fig. 2.4. We distinguish a pre-synaptic neuron and a post-synaptic neuron. Signals coming from the pre-synaptic neuron travel along the pre-synaptic axon based on a mechanism of action potentials. An action potential is a short-lasting event during which the membrane potential of the axon rapidly rises and falls based on the active movements of $K^+$and Na^+ions. The action potential travels along the axon from the axon hillock, near the cell body, to the axon terminal, as represented in panel 1. The + and − signs represent the collection of extracellular charges corresponding with the movement of the action potential. When the action potential reaches the axon terminal, a synaptic transmission of the propagating signal takes place based on chemical conduction, as represented in panel 2. The chemical conduction between the pre-synaptic axon terminal and the post-synaptic dendrite is based on neurotransmitters such as dopamine, glutamate and gamma-aminobutyric acid (GABA). The release of neurotransmitters in the synaptic cleft, evoked by the action potentials, triggers a mechanism in the post-synaptic dendrite that initiates the propagation of a post-synaptic potential to the cell body. The propagation of post-synaptic potentials is based on the passive spread of charges corresponding with the movement of $K^+$and Na^+ions. This is presented in panel 3. In this case, the + and − signs represent the collection of extracellular charges corresponding with the movement of the post-synaptic potential. Excitatory and inhibitory post-synaptic potentials can be distinguished. Excitatory post-synaptic potentials (EPSP)

are a direct consequence of an excitatory synapse corresponding with the influx of Na^+ions in the post-synaptic dendrite. Inhibitory post-synaptic potentials (IPSP) are a direct consequence of an inhibitory synapse corresponding with the outflux of K^+ions from the post-synaptic dendrite. Depending on the balance between EPSP and IPSP, the arrival of the post-synaptic potential in the cell body may trigger the neuron cell body to fire a new action potential along its axon in order to communicate with other neurons, represented in panel 4. Note that this is a simplified representation of neuronal communication. For a detailed description we refer the reader to [5].

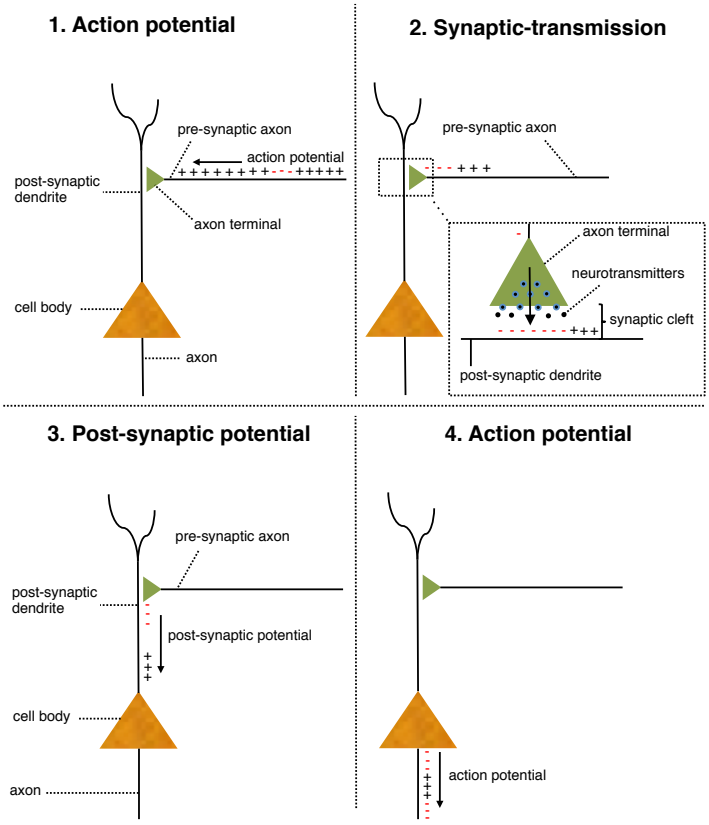

Figure 2.4: Schematic drawing to illustrate the principle of neuronal communication.

2.3.2 Brain structures

In order to visualize and denote specific structures or areas in the brain, we first introduce some conventions in Fig. 2.5. We show an axial, sagital and coronal plane or section, typically used for visualization. The location of an area is described according to the distance to the centre of the brain. Medial or lateral parts respectively depict areas or sections close or distant from the center of the brain. Posterior and anterior parts respectively depict backwards and frontal areas. Superior and inferior parts respectively depict upper and lower areas.

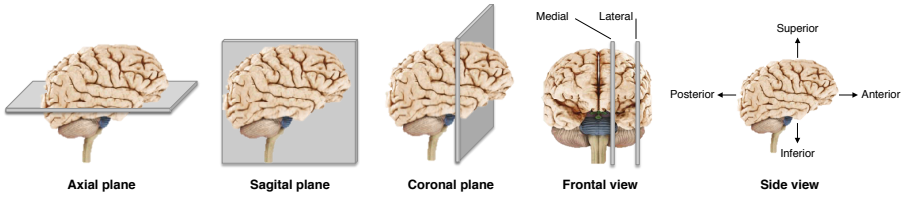

Figure 2.5: Left: the 3 primary orthogonal planes to visualize the brain. Right: a frontal view of the brain with a lateral and medial line denoting the position of the line to the midline of the brain. Figure adapted with permission from [6].

Both a frontal view of the brain and a sagital cross section of the human head are shown in Fig. 2.6. Different anatomical brain structures can be distinguished as a consequence of biological evolution. They are characterized by the typical arrangement of the neurons in these structures. The oldest part of the brain is known as the brain stem and is mainly responsible for the basic functioning of the human body: heart rate, breathing, sleeping etc. The cerebellum, meaning "little brain", is attached to the rear of the brainstem and is in charge of processing sensory input, coordinates movement output, and balance. The youngest part of the human brain is the cerebrum which is responsible for higher order human functioning and is divided into the left and right hemisphere.

The brain is covered by the scalp, skull, 3 meninges and the cerebrospinal fluid (CSF). The meninges are the pia mater, the arachnoid and dura mater, which protect the brain from rubbing against the bone of the skull. The CSF acts as a protective layer for the cerebral cortex and serves as a transport conduit for nutrients to the brain and waste from the brain. The ventricles are four spaces within the brain that are

filled with CSF. The ventricles foster circulation of CSF into the brain and also acts as a protective cushion against trauma.

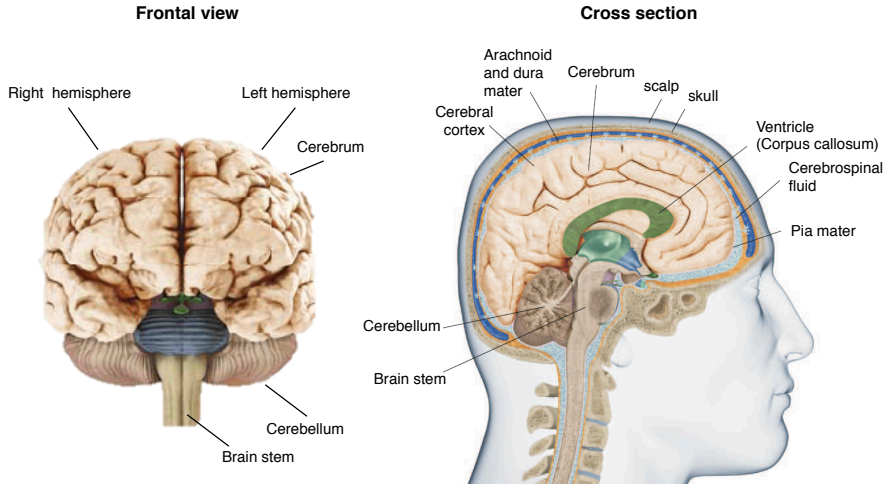

Figure 2.6: Frontal view and cross-sectional view of the brain. Figure adapted with permission from [6].

The most outer layer of the cerebrum is the cerebral cortex which consist of gray matter containing the neurons' cell bodies and dendrites, see Fig. 2.7 for a coronal slice through the brain. The cerebral cortex controls higher brain functions such as sensation, voluntary muscle movement, thought, reasoning and memory. The inner layer of the cerebrum is the white matter, which contains the neuron's axons covered by the myelin sheets which gives them the white color.

The cerebral cortex has a layered structure containing the cell bodies and dendrites of interconnected pyramidal neuron cells. It is typically 2 to 4 millimeters thick. The largest part of the cerebral cortex, covering both hemispheres, is the neocortex which contains 6 main layers that can be distinguished based on the grouping of the pyramidal neurons shown in Fig. 2.8.

The cerebral cortex is heavily folded resulting in a much greater surface area inside the skull volume. The foldings in the cortex are termed as the gyri (singular: gyrus) and the grooves in the cortex are termed as the sulci (singular: sulcus). In Fig. 2.9 an overview is given of the largest sulci and gyri in the cerebral cortex.

Based on topographical conventions related to the gyri and sulci, the

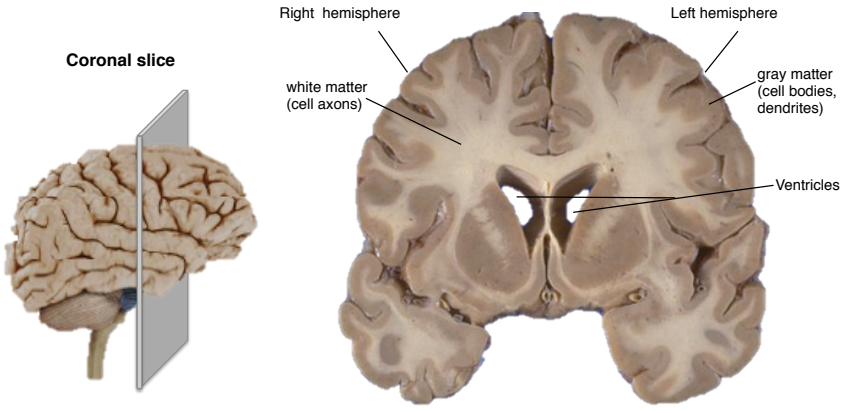

Figure 2.7: A coronal slice of the brain's cerebrum. The outer layer of the cerebrum is the cerebral cortex and consists of gray matter. The inner layer consist of white matter. Figure adapted with permission from [6].

cerebral cortex is classified into four main lobes: the temporal lobe, the occipital lobe, the parietal lobe and the frontal lobe, shown in Fig. 2.10. Furthermore, based on the histological differences in the neocortex, different neocortical regions, known as the Brodmann areas [7] can be distinguished.

2.3.3 Brain functioning

Particular, anatomically segregated regions in the cerebral cortex or cortical maps have specialized functions to process information or cause responses. These regions in the brain consist of large clusters of neurons, i.e. cortical columns of neurons, ranging from thousands to millions. Particular clusters work closely together in order to perform a specific function. An overview of some of the functionally specialized regions in the left hemisphere of the brain is given in Fig. 2.11. Some areas in the cerebral cortex are specialized in memory, language, emotions, sensations, perceptions and thought, or in producing body movement. The areas of the brain responsible for perceptions are spread over the temporal, occipital and parietal lobe. We can distinguish areas responsible for spatial awareness, visual processing and recognition. The areas responsible for thought are located in the frontal lobe. They can be subdivided into areas specialized in thinking, judging, spelling, planning, etc. The sensations areas are spread over the frontal, parietal and oc-

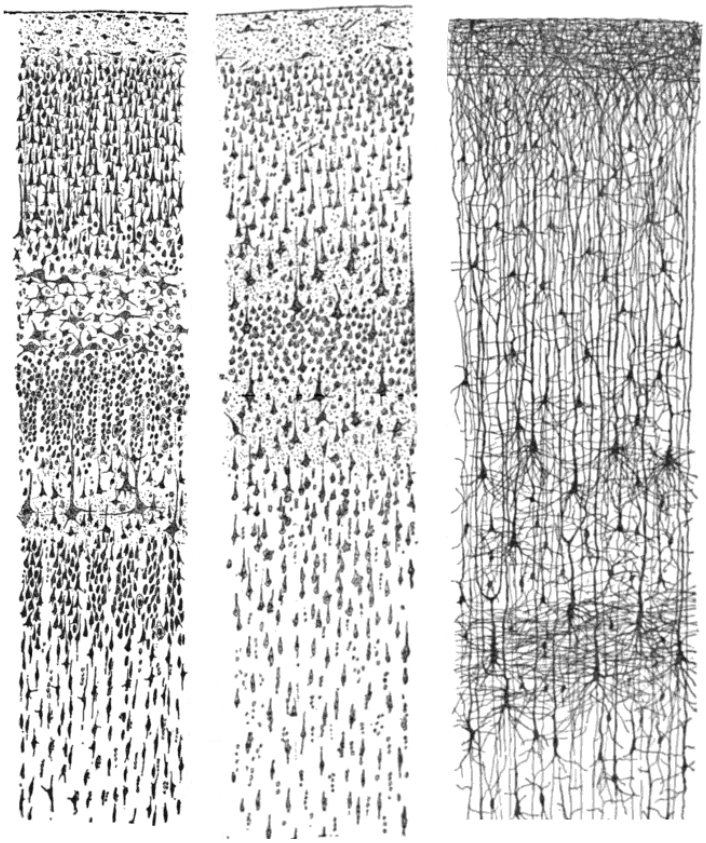

Figure 2.8: The layered structure of the cerebral cortex with the surface of the cortex shown on top. Left: Nissl-stained cortex of a human adult. Middle: Nissl-stained cortex of a human adult. Right: Golgi-stained cortex of a 1.5 month old infant. (Image obtained from `http://en.wikipedia.org/wiki/Cerebral_cortexmediaviewer/File:Cajal_cortex_drawings.png`, used under a Creative Commons Attribution-ShareAlike license: `http://creativecommons.org/licenses/by-sa/3.0/`)

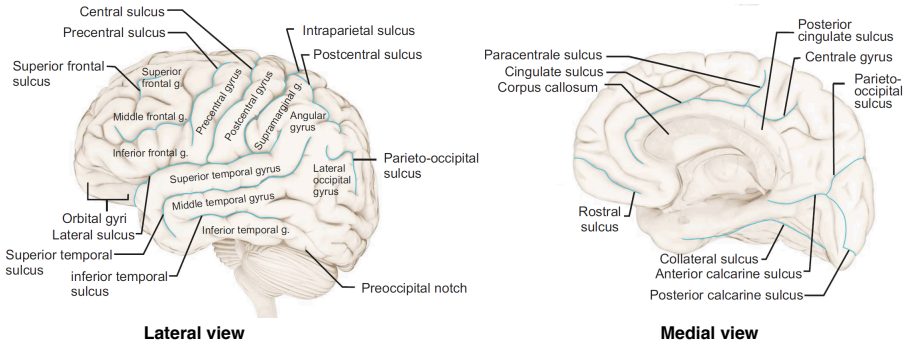

Figure 2.9: The cerebral cortex has a heavily folded structure with gyri and sulci. The names of the different gyri and sulci of the cerebral cortex are depicted. Figure adapted with permission from [6].

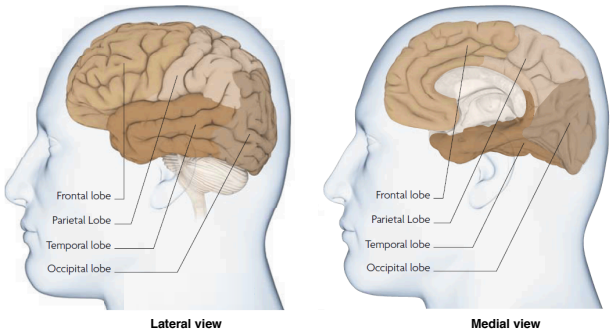

Figure 2.10: Naming of the different lobes in the cerebral cortex. Figure adapted with permission from [6].

cipital lobe. They can be subdivided into specialized regions for taste, smell, sound, touch and vision, each with a distinct location in the brain. The areas responsible for language are spread in the frontal, parietal and temporal lobe. There is a specialized area responsible for speech and one responsible for language comprehension. The cerebellum is responsible for coordination whereas the brainstem controls the arousal state.

In the modern view of brain functioning, the cortical infrastructure supporting a process or response may involve neuronal activity in several functionally specialized areas of the brain, all of which are functionally integrated. This means that the brain performs a task or function as an interconnected network of several specialized regions.

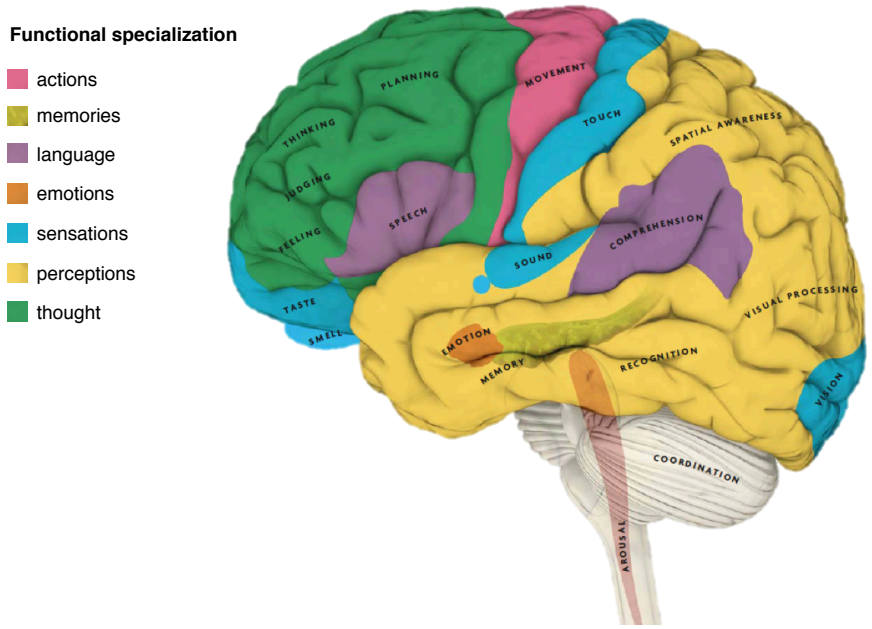

Figure 2.11: Different areas in the brain have different specialized functions depicted by the different colors in the left hemisphere. Figure adapted with permission from [6].

2.4 From neural activity to electrical potentials on the scalp

In the following section we explain at which spatial scales the neuronal activity takes place in order to describe which kind of neural activity is necessary in order to generate measurable EEG signals on the scalp surface.

Invasive neurophysiological recordings in animals allow to characterize neural activation at different spatial scales, going from intracellular recordings of individual neurons to nearby extracellular recordings. At the single neuron level, the dominant electrical events are the action potentials corresponding with a rise and fall of the membrane potential of the axon over 80 mV. The action potentials propagate rapidly, within less than 1 ms from the axon hillock to the axon terminals. The nearby extracellular activity corresponding with the propagating action potential,

can reach at least 600 μV close to the membrane and falls off rapidly to a tenth (<60 μV) outside a 50 μm radius from the membrane [8]. Therefore the extracellular spatial spread of action potentials is limited to sub-millimeters. This is important to know, because it prevents the extracellular fields caused by an action potential to be potentially measurable in the EEG, since the scalp surface is at least 2 cm away from the brain tissue. Moreover, because of the short duration of individual action potentials (<1 ms) summation in time of several action potentials is unlikely.

Another type of observable electrical activity in the brain, which is less focal and has slower and weaker fields, is the extracellular field potential [9]. Extracellular field potentials reflect the summation of the extracellular post-synaptic potentials in a large group of neurons in both space and time. They can be measured in the brain when neurons are both arranged in parallel over some distance, and receive synchronized synaptic input [10]. These conditions are typical for the pyramidal cells located in the cerebral cortex. They are organized in such a way that the neighboring dendritic trees lie parallel to each other, orthogonally to the cortical surface (see also the introduction of the pyramidal cell in section 2.3.1.1). The extracellular post-synaptic currents caused by synchronized synaptic input are matched by reverse intracellular currents resulting in arrangements of sinks and sources in the different cortical layers, see Fig. 2.12. The electrical fields caused by the sinks and sources propagate trough the skull to the scalp and evoke measurable potential fields on the scalp surface in the range of $\approx$ 100 μV.

2.5 Recording EEG signals

2.5.1 EEG recording hardware

In order to perform an EEG registration, 4 main hardware components are required: (i) a system of electrodes that are placed on top of the scalp, (ii) an amplifier to amplify the measured signals, (iii) an analog to digital convertor and (iv) a recording device. Modern commercially available EEG recording systems use silver/silver-chloride electrodes, 1 to 3 mm in diameter, and have long flexible leads to plug into the amplifier. A ground electrode is required to amplify a differential voltage with a typical amplification factor around 10.000. The amplified signal is subsequently digitized with a high sampling rate (typically 1000 Hz)

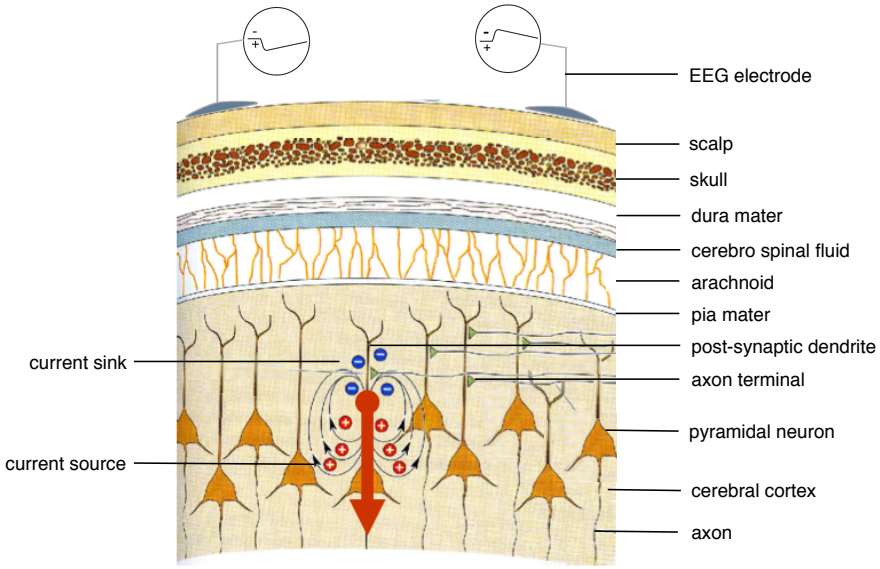

Figure 2.12: Simplified illustration of the extracellular currents (represented by current sinks and current sources) that originate due to post-synaptic activity in the dendrites of aligned pyramidal neurons. The generation of massive synchronized post-synaptic activity causes electrical fields that are measurable on the scalp surface.

using an analog to digital convertor. This leads to millisecond time resolution. A recording device such as a regular computer stores and displays the recorded data.

To acquire high quality data, the proper functioning of the EEG recording electrodes is most critical. To reduce the scalp-electrode impedance, a conductivity gel is used. This gel serves as a conductive medium between the electrode and the scalp surface. Typically an impedance below 5 kΩ is adequate to record high quality scalp potentials. The digitized potentials are then represented over time with respect to a designated reference electrode (see section 2.6).

2.5.2 Positions of the electrodes and spatial sampling

An internationally accepted standard to position the EEG electrodes on the scalp surface is the so called 10-20 or 10-10 system (see Fig. 2.13 for an example of the 10-20 system) [11]. This system determines the

electrode positions with respect to fractions (10 % or 20 %) of the distance between the nasion-inion position and the pre-auricular points. Each electrode channel gets a label. Each label corresponds with the anatomical conventions used to locate the various brain regions. 'F', 'T', 'P', 'O' or 'A', corresponds with an electrode that covers the frontal, temporal, parietal, occipital or auricular regions, respectively. The 'C' label is given for the central electrodes. The even subscripts depict electrodes that are located above the right hemisphere, odd subscripts depict electrodes that are located above the left hemisphere. The z subscripts corresponds with electrodes located on the midline of the brain. 'Fp1' and 'Fp2' depict frontal polar electrode 1 and 2, covering the area on the forehead. In recent EEG systems, more electrodes are used with a higher spatial sampling of the scalp surface. To denote these electrodes, combinations of brain regions are used to indicate the position of the electrode, for example FT, corresponds with a frontal temporal electrode.

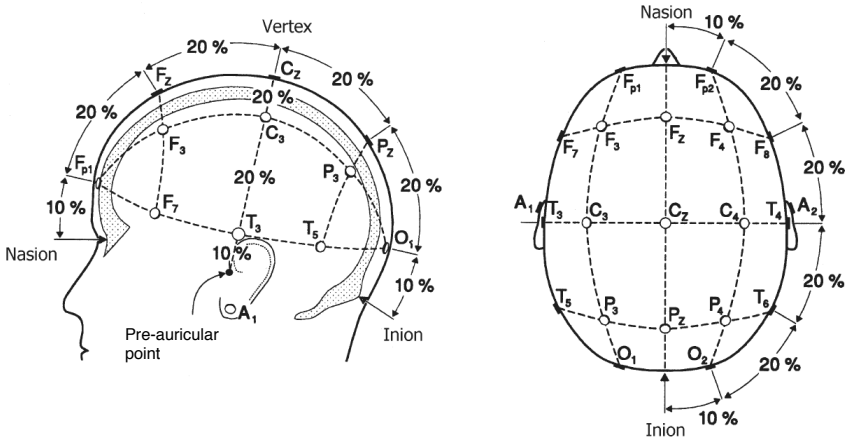

Figure 2.13: The 10-20 system for EEG recordings. Figure adapted from [4].

The spatial sampling depends on the number of electrodes that are used, the application and the hardware provider. In clinical practice for example usually 27 to 32 electrodes are used, see Fig. 2.14a. In modern systems there is a trend to use up to 128 or even 256 electrodes in order to achieve a higher spatial sampling, see Fig. 2.14b and c. These are so called high density EEG recordings. The recordings have a higher sensi-

tivity than regular systems when it comes to measuring the underlying brain activity.

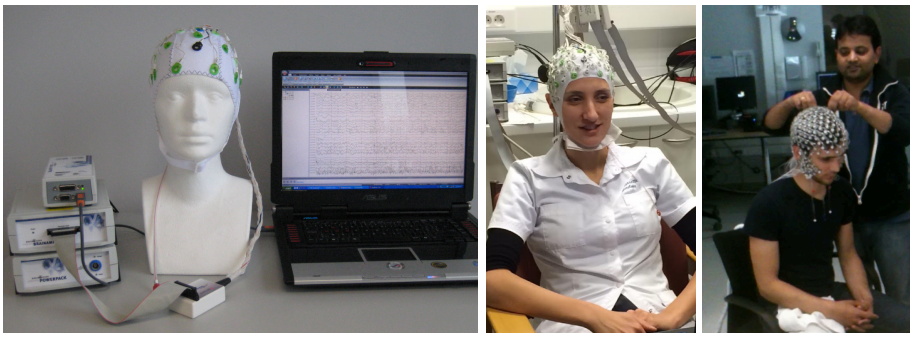

(a) (b) (c)

Figure 2.14: Example of the spatial sampling with (a) 32 electrodes, (b) 128 electrodes, (c) 256 electrodes.

2.6 Visualizing EEG signals

2.6.1 Choice of the reference

An example of an EEG recording is given in Fig. 2.15. The channels are typically presented on the y-axis and the time on the x-axis. In this example, the EEG recording is shown with a single reference, which means that the measured voltages from the reference electrode channel are subtracted from the other electrode channels for each time sample. The choice of the reference electrode channel can differ depending on the purpose of the EEG recording. In order to remove brain unspecific activity, the reference electrode should be affected by global voltage changes in the same way as all the other electrodes because in that case, the unspecific activity is subtracted from the recording by referencing [12]. Moreover, the reference should not pick up signals which are not intended to be recorded, like electrical activity from the heart. Reference choices can be the ear-lobes, the nose, the mastoids (i.e. the bone behind the ears) or central electrodes. When using > 32 electrodes, it is common to compute the "average reference". For this type of referencing, the average over all electrodes is subtracted from each measured electrode signal for each time point. Sometimes, especially in a clinical setting, bipolar

montages are used showing the potential difference over time between adjacent electrodes.

2.6.2 Scalp topography

The measured EEG activity is frequently visualized in a 2-dimensional scalp topography. This makes it easier to determine the most active areas on the scalp. A 2-dimensional topography shows the measured EEG activity at a specific time point for each electrode represented by means of color coding on a plane. The activity corresponding with each electrode is shown on the locations corresponding with the projection of the electrodes on the plane and the points between the electrodes are calculated by interpolation. An example is given in Fig. 2.15. The activity shown in the topography on the right directly corresponds with the peak activity indicated by the vertical blue line on the left.

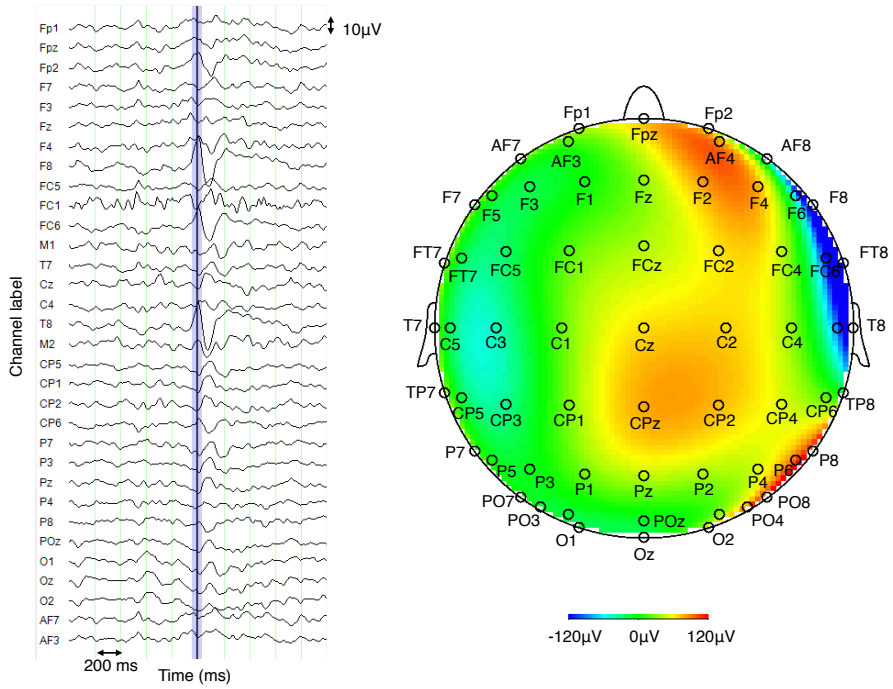

Figure 2.15: Left: Example of an EEG registration in which the electrical potentials are represented with respect to a single reference. Right: Example of the representation of the measured EEG activity by the vertical line in blue shown in a 2D topography on the right.

2.7 Observed activity in EEG

As introduced in section 2.4, the synchronized activity in large groups of pyramidal neurons can produce electrical activity that is observable in the EEG. Typically, two types of EEG phenomena are distinguished. These correspond with rhythmic brain activity or transient brain activity. Often the brain activity is monitored during the presentation of a stimulus or event, for example a picture with a face on it, causing an Event Related Potential (ERP) in the EEG. This kind of activity is usually too weak to be clearly visible in the EEG recording. In order to increase the signal to noise ratio, the EEG data recorded during the presentation of many similar stimuli is averaged.

2.7.1 Rhythmic activity

The rhythmic activity that can be observed in the EEG is a consequence of the rhythmic patterns of actions potentials or rhythmic oscillations in the membrane potentials of pre-synaptic neurons that give rise to oscillating extra-cellular currents in the post-synaptic dendrites. The rhythmic patterns arise from feedback connections between the neurons and can be classified according to the observed frequency content [13]. We distinguish: delta rhythms (frequencies < 4 Hz), theta rhythms (frequencies between 4 and 7 Hz), alpha rhythms (frequencies between 8 and 13 Hz), beta rhythms (frequencies between 14 and 30 Hz) and gamma rhythms (frequencies > 30 Hz) shown in Fig. 2.16A. Based on the amplitude and frequency of the rhythms, the observed EEG signals can be used to study and identify normal and abnormal brain conditions (see section 2.9 for some examples).

2.7.2 Transient activity

Next to the rhythmic activity, transient phenomena can be observed in the EEG. In panel B of Fig. 2.16, an example is given of spiking activity which is often observed in EEG recordings of patients with epilepsy. During sleep, the EEG shows transient features such as vertex waves and sleep spindles. Each transient feature reflects a certain condition of the brain and the origin and morphology of the feature can be used to characterize this condition.

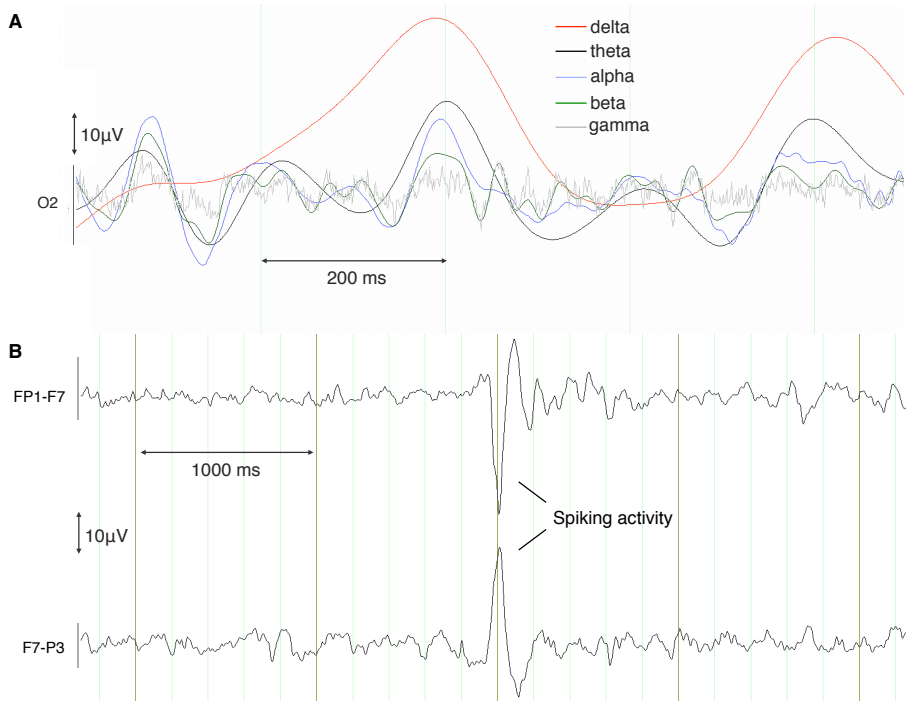

Figure 2.16: Panel A: Different kinds of rhythmic activity observed in a right occipital channel O2. The delta, theta, alpha, beta and gamma activity is respectively shown in red, black, blue, green and gray. Panel B: Example of an epileptic spike shown on 2 channels of a bipolar montage.

2.7.3 Event related potentials

The response of the brain is often monitored after the presentation of a stimulus or event during a continuous EEG recording. After the recording of the EEG data, the data is divided into separate segments corresponding with the presentation of a stimulus, called a trial, in which the zero time point is defined as the stimulus onset, see Fig. 2.17. The trails can then be averaged in order to increase the signal-to-noise ratio (SNR).

2.7.3.1 Evoked responses

If it is assumed that the brain response is very similar across trials, the averaged activity across the trials, time-locked to the stimulus is called an event related response. See the left part of Fig. 2.18 for an illustrative example. If the noise is assumed to be random, decreasing the noise level

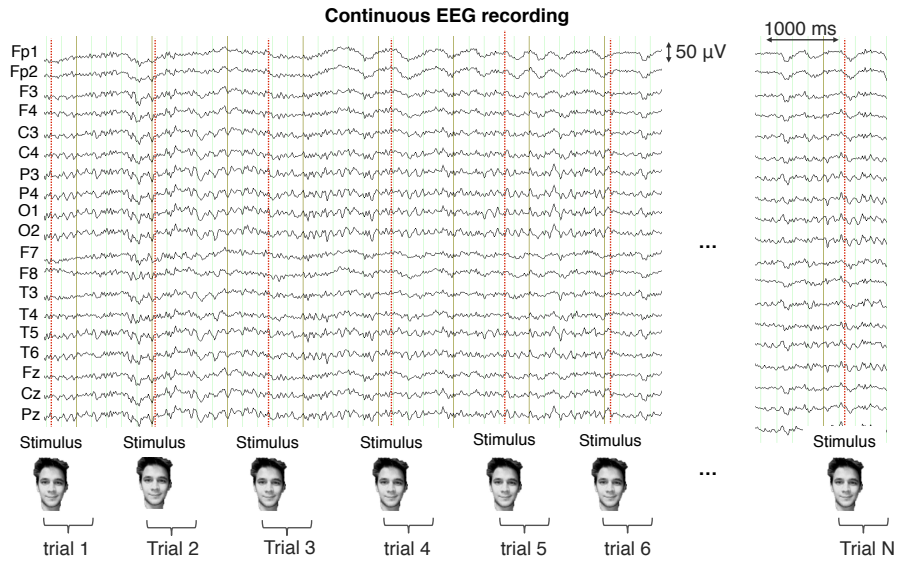

Figure 2.17: Illustrative example of a continuous EEG registration in which stimuli of faces are presented to the participant. The brain response, time locked to the presentation of the stimulus, is called a trial. N trials are presented to the participant.

with a factor N would require N^2 trials that have to be averaged. If we assume the noise level in an EEG recording is typically around 20 μV, and the signal of interest around 5μV, this means that averaging over 100 trials, would reduce the noise level to 2 μV. This is important when designing a study to analyze brain activity because it defines the duration of the experiment.

2.7.3.2 Induced responses

If the brain response is similar across trials, but the phase of the activity is changing for each of the stimuli, a different averaging technique is needed. Especially for high frequency oscillations, like gamma activity (with frequencies $>$ 30 Hz), the phase of the oscillating activity can be different from trial to trial, so averaging would result in zero activity. Such brain responses are termed as induced responses so as to differentiate them from evoked responses. In order to increase the signal to noise level for induced responses, the phase information needs to be included in the averaging procedure. This is typically done by computing a spectrogram, in which the frequency spectrum is plotted over time and the

trials can be aligned depending on the occurrence of activity in a certain frequency band. For a more detailed explanation we refer the reader to [14]. An illustrative example is given in Fig. 2.18.

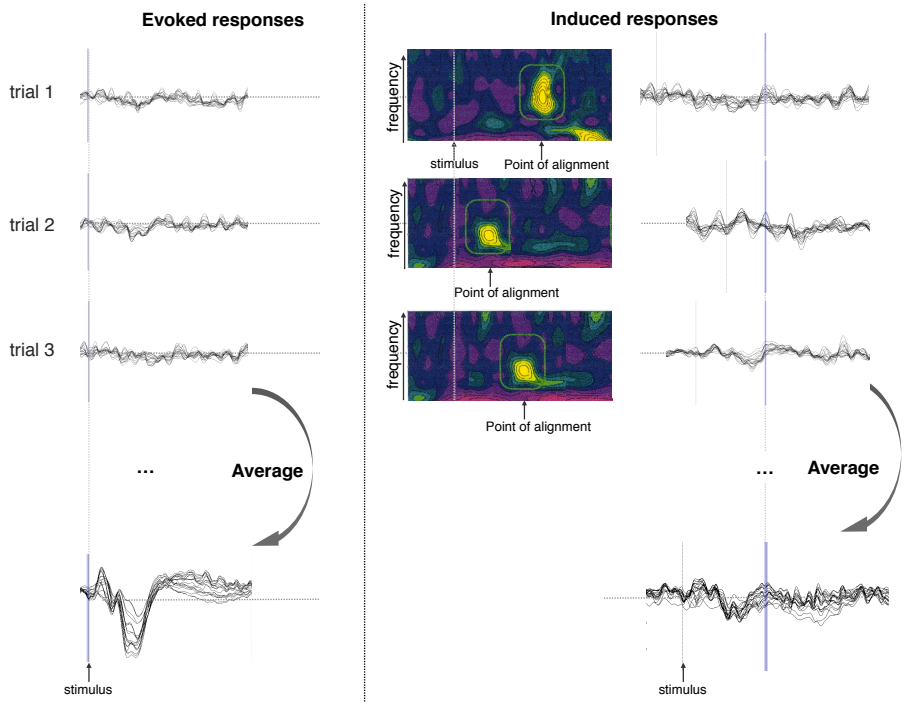

Figure 2.18: Illustrative example of the averaging procedures for evoked and induced responses.

2.8 EEG artifacts

2.8.1 Biological or environmental

Because the EEG electrodes register electrical activity generated by every source in their vicinity, the EEG recordings are often contaminated by activity from sources that are not related to brain activity. This kind of recorded activity, called artifacts (or noise), can either be of biological (when it is caused by the subject) or environmental (when it is caused by the environment) nature. Typical biological artifacts are ocular, muscle and cardiogenic artifacts. The artifacts originating from the environment are commonly caused by the power line (50 Hz in Europe) and the EEG

hardware, for example when an EEG electrode is not functioning well or is not attached on the scalp surface. Some examples of common artifacts are shown in Fig. 2.19. The ocular artifacts are especially observed in the frontal polar channels, 'Fp1', 'Fp2', 'Fpz' and typically have a duration of ≈ 200 ms. Muscle artifacts can be caused by chewing or teeth grinding, jaw movements, activity of the facial muscles, etc. They can exhibit high amplitudes, high frequencies (> 100 Hz), and a long duration. The power line typically causes a 50 Hz buzz in the EEG recording.

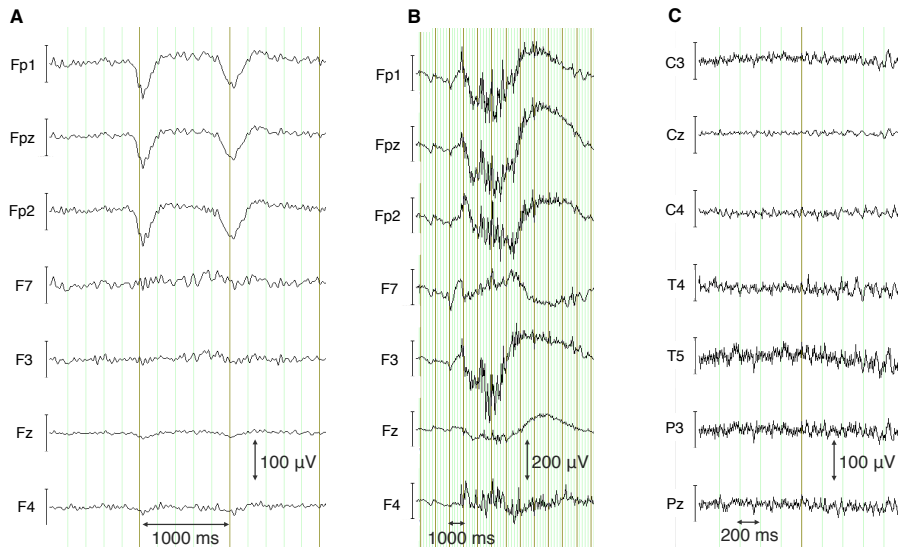

Figure 2.19: Panel A: example of ocular artifacts due to eye blinks. The frontal polar channels, 'Fp1', 'Fp2' and 'Fpz' pick up electrical activity caused by eye movements. Panel B: example of muscle artifacts. Panel C: example of the 50 Hz noise due to the power line.

2.8.2 Artifact handling

Five strategies to deal with EEG artifacts can be distinguished. The first and most straightforward strategy is to avoid recording unwanted activity. To avoid environmental activity, the EEG signals can be recorded in a Faraday cage. However this limits the recording of EEG signals to specialized rooms which are expensive and can be inconvenient. Also the proper usage of a conductive gel between the electrodes and the scalp can remove environmental activity and increases the signal to noise ratio. To reduce the biological artifacts, the subject can be instructed in

such a way as to limit as much as possible the biological noise during the periods of interest in the EEG. One can ask the subject to relax, to refrain from grinding his teeth, or from making too many movements using the facial muscles or the jaw during these periods.

The second strategy of artifact handling is to use an averaging approach to the EEG signals as was presented in section 2.7.3. The main assumption is that the noise present in the recording, is random and the signal of interest is stable. When several trials of the same EEG signals of interest, locked to a certain event, are averaged, the random noise will cancel itself out.

The third strategy involves the rejection of the parts in the EEG recordings that contain artifacts. For example by removing the EEG segments that contain eye-movement artifacts. This approach can however be a time-consuming process because it mainly relies on visual inspection. Moreover, some artifacts are not always clearly visible in the recording. Methods have been developed that allow identification of bad channels in the EEG recordings and detection of bad segments. These methods are usually based on tresholding or time-frequency analysis because artifacts usually contain high power at certain frequencies [15]. The disadvantage of these methods is that they rely on specific rejection criteria and additional visual inspection is often necessary to remove the false positives and false negatives. Another approach is to detect the artifacts based on additional measurements. For example eye movement artifacts can be detected by placing electrodes above and below the eye to record the electric field around the eye in the so called electrooculogram (EOG). Based on these signals the eye movement artifact can be removed by a simple subtraction of the propagated EOG activity at each channel [16].

The fourth strategy is based on filtering techniques. This is probably the fastest and easiest way to remove artifacts. The 50 Hz noise from the powerline can for example be filtered out by a simple notch filter at 50 Hz. Usually high-pass filtering is applied to filter out frequencies below 0.01 Hz. This way, slow changes in the signals that can be caused by sweating and drifts in the electrode impedances, can be filtered out. High frequency activity caused by contraction of the muscles can be removed from the recordings using low-pass filtering with a cut-off frequency of 100 Hz for example. Note however that one has to be careful with filtering techniques because the used filters can also remove signals of interest from the recordings.

The final approach is to select the relevant activity using data decomposition techniques. The currently most popular approach to correct for artifacts is based on independent component analysis (ICA) [17]. This technique relies on the hypothesis that brain activity is the result of a superposition of several independent activities. The activity produced by an eye blink or eye movement is considered to be represented as one such independent component. This interpretation is physiologically well justified and ICA has proven its strength in detecting and removing of ocular artifacts [18, 19]. Other types of artifacts, i.e. from muscle activity and electrical noise, have been successfully characterized and removed by ICA as well, making it the method of choice to clean up EEG recordings [20].

2.9 Applications

Since EEG is a relatively cheap and easy applicable technique to record brain activity, it can be applied into various fields: medicine, research, brain computer interfaces and neuromarketing. Note that this is not a strict classification because the application fields often overlap. Some examples for each category are given in the next sections.

2.9.1 Medical

2.9.1.1 Epilepsy

EEG is the technique of choice to record brain activity for diagnosing epilepsy. Epilepsy is a neurological disorder characterized by recurrent epileptic seizures and epileptiform discharges in the brain. These seizures and dischagers are expressed in the EEG as ictal epileptic seizure activity and interictal epileptiform discharges (IED). Based on the topography, morphology and typical signature of the ictal and interictal activity, clinicians are able to classify the type of epilepsy. This is used to plan treatment. An example of an interictal spike, a special type of interictal epileptiform discharge, is given in Fig. 2.16B. An example of ictal seizure activity is shown in Fig. 2.20.

2.9.1.2 Sleep

In clinical investigations of sleeping behavior, EEG is commonly used to study the different stages of sleep. The sleep of the patient is typi-

Figure 2.20: Example of EEG seizure activity. The starting point of the seizure is marked by the vertical red line.

cally registered with EEG electrodes during the whole night to identify different types of brain waves that are generated during sleep. These types of brainwaves can be divided into rapid eye movement (REM) and non-rapid eye movement (NREM) types of sleep. The NREM type is further subdivided into 3 main stages depending on the features of the brain waves such as theta and delta activity. Depending on the sequence and duration of the different sleep stages, clinicians can observe whether the patient suffers from sleep disorders such as insomnia, sleep apnea, hypersomnia, REM behavior disorders, etc.

2.9.2 Research

In general, EEG is a technique that is often used in cognitive neuroscience to monitor brain activity during the execution of a specific cognitive task corresponding with a certain event or stimulus. There are a lot of different research paradigms to study brain activity. They differ depending on the stimuli, timing of the stimuli, sequence of the different stimuli, etc. As mentioned in section 2.7.3, the response of the brain to specific events or stimuli typically elicits an event related potential (ERP) in the EEG, i.e. an evoked or induced response. The study of

event related potentials can help to depict the regions in the brain that are functionally integrated (see section 2.3.3) in order to perform a cognitive task. In chapter 5 and 6, two types of event related potentials are investigated corresponding with respectively, checkerboard stimuli and stimuli of house, faces, inverted faces and words.

2.9.3 Brain Computer Interfaces

The recording of brain activity can be used in order to communicate directly with an external device, which is called a brain computer interface. Based on a well-chosen paradigm, the brain activity of a user can be monitored with EEG and processed in such a way that features reflecting the user's intent can be extracted. For example in awake people, the primary sensory and motor cortical areas typically evoke 8-14 Hz activity in the EEG recordings when the areas are not engaged in processing sensory input or producing motor output. Movement, or preparation for movement is typically accompanied by a decrease of this activity, in the motor areas contralateral to the movement. These effects also occur during imaginary movement of the limbs and can be detected in the EEG using advanced signal processing techniques. A clinical application of this phenomenon is to restore the communication for patients with the locked-in syndrome, a condition in which the patient is aware but cannot move or communicate due to complete paralysis [21].

2.9.4 Neuromarketing

A rapidly growing and new application is related to the field of neuromarketing. Neuromarketing investigates the behavior of customers by studying the brain in order to advice companies in their marketing campaigns. EEG recordings of subjects are used to investigate how the subject is responding when a specific product or brand is presented as a stimulus. Based on the measured activity neuroscientists develop techniques that allow to measure "the physiological state" of the subject in order to optimize the customers experience. It is a new application field which is still very experimental but has high potential [22, 23].

The described applications in this chapter are all related to the processing of the signals at the level of the electrodes. The signals however indirectly provide spatial information of the active areas in the brain. In order to reveal this information, EEG source imaging techniques are applied. An overview of EEG source imaging together with the recent

development is given in the next chapter.

Chapter 3

EEG source imaging

"The pot is full of secrets to be told"
Radiohead - Staircase

3.1 Introduction

Several physical phenomena in nature are characterized by sources of activity that propagate their energy through a medium reaching the place where they can be observed. The estimation of the activity and location of these sources based on the observations requires solving an inverse problem. Depending on the application, there may not be enough information to find a unique solution, i.e. to clear the unknowns, making the problem ill-posed.

The estimation of the sources that generate the measured EEG activity, a process called EEG source imaging (ESI), requires solving an ill-posed problem [24]. The recorded electrical EEG activity originates from several areas in the brain and propagates trough different tissues in the human head before reaching a limited number electrodes on the scalp. Consequently, deriving a realistic and unique solution rests on prior knowledge, in addition to the observed EEG measurements.

Any EEG source imaging approach is characterized by a generative model or forward model of the EEG data and an inverse technique to find a solution, see Fig. 3.1. The forward model includes a biophysical source model of the brain sources and the definition of a source space. It includes information about the physical and geometrical properties of the head, included in the head model. Using techniques to calculate

the field propagation of the sources through the different tissues in the head, EEG signals can be generated in function of the sources. An inverse technique defines then a cost function based on the difference between the generated and measured EEG data, i.e. the residuals, that is optimized in order to find the optimal solution of the sources.

In the following sections we will introduce a brain source model and explain how we model the field propagation of the sources through the various tissues in the human head to the electrodes. We subsequently discuss several inverse techniques that were developed over the last 20 years. Next an overview is given of the features of EEG source imaging related to other functional neuroimaging techniques. We finally present some applications.

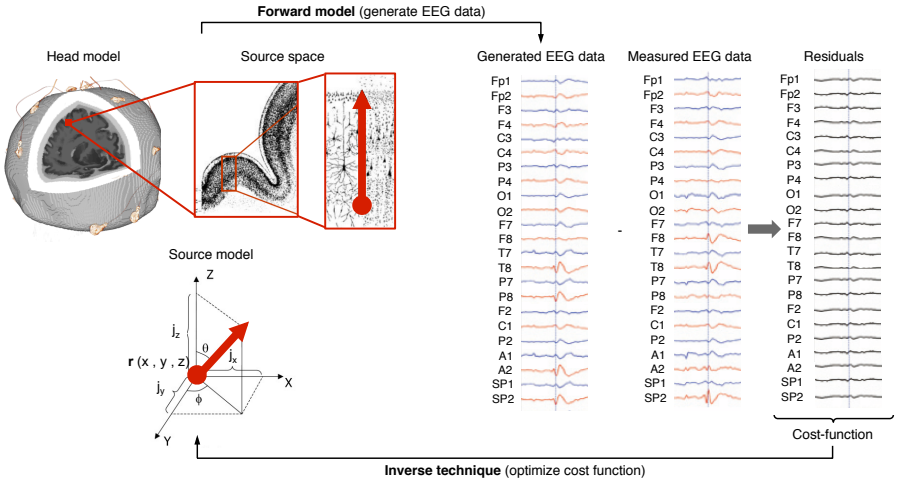

Figure 3.1: Illustration of the EEG source imaging principle using a forward model and an inverse technique.

3.2 EEG forward modeling

3.2.1 The current dipole

In order to model the measured EEG signals, a biophysical model of the sources that are generating the activity is required. As discussed in section 2.4, the major generators of scalp EEG signals are the synchronized extracellular post-synaptic currents which flow between the layers

of parallel pyramidal neurons in the cerebral cortex. These currents can be represented using a current dipole. It represents the postsynaptic currents at the apical dendrites (see Fig. 3.2) and has 6 parameters: the position $\mathbf{r} = [x,\ y,\ z]$, the orientation (ϕ and θ) and the intensity (I). The orientation and intensity can also be described by the dipole moment $\mathbf{j} = [j_x\ j_y\ j_z]$, with $||\mathbf{j}|| = 2sI$ and s the inter-distance between the current sink (-I) and current source (+I) [25].

Typically an arrangement of current sinks and sources in a cortical area of 4 mm $\times$ 4 mm $\times$ the thickness of the cortex (4 or 5 mm) is needed to generate EEG signals that are measurable on the scalp surface. This criterium determines the intrinsic spatial resolution of EEG source imaging.

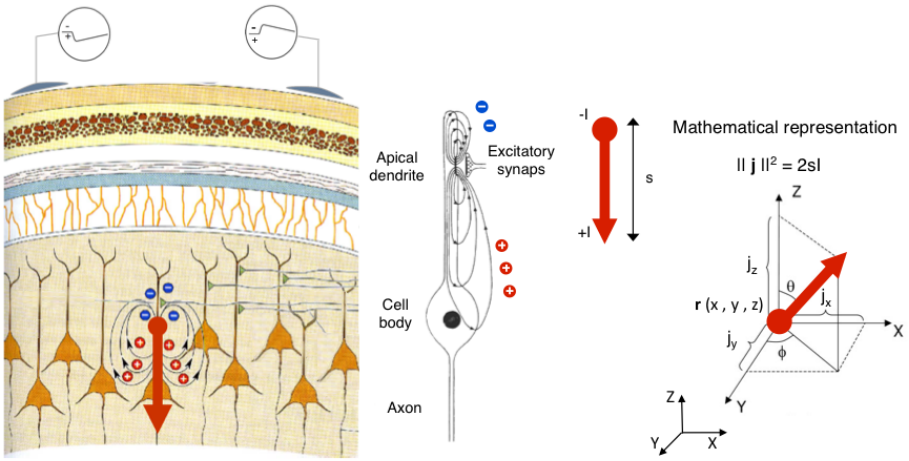

Figure 3.2: The current dipole representation of the synchronized postsynaptic currents at the apical dendrites. We consider a current sink (-I) and a current source (+I) with interdistance equal to s. The current dipole can be characterized by 6 paramaters: the position $\mathbf{r} = [x,\ y,\ z]$, the orientation (ϕ and θ) and the intensity (I) or equivalently, the orientation and intensity can also be described by the dipole moment $\mathbf{j} = [j_x\ j_y\ j_z]$.

3.2.2 The head model

To model the field propagation of the current dipole sources to the electrodes, a description of the electromagnetic and geometrical properties

of the head is required. Due to computational limitations, early EEG source imaging techniques used (multi-layer) spherical models to approximate the human head [26], which is an oversimplification of reality. As a first step towards more realistic head modeling, extra anatomical information about the human head can be incorporated based on structural images of the head.

3.2.2.1 Geometry

Magnetic Resonance Imaging (MRI) is a noninvasive technique that allows to produce a high resolution 3D image of the head. It provides excellent soft tissue contrast, e.g. between the gray and white matter in the brain. An example of a structural MR image is shown in Fig. 3.3A.

Computed Tomography (CT) is a technique in which X-rays are used to make tomographic images of the brain. Detailed anatomical images of the skull, which is not visible in MR images, can be acquired. An example of a CT image is shown in Fig. 3.3B.

In order to construct a realistic head model including the geometry and electromagnetic properties of the head, MR images and sometimes CT images are used. The overall structure of the head is rather complicated. The brain, skull, scalp and other parts of the head such as the eyes, vessels, nerves, cerebrospinal fluid, etc. comprise various tissues and cavities of different electrical conductivity. In the construction process of the head model, these complications are generally ignored.

In Fig. 3.3C we show 2 typical types of head models constructed based on a high resolution anatomical Magnetic Resonance (MR) image of the human head. The head model contains 3 or 4 different layers: scalp, skull, brain and cerebrospinal fluid which are segmented from the MR image. Each tissue has a specific conductivity value (see the next section). A more advanced, 7-layered, head model constructed using both MR images and CT images is shown in Fig. 3.4. The most widely used open source packages to segment MR images in order to extract the different layers in the head are the Statistical Paramateric Mapping Software [27], the Freesurfer toolbox [28], the FSL toolbox [29] and the Brainstorm toolbox [30].

MR and CT images are however not always available due to additional costs for the acquisition of the images and the subject or patient is radiated with X-rays during the acquisition of a CT image. In case no anatomical images are available, template MR images are used, for ex-

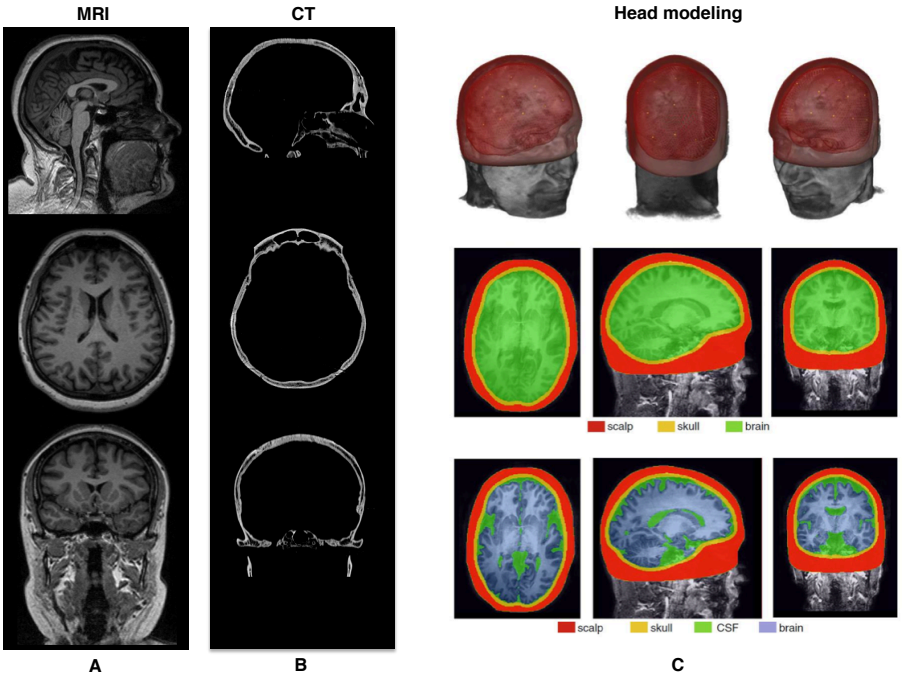

Figure 3.3: A: Example of a sagittal, horizontal and coronal slice of an MR image of the human head. B: Example of a sagittal, horizontal and coronal slice of a CT image of the human head. C: head model constructed based on segmentation of an anatomical MR image.

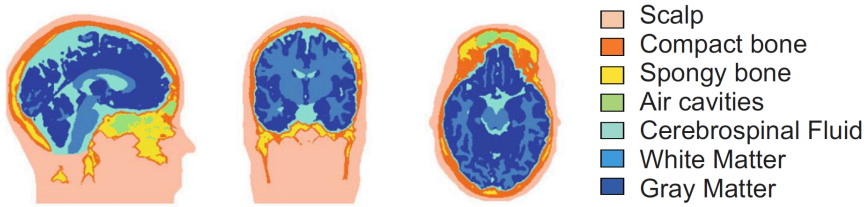

Figure 3.4: Example of a 7-layered head model including scalp, compact bone, spongy bone, air cavities, cerebrospinal fluid, white and gray matter segmented from MR and CT images.

ample the colin template [31], to construct a template head model (see also chapter 5).

3.2.2.2 Conductivity

The electrical conductivity of brain tissue is highly anisotropic. The conduction is 10 times greater along an axon fibre than in the transverse direction. It is currently impossible to accurately measure the detailed conductivity of all tissues in vivo and to account for them in the solution of the forward model [32, 33]. Therefore, the head is usually modeled simplified as a set of homogeneous volume conductors with isotropic conductivity values that are reported in literature based on in-vivo measurements (see table 3.1).

	Conductivity (S/m)			
	[34]	[35]	[36]	[37]
Scalp	0.33	0.22	0.3279	0.43
Compact bone	-	-	0.0064	0.008
Spongy bone	-	-	0.02865	0.025
Skull	0.0041	0.015	0.0041	0.01
Gray Matter	0.33	0.22	0.3333	0.33
White Matter	0.33	0.22	0.1428	0.14
CSF	-	-	1.79	1.79
Air	-	-	0	0

Table 3.1: Overview of the isotropic conductivity values reported in literature.

3.2.2.3 Electrode positions

The accurate modeling of the positions of the electrodes on top of the scalp in the head model is crucial in the forward model because the electrode positions directly relate to the position of the sources, the different tissues in the head model and the field propagation of the sources. We distinguish 3 main strategies depicted in Fig. 3.5 to derive the electrode positions.

Often the default electrode positions are used corresponding with the 10-10 or 10-20 system for example. In this approach, the default electrode positions are coregistered to the head model and are warped onto the scalp surface of the head model.

A more accurate approach is to determine the electrode positions based on electromagnetic measurements of the position for each electrode using a Polhemus (Colchester, USA) digitizer system for example, shown in Fig. 3.5B. The measured positions are subsequently coregistered with the head model and warped onto the scalp surface.

A final approach is to segment the electrode positions from structural images such as a CT image shown in Fig. 3.5C. Also markers are used placed on top of the electrodes that are clearly visible in an anatomical MR image.

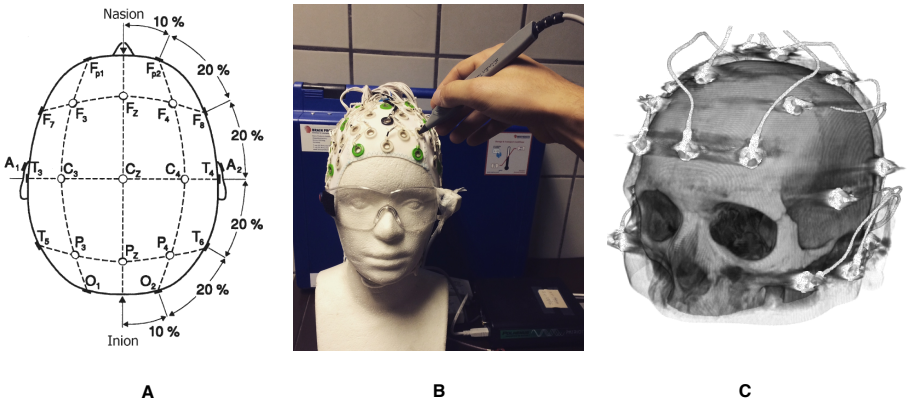

Figure 3.5: Approaches to determine the positions of the electrodes. A: the default electrode positions, B: based on a positioning system, C: using a CT image.

3.2.2.4 Dipole source space

Because the major generators of scalp EEG signals are located in the cerebral cortex (see section 2.4), the dipole source space is typically restricted to the gray matter. The cortical surface is often extracted from an anatomical (template) MR image and the dipoles are restricted to the meshes of the surface, see Fig. 3.6A. A more general approach is to restrict the sources to the segmented gray matter segmented from a (template) MR-image, see Fig. 3.6B. The orientation of the dipoles are usually chosen orthogonally to the cortical surface. This is based on the fact that the layers of parallel pyramidal neurons in the cortex are orientated orthogonally to the cortical surface [38].

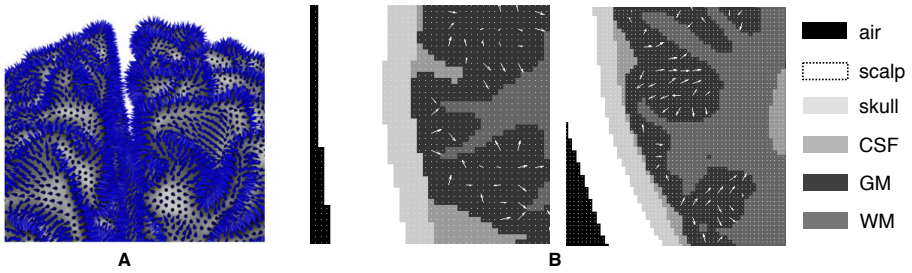

Figure 3.6: Dipole sources restricted to A: the cortical surface (in blue), B: inside the gray matter (depicted by the arrows in white). The orientations of the dipole sources are chosen orthogonally to the cortical surface.

3.2.3 Algebraic representation of the forward model

With the source model and head model in mind, the EEG forward model can be represented algebraically as the potentials, assume $\mathbf{V} \in \mathbb{R}^{N_c \times 1}$ of N_c channels, that are generated by a current dipole source at the position $\mathbf{r} = [x,\ y,\ z]$ and intensity of the dipole moment $\mathbf{j} = [j_x\ j_y\ j_z]$:

$$\mathbf{V} = \mathbf{L}(\mathbf{r})\mathbf{j}(\mathbf{r}) \tag{3.1}$$

where $\mathbf{V} \in \mathbb{R}^{N_c \times 1}$ represents the EEG signals of N_c channels and $\mathbf{j}(\mathbf{r}) \in \mathbb{R}^{3 \times 1}$ the amplitude of a current dipole at location $\mathbf{r}$ in 3 orthogonal directions. The lead fields $\mathbf{L}(\mathbf{r}) \in \mathbb{R}^{N_c \times 3}$, represent the field propagation of the current dipole to the electrodes on the scalp and embodies the forward model.

Because of the superposition principle, Eq. (3.1) also holds for multiple active sources:

$$\mathbf{V} = \mathbf{L}(\mathbf{r}_1)\mathbf{j}(\mathbf{r}_1) + \mathbf{L}(\mathbf{r}_2)\mathbf{j}(\mathbf{r}_2) + \cdots + \mathbf{L}(\mathbf{r}_P)\mathbf{j}(\mathbf{r}_P) \tag{3.2}$$

With P the number of dipoles on a variable location $\mathbf{r}_1, \mathbf{r}_2, \ldots \mathbf{r}_P$. As such, we can assume that the EEG measurements are generated by P sources.

We can also assume that N_d sources defined at fixed locations $\mathbf{r}_i$ ($i = 1 \ldots N_d$) and with dipole moments $\mathbf{j}_i$ ($i = 1 \ldots N_d$) are generating the EEG signals. In this case the forward model can be rewritten as:

$$\mathbf{V} = \mathbf{L}\mathbf{J} \tag{3.3}$$

where $\mathbf{J} = [\mathbf{j}_1, \mathbf{j}_2, \ldots, \mathbf{j}_{N_d}]^T$ is a vector of current dipoles at N_d locations and where $\mathbf{j}_i = [\mathbf{j}_{x,i}, \mathbf{j}_{y,i}, \mathbf{j}_{z,i}]^T$ is encoding both the orientation and amplitude of the i-th dipole. $\mathbf{L} = [\mathbf{L}(\mathbf{r}_1), \mathbf{L}(\mathbf{r}_2), \cdots, \mathbf{L}(\mathbf{r}_{N_d})] \in \mathbb{R}^{N_c \times 3N_d}$ is the lead field matrix linking the source amplitudes in $\mathbf{J}$ of the assumed dipoles on fixed locations to the electrical potential $\mathbf{V}$.

3.2.4 Modeling the field propagation of the current dipole

In order to calculate the field propagation of the current dipole to the electrodes on the scalp, i.e. to compute the lead fields, an electromagnetic problem has to be solved that can be expressed with classical electromagnetism. In what follows we describe the equations of classical electromagnetism corresponding with the description of a current dipole and the head model including different layers with different electromagnetic properties. We derive the poisson equation which is used to calculate the electrical potentials on the scalp surface caused by a current dipole.

3.2.4.1 Derivation of Poisson's equation

The Maxwell's equations are:

$$\nabla \cdot \mathbf{E} = \frac{\rho}{\epsilon} \tag{3.4}$$

$$\nabla \cdot \mathbf{B} = 0 \tag{3.5}$$

$$\nabla \times \mathbf{E} = -\frac{\partial \mathbf{B}}{\partial t} \tag{3.6}$$

$$\nabla \times \mathbf{B} = \mu\mathbf{j} + \mu\epsilon\frac{\partial \mathbf{E}}{\partial t} \tag{3.7}$$

where $\mathbf{E}$ and $\mathbf{B}$ are the electric field and magnetic field respectively, $\mathbf{j}$ is the current density vector field, ρ is the charge density, ϵ the electrical

permittivity, and μ) the magnetic permeability each of them dependent on the position. The electrical permittivity represents the resistance of the medium, i.e. the different modeled layers in the head model, when forming an electrical field in the medium. The magnetic permeability represents the ability of the medium to support the formation of a magnetic field in the medium. Eq. (3.4) represents Gauss' law that describes the relation between the distribution of electrical charge and the resulting electrical field. Eq. (3.5) represents Gauss' law for magnetic fields, which states that there are no sources of magnetic fields, analogue to electrical charges. Eq. (3.6) represents Faraday's law that describes that a changing magnetic field generates electrical fields. Eq. (3.7) represents Ampères law that describes the relation between the magnetic field induced by an electrical current and a changing electrical field.

Assuming isotropic conductivities in the head model Ohm's law states that:

$$\mathbf{j} = \sigma \mathbf{E} \tag{3.8}$$

where $\sigma(x, y, z)$ is the position dependent conductivity. The law describes that the current through a conductor is directly proportional to the electrical field. If we furthermore add the continuity equation for electrical charges:

$$\nabla \cdot \mathbf{j} = \frac{\partial \rho}{\partial \mathbf{t}} \tag{3.9}$$

that states that electric charge can neither be created nor destroyed, we are able to describe all electromagnetic phenomena based on Eq. (3.4)-(3.9).

For EEG measurements, we are only interested in the electrical field $\mathbf{E}$. The Maxwell's equations can be simplified significantly by noting that the media comprising the head model have no significant capacitance, i.e. charge does not accumulate in the volume or on tissue interfaces and the charges are redistributed in negligible time. This means there are no electromagnetic wave propagation phenomena [39]. This simplification allows us to adopt a quasistatic approximation of Maxwell's equations, which means that, in the calculation of $\mathbf{E}$, $\frac{\partial \mathbf{B}}{\partial t}$ and $\frac{\partial \mathbf{E}}{\partial t}$ can be ignored as source terms. Physically, these assumptions mean that the instantaneous current density only depends on the instantaneous current sources. Eq. (3.6) then becomes $\nabla \times \mathbf{E} = 0$ and the electric field $\mathbf{E}$ can be expressed as the negative gradient of a scalar field, the electrical position dependent

potential U(x,y,z):

$$\mathbf{E} = -\nabla U. \tag{3.10}$$

Due to the linearity of the Maxwell equations the current density in the head model, consists of a current density imposed by the dipole source, or forced current density $\mathbf{j}_f$, and the return current $\mathbf{j}_r$ which is the result of the macroscopic electric field in the conducting medium, as expressed by Ohm's law. The total current density $\mathbf{j}_{tot}$ flowing through the media becomes:

$$\mathbf{j}_{tot} = \mathbf{j}_r + \mathbf{j}_f = \sigma\mathbf{E} + \mathbf{j}_f = -\sigma\nabla U + \mathbf{j}_f \tag{3.11}$$

based on Ohm's law and Eq. (3.10). Neglecting the capacitance of the head tissues translates mathematically into zero divergence of the current density $\nabla \cdot \mathbf{j}_{tot} = 0$. By taking the divergence of Eq. (3.11), we obtain the Poisson's equation:

$$\nabla \cdot (\sigma\nabla U) = \nabla \cdot \mathbf{j}_f \tag{3.12}$$

which is at the heart of the forward problem in EEG. It links the current source $\mathbf{j}_f$ and the electrical potential U.

3.2.4.2 Numerical solvers: overview

Eq. (3.12) can be solved for U in various ways, depending on the geometry of the head model, the form of the conductivity σ in the head model and the location of the sources $\mathbf{j}_f$. An overview of the open-source toolboxes including different techniques to calculate the field propagation of the sources is given in table 3.2.

An analytical solution is possible only for particular cases: a highly symmetrical geometry (e.g. concentric spheres) and homogenous isotropic conductivities. This approach is implemented in the CARTOOL software, a toolbox designed for the localization of epileptic spikes [40].

For other more general cases, numerical methods are required. Typical methods include the 'Finite Element Method' (FEM) [37, 41–45], the

'Finite Difference Method' (FDM) [46–50] and the 'Boundary Element Method' (BEM) [51–53].

The BEM approach is based on the hypothesis that the head volume is divided into subvolumes of homogeneous and isotropic conductivity, and the potentials are only estimated on the surfaces separating these subvolumes. The BEM only allows to use closed compartments with the limitation that usually only 3-layered head models can be modeled. BEM models are used in the OpenMEEG, Fieldtrip and Statistical Parametric Mapping Software.

The FEM and the FDM approach are similar and are based on the hypothesis that the head volume is divided in small volume elements. The only difference is the fact that the volume elements are of arbitrary shape (usually tetrahedron or regular polyhedron) using the FEM while the volume elements are cubic with the FDM. Therefore the FEM approach is more flexible but also computationally more intensive. The MRI (or CT) images used to construct the head models are however intrinsically cubic so there is a direct correspondence with the FDM approach. The FEM and FDM make no assumptions about the shape of the volume conductivity and allow the estimation of U at any location in the volume. The volume is tessellated into small volume elements in which Maxwell's equations are solved locally. As each volume element is characterized by its own conductivity. Any configuration of conductive volume can be modeled. Therefore the FDM and FEM are the techniques of choice to construct accurate and realistic head models based on structural images. In chapter 5 a more extensive discussion is presented. We refer the reader to [54], for a comprehensive overview on the field of EEG forward modeling.

	Toolbox
spherical	CARTOOL [40]
BEM	OpenMEEG [55], Fieldtrip [34] (SPM [56])
FEM	Simbio (neuroFEM) [57]
FDM	Developed at Ghent University [58, 59]

Table 3.2: Overview of the toolboxes to calculate the field propagation of a current dipole to the electrodes. Note that the Statistical Paramateric Mapping (SPM) toolbox relies on the Fieldtrip toolbox.

In this dissertation, we made use of the finite difference method based on reciprocity for isotropic media [49, 50]. The implementation of the approach is explained in the next section.

3.2.4.3 The Finite Difference Method

Implementation

For the finite difference approach, the head model consists of volume elements defined by a cubic grid as illustrated in Fig. 3.7, where h_x, h_y and h_z correspond with the size of the cubic volume elements in x, y or z direction. The potentials on the nodes surrounding the central node (depicted by 0) of the cubic grid are defined as U_i, with $i = 1 \ldots 6$.

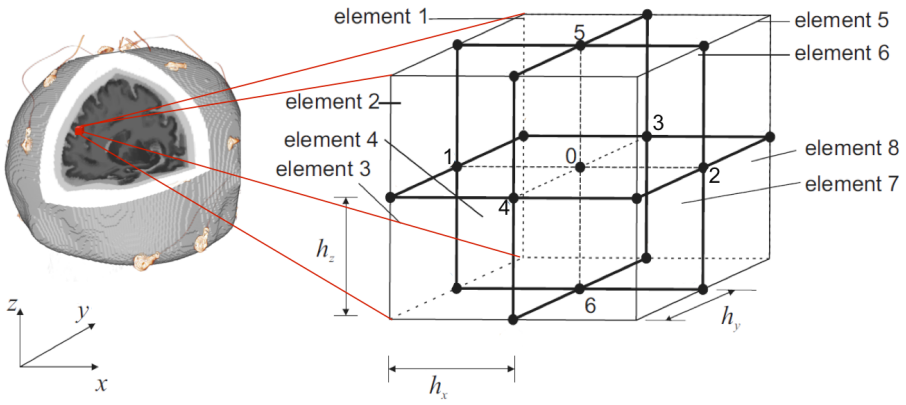

Figure 3.7: The 3D cubic grid. The potentials in the nodes surrounding the node in the center, i.e. 0, are numbered from 1 to 6.

We assume a dipole model in which the dipole is represented by 2 monopoles ($-I$ and $+I$) extending over 3 voxel nodes in x, y or z direction and the center node represents the dipole position, see Fig. 3.8 for an example of a dipole in the z-direction. For such a current dipole model, we can write Eq. (3.12) as [49, 60]:

$$\nabla \cdot (\sigma \nabla U) = -I\delta(\mathbf{r} - \mathbf{r}_2) + I\delta(\mathbf{r} - \mathbf{r}_1) \tag{3.13}$$

where $\mathbf{r}_1 = [x_1, y_1, z_1]^T$ and $\mathbf{r}_2 = [x_2, y_2, z_2]^T$ correspond with the locations of the nodes and representing a current sink and source respectively. Expanding Eq. (3.13) yields:

$$\begin{aligned}
&\sigma\frac{\partial^2 U}{\partial x^2}+\sigma\frac{\partial^2 U}{\partial y^2}+\sigma\frac{\partial^2 U}{\partial z^2}+\\
&+\frac{\partial\sigma}{\partial x}\frac{\partial U}{\partial x}+\frac{\partial\sigma}{\partial y}\frac{\partial U}{\partial y}+\frac{\partial\sigma}{\partial z}\frac{\partial U}{\partial z}=\\
&-I\delta(x-x_2)\delta(y-y_2)\delta(z-z_2)+\\
&I\delta(x-x_1)\delta(y-y_1)\delta(z-z_1).
\end{aligned} \tag{3.14}$$

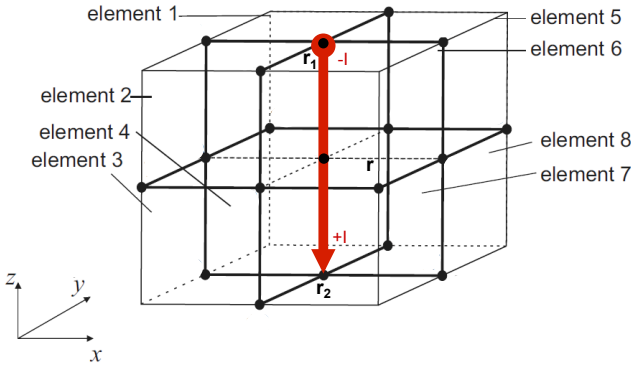

Figure 3.8: Example of the representation of a current dipole on a cubic grid in the negative z-direction. The dipole is represented by 2 monopoles (-1 and $+1$) extending over 3 voxel nodes in z direction and the center node represents the dipole position.

The finite difference formulation of Eq. (3.14) for the central node in a cubic volume element as shown in Fig. 3.8, was first introduced by [61] and [47] based on the surrounding potentials U_i and adopted by [50] resulting in:

$$\sum_{i=1}^{6} A_i U_i - \left(\sum_{i=1}^{6} A_i\right) U_0 = I_P \tag{3.15}$$

where U_0 is the potential at the central point. The A_i coefficients, with $i = 1, \ldots, 6$, are the Saleheen coefficients depending on the conductivity of the 8 volume elements shown in Fig. 3.7:

$$A_1 = \frac{1}{4h_x^2}[\sigma_1 + \sigma_2 + \sigma_3 + \sigma_4] \tag{3.16}$$

$$A_2 = \frac{1}{4h_y^2}[\sigma_1 + \sigma_5 + \sigma_4 + \sigma_8] \tag{3.17}$$

$$A_3 = \frac{1}{4h_x^2}[\sigma_5 + \sigma_6 + \sigma_7 + \sigma_8] \tag{3.18}$$

$$A_4 = \frac{1}{4h_y^2}[\sigma_2 + \sigma_3 + \sigma_6 + \sigma_7] \tag{3.19}$$

$$A_5 = \frac{1}{4h_z^2}[\sigma_1 + \sigma_2 + \sigma_5 + \sigma_6] \tag{3.20}$$

$$A_6 = \frac{1}{4h_z^2}[\sigma_3 + \sigma_4 + \sigma_7 + \sigma_8] \tag{3.21}$$

where σ_p, with $p = 1, \ldots, 8$ is the conductivity defined at element p. Each of the coefficients A_i corresponds with 4 volume elements with a fixed position relative to the center node as is illustrated in Fig. 3.9.

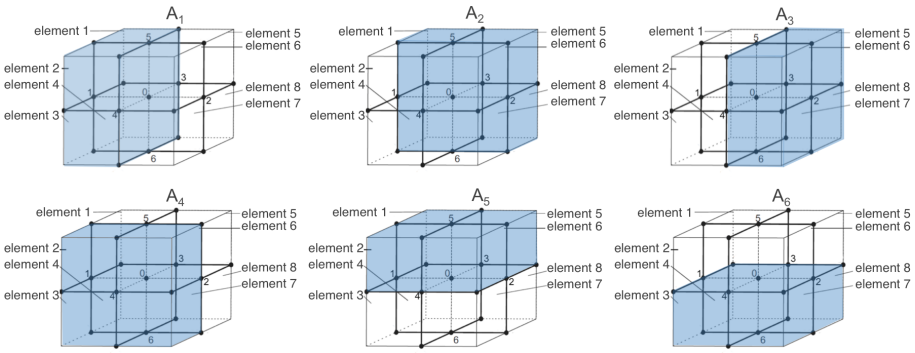

Figure 3.9: Geometrical representation of the volume elements containing the conductivity values used to compute A_1 to A_6. For A_1 the conductivity of the 4 volume elements left to the center node is used, For A_2 to A_6 the volume elements behind, right to, before, above and under the center node are used respectively.

Note that the volume elements indicate the conductivity and the geometry of the head model, but the potential values are computed at the nodes between the voxels. I_P denotes the current depending on the position of the center node. If the center node is at a monopole of the current source or sink, then $I_P = 1$ or $I_P = -1$, respectively, else $I_P = 0$.

For each node of the cubic grid in the head model we obtain a linear equation given by Eq. (3.15). Assume we have n nodes. In matrix notation we can write:

$$\mathbf{A} \cdot \mathbf{U} = \mathbf{I} \tag{3.22}$$

where $\mathbf{U} = (U_1, \ldots, U_n)^T \in \mathbb{R}^{n \times 1}$ is a vector with the potential values at each computational point and $\mathbf{I} \in \mathbb{R}^{(n \times 1)}$ is a vector indicating the current sources and sinks. If the current source (or sink) monopole is placed at the k-th (or l-th) node of the computational grid, then $I_k = 1$ (or $I_l = -1$), else $I_p = 0$ with $p \neq k, l$. $\mathbf{A} \in \mathbb{R}^{(n \times n)}$ is a stiffness matrix, with A_{ij} the j-th coefficient if the i-th node is assigned as the center node. Notice that in the linear Eq. (3.15) only the neighboring computational points are included. The system matrix $\mathbf{A}$ has at most six off-diagonal elements per row and is therefore a sparse matrix.

The linear system in Eq.(3.22) can be solved using direct or iterative techniques to obtain the potentials in each node:

$$\mathbf{U} = \mathbf{A}^{-1} \cdot \mathbf{I} \tag{3.23}$$

In this dissertation we used the Biconjugate gradient stabilized method with Incomplete LU preconditioning, both implemented in MATLAB (The MathWorks Inc., Natick, USA) for an optimal computation speed and accuracy of the solution. By evaluating Eq. (3.23) on the coordinates for each of the electrodes, we obtain the potentials caused by the current dipole.

The lead fields introduced in Eq. (3.1) are then computed using Eq. (3.23), 3 times for 3 dipolar sources introduced on the same location $\mathbf{r}$ in each direction x, y and z. By evaluating $\mathbf{U}$ in the N_c indices of the electrode positions on the scalp of the head model for each of the three sources and assuming a unit amplitude, i.e. $I = 1$, we become the electrode potentials $\mathbf{V}_u \in \mathbb{R}^{N_c \times 3}$. $\mathbf{V}_u$ represents the lead field $\mathbf{L}$ for that particular source location.

The reciprocity principle

The forward model is typically calculated for all the sources assumed in the source space, i.e. for 10.000 up to 1.000.000 sources, in order to find the optimal solution. The computation of the lead fields for

all these sources is therefore computational intensive. The reciprocity principle states that the roles of the dipoles and the electrodes can be reversed, compared to the direct computation of the lead fields. As such the computation time reduces drastically because it is limited to the number of computations corresponding with the number of electrodes. The reciprocity principle is explained in detail in appendix A.

3.3 Inverse techniques

3.3.1 Background

As stated in the introduction, EEG source imaging involves solving an inverse problem. The basic principle to solve the EEG inverse problem is illustrated in Fig. 3.1. Based on the forward model, EEG data can be generated assuming a number of active current dipoles. An inverse technique allows to find a unique solution by minimizing the difference between the generated EEG data and the measured EEG data, i.e. the residuals. Each inverse technique will differ depending on the nature of the forward model and the cost-function that is optimized in order to find the optimal dipole parameters, i.e the locations and the intensities of the dipoles. Depending on the nature of the forward model described in the previous section, we separate the inverse techniques for EEG source imaging in two categories:

- The equivalent current dipole (ECD) approaches, where the EEG signals are assumed to be generated by a relatively small number (< 10) of focal sources [62, 63]. In this case the forward model is characterized by Eq. (3.1) for a single dipole or (3.2) for multiple dipoles.

- Distributed dipoles approaches, where all possible source locations (typically around 10.000) are considered simultaneously [64–66]. In this case the forward model is characterized by Eq. (3.3).

3.3.2 ECD approaches

Equivalent current dipole approaches are based on iterative algorithms that estimate the source parameters in order to explain the data as accurately as possible. In the iterative process, the source parameters are

modified to minimize the residual error [67]. ECD approaches are especially suited when the sources are assumed to be focal, for example corresponding with the generation of an epileptic spike in epilepsy patients. The solution is however very sensitive to the number of sources and initial parameters (dipole locations and orientations), which need to be specified a priori. ECD models require non-linear optimization with the possibility of local minima. Moreover, determining the optimal number of ECDs is a non-trivial issue [68].

3.3.2.1 Single dipole model at one time point

Assume the measured electrode potentials $\mathbf{V_m} \in \mathbb{R}^{N_c \times 1}$ at a specific time point. The inverse problem for a single ECD is solved by minimizing the relative residual energy (RRE):

$$RRE = \frac{\|\mathbf{V_m} - \mathbf{L}(\mathbf{r})\mathbf{j}(\mathbf{r})\|}{\|\mathbf{V_m}\|} \tag{3.24}$$

The dipole parameters $\mathbf{r}$ and $\mathbf{j}(\mathbf{r})$ are optimized so that they minimize the RRE, i.e. the energy that cannot be explained by the model. This is a 6D optimization problem that can be simplified to a 3D problem if the optimal dipole moment at position $\mathbf{r}$ is assumed to be given by [69, 70]:

$$\mathbf{j}_{opt}(\mathbf{r}) = \mathbf{L}(\mathbf{r})^{\dagger}\mathbf{V_m} \tag{3.25}$$

with $\mathbf{L}^{\dagger}$ the Moore-Penrose pseudo-inverse of matrix $\mathbf{L}$ [71]. This way Eq.(3.24) reduces to a minimization problem with respect to parameter $\mathbf{r}$:

$$RRE = \frac{\|\mathbf{V_m} - \mathbf{L}(\mathbf{r})\mathbf{L}(\mathbf{r})^{\dagger}\mathbf{V_m}\|}{\|\mathbf{V_m}\|} \tag{3.26}$$

Based on a 3D scanning approach or optimization techniques like the Nelder-Maede simplex method, this problem can be solved [72].

3.3.2.2 Multiple dipole modeling

An example of a multiple dipole modeling approach is the multiple signal classification (MUSIC) algorithm. The algorithm can be used to localize multiple asynchronous dipolar sources through a 3D head volume by

computing projections onto an estimated signal subspace. To locate the sources, the user must search the head volume for multiple local peaks in the projection metric. For more details see [53].

An alternative signal subspace algorithm is the FINES approach [73]. This approach employs projections onto a subspace spanned by a small set of particular vectors (FINES vector set) in the estimated noise-only subspace instead of the entire estimated noise-only subspace as in case of classic MUSIC. For a comprehensive review on this topic we refer the reader to [74].

3.3.3 Distributed solutions

In contrast to ECD approaches, distributed dipoles approaches represent a highly under-determined but linear system since the number of assumed dipoles is much higher than the number of EEG channels. The linear model (see Eq. (3.3)) is formally similar to those encountered in signal and image processing. They all obtain a unique solution by optimizing a goodness-of-fit term and a regularization term in a carefully balanced way. Most distributed dipoles approaches can be framed in terms of a Weighted Minimum Norm criterion (WMN) (see section 3.3.3), which represents the classical and most popular distributed approach.

3.3.3.1 Weighted minimum norm solutions

The distributed dipoles approach can be expressed as a general linear model in Eq. (3.3). One common approach to this problem is the weighted minimum norm (WMN) solution or Tikhonov regularization method [75]. The WMN solution constrains the reconstructed source distribution by minimizing a linear mixture of some weighted norm $||\mathbf{HJ}||$ of the source amplitudes $\mathbf{J}$ and the residuals of the fit. Assuming that the noise on the measurements is Gaussian $\boldsymbol{\epsilon} \sim N(\mathbf{0}, \mathbf{C}_{\boldsymbol{\epsilon}})$ with known covariance matrix $\mathbf{C}_{\boldsymbol{\epsilon}}$, the regularized problem is expressed as:

$$\hat{\mathbf{J}} = \arg\min_{\mathbf{J}}(||\mathbf{LJ} - \mathbf{V_m}|| + \mu||\mathbf{HJ}||) \tag{3.27}$$

With $\hat{\mathbf{J}}$ the estimated activity and the paramater μ expressing the balance between fitting the model $||\mathbf{LJ} - \mathbf{V}_m||$ and minimizing the a priori constraint $||\mathbf{HJ}||$. The solution of Eq. (3.27) for a given μ is:

$$\hat{\mathbf{J}} = (\mathbf{H}^T\mathbf{H})^{-1}\mathbf{L}^T[\mathbf{L}(\mathbf{H}^T\mathbf{H})^{-1}\mathbf{L}^T + \mu\mathbf{C}_{\boldsymbol{\epsilon}}]^{-1}\mathbf{V}_{\mathbf{m}} \tag{3.28}$$

The WWN solution depends on the parameter μ that balances the relative contribution of fitting the model and the constraint on the solution. As μ varies, the regularized solution of Eq. (3.28) varies. Therefore the choice of μ is crucial. In most cases μ is estimated using an L-curve approach [76].

3.3.3.2 LORETA

A well known and often used approach is the low resolution electrical tomography algorithm (LORETA). In the approach, it is assumed that the sources are smoothed and multiple dipoles are related in focal regions [77, 78].

3.3.3.3 Beamformers

The basic assumption in beamforming is that the sources are uncorrelated, and therefore the activity of each source in the distributed source model is estimated independent of the others. In a beamformer approach, spatial filters are designed for each dipole source that passes the signal coming from the location of the dipole and attenuates all signals coming from other dipoles. We refer the reader to [79–81] for more details and chapter 4 for a mathematical representation.

3.4 Applications

ESI can be applied in each of the applications we introduced for EEG in section 2.9. In the following sections we discuss the main application of ESI in epilepsy studies, ERP research and BCI experiments.

3.4.1 Epilepsy

Approximately 30 % of the patients with epilepsy suffer from refractory epilepsy, a condition in which epileptic seizures are not adequately controlled with anti-epileptic drugs. One of the treatments for refractory epilepsy patients is epilepsy surgery [82]. The possibility for a surgical

procedure to treat the patient is assessed during the pre-surgical evaluation. During the pre-surgical evaluation the results of different techniques that characterize the epilepsy are combined in order to delineate the zone in the brain where the epileptic activity originates from. One such technique is ESI.

As introduced in section 2.9.1.1, Interictal epileptiform discharges (IEDs) are typical manifestations of epileptic activity in the EEG. They possess information to identify the irritative zone (IZ), i.e. the zone where the IEDs originate. In Fig. 3.10A an example is given of a single dipole ECD approach in order to localize the source generating the intertictal epileptiform activity shown in the scalp topography. This 3D information of the epileptic activity can help neurologist and neurosurgeons to evaluate whether surgery is the optimal treatment.

Several studies attempting to determine the accuracy of ESI to localize the IZ have been reported and showed high positive predictive value [83–91]. The latest studies that applied ESI techniques to epileptic activity recorded in the EEG to guide brain surgery are very promising. A study of Geneva Hospital [91] based on 152 operated patients recently quantified the sensitivity and specificity of ESI based on the brain area that was removed during surgery, i.e. the resected zone. The sensitivity was defined as the ability to estimate the epileptic focus inside the resected zone when the patient was rendered seizure free after surgery. The specificity was defined as the ability to estimate the epileptic focus outside the resected zone when the patient was not rendered seizure free after surgery. The authors showed that the sensitivity and specificity of ESI to delineate the epileptic focus were respectively 66% and 54% when < 32 electrodes were used. These values are comparable to other functional imaging techniques (see section 3.5) that are used to delineate the epileptic focus such as Positron Emission Tomography (PET) with a sensitivity and specificity of respectively 68% and 43%, and Single Photon Emission Computed tomography (SPECT) with a sensitivity and specificity of respectively 57% and 46% . For the patients registered with a higher number of electrodes, 128 or 256, the sensitivity and specificity of ESI increased to respectively 84.5% and 87.5% which was much higher than the sensitivity and specificity of SPECT and PET, typically both $< 65\%$, in these patients.

In chapter 7 we devoted an entire chapter to an application of ESI in epilepsy. A nice overview of the clinical use of ESI in epilepsy is given in [92].

3.4.2 Research

ESI is often used in cognitive neuroscience to extract and characterize the active sources in the brain during a cognitive task based on event related potentials. In Fig. 3.10 an example is given of a study to characterize the sources during visual attention [93]. EEG recordings of ERPs were used corresponding with small checkerboard stimuli that were flashed in the lower left quadrant of the visual field at a rapid rate. During the stimuli the subjects were instructed to either attend to the stimuli in the left quadrant or were unattended. A multiple dipole modeling ECD approach was used to characterize the time course of 7 sources corresponding with the ERP activity at a specific location in the brain. The earliest ERP component (C1 at 50-90 ms) was localized to the calcarine cortex, source 1. A longer latency deflection, P1 and N1, was found in higher extrastriate areas, source 2 to 7. In the 150-225 ms range again a deflection was found in the same calcarine cortex, source 1, especially for attended stimuli. These results provided support to the hypotheses that spatial attention in humans is associated with delayed feedback to the calcarine area from higher extrastriate areas.

In chapter 5 and 6, ESI of ERP components for visual processing is discussed in detail.

3.4.3 Brain computer interfaces

A more recent application field is related to BCI systems. A general problem in the design of an EEG-BCI system is the poor quality and low robustness of the extracted features, affecting the overall performance. ESI techniques can help to enhance the extracted features. As introduced in section 2.9.3, movement, or preparation for movement is typically accompanied by a decrease of beta band activity, in the motor areas contralateral to the movement. ESI can be used to localize the sources corresponding with the movement. In Fig. 3.11 an example is given of an ERP experiment we performed during which a subject was instructed to press a button with his right hand forefinger [94]. We localized the sources generating the ERP based on a linearly constrained minimum variance (LCMV) beamformer [95]. The area of the sources can be used subsequently as a region of interest to project the recorded activity into, in real-time, during a BCI experiment based on motor-imagery, for better feature extraction [96–99].

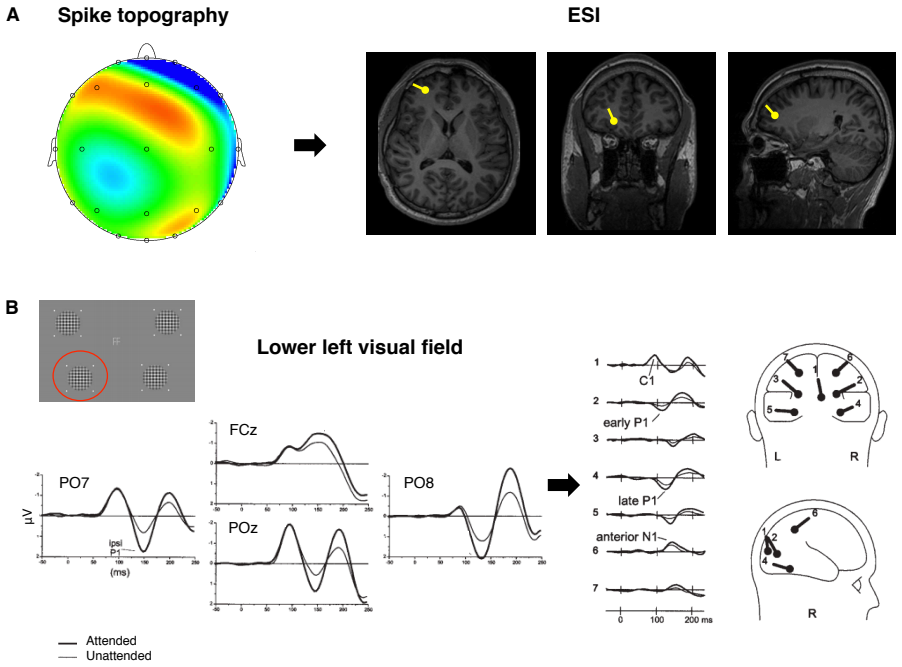

Figure 3.10: A: Example of a single dipole ECD approach to localize the generating source of an interictal epileptic spike. B: Example of a multiple dipole ECD approach to localize the generating sources corresponding with the processing of stimuli in the left visual field, attended and unattended. The time course of 7 sources is given, each with a specific location in the brain (Figure adapted with permission from [93]).

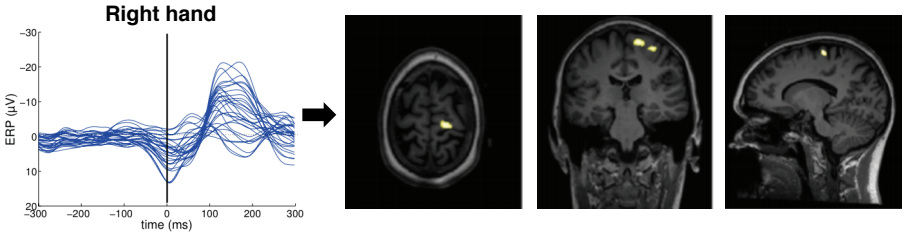

Figure 3.11: Example of a beamforming approach to localize the sources corresponding with right hand button pressing. The activity is located in the left motor cortex. These locations in the brain can be used to project the activity into a region of interest during a BCI experiment for better feature extraction.

3.5 Positioning within the field of functional neuroimaging

3.5.1 Different techniques

In order to position EEG, and by extension EEG source imaging as a neuroimaging technique, i.e. a technique to image brain activity, we give an overview of the currently used most common non-invasive functional neuroimaging techniques presented in Fig. 3.12. We distinguish Positron Emission Tomography (PET), Single Photon Emission Computed Tomography (SPECT), functional Magnetic Resonance Imaging (fMRI), MagnetoEncephaloGraphy (MEG) and Near InfraRed Spectroscopy (NIRS). Each functional neuroimaging technique is based on a different measuring principle of brain activity and therefore each technique is characterized by a typical spatial and temporal resolution (see Fig. 3.13). In what follows the different techniques are briefly discussed.

Positron Emission Tomography (PET) is a nuclear imaging technique that can be used to image the distribution of an injected radio tracer in the brain, typically ^{18}F-fluorodeoxyglucose (^{18}F-FDG). This is a glucose molecule labeled with a positron emitting radionuclide to investigate and visualize the glucose uptake in the different brain regions. PET imaging allows to characterize brain activity with minute temporal resolution and a spatial resolution from 3 to 10 mm.

Single Photon Emission Computed Tomography (SPECT) is also a nuclear imaging technique that allows to image the distribution of a radio tracer in the brain labeled with a single photon emitting isotope, typically ^{99m}Tc-HMPAO (Technetium - hexamethylpropylene amine oxime). ^{99m}Tc-HMPAO-SPECT allows to image the perfusion, i.e. the blood flow in the brain. After the tracer is injected the tracer flows to the brain cells that take up the isotope. The SPECT recording is performed several hours later to asses the regional cerebral blood flow at the time of injection. The temporal resolution is several minutes and the spatial resolution is worse compared to PET, i.e. typically > 1 cm.

Functional Magnetic Resonance Imaging (fMRI) is a technique that uses MRI acquisition technology to measure brain activity. The technique relies on the fact that active areas in the brain require a higher blood flow to these areas, i.e. the direct coupling between brain activity and cerebral blood flow. The most widely used fMRI technique is based on the Blood-Oxygenation-Level-Dependent (BOLD) contrast.

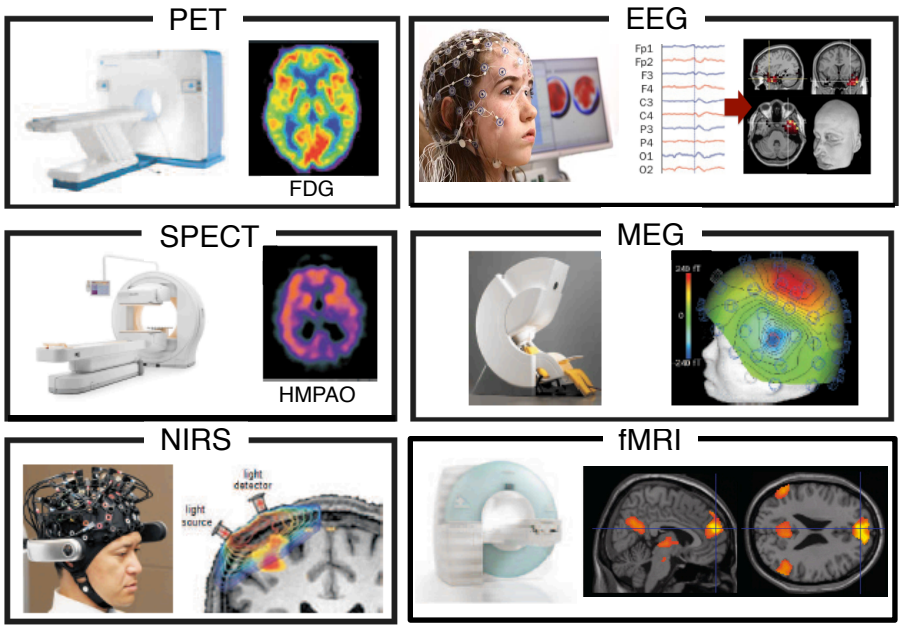

Figure 3.12: Overview of the most common non-invasive functional neuroimaging techniques. PET = Positron Emission Tomography, FDG = FluoroDeoxyGlucose, EEG = ElectroEncephaloGraphy, SPECT = Single Photon Emission Tomography, HMPAO = HexaMethylPropyleneAmine Oxime, NIRS = Near InfraRed Spectroscopy, fMRI = functional Magnetic Resonance Imaging. Figure adapted from [100].

This contrast allows to indirectly investigate neuronal activation based on the oxygenation level of the blood in different brain areas. fMRI is a very popular functional neuroimaging technique because it has a high spatial resolution, i.e. up to the sub-millimeter scale and temporal resolution of several seconds.

Magnetoencephalography (MEG) is a technique similar to EEG that allows to record the magnetic field produced by the electrical currents in the brain. The magnetic field of the brain is very small in the order of 10 to 1000 femtotesla (fT) while the environment noise is around 10^8 fT. Therefore, MEG recordings need to be registered in a special shielded magnetic room with highly sensitive magnetometers. MEG source imaging (MSI) techniques are developed similar to ESI that allow to characterize the sources that are generating the measured MEG signals. The temporal and spatial resolution of MEG and MSI are equivalent to EEG and ESI, i.e. a milliseconds temporal resolution and a spatial resolution

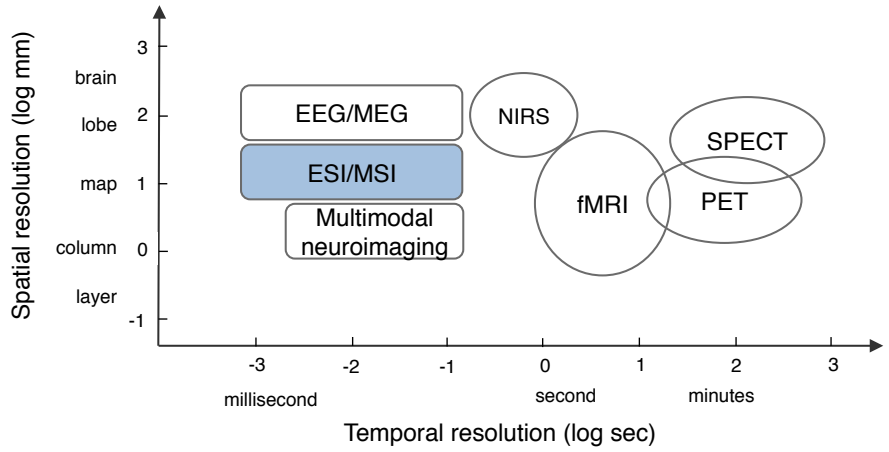

Figure 3.13: The spatial and temporal resolution of the most common non-invasive functional neuroimaging methods. The spatial resolution is depicted in terms of anatomical regions in the cerebral cortex with different sizes: brain, lobe, cortical map, column or layer.

of centimeters. MSI has the advantage over ESI that it is less sensitive to the forward model, i.e. it is less sensitive to accurate head modeling incorporating the skull, and different tissues in the brain. In contrast to that, MEG is more sensitive to tangential sources (originating in the sulci) than radial sources, while EEG is sensitive to both tangential and radial sources. Compared to EEG, MEG is much more expensive (typically EUR 1000,- for a 1 hour MEG registration).

Functional Near-Infrared Spectroscopy (fNIRS) is a more recent technique to measure brain activity by analyzing the absorption patterns of near-infrared light in the brain. In a typical fNIRS study, the cerebral cortex is irradiated with near infrared light via laser sources and optical fibers, i.e. the emission probes, at the scalp surface. The light penetrates through the skull into the cerebral cortex. After absorption and scattering of the light in the cortex it is observed again on the scalp surface via the receiver probes with a light detector, typically at a distance of 30 mm to the emission probes. By analyzing the absorption patterns of the detected light, corresponding with varying oxygenated hemoglobin or deoxygenated hemoglobin levels in the blood (similar to fMRI), neuronal activity can be detected. It is a promising technique because it is portable, has a high intrinsic temporal resolution in the order of seconds and a spatial resolution comparable to EEG and MEG. A disadvantage

of fNIRS is that it currently only allows to visualize superficial brain activity close to the scalp surface.

3.5.2 Multimodal neuroimaging

As introduced in the previous section, there exist several techniques or modalities to investigate brain activity. The question one can ask here is which of the techniques is the best or most optimal technique to characterize brain activity. The answer to the question strongly depends on the type of study to investigate the activity. For example whether it is required to characterize the brain activity with a high temporal resolution, it is necessary to the determine the activity of deeper sources in the cerebral cortex, or whether the accurate localization of the brain activity is important. Often the most powerful way to study brain activity is to use different modalities, combine them, and interpret the results together in order to improve the characterization of the process being studied. In a multimodal characterization of brain activity it is important to realize the limitations and strengths of each of the modalities.

Much effort is already put into the development of techniques to simultaneously measure the EEG and fMRI or the EEG and the MEG. In a combined registration of EEG and fMRI the high spatial resolution of the fMRI study can be coupled to the high temporal resolution of the EEG registration [101–103]. A registration of EEG and MEG together can result in more accurate source imaging results [104–106].

To illustrate the principle of multimodel neuroimaging, we present the results of a study we performed in which we tried to determine the origin of the epileptic activity in the brain of a patient using several modalities in Fig. 3.14. MR en CT structural images were recorded. ESI and MSI were performed on epileptic spikes. An ictal subtraction HMPAO-SPECT was performed, i.e. an interictal SPECT fused, normalized and subtracted from an ictal SPECT investigation. And finally an interictal FDG-PET investigation was performed. Comparing the results of each of the modalities and by combining them it was possible to pinpoint the origin of the epileptic activity in the frontal areas of the right temporal lobe.

Several open-source software toolboxes are already developed that allow the analysis of multimodal neuroimaging data. The most widely used toolbox is the Statistical Parametric Mapping software [107]. This is a A MATLAB (The Mathworks. Inc., Natick, USA) toolbox for the analysis

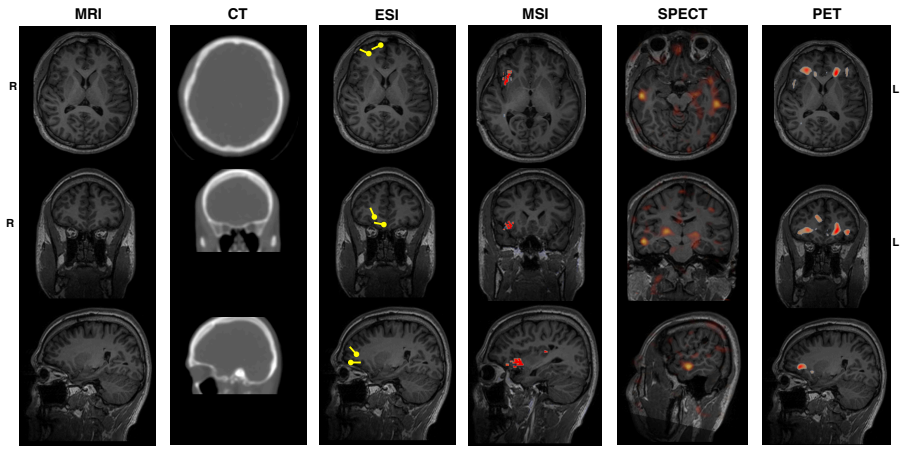

Figure 3.14: Example of a multimodal neuromaging study to determine the origin of the epileptic activity. The MSI, ESI, SPECT and PET investigations pinpoint the frontal areas in the right temporal lobe.

of EEG signals, MagnetoEncephaloGraphy (MEG), Positron Emission Tomography (PET), Single Photon Emission Tomography (SPECT) and functional Magnetic Resonance Imaging (fMRI) data. In the next chapter the framework for ESI in SPM is described. Based on this framework we present some extensions and applications in the following chapters.

Chapter 4

Bayesian framework for ESI

"Somewhere I remain inside this house of all big thoughts that linger"
Geppetto & the whales - Cocklane ghosts

4.1 Introduction

In this chapter we introduce a Bayesian statistical framework to solve the inverse problem for EEG source imaging. The chapter begins with an explanation of Bayes' theorem, followed by the hierarchical Bayesian formulation of the inverse problem based on a distributed source model. Also the Bayesian interpretation of the classic ESI methods is discussed. Next, the framework is introduced that allows to introduce multiple source priors for EEG source imaging. A generalized cost function is derived, i.e. the free energy, that is optimized to find a unique solution using the Restricted Maximum Likelihood (ReML) algorithm. Finally, we show how the framework can be used to compare different forward models depending on the measured EEG data. The methods that are described in this chapter are all implemented in the Statistical Parametric Mapping software (SPM) for neuroimaging that was introduced in the previous chapter.

4.2 Probability and Bayesian inference

The notion of probability in inferential statistics is used to express the belief that an event has or will occur. It is introduced to account for randomness and uncertainty in the data, for hypotheses testing, inferring

hidden paramaters etc. Probability has different interpretations. In the classical interpretation, the probability corresponds with the frequency of the occurrence of an event, given an infinite number of trials. It is only defined for random processes that can be observed many times and it is meant to be objective. In the Bayesian interpretation the probability expresses the degree of belief a certain event occurs. It is a measure of uncertainty. In the Bayesian interpretation, the probability can be defined for any type of event and is considered to be subjective in essence.

Based on the axioms of Kolmogorov [108] some calculation principles can be derived. Assume we have 2 events A and B, and $p(A)$ and $p(B)$ denote the probability of event A or event B, with $0 \leq p(A) \leq 1$ and $0 \leq p(B) \leq 1$. The probability $p(A, B)$ expresses the joint probability of A and B. If A and B or mutually exclusive events, i.e. if either event A or event B occurs, it follows that:

$$p(A, B) = 0 \tag{4.1}$$

and if A and B are independent events it follows that:

$$p(A, B) = p(A)p(B) \tag{4.2}$$

The conditional probability of A given B is defined as $p(A|B)$ and is equal to:

$$p(A, B) = p(A|B)p(B) \tag{4.3}$$

Note that if A and B are independent, $p(A|B) = p(A)$ and p(A,B) = $p(A)p(B)$. If we furthermore consider:

$$p(A, B) = p(B, A) = p(B|A)p(A) \tag{4.4}$$

Bayes' theorem can be derived from Eq (4.3) and (4.4):

$$p(A|B) = \frac{p(B|A)p(A)}{p(B)} \tag{4.5}$$

Bayes' theorem describes that the conditional probability of A given B is equal to the conditional probability of B given A times the probability of A divided by the probability of B. Assume for example that 10% of happy people are rich, 40% of people are happy and 5% of people are rich. The people that are rich are defined as event A and the people that

are happy are defined as B. What is interesting to know is the percentage of rich people that are happy. This can be derived with Bayes' theorem. The people that are rich and happy $p(A|B)$ is equal to $\frac{10\% \times 40\%}{5\%} = 80\%$, meaning that the majority of rich people are happy. Therefore proving in this hypothetical situation that money buys happiness.

4.3 Hierarchical Bayesian model

In what follows we introduce a hierarchical Bayesian framework for a distributed source model and explain how Bayes' theorem is used to derive a solution of the source intensities.

4.3.1 The model

The problem of finding the source intensities in a distributed source model introduced in Eq. (3.3) can also be expressed in the context of a two-level hierarchical Parametric Empirical Bayes (PEB) model [109]:

$$\begin{aligned} \mathbf{V}_m &= \mathbf{L}\mathbf{J} + \boldsymbol{\epsilon}^{(1)} \\ \mathbf{J} &= \boldsymbol{\epsilon}^{(2)} \end{aligned} \tag{4.6}$$

where $\mathbf{V}_m \in \mathbb{R}^{N_c \times N_t}$ represents the EEG signals of N_c electrode channels over N_t time samples. $\mathbf{J} = [\mathbf{j}_1, \mathbf{j}_2, \ldots, \mathbf{j}_{N_d}]^T$ is a vector of current dipoles at N_d locations each over N_t time samples, $\mathbf{L} = [\mathbf{L}(\mathbf{r}_1), \mathbf{L}(\mathbf{r}_2), \cdots, \mathbf{L}(\mathbf{r}_{N_d})] \in \mathbb{R}^{N_c \times N_d}$ is the lead field matrix linking the source amplitudes in $\mathbf{J}$ of the assumed dipoles on fixed locations to the electrical potentials $\mathbf{V}_m$; $\boldsymbol{\epsilon}^{(1)}$ and $\boldsymbol{\epsilon}^{(2)}$ are the noise at the level of the electrode channels and at the source level respectively. Given the prior probability of the source activity: $p(\mathbf{J})$ and the likelihood of fitting the data: $p(\mathbf{V}_m|\mathbf{J})$, the posterior source activity distribution can be estimated using Bayes' theorem:

$$p(\mathbf{J}|\mathbf{V}_m) = \frac{p(\mathbf{V}_m|\mathbf{J})p(\mathbf{J})}{p(\mathbf{V}_m)}. \tag{4.7}$$

We define:

- $p(\mathbf{J}|\mathbf{V}_m)$ as the posterior probability distribution of the sources

- $p(\mathbf{V}_m|\mathbf{J})$ as the likelihood
- $p(\mathbf{J})$ as the prior knowledge of the sources
- $p(\mathbf{V}_m)$ as the evidence.

The likelihood and the prior knowledge are directly related to the forward model of the EEG measurements and the magnitudes of the sources can be recovered applying the expectation operator: $\langle \mathbf{J} \rangle = E[p(\mathbf{J}|\mathbf{V}_m)]$. In the next section we explain how to compute the solution for $p(\mathbf{J}|\mathbf{V}_m)$.

4.3.2 Solution

Given the evidence $p(\mathbf{V}_m)$ is constant because the dataset is fixed, we get:

$$p(\mathbf{J}|\mathbf{V}_m) \propto p(\mathbf{V}_m|\mathbf{J})p(\mathbf{J}). \tag{4.8}$$

We assume that the noise at the channel and source level is both Gaussian distributed with zero mean and covariances $\mathbf{C}_{\boldsymbol{\epsilon}}$ and $\mathbf{C}_{\mathbf{J}}$: $\boldsymbol{\epsilon}^{(1)} \sim \mathbf{N}(\mathbf{0}, \mathbf{C}_{\boldsymbol{\epsilon}})$ and $\boldsymbol{\epsilon}^{(2)} \sim \mathbf{N}(\mathbf{0}, \mathbf{C}_{\mathbf{J}})$, with $\mathbf{N}(\cdot)$ the matrix normal distribution. Under these assumptions, the likelihood $p(\mathbf{V}_m|\mathbf{J})$ is Gaussian with mean $\mathbf{LJ}$ and covariance $\mathbf{C}_{\boldsymbol{\epsilon}}$: $\mathbf{N}(\mathbf{LJ}; \mathbf{C}_{\boldsymbol{\epsilon}})$. The likelihood gives us the probability of the data for a given distributed source activity. Because the prior on the sources and likelihood are both Gaussian, we can rewrite Eq. (4.8) as:

$$p(\mathbf{V}_m|\mathbf{J})p(\mathbf{J}) \propto \exp\left(\frac{1}{2}tr((\mathbf{V}_m - \mathbf{LJ})^T\mathbf{C}_{\boldsymbol{\epsilon}}^{-1}(\mathbf{V}_m - \mathbf{LJ}) - \frac{1}{2}\mathbf{J}^T\mathbf{C}_{\mathbf{J}}^{-1}\mathbf{J})\right). \tag{4.9}$$

With:

$$\boldsymbol{\phi} = \exp\left(\frac{1}{2}tr((\mathbf{V}_m - \mathbf{LJ})^T\mathbf{C}_{\boldsymbol{\epsilon}}^{-1}(\mathbf{V}_m - \mathbf{LJ}) - \frac{1}{2}\mathbf{J}^T\mathbf{C}_{\mathbf{J}}^{-1}\mathbf{J})\right) \tag{4.10}$$

the optimal source intensities correspond with the intensities that optimize $\boldsymbol{\phi}$. This is equivalent to finding the intensities where the derivative of $\log(\boldsymbol{\phi})$ with respect to $\mathbf{J}$ is equal to zero [110]:

$$\left.\frac{d(\log \boldsymbol{\phi})}{d\mathbf{J}}\right|_{\mathbf{J}=\hat{\mathbf{J}}} = \mathbf{0} \tag{4.11}$$

$$= tr(\mathbf{L}^T\mathbf{C}_{\boldsymbol{\epsilon}}^{-1}\mathbf{L}\hat{\mathbf{J}} - \mathbf{L}^T\mathbf{C}_{\boldsymbol{\epsilon}}^{-1}\mathbf{V}_m + \mathbf{C}_{\mathbf{J}}^{-1}\hat{\mathbf{J}}) \tag{4.12}$$

$$\tag{4.13}$$

from which $\hat{\mathbf{J}}$ can be derived [104]:

$$\hat{\mathbf{J}} = [\mathbf{L}^T\mathbf{C}_{\boldsymbol{\epsilon}}^{-1}\mathbf{L} + \mathbf{C}_{\mathbf{J}}^{-1}]^{-1}\mathbf{L}^T\mathbf{C}_{\boldsymbol{\epsilon}}^{-1}\mathbf{V}_m \tag{4.14}$$

$$= \mathbf{C}_{\mathbf{J}}\mathbf{L}^T[\mathbf{L}\mathbf{C}_{\mathbf{J}}\mathbf{L}^T + \mathbf{C}_{\boldsymbol{\epsilon}}]^{-1}\mathbf{V}_m \tag{4.15}$$

which is the commonly used equation for inverse problems based on distributed sources with Gaussian assumptions and known values of $\mathbf{C}_{\mathbf{J}}$ and $\mathbf{C}_{\boldsymbol{\epsilon}}$ [74]. Comparing Eq. (3.28) wtih Eq. (4.15) provides the motivation for choosing forms of $\mathbf{H}$, where:

$$\mu\mathbf{H}^T\mathbf{H} = \mathbf{C}_{\mathbf{J}}^{-1} \tag{4.16}$$

Or in other words, $\mathbf{H}$ specifies the form of the precision or our prior belief on where the source activity is expressed (knowing that precision is the inverse of the variance).

4.4 Multiple priors in the hierarchical Bayesian framework

Within a Bayesian framework, the covariance matrices $\mathbf{C}_{\boldsymbol{\epsilon}}$ and $\mathbf{C}_{\mathbf{J}}$ do not necessarily have to be fixed before calculating the solution. In the most general case $\mathbf{C}_{\boldsymbol{\epsilon}}$ and $\mathbf{C}_{\mathbf{J}}$ can be modeled as a linear combination of covariance components:

$$\begin{aligned}\mathbf{C}_{\boldsymbol{\epsilon}} &= \lambda_1^{(1)}\mathbf{Q}_1^{(1)} + \lambda_2^{(1)}\mathbf{Q}_2^{(1)} + ... \\ \mathbf{C}_{\mathbf{J}} &= \lambda_1^{(2)}\mathbf{Q}_1^{(2)} + \lambda_2^{(2)}\mathbf{Q}_2^{(2)} + ...\end{aligned} \tag{4.17}$$

with $\lambda_1^{(1)}, \lambda_2^{(1)}, \ldots$ and $\lambda_1^{(2)}, \lambda_2^{(2)}, \ldots$ the hyperparameters that balance the various covariance components either at the first (electrode channels) or second (source) level [109]. The hyperparameters can be estimated from the EEG measurements and control the power allocated to each of the components. In the following sections different choices of covariance components are discussed.

4.4.1 Choices of covariance components

The covariance components may embody different types of informative priors, e.g., different smoothing functions, mathematical priors, medical knowledge, fMRI priors, etc. [111]. In this dissertation we assume the same amount of noise variance on all sensors: $\mathbf{C}_{\boldsymbol{\epsilon}} = \lambda_\epsilon \mathbf{I}_{N_c}$, where $\mathbf{I}_{N_c} \in \mathbb{R}^{N_c \times N_c}$ is an identity matrix, and λ_ϵ is the sensor noise variance.

There are different examples of covariance components that can be introduced at the source level. They are represented visually in Fig. 4.1. We first describe covariance components that can be introduced corresponding with classical methods: the minimum norm solution, A LORETA-like solution and a beamformers solution. Subsequently, the most general solution formed by hundreds of covariance components is discussed. We denoted the set of covariance components as $\mathbf{Q}^{(2)} = \{\mathbf{Q}_1^{(2)}, \mathbf{Q}_2^{(2)}, \dots\}$.

4.4.1.1 Examples of typical classical methods

Weighted minimum norm solutions

Following the classical weighted minimum norm approaches, introduced in section 3.3.3.1, one may just choose 1 covariance component as the identity matrix: $\mathbf{Q}^{(2)} = \mathbf{Q}_1^{(2)} = \mathbf{I}_{N_d}$. See Fig. 4.1A for an example.

Coherence priors

For a solution similar to the LORETA approach an extra covariance component can be added: $\mathbf{Q}^{(2)} = \{\mathbf{I}_{N_d}, \mathbf{Q}_G\}$, where $\mathbf{Q}_G$ represents a coherence prior on the sources. The coherence prior expresses that the sources are smoothed and multiple dipoles are related in focal regions (see Fig. 4.1B for an example). Such a coherence function was proposed in [113]. The authors presented a Green's function based on a graph Laplacian calculated using the locations of the dipoles and the dipole source space. The Green's function $\mathbf{Q}_G \in \mathbb{R}^{N_d \times N_d}$ is defined as:

$$\mathbf{Q}_G = \exp(\omega \mathbf{G}_L) \tag{4.18}$$

with ω a positive constant value that determines the smoothness of the current distribution or spatial extent of the activated regions, and $G_L \in \mathbb{R}^{N_d \times N_d}$, a graph Laplacian with inter-dipole connectivity information. The graph Laplacian G_L is calculated using an adjacency matrix

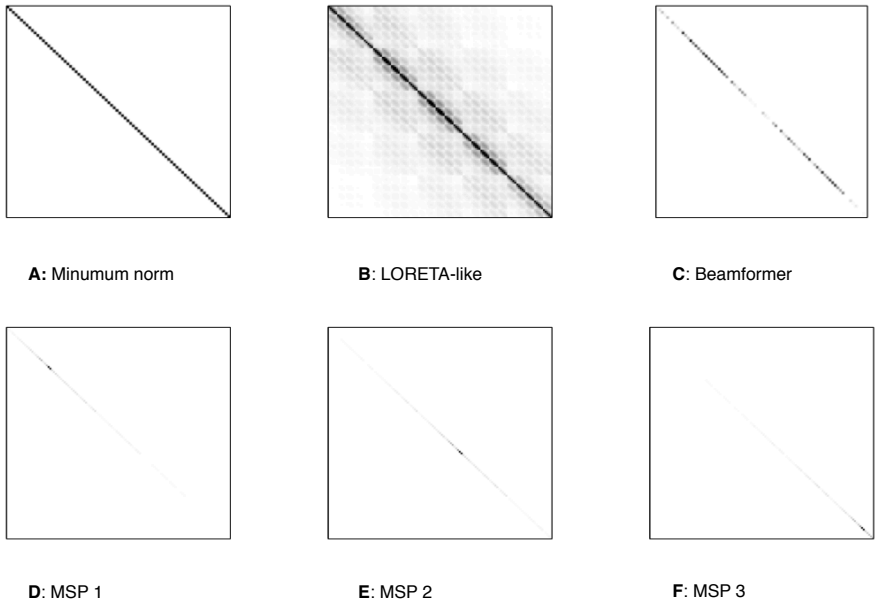

Figure 4.1: Choices of covariance components: (A) a minimum norm solution does not include prior information. (B) A LORETA-like is based on a fixed smoothing function relating each dipole with its nearest neighbors. (C) A beamformer weights the main diagonal giving priority to those dipoles with higher probability of activity. (D), (E) and (F) multiple sparse covariance components each with a different possible location. Figure adapted from [112]

corresponding with the dipole locations and defining the neighboring dipoles based on the dipole source space.

Beamforming

The beamforming solution can be introduced as a single covariance matrix: $\mathbf{Q}^{(2)} = \mathbf{B}$ with $\mathbf{B} \in \mathbb{R}^{N_d \times N_d}$ a diagonal matrix formed directly from the data by a projection into the source space with the lead field matrix and normalized to give the same priority to deep and external sources. Each diagonal element of $\mathbf{B}$ is defined as:

$$B_{ii} = \frac{1}{\Delta_i}\left(\mathbf{L}_i^T(\mathbf{V}_m\mathbf{V}_m^T)\mathbf{L}_i\right) \tag{4.19}$$

for each $i = 1, \ldots, N_d$ and B_{ii} the i-th main diagonal element of $\mathbf{B}$, $\mathbf{L}_i$ is the lead field of the i-th source, and the normalization parameters Δ_i is defined as:

$$\Delta_i = \frac{1}{\mathbf{L}_i^T \mathbf{L}_i} \tag{4.20}$$

for each $i = 1, \ldots, N_d$. See Fig. 4.1C for an example.

4.4.1.2 Multiple sparse priors algorithm

In the multiple sparse priors (MSP) algorithm [114], N_q covariance components at the source level $\mathbf{Q} = \left\{\mathbf{Q}_1^{(2)}, \ldots, \mathbf{Q}_{N_q}^{(2)}\right\}$ are assumed for which each of the components defines a potential activated region of cortex, with scalar hyperparameters, $\boldsymbol{\lambda} = \left\{\lambda_i^{(2)}\right\}$, and $i = 1, \ldots, N_q$. Typically around 500 active patches of sources with locally identical variance are assumed. Each covariance component is a diagonal matrix and the diagonal elements are constructed using the columns of the Green's function. Each column in the Green's function corresponds with a specific source assumed in the source space and models a patch on the cortex formed around that source. Each patch has a bell shape, with a full width half maximum depending on the neighboring dipoles and the smoothing factor ω. See Fig. 4.1D, E and F for 3 examples of covariance components. Note that each covariance component has a column of the coherence prior on its diagonal as shown in Fig. 4.1B.

The size and the number of the patches to construct the covariance components can be defined based on prior knowledge. In the default approach in the SPM software, the number of patches is set to $N_q = 512$ so the the entire cortical area is covered (see Fig. 4.2B), the centers of these patches are selected from a set of $N_d = 8196$ dipoles shown in Fig. 4.2A. Fig. 4.2C, D and E show different sizes of the patches obtained with different values of ω equal to 0.1, 0.6 and 1, respectively. In the SPM software, $\omega = 0.6$ by default.

In the next section of this chapter a cost function for determining the optimal set op hyperparameters, i.e. the $\boldsymbol{\lambda}$ values corresponding to each of the components, will be derived.

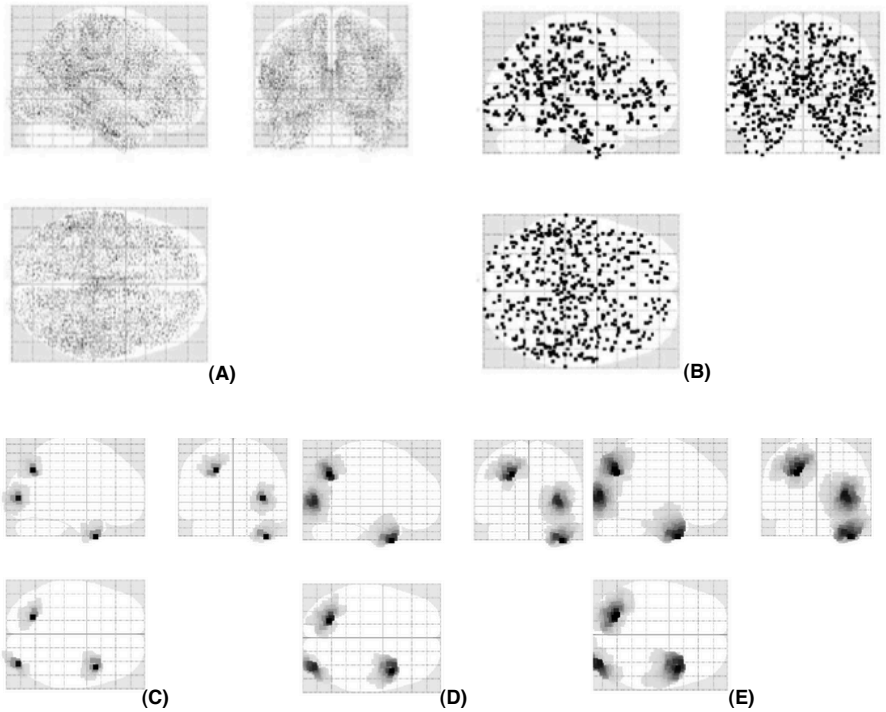

Figure 4.2: Generation of covariance components: (A) The sources of neural activity are limited to a set of 8196 current dipoles distributed over the cortical area, (B) each dot represents the centre of 512 assumed patches. The Green's function allows to modify the size of the patches depending on ω, ω is equal to 0.1 in (C), 0.6 in (D) and 1 in (E). In all figures, the sources are shown in the glass brain, often used in the SPM software in a sagittal, coronal and axial view.

4.4.2 Free Energy

4.4.2.1 Derivation

Since $\boldsymbol{\lambda}$ is not known, a suitable approximation $\boldsymbol{\lambda} \approx \hat{\boldsymbol{\lambda}}$ can be used to calculate the posterior distribution of the source intensities based on the covariance and expectation of $p(\mathbf{J}|\mathbf{V})$ as in Eq. (4.17).

To calculate the optimal set $\hat{\boldsymbol{\lambda}}$, we now introduce the joint probability distribution of the hyperparameters and the measured EEG data $p(\mathbf{V}_m, \boldsymbol{\lambda})$. The hyperparameters that correspond with the highest evidence value are selected.

Since the source intensities in $\mathbf{J}$ are fully dependent on $\boldsymbol{\lambda}$, we can define the joint probability of $\mathbf{V}_m$, $\mathbf{J}$ and $\boldsymbol{\lambda}$ as:

$$p(\mathbf{V}_m, \mathbf{J}, \boldsymbol{\lambda}) = p(\mathbf{V}_m|\mathbf{J})p(\mathbf{J}|\boldsymbol{\lambda})p(\boldsymbol{\lambda}). \tag{4.21}$$

Given that the parameters $\mathbf{J}$ fully depend on $\boldsymbol{\lambda}$, they can be marginalized from the optimization problem:

$$p(\mathbf{V}_m, \boldsymbol{\lambda}) = \int p(\mathbf{V}_m, \mathbf{J}, \boldsymbol{\lambda}) d\mathbf{J} \tag{4.22}$$

Together with Eq. (4.21) this becomes:

$$p(\mathbf{V}_m, \boldsymbol{\lambda}) = \int p(\mathbf{V}_m|\mathbf{J})p(\mathbf{J}|\boldsymbol{\lambda})p(\boldsymbol{\lambda}) d\mathbf{J}. \tag{4.23}$$

and because $p(\boldsymbol{\lambda})$ is independent of $\mathbf{J}$, it can be placed outside the integral:

$$p(\mathbf{V}_m, \boldsymbol{\lambda}) = \left(\int p(\mathbf{V}_m|\mathbf{J})p(\mathbf{J}|\boldsymbol{\lambda}) d\mathbf{J} \right) p(\boldsymbol{\lambda}). \tag{4.24}$$

Because:

$$p(\mathbf{V}_m, \boldsymbol{\lambda}) = p(\mathbf{V}_m|\boldsymbol{\lambda})p(\boldsymbol{\lambda}). \tag{4.25}$$

it follows that:

$$p(\mathbf{V}_m|\boldsymbol{\lambda}) = \int p(\mathbf{V}_m|\mathbf{J})p(\mathbf{J}|\boldsymbol{\lambda}) d\mathbf{J} \tag{4.26}$$

The solution of this equation is a Gaussian distribution:

$$p(\mathbf{V}_m|\boldsymbol{\lambda}) \propto \exp(-\frac{1}{2}\mathbf{V}_m^T \boldsymbol{\Sigma}_{\mathbf{V}_m}^{-1} \mathbf{V}_m) \tag{4.27}$$

with

$$\boldsymbol{\Sigma}_{\mathbf{V}_m} = \mathbf{C}_{\boldsymbol{\epsilon}} + \mathbf{L}\mathbf{C}_{\mathbf{J}}\mathbf{L}. \tag{4.28}$$

We refer the reader to appendix B for a detailed mathematical description. This result is important because it obviates the use of $\mathbf{J}$ in the optimization problem, and allows to formulate a cost function for $\boldsymbol{\lambda}$ exclusively in terms of the data $\mathbf{V}_m$.

There are two other advantages of using $\mathbf{\Sigma_V}$ instead of $\mathbf{C_J}$ for optimizing the hyperparameters: (i) the size of the matrices is highly reduced due to its projection into sensor space, and (ii) the inclusion of noise variance $\mathbf{C_\epsilon}$ into the equation allows adding the noise regularization parameter λ_ϵ (see section 4.4.1.1) as another hyperparameter for optimization.

With the definition of the hyperparameters exclusively in terms of the data it is possible to define the optimization problem:

$$\hat{\boldsymbol{\lambda}} = \underset{\boldsymbol{\lambda}}{\operatorname{argmax}}[p(\mathbf{V}_m|\boldsymbol{\lambda})p(\boldsymbol{\lambda})] \tag{4.29}$$

which can be obtained by maximizing the cost function:

$$\Theta(\boldsymbol{\lambda}) = \log[p(\mathbf{V}_m|\boldsymbol{\lambda})p(\boldsymbol{\lambda})]. \tag{4.30}$$

Replacing $p(\mathbf{V}_m|\boldsymbol{\lambda})$ with Eq.(4.27), the following generalized cost function can be derived [112]:

$$\Theta(\boldsymbol{\lambda}) = \log\left(\frac{1}{(2\pi)^{N_c/2}\sqrt{|\mathbf{\Sigma_V}|}}\exp\left(-\frac{1}{2}tr(\mathbf{V}_m^T\mathbf{\Sigma}_\mathbf{V}^{-1}\mathbf{V}_m)\right)p(\boldsymbol{\lambda})\right) \tag{4.31}$$

In what follows we define $p(\boldsymbol{\lambda})$ to obtain the free energy cost function used in the Statistical Parametric Mapping software. We define $p_0(\boldsymbol{\lambda})$ as the prior knowledge about the hyperparameters and $q(\boldsymbol{\lambda})$ as an approximate posterior. Following the maximum entropy principle [115], we can specify $p(\boldsymbol{\lambda})$ based on 2 Gaussian distributions:

$$p_0(\boldsymbol{\lambda}) = N(\boldsymbol{\lambda}; \boldsymbol{\nu}, \mathbf{C}_{\boldsymbol{\nu}}) \tag{4.32}$$
$$q(\boldsymbol{\lambda}) = N(\boldsymbol{\lambda}; \hat{\boldsymbol{\lambda}}, \mathbf{\Sigma}_{\boldsymbol{\lambda}}). \tag{4.33}$$

with, $\boldsymbol{\nu} \in \mathbb{R}^{N_p \times 1}$ the initial values of the hyperparameters, $\mathbf{C}_{\boldsymbol{\nu}} \in \mathbb{R}^{N_p \times N_p}$ their prior covariance, $\hat{\boldsymbol{\lambda}}(\boldsymbol{\lambda}) \in \mathbb{R}^{N_p \times 1}$ the posterior mean of the hyperparameters and $\mathbf{\Sigma}_{\boldsymbol{\lambda}}(\boldsymbol{\lambda}) \in \mathbb{R}^{N_p \times 1}$ their posterior covariance. Based on the the maximum entropy principle we can write the log-prior $p(\boldsymbol{\lambda})$ as:

$$\log p(\boldsymbol{\lambda}) = -\frac{1}{2}tr\big((\boldsymbol{\lambda}-\boldsymbol{\nu})^T\mathbf{C}_{\boldsymbol{\nu}}^{-1}(\boldsymbol{\lambda}-\boldsymbol{\nu})\big) + \frac{1}{2}\log|\mathbf{\Sigma}_{\boldsymbol{\lambda}}\mathbf{C}_{\boldsymbol{\nu}}^{-1}| \tag{4.34}$$

Using Eq. (4.34) to complete the cost function of Eq. (4.31) gives the free energy F used in [114]:

$$F = -\frac{N_t}{2} tr(\mathbf{C_V}\mathbf{\Sigma_V^{-1}}) - \frac{N_t}{2}\log|\mathbf{\Sigma_V}| - \frac{N_c N_t}{2}\log(2\pi) \\ -\frac{1}{2} tr\big((\boldsymbol{\lambda}-\boldsymbol{\nu})^T \mathbf{C}_{\boldsymbol{\nu}}^{-1}(\boldsymbol{\lambda}-\boldsymbol{\nu})\big) + \frac{1}{2}\log|\mathbf{\Sigma}_{\boldsymbol{\lambda}}\mathbf{C}_{\boldsymbol{\nu}}^{-1}| \quad (4.35)$$

with $\mathbf{C_V} = \frac{1}{N_t}\mathbf{V}_m\mathbf{V}_m^T$. For a more detailed derivation of the free energy function we refer the reader to [116].

4.4.2.2 Interpretation

Maximizing the free energy cost function implies a trade off between the accuracy of the solution and the complexity of the solution. The accuracy term penalizes the difference in variance between the measured EEG data $\mathbf{V}_m$ and the estimated solution $\mathbf{LJ}$. The complexity term gives a measure of how difficult it is to optimize the hyperparameters for a given prior. The free energy defined in Eq. (4.35) can be divided into these terms:

$$F = \text{accuracy}(\boldsymbol{\lambda}) - \text{complexity}(\boldsymbol{\lambda}). \quad (4.36)$$

where the accuracy is defined as:

$$\text{accuracy}(\boldsymbol{\lambda}) = -\frac{N_t}{2} tr(\mathbf{C_V}\mathbf{\Sigma_V^{-1}}) - \frac{N_t}{2}\log|\mathbf{\Sigma_V}| - \frac{N_c N_t}{2}\log(2\pi) \quad (4.37)$$

and the complexity as:

$$\text{complexity}(\boldsymbol{\lambda}) = -\frac{1}{2} tr\big((\boldsymbol{\lambda}-\boldsymbol{\nu})^T \mathbf{C}_{\boldsymbol{\nu}}^{-1}(\boldsymbol{\lambda}-\boldsymbol{\nu})\big) + \frac{1}{2}\log|\mathbf{C}_{\boldsymbol{\nu}}^{-1}\mathbf{\Sigma}_{\boldsymbol{\lambda}}|. \quad (4.38)$$

Each term in the free energy cost function of Eq. (4.35), can be expressed in words as follows [117]:

$$\begin{aligned} F = &-[\text{Model error}] \\ &-[\text{Size of model covariance}] \\ &-[\text{Number of data samples}] \\ &-[\text{Error in hyperparameters}] \\ &+[\text{Error in covariance of hyperparameters}]. \end{aligned} \quad (4.39)$$

This trade-off reflects the principle of parsimony, i.e. Occam's razor [118], that states that complex models should not be considered without necessity (see also section 4.4.2.4). In the next section we show how the free energy cost function is optimized.

4.4.2.3 Optimization

The optimal combination of hyperparameters $\hat{\boldsymbol{\lambda}}$ is achieved for the maximum free energy value. Based on these optimal hyperparameters, $\mathbf{C}_{\boldsymbol{\epsilon}}$ and $\mathbf{C}_{\mathbf{J}}$ can be calculated using Eq. (4.17), and the source intensities $\hat{\mathbf{J}}$ can be calculated using Eq. (4.15). In what follows we describe 2 optimization techniques of the free energy.

Expectation Maximisation

To select the optimal hyperparameters $\hat{\boldsymbol{\lambda}}$, iterative algorithms such as Expectation-Maximization (EM) can be used, treating $\mathbf{J}$ as hidden data [119]. In the E-step the hyperparameters are fixed and the problem is solved for the free energy in Eq. (4.35). In the M-step the hyperparameters $\boldsymbol{\lambda}$ are updated with the gradient and Hessian of the Free energy. Within this process all non relevant hyperparameters are eliminated to reduce the computational cost. The derivative of $F(\boldsymbol{\lambda})$ in Eq. (4.35) is:

$$\frac{\partial F(\boldsymbol{\lambda})}{\partial \lambda_i} = -\frac{N_t}{2} tr(\mathbf{P}_i(\mathbf{C}_{\mathbf{V}} - \boldsymbol{\Sigma}_{\mathbf{V}})) - \mathbf{C}_{\boldsymbol{\nu}_{ii}}(\lambda_i - \nu_i) \tag{4.40}$$

with

$$\mathbf{P}_i = \frac{\partial \boldsymbol{\Sigma}_{\mathbf{V}}^{-1}}{\partial \lambda_i} = \lambda_i \boldsymbol{\Sigma}_{\mathbf{V}} \mathbf{Q}_i \boldsymbol{\Sigma}_{\mathbf{V}} \tag{4.41}$$

and its Hessian is obtained with the derivative of the gradient:

$$\frac{\partial^2 F(\boldsymbol{\lambda})}{\partial \lambda_i \partial \lambda_j} = -\frac{N_t}{2} tr(\mathbf{P}_i \mathbf{Q}_i \mathbf{P}_i \mathbf{Q}_j) - \mathbf{C}_{\boldsymbol{\nu}_{ii}} \tag{4.42}$$

Note that the first term of both Eqs. (4.40) and (4.42) is only defined by the accuracy, and the second term only depends on the complexity.

Restricted Maximum Likelihood

The iterative computation of the E and M steps is not computationally efficient. In the original implementation of the MSP algorithm in the SPM software [114], the Restricted Maximum Likelihood (ReML) algorithm was proposed for computing the E-step once and optimizing over the M-step. The hyperparameters are initialized in the algorithm as $\log(\boldsymbol{\nu}) = -32$ and $\log(\mathbf{C}_{\boldsymbol{\nu}}) = 256\mathbf{I}_{N_q}$. The ReML algorithm then goes as follows:

1. For the k-th iteration compute the covariance matrix $\boldsymbol{\Sigma}_{\mathbf{V}}^{(k)}$.
2. Compute the gradient of the free energy with Eq. (4.40) for each hyperparameter.
3. Compute the curvature of the free energy with Eq. (4.42) for each hyperparameter.
4. Update the hyperparameters:

$$\lambda_i^{(k)} = \lambda_i^{(k-1)} + \Delta\lambda_i \tag{4.43}$$

   where the variation on each hyperparameter $\Delta\lambda_i$ is computed with a Fisher scoring over the free energy variation:

$$\Delta\lambda_i = -\left(\frac{\partial^2 F(\boldsymbol{\lambda})}{\partial\lambda_i \partial\lambda_j}\right)^{-1} \frac{\partial F(\boldsymbol{\lambda})}{\partial\lambda_i} \tag{4.44}$$

5. Eliminate those hyperparameters near to zero, and their corresponding covariance component.
6. Update the free energy variation

$$\Delta F = [\frac{\partial F}{\partial\lambda_1}, \ldots, \frac{\partial F}{\partial\lambda_{N_q}}].[\Delta\lambda_1, \ldots, \Delta\lambda_{N_q}]^T \tag{4.45}$$

   and finish if it is less than a given tolerance (here $\Delta F < 0.01$). Otherwise go back to step 1.

Note that the total free energy was not computed within ReML, it is done just once at the end of the iterative process. Although, the ReML by itself is enough to compute the optimal set of hyperparameters, it is computationally too intensive for a large number of covariance components. In order to reduce the computational burden, two main improvements

are proposed in the SPM software: A Greedy Search (GS) over the multiple sparse priors, for more information see [120, 121] and an Automatic Relevance Determination (ARD) optimized for sparse patterns, see [114].

4.4.2.4 Bayesian model selection

Assume we want to compare different forward models using the hierarchical Bayesian framework. By making the dependency of the forward model, assume model n given the lead fields, explicit, Eq. (4.7) becomes [117]:

$$p(\mathbf{J}_n|\mathbf{V}_m, n) = \frac{p(\mathbf{V}_m|\mathbf{J}_n, n)p(\mathbf{J}_n)}{p(\mathbf{V}_m|n)} \tag{4.46}$$

where $p(\mathbf{J}_n)$ represents the prior assumptions about the source activity and $p(\mathbf{V}_m|n)$ the model evidence.

The log evidence after inversion, i.e. the free energy computed with the optimal set of hyperparameters: $\log p(\mathbf{V}_m, \hat{\boldsymbol{\lambda}})$, is a rigorous upper bound on the log model evidence: $\log p(\mathbf{V}_m|n)$ [112, 117]. Therefore the free energy can be used for Bayesian model selection.

In the next sections we defined some metrics based on the free energy values in order to test the likelihood of obtaining a model in favor of the other model given the data.

Fixed effects analysis

The free energy values corresponding with the inversion of different models can be evaluated in a fixed effects analysis comparing the log Bayes factors (BF). The log Bayes factor for two models n_1 and n_2 is defined as [122]:

$$\log(BF_{12}) = \frac{p(\mathbf{V}_m|n_1)}{p(\mathbf{V}_m|n_2)} = F(n_1) - F(n_2) \tag{4.47}$$

where $F(n_1)$ is the free energy corresponding with model 1 and $F(n_2)$ the free energy corresponding with model 2. The group log Bayes factor (GBF) is defined as the sum of the Bayes factors over N subjects:

$$\log(GBF_{12}) = \sum_{i=1}^{N} F(n_1)^i - F(n_2)^i \tag{4.48}$$

According to the decision rule described in [123] one model can then be chosen in favor of the other when there is a difference larger than 3. This criterium is valid for both the BF and the GBF at the group level. The GBF is a simple and straightforward index for model comparison but it does not account for group heterogeneity or outliers.

Random effects analysis

The expected posterior model frequencies and exceedance probabilities are typically reported to quantify the probability that a particular model generated the data for any randomly selected subject, relative to other models. These metrics are calculated using a random effects approach treating each model as a random variable and estimating the parameters of a Dirichlet distribution that describes the probabilities for all considered models [124]. This approach is robust to the presence of outliers. The expected posterior model frequency reflects the proportion of participants that favor a certain model:

$$\langle r_k \rangle = \frac{\alpha_k}{\alpha_1 + \cdots + \alpha_K} \tag{4.49}$$

with $k = 1, \ldots, K$ and K the number of models, α_i with $i = 1, \ldots, K$, the Dirichlet parameters and $\langle r_k \rangle$ representing the expected likelihood of obtaining the k-th model over all the other models. The exceedance probability expresses belief that a model has the highest posterior probability, relative to other models, given the group data $\mathbf{V}$:

$$\phi_k = p(r_k > r_j | \mathbf{V}; \boldsymbol{\alpha}) \tag{4.50}$$

with $k = 1, \ldots, K$ and K the number of models, $j = 1 \ldots K$ and $j \neq k$, $\boldsymbol{\alpha} = [\alpha_1, \ldots, \alpha_K]$, the Dirichlet parameters and r_k the probability of model k.

In order to quantify the reliability of the results obtained based on the exceedance probabilities and the expected posterior model frequency, the Bayesian omnibus risk (BOR) is typically reported [125]. The BOR directly quantifies the probability that the expected posterior model frequencies are all equal to each other and therefore evaluates the probability that the observed findings may have occurred by chance. The BOR can be compared to any desired error rate, for example the 5% rate in analogy to the classical p-values. The rule of thumb states that when the BOR is smaller than 0.25, we can be confident in choosing

the best model based on the results of the exceedance probabilities [125].

Remarks

Two additional comments should be made. First, the free energy only provides an approximation to the Bayesian log evidence (see [121] for a detailed discussion). Nevertheless, there is enough confidence based on almost 30 years of advances and successful results in the field that it is a good measure to compare models [116, 124, 126]. Second, there is no absolute information how good the models are, but only which model is more probable depending on the data.

In the next chapters of this dissertations we used the free energy corresponding with the Bayesian inversions of realistic EEG data to compare different forward modeling assumptions using the metrics described above.

Chapter 5

Template forward models

"There was no preconception of what to do"
Daft Punk - Giorgio by Moroder

5.1 Introduction

As shown in the previous chapter, the PEB framework allows to compare forward models based on the free energy bound on the Bayesian log model evidence. It provides an alternative way of testing forward models, using real data, rather than the more traditional simulated data from an assumed true forward model. Only a few forward modeling approaches have been compared within the PEB framework for MEG source imaging. Based on event related fields (ERF) for visual processing of faces and scrambled faces, [127] recommends to use a 3-layered Boundary Element Method (BEM) approximation of the head containing 3 homogenous isotropic conducting compartments corresponding with scalp, skull and brain tissue. In this study, the authors compared 3-layered BEM template head models with multi-layer spherical models.

To our knowledge, no prior studies have been published that used the PEB framework to compare forward modeling approaches for EEG source imaging. The forward model is however more crucial for EEG source imaging than for MEG source imaging [128]. In this chapter we therefore extended the [127] study to EEG forward modeling approaches. In the context of group studies, we used an anatomical template MR image (i.e. the Colin27 template [31]) to construct the head models. In addition to the currently used 3-layered BEM approach we introduced

models based on the finite difference reciprocity method introduced in section 3.2.4.3. As such we were able to construct a head model including cerebrospinal fluid (CSF) segmented from the template MRI.

In previous studies, EEG and MRI experiments in supine and prone subject position experimentally proved how important the effect of CSF on the EEG is [129]. Also simulation studies showed that it is crucial to model the CSF [130–132], and it was recently shown that the CSF effect is far bigger than differences in numerical errors between state-of-the-art forward modeling approaches [133]. The study in this chapter is complementary to these studies. Different head models with and without CSF are compared based on using realistic EEG data.

Using a 96-channels ERP datasets of 20 subjects in 4 stimulus conditions and using Bayesian model selection for group studies [124, 125], we investigated the effect of using three different template head models. We therefore used three different types of source priors related to the type of inversion used in the PEB framework. The default BEM model used in the SPM software was considered, a FDM model equivalent to the 3-layered BEM model and a FDM model extended with CSF compartments segmented from the template MRI. Three different types of source priors were compared for each of these head models: independent and identically distributed (IID) sources, coherence (COH) priors and multiple sparse priors (MSP) that we introduced in section 4.4.1. In addition, the reconstructed activity was also compared with the findings of previous studies using functional magnetic resonance imaging (fMRI) in similar stimulus conditions.

In the next methods section, we will introduce the FDM forward modeling approach. For numerical validation, we first compare the FDM approach numerically to a state-of-the-art BEM approach based on an analytical spherical reference model. In the following subsections we will describe how we constructed the different head models based on the anatomical template MR image. We explain how we compared the models numerically and how the models were compared for each of the assumed source priors using Bayesian model selection based on free energy (see section 4.4.2.4).

5.2 Methods

5.2.1 Forward modeling

To calculate the BEM based field propagation, the OpenMEEG toolbox was used within FieldTrip [34] using the symmetric BEM [55]. The FDM lead fields were computed using an implementation based on reciprocity (FDRM) as described in section 3.2.4.3.

5.2.1.1 Spherical model

Triangulated spherical meshes were built using the FieldTrip toolbox [34] with origin-to-vertex radii of 80, 85 and 92 mm and 2562 vertices per surface. The meshes were subsequently rotated around the x, y and z axis in random angles to avoid excessive symmetry. The mean Triangle-Side Length (TSL) was 6 mm of the innermost mesh. These surfaces were subsequently voxelized in a $1 \times 1 \times 1$ mm volume in order to be able to compare with the FDRM based volumetric approach. The conductivities of the brain and scalp were set to 0.33 S/m and 0.022 S/m for the skull [35]. On the scalp we assumed 96 electrodes embedded inside the boundary of the scalp surface to calculate the lead fields for the analytical, BEM and FDRM solution.

For numerical validation, we used a similar approach to the one explained in [134, 135]. A set of 50 random positions were generated in an upper left quadrant of the inner skull surface at various nominal depths orthogonal to and measuring from the innermost sphere. For each position, unit dipoles were placed in x, y and z direction. We only used the upper left quadrant because of symmetry, see Fig. 5.1.

5.2.1.2 Forward models based on the Colin27 template

The geometry of the considered template head models used for reconstruction is based on the default Boundary Element Method (BEM) geometry used in the SPM software. This geometry relies on surface meshes of the scalp, outer skull and inner skull that are constructed from a template anatomical MR image registered to the ICBM152 MNI stereotaxic space, known as the Colin27 template [31].

Three layered scalp-skull-brain model
We used the scalp, outer skull and inner skull meshes containing 2562

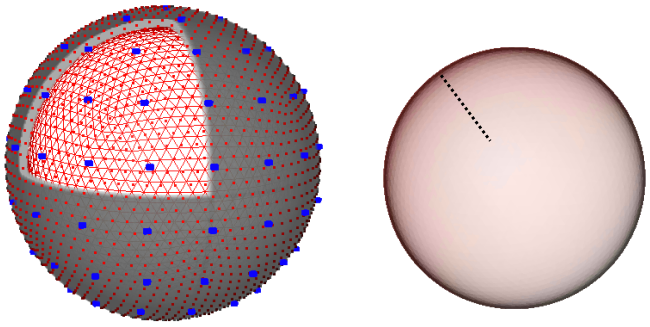

Figure 5.1: Illustration of the approach for validation in a 3-layered spherical head model using dipoles in the upper left quadrant related to the electrodes. 50 random dipole positions were generated in the upper left quadrant of the inner skull surface at various nominal depths orthogonal to and measuring from the innermost sphere. This is depicted by the dashed line in the right figure.

vertices per surface to construct a 3-layered BEM based geometry. These surfaces were subsequently discretized on a 3D, $1\times1\times1$ mm cubic grid to compare with a FDRM based volumetric approach. For these 3-layered head models we used the BEM_{3lay}, $\text{FDRM}_{\text{3lay}}$ notation respectively. On the scalp surface we assumed 96 electrodes embedded inside the boundary of the scalp to calculate the lead fields for both the FDRM and BEM solution. The conductivities of the brain and scalp were set to 0.33 S/m and 0.022 S/m for the skull [35].

Incorporation of CSF

We extended the 3-layered scalp-skull-brain isotropic $\text{FDRM}_{\text{3lay}}$ head model with isotropic conducting cerebrospinal fluid (CSF) compartments. For this model we used the $\text{FDRM}_{\text{4lay}}$ notation. The CSF was modeled based on the volume between the cortical surface and the discretized inner skull mesh. The CSF in the ventricles and the cerebellum were segmented from the MRI template using the SPM software [27]. The conductivity of CSF was set to 1.79 S/m according to [136]. The conductivity of the brain compartment was set to 0.33 S/m. This resulted in a model including scalp, skull, CSF and brain tissue.

Source space

For all the considered head models for reconstruction, the source space was constructed using a template cortical mesh corresponding with the Colin27 template, also available in the SPM software [137]. In order to build a state-of-the-art BEM and FDM model, this cortical mesh was resampled according to some restrictions. For the BEM, the dipoles had to be at least 1/2 mean triangle side length (TSL) vertex-to-vertex distance away from the inner skull according to [135]. The mean TSL of the inner skull was 5.11 mm, so we ensured that the dipoles were at least 2.56 mm vertex-to-vertex distance away from the inner skull surface. For the FDRM, the dipole model extends over 3 nodes of the voxel elements in the x,y and z direction [50]. In order to have a physically correct model, we ensured that at least 2 voxels of gray matter were between the central node of the dipole model and the boundaries with other tissues in the x,y and z direction. In addition, we ensured that the vertices of the mesh were corresponding with unique voxel nodes of the discretized volume. This resulted in 7002 dipoles we modeled with fixed orientations orthogonal to the cortical surface (see section 3.2.2.4). The closest vertex-to-vertex distance from a dipole to the inner skull surface was 2.61 mm.

For the MSP approach, a set of $N_p = 512$ patches was assumed covering the entire cortical surface. The centers of these patches were a sparse sample of the original set of the 7002 dipoles assumed on the cortical surface. Rather than each covariance component corresponding to a single patch, the set was supplemented by 256 covariance components, in which patches in opposite hemispheres were correlated. The size of the patches was fixed ($\omega = 0.6$ in Eq. (4.18)).

Overview of the resulting models

Fig. 5.2 shows an overview of the construction of the different head models. We used the default electrode positions, corresponding with the ERP data, coregistered to the MRI template. Step (1) corresponds with the resampling process of the template cortical mesh. Step (2) represents the coregistration process of the default electrode positions to the MRI template. Step (3) and (4) show how the BEM_{3lay} model was constructed based on the surface meshes and how the FDRM three-layered model ($\text{FDRM}_{\text{3lay}}$) was constructed based on a volumetric approximation of it. Step (5) corresponds with the CSF and cerebellum segmentation. Step (6) shows the extension of $\text{FDRM}_{\text{3lay}}$ with CSF to $\text{FDRM}_{\text{4lay}}$.

Fig. 5.3 shows 3 orthogonal slices of the three-layered scalp-skull-brain

$FDRM_{3lay}$ model and the $FDRM_{4lay}$ model with CSF. The white spots correspond with dipoles located on the discrete cortical mesh.

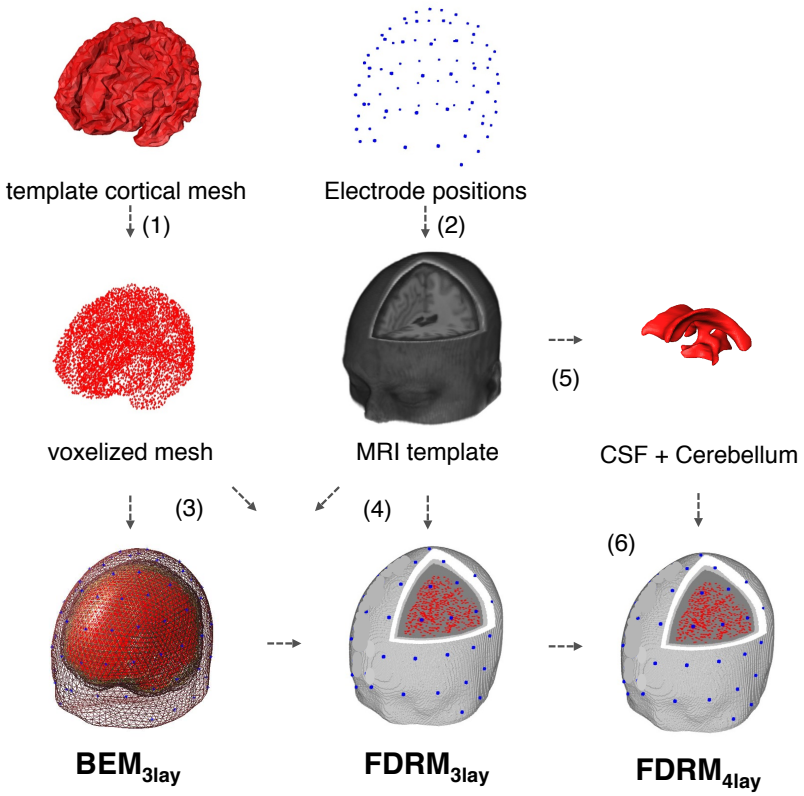

Figure 5.2: Comparison of the BEM_{3lay}, $FDRM_{3lay}$ and $FDRM_{4lay}$ head models constructed based on a MRI template (Colin27) and the default electrode positions corresponding with the ERP data. In step (1) the template cortical mesh used in SPM was resampled in order to be able to use it in a volumetric model. The dipoles depicted by the red spots are located on the template cortical mesh. Step (2) corresponds with the coregistration process of the default electrode positions to the MRI template. In step (3) the BEM_{3lay} model was constructed based on the surface meshes extracted from the template and in step (4) the FDRM three-layered model ($FDRM_{3lay}$) was constructed based on a volumetric approximation of it. In step (5) the CSF and cerebellum were segmented form the template. Step (6) corresponds with the extension of $FDRM_{3lay}$ with CSF to $FDRM_{4lay}$.

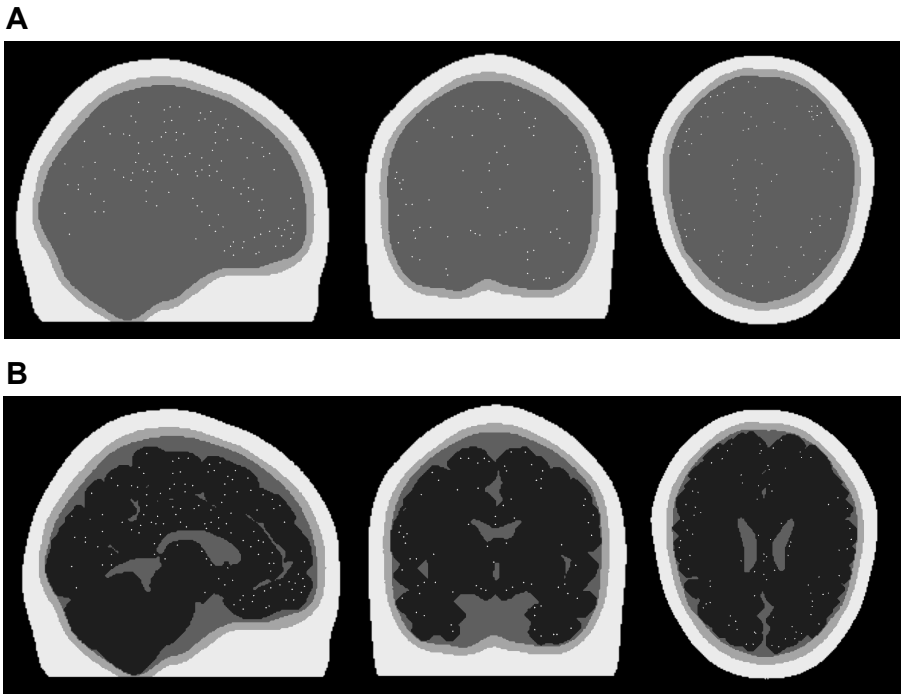

Figure 5.3: Sagittal, coronal and horizontal slices of the FDRM head models including the dipoles, depicted by the white spots, located on the discretized cortical mesh. A: the 3-layered isotropic scalp-skull-brain head model ($\text{FDRM}_{3\text{lay}}$), B: the 3-layered FDRM model including CSF ($\text{FDRM}_{4\text{lay}}$).

5.2.1.3 Numerical model comparison

In order to numerically compare the lead fields corresponding with the head models that are considered in this study, we used the Magnitude (MAG) ratios and Relative difference measures (RDM) [55]:

$$MAG(\mathbf{L}_1, \mathbf{L}_2) = \frac{||\mathbf{L}_2||}{||\mathbf{L}_1||} \tag{5.1}$$

$$RDM(\mathbf{L}_1, \mathbf{L}_2) = \left|\left| \frac{\mathbf{L}_2}{||\mathbf{L}_2||} - \frac{\mathbf{L}_1}{||\mathbf{L}_1||} \right|\right| \tag{5.2}$$

L denotes the lead fields and subscript 1 and 2, correspond with the considered head models. The closer to 1 (respectively to 0) the MAG (respectively the RDM), the closer model 2 is to model 1.

5.2.2 Realistic EEG data

We used ERP datasets of 20 subjects expressing a N170 component in 4 different stimulus conditions. In brief, twenty healthy individuals performed 150 trials of faces, houses, inverted faces and words stimuli. The EEG data were collected from 96 EEG electrodes using a BrainAmp system (BrainProducts, Gilching, Germany). To extract task-related ERPs, the data were then segmented from -100 ms before until 500 ms after stimulus onset, and baseline corrected. Finally, the data were averaged over trials and average referenced resulting in 4 different ERP datasets for each subject corresponding with each condition: faces, houses, inverted faces or words. A detailed description of the experimental set-up and previous data analysis is presented in [138].

5.2.2.1 Bayesian model selection based on free energy

To compare the different models considered in this chapter - i.e. the BEM_{3lay} , $\text{FDRM}_{\text{3lay}}$ and $\text{FDRM}_{\text{4lay}}$ model for each of the source priors, IID, COH or MSP, resulting in 9 models - we applied Bayesian model selection based on the free energy, for group studies [124, 125]. This is based on the assumption that the maximum free energy approximates the logarithm of the model evidence (see section 4.4.2). For all the comparisons reported in this chapter we calculated the free energy values corresponding with the reconstructions of the whole ERP, this means from 100 ms before stimulus to 500 ms after stimulus. This resulted in 9 different free energy values for each of the 20 subjects and each of the stimulus conditions. Bayesian model selection was used to identify the best model. The best model was identified using 3 measures: the log group Bayes factor, the expected posterior model frequencies and the exceedance probabilities.

For each stimulus condition we performed a fixed effects analysis comparing the log model evidences for each stimulus condition at the group level. This is accomplished by calculating the log group Bayes factor which is the sum across subjects of individual log Bayes factors (as introduced in section 4.4.2.4). According to the decision rule described in [123] one model can be chosen in favor of the other when there is a

difference larger than 3.

We also performed a random effects analysis and reported the expected posterior model frequency and exceedance probabilities (see section 4.4.2.4). In addition, as advised in [125] and computed with the VBA toolbox [139], we reported the Bayesian omnibus risk (BOR). If the BOR is smaller than 0.25, then we could be confident in choosing the best model based on the results of the exceedance probabilities.

5.2.2.2 Comparing the reconstructed activity

We verified the reconstructed activity corresponding with the N170 component by comparing our results with the findings of previous studies using fMRI in similar stimulus conditions. For the faces stimuli we expected the bilateral activation of the fusiform face areas (FFA) located in the left and right fusiform gyrus dominant in the right hemisphere [138, 140–143]. For the houses stimuli we expected the activation of the parahippocampal place areas (PPA). For the inverted faces stimuli, it is less clear which brain areas are dominantly activated. In general, the effect of inversion causes a shift from specialized faces processing streams towards generic object-processing mechanisms [144–146]. For the words stimuli we expected the activation of the left mid fusiform (MF) gyrus, sometimes called the visual word forming area (VWFA) [147, 148]. The MNI coordinates of the aspected active areas are shown in table 5.1.

	Left	**Right**	**Reference**
FFA	[-37 -42 -22]	[39 -40 -21]	[149]
PPA	[-27 -52 -8]	[28 -47 -9]	[150]
MF	[-42 -57 -10]	[42 -57 10]	[151]

Table 5.1: The MNI coordinates of the aspected active areas.

In Fig. 5.4 an example is shown of the ERP data averaged over trials for one of the subjects in the different stimulus conditions on a left and right lateral occipital channel. To compare the reconstructed activity we reported the mean evoked energy across subjects of the reconstructed activity corresponding with the time windows depicted by the arrows.

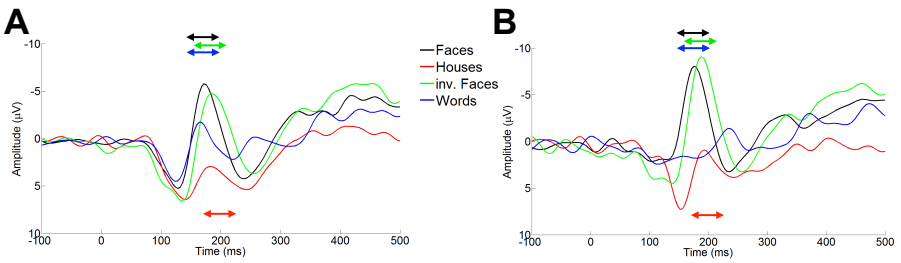

Figure 5.4: ERP data averaged over trials of one of the subjects for a (A) left lateral occipital and a (B) right lateral occipital channel. The arrows depict the time windows for which the mean evoked energy across subjects is reported to compare the reconstructed activity: 140 - 180 ms for faces, 180 - 220 ms for houses, 150 - 190 ms for inverted faces and 140 - 180 ms for words.

5.3 Results

5.3.1 Numerical forward model comparison

5.3.1.1 Spherical analytical reference

At each depth, starting from 3 mm from the skull (see section 5.2.1.1), the MAG/RDM values for the 50 dipoles were calculated for both the FDRM and the BEM (see Fig. 5.5). The thick lines show the median MAG/RDM, and the thin lines the minimum and maximum MAG/RDM corresponding with each depth from the inner skull surface. The dashed vertical lines mark the depths of one and two mean TSL. In general the BEM performs better than the FDRM but the FDRM is still performing reasonably well with median ln(MAG) nearly at 0 and median RDM below 0.03. The MAG/RDM differences between the FDRM and BEM are mainly expressed for source depths smaller than 1 TSL (6 mm). From that point, the MAG/RDM values start to rise quickly for the BEM compared to the FDRM which tends to stay more stable for superficial sources in this geometry.

5.3.1.2 Forward models based on the colin27 template

In Fig. 5.6 A and B, boxplots of the MAG and RDM are shown for the 7002 dipoles assumed inside the brain compartment. For both A and B, in the first row the BEM_{3lay} lead fields are compared to the $FDRM_{3lay}$ lead fields, in the second row the BEM_{3lay} lead fields are compared to

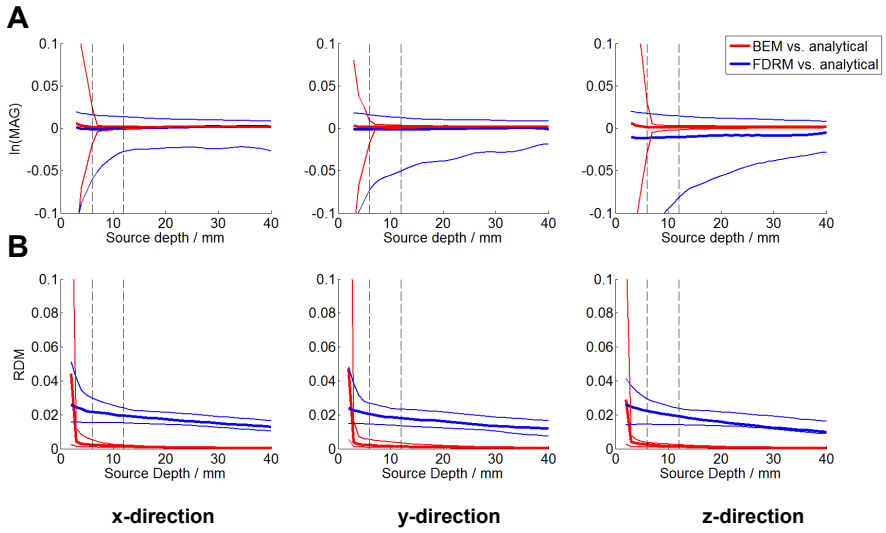

Figure 5.5: A) Magnitude ratios (MAG) and B) Relative Difference Measures (RDM) of the BEM and FDRM versus a spherical analytical reference model in x, y and z direction. The thick lines show the median MAG/RDM, and the thin lines the minimum and maximum MAG/RDM corresponding with each depth from the inner skull surface. The dashed vertical lines mark the depths of one and two mean triangle side length (TSL).

the $\text{FDRM}_{4\text{lay}}$ lead fields and in the last row the $\text{FDRM}_{3\text{lay}}$ lead fields are compared to the $\text{FDRM}_{4\text{lay}}$ lead fields. The mean and standard deviations for the MAG and RDM are given for clarity. It is clear that the modeling of CSF using the FDRM has a bigger influence on the MAG and RDM values than comparing the techniques themselves in the same scalp-skull-brain geometry.

5.3.2 Model comparison based on free energy

In Fig. 5.7 an overview is given of the log group Bayes factor (log GBF), the expected posterior model frequency and the exceedance probabilities for the different stimulus conditions. The log group Bayes factor is shown in the first row for each stimulus condition and is calculated for each model versus model MSP - $\text{FDRM}_{4\text{lay}}$. For each of the stimulus conditions the log group Bayes factor is much lower than -3 which corresponds with strong evidence in favor of model MSP - $\text{FDRM}_{4\text{lay}}$.

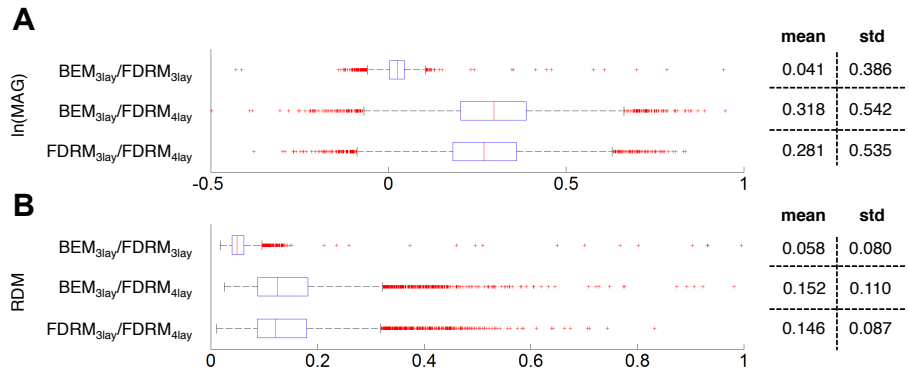

Figure 5.6: A) Boxplot of the Magnitude ratios (MAG) and B) boxplot of the Relative Difference Measures (RDM) expressing the verification of the lead fields corresponding with BEM_{3lay}, $FDRM_{3lay}$ and $FDRM_{4lay}$ for the 7002 dipoles we assumed inside the brain compartment. In the table on the right, the mean and standard deviations are depicted for each comparison.

The expected posterior model frequency and the exceedance probabilities are shown in the second and third row. For each of the stimulus conditions also the BOR values are shown. They are much below 0.25 which suggests that we can be very confident about the results of the exceedance probability. For the faces condition, the exceedance probability is 0.84 for model MSP - $FDRM_{4lay}$. Similar results have been found for the other conditions. The exceedance probabilities are 0.998, 0.999 and 0.996 for the houses, inverted faces and words stimuli respectively. Based on these results we have strong evidence in favor of the MSP - $FDRM_{4lay}$ model for all datasets.

5.3.3 Comparing the reconstructed activity

We compared the mean reconstructed activity over subjects of the MSP inversions corresponding with the event related potentials elicited by faces, houses, inverted faces and words stimuli for the BEM_{3lay}, $FDRM_{3lay}$ and $FDRM_{4lay}$ head models. The mean evoked energy across subjects of the MSP inversions corresponding with the N170 peak is presented in Fig. 5.8. Each panel shows a maximum intensity projection (MIP) of the 512 greatest source strengths within MNI space. The columns in the figure correspond with the type of head model that was assumed and the rows correspond with the different stimulus conditions.

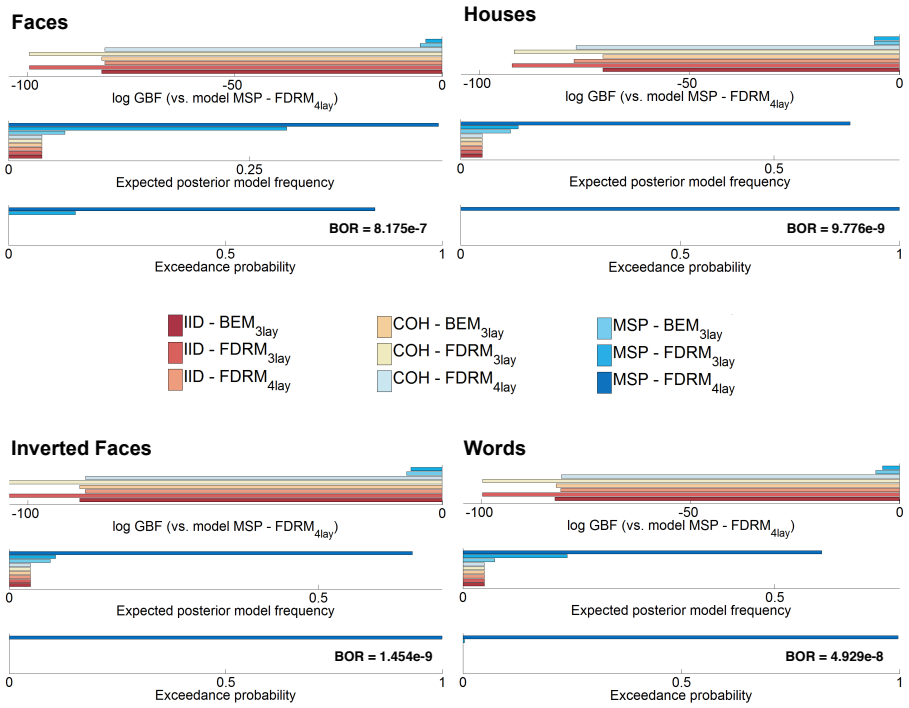

Figure 5.7: Bayesian model selection results of the different models we assumed for reconstructing the ERP data corresponding with faces, houses, inverted faces and words stimuli. We show the log group Bayes factor (log GBF), the expected posterior model frequency and the exceedance probabilities. The different models we used for reconstruction are depicted by the different colors shown in the legend. The log GBF is calculated versus $\text{FDRM}_{4\text{lay}}$. For each of the stimulus conditions we also show the Bayesian omnibus risk (BOR). If the BOR is smaller than 0.25, then we can be confident in choosing the best model based on the results of the exceedance probabilities.

For all the head models we checked the activation near the MNI coordinates reported in literature (see section 5.2.2).

For each of the subjects and stimulus conditions we moreover generated 3D images containing the reconstructed activity. Based on these images we performed statistical analysis to see the main effect over subjects, i.e. at the group level, corresponding with each of the stimulus conditions. The statistical analysis was performed in the Statistical Parametric Mapping software and included a classical T-test corrected for multiple comparisons (see [56] for more details on the procedure).

5.3.3.1 Faces stimuli

For the faces stimuli, the evoked energy of the reconstructed activity is shown between 140 and 180 ms after stimulus to represent the activity corresponding with the N170 peak. Based on literature we expected bilateral activation of the fusiform face areas (FFA) dominant in the right hemisphere which is depicted by the red squares in the glass brain. For the 3 models, the dominant activity was more or less the same. We did not find a clear difference for this stimulus condition.

The results of the group level statistical analysis are presented in Fig. 5.9. The activity with the highest significance is depicted by the red arrow, with the same location for each of the methods. Note that the FWE correction for the BEM_{3lay} was chosen < 0.1 because for the default < 0.05 we did not find any significant activity. It is also clear that the significant blob of activity using $\text{FDRM}_{\text{4lay}}$ was the largest.

5.3.3.2 Houses stimuli

For the houses stimuli, the evoked energy of the reconstructed activity is shown between 180 and 220 ms after stimulus. Based on literature we expected bilateral activation around the PPA depicted by the green squares in the glass brain. For this stimulus condition the difference between both 3 layered models and the extended model is bigger. Using $\text{FDRM}_{\text{4lay}}$, the sources with the maximum intensity are estimated more medial compared to the reconstructions based on the other models, this is depicted by the arrow. It suggests a correspondence with the PPA which is located more medial.

The results of the group level statistical analysis are presented in Fig. 5.10. The activity with the highest significance is depicted by the red

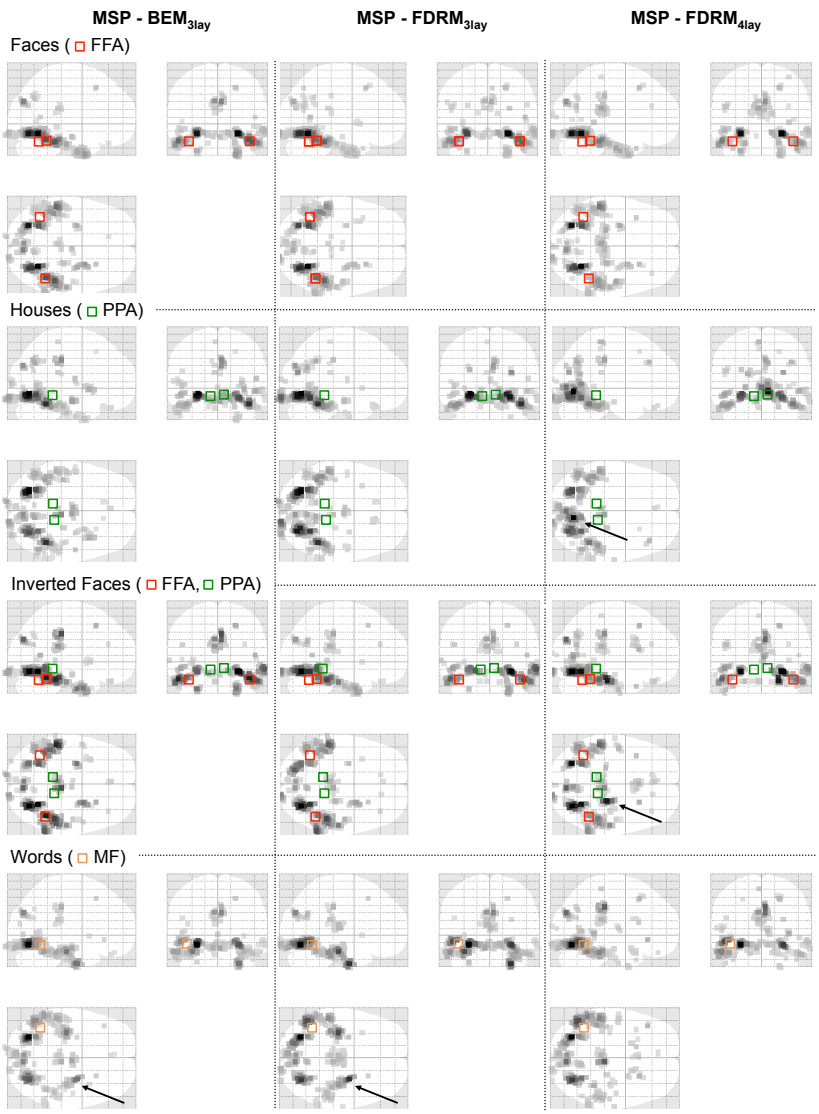

Figure 5.8: The mean evoked energy across subjects of the MSP inversions corresponding with the N170 peak. Each panel shows a Maximum Intensity Projection (MIP) of the 512 greatest source strengths within MNI space (in the glass brain view) for the three head models shown in separate columns. Each row corresponds with a different stimulus condition. The (centers of the) squares show the location of the activity which we expected from the findings of previous studies using fMRI (see section 5.2.2): FFA = fusiform face area, PPA = parahippocampal place area, MF = mid fusiform (MF) gyrus. The arrows depict the main differences between the 3-layered models and the 4-layered model including CSF.

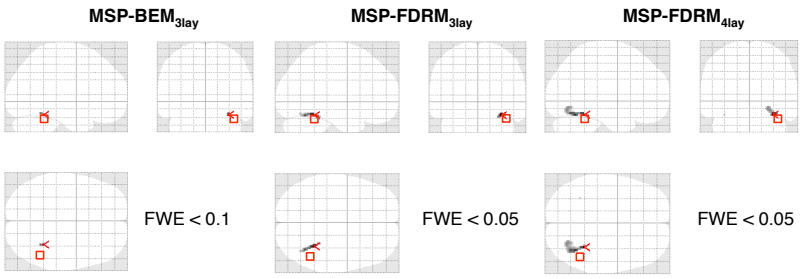

Figure 5.9: Statistical analysis of the reconstructed activity for the faces stimuli over subjects. The main effect is shown of a t-test corrected for multiple comparisons with a FWE < 0.1 for the BEM_{3lay} inversions and FWE < 0.05 for both FDRM inversions. The activity with the highest significance is depicted by the red arrow. The location of the right FFA area is depicted by the red square.

arrow, with different locations for each of the methods. For the BEM_{3lay} and $\text{FDRM}_{\text{3lay}}$ models the significant activity was mainly located in the right hemisphere. For the $\text{FDRM}_{\text{4lay}}$ the most significant activity was found in a right occipital region, but also bilateral activity was found near the PPA regions.

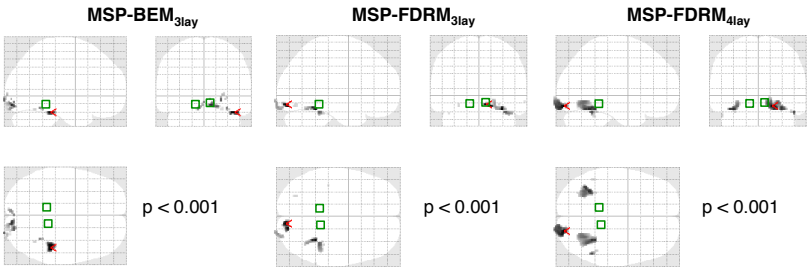

Figure 5.10: Statistical analysis of the reconstructed activity for the houses stimuli over subjects. The main effect is shown of a t-test with a p-value $<$ 0.001. The activity with the highest significance is depicted by the red arrows. The location of the PPA regions is depicted by the green squares.

5.3.3.3 Inverted Faces stimuli

For the inverted faces stimuli, the evoked energy of the reconstructed activity is shown between 150 and 190 ms after stimulus. Based on literature we expected a shift from specialized faces processing streams towards generic object-processing mechanisms. Therefore both the FFA and PPA are depicted in the glass brain. Again both 3 layered models are very similar. The $FDRM_{4lay}$ model, results in an extra patch of activity located medial close to the right PPA, this is depicted by the arrow.

The results of the group level statistical analysis are presented in Fig. 5.11. The activity with the highest significance is depicted by the red arrow, with roughly the same locations for each of the models. The most significant activity estimated based on $FDRM_{4lay}$ is more focal, located in 2 bilateral regions compared to BEM_{3lay} and $FDRM_{3lay}$.

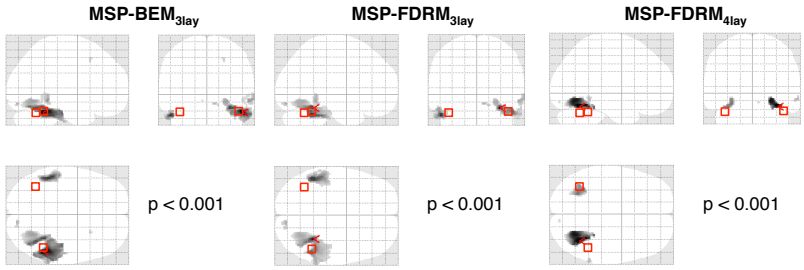

Figure 5.11: Statistical analysis of the reconstructed activity for the inverted faces stimuli over subjects. The main effect is shown of a t-test with a p-value < 0.001. The activity with the highest significance is depicted by the red arrow. The locations of the FFA regions are depicted by the red squares.

5.3.3.4 Words

For the words stimuli, the evoked energy of the reconstructed activity is shown between 140 and 180 ms after stimulus. Based on literature we expected the activation of the left mid fusiform (MF) gyrus. This region is depicted by the dark yellow square in the glass brain. Again both 3 layered models are very similar. Compared to assuming $FDRM_{4lay}$, the reconstructions based on the 3 layered models show a right temporal high intensity region, depicted by the arrows. The left MF activity is found for the 3 models.

The results of the group level statistical analysis are presented in Fig.

5.12. The activity with the highest significance is depicted by the red arrows. The most significant activity estimated based on $FDRM_{4lay}$ and $FDRM_{3lay}$ is located close to the MF region. For the inversions based on BEM_{3lay} the most significant activity was located in the opposite hemisphere close to the FFA region.

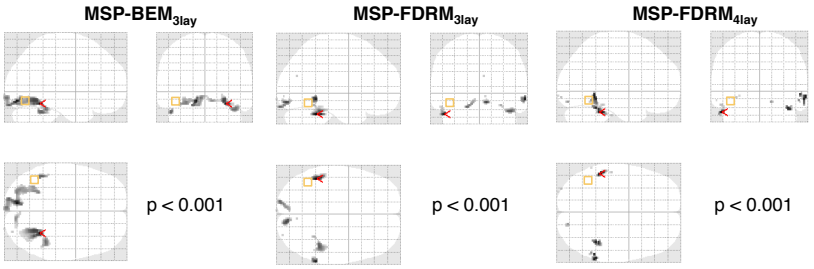

Figure 5.12: Statistical analysis of the reconstructed activity for the words stimuli over subjects. The main effect is shown of a t-test with a p-value $<$ 0.001. The activity with the highest significance is depicted by the red arrow. The location of the MF region is depicted by the orange squares.

5.4 Discussion

In this chapter, we compared different EEG forward modeling options within the SPM-PEB framework for distributed EEG source imaging. By assessing the free energy of ERP source imaging, we explored the effect of assuming different source priors and different head models constructed based on the Colin27 template. We introduced volumetric FDRM head models in addition to the default available 3-layered BEM_{3lay} model.

The results in favor of the MSP approach are consistent with earlier studies comparing the different source priors (IID, COH, MSP) based on EEG and MEG data and a 3-layered BEM approximation of the head [114, 127]. However, assuming a 3-layered isotropic conducting approximation of the head is a strong simplification of reality. By extending this head model with CSF using FDRM modeling, we built a more realistic template head model. Based on grand average ERP data we showed empirically with strong evidence that assuming MSP, this model is better than the competing models. These findings are concordant with previous studies [129, 130, 132, 152, 153].

We numerically compared the FDRM and openMEEG symmetric

BEM versus an analytical spherical reference model. The BEM performed better than the FDRM in this geometry. This is mainly a consequence of the volumetric approximation of the spherical surfaces for the FDRM method. Regarding the boxplots of Fig. 5.6, it is clear that the modeling of CSF using the FDRM has a bigger influence on the RDM and MAG values than comparing the techniques themselves in the same scalp-skull-brain geometry. According to this we can conclude that the influence of introducing CSF is much bigger compared to the influence of using a different forward modeling technique in the same head model geometry. This result was also found in [133]. Including the CSF in the BEM model is a difficult task due to the complex geometrical structure of the CSF, demanding a high number of additional nodes for an accurate modeling, and a strongly increased computational effort. Compared to the BEM, the CSF and other tissue types can be included at negligible computational costs when applying FDRM or other volumetric techniques like finite element modeling (FEM) approaches [133].

We also compared the reconstructed activity. Therefore we showed the mean evoked energy of the reconstructed activity over subjects in a time window corresponding with the N170 peak. Because we could not rely on a ground truth, we could not explain the differences in reconstructed activity quantitatively. However, we did find clear differences between the reconstructed activity assuming the $\text{FDRM}_{\text{4lay}}$ and both the 3-layered models assuming MSP. We showed this qualitatively by using maximum intensity projections and by reporting the area of expected activity based on the findings of previous studies using fMRI in similar stimulus conditions. Also the statistical analysis at the group level showed clear differences assuming each of the 3 considered forward models for which the $\text{FDRM}_{\text{4lay}}$ results provided the most consistent results when comparing with the findings of previous studies.

Note that the use of template models is, in general, very approximative compared to using subject specific models [153]. To model the CSF for example, we used the cortical surface of the Colin27 template as the CSF boundary. As such, there could be discrepancies between the modeled CSF and the subjects' anatomy. Nevertheless, the CSF conductivity is well known and nearly not varying inter-individually [136]. Therefore it is not surprising that the incorporation of CSF in a template head model seems to be better than not modeling it for the reconstructions of the ERP data used in this chapter. Also template head models can introduce additional noise and cause systematic errors in the reconstructed activity. For example for the houses stimuli, regardless of the used forward model,

the focus of the activity is rather lateral, although for the houses it should be more medial.

An important major issue is to assign the conductivity values to the different modeled tissues in the head model. The skull conductivity for example is strongly debated. Assuming a lower conductivity, for example 0.0041 S/m assumed in the Fieldtrip software package [154], would cause differences in source depths [36, 155]. The PEB framework could offer an elegant opportunity to determine the conductivity empirically, by assessing the free energy values corresponding with reconstructions assuming head models with different conductivity values.

Being able to use volumetric forward modeling techniques gives many advantages over surface based approximations of the head. First of all, the head models are constructed using 3D cubic MR images so it is straightforward to construct 3D cubic head models from it. Second, It is possible to model tissue anisotropy [36, 54]. Third, by creating more advanced head models incorporating white and gray matter, more advanced dipolar source spaces can be constructed. This means sources do not necessarily have to be modeled based on a template mesh of the cortical surface but can also be located inside a modeled gray matter layer. Finally, volumetric techniques are able to take care of skull holes easily. Even if there are BEM approaches that can take care of skull holes [154], the construction of the BEM surfaces is extremely difficult. On the other side, in areas where the skull is very thin the FDRM approach used in this chapter might create skull representation errors, namely that current is shunted in areas where two skull elements are only connected by one single node. It is important to take care of these skull holes during the construction of a head model [36].

Note that we did not consider to reconstruct the activity with multiple sparse priors that were kept fixed over subjects, as is suggested in [156] for group studies. This is an option that can be investigated in future work. In the next chapter we will explore the use of subject-specific volumetric head models using the FDRM (or FEM) including more tissues based on the segmentation of high resolution anatomical MR images within the PEB framework. In the chapter we especially focus on the development of volumetric dipolar regions to use as empirical priors in the MSP algorithm.

5.5 Conclusion

In this chapter, we introduced volumetric template head models based on the finite difference method (FDM). We constructed a FDM head model equivalent to the standard BEM model in the SPM software and an extended FDM model including CSF. These models were compared within the context of three different types of source priors related to the type of inversion used in the PEB framework: independent and identically distributed (IID) sources, equivalent to classical minimum norm approaches, coherence (COH) priors similar to methods such as LORETA, and multiple sparse priors (MSP). The resulting models were compared based on ERP data of 20 subjects using Bayesian model selection for group studies. The reconstructed activity was also compared with the findings of previous studies using functional magnetic resonance imaging. We found strong evidence in favor of the extended FDM head model with CSF and assuming MSP. These results suggest that the use of realistic volumetric forward models can improve PEB EEG source imaging.

5.6 Original Contributions

The use of the PEB framework for forward model comparison based on finite differences was first presented at the 18th Annual Meeting of the Organization for Human Brain Mapping [157]. The comparison of forward models based on the boundary element method and finite difference method was first presented at the 18th International Conference on Biomagnetism [158]. The results presented in this chapter were presented in the A1-journal NeuroImage [159]. The validation of the Finite Difference Method based on spherical head models and the implementation to calculate the lead fields was also incorporated in a publication in the A1-journal Brain Topography [36].

Chapter 6

Subject specific forward models

"Where are we, this everything?"
The war on drugs - Red Eyes

6.1 Introduction

In this chapter we investigate subject specific forward models using the parametric empirical Bayesian (PEB) framework. We depart from the framework that was introduced in chapter 4 and applied in chapter 5. In the present implementation of the MSP algorithm, multiple cortical patches of sources are constructed from the dipoles in the source space that are constrained to a cortical surface mesh [137] and the field propagation of the surface patches is calculated based on a 3-layered scalp-skull-brain BEM head model [127]. Constraining the dipolar sources to a cortical mesh does only allow the reconstruction of brain activity on the cortical surface. This way deep sources in the cerebral cortex cannot be reconstructed. Moreover, it is not straightforward to use more complex head models that extend the 3-layered BEM model with extra layers such as cerebrospinal fluid (CSF). Because the dipoles are located on the boundary between the CSF and the brain, they will either be located inside the CSF or brain compartment which does not satisfy the restrictions that apply to the source space of commonly used numerical methods, such as the boundary element method, finite difference method or finite element method that were introduced in section 3.2.4.2,

to properly calculate the dipole field propagation [135, 159].

In this chapter, we propose a technique to construct volumetric regions based on a dipole source space restricted to gray matter, segmented from an anatomical MR image, and using a region growing technique. This approach allows the inclusion of more prior information incorporating the anatomy and shape of the sources and does not require the extraction of the cortical surface. It provides the possibility to use the MSP algorithm to reconstruct brain structures outside the cortical surface and facilitates the use of more realistic volumetric subject specific head models including cerebrospinal fluid (CSF).

To illustrate the volumetric MSP approach, we used realistic ERP datasets and anatomical MR images in 12 subjects. Based on the segmented gray matter for each of the subjects, cortical regions were created and introduced as source priors for MSP-inversion assuming two types of head models. For every subject, a 3-layered volumetric subject specific head model was constructed. Also extended 4-layered head models including CSF were built to investigate the influence of increasing the head model complexity. We compared with the present implementation by assessing the free energy corresponding with the reconstructions using Bayesian model selection for group studies [124, 125]. The reconstructed activity was also compared with the results of previous studies using similar ERP datasets [160].

In the first section of this chapter, we explain how we extended the currently used approach based on cortical patches to volumetric regions and subsequently describe how the different head models used in this study were constructed. Next, we explain how we compared the models using Bayesian model selection and how we verified the reconstructed activity.

6.2 Methods

6.2.1 Multiple sparse priors (MSP) based on cortical surface mesh

In the currently used MSP approach implemented in the SPM software package that was introduced in section 4.4.1.2, the dipole source space is constrained to the nodes of a cortical surface mesh. Based on this surface mesh, covariance components $\{\mathbf{Q}_1^{(2)}, \mathbf{Q}_2^{(2)} \ldots, \mathbf{Q}_{N_p}^{(2)}\}$ are constructed that are each corresponding to a different locally smooth focal patch of

cortex. The covariance components are constructed using the columns of a Green's function, $\mathbf{Q}_G \in \mathbb{R}^{N_d \times N_d}$ defined as:

$$\mathbf{Q}_G = \exp(\omega \mathbf{G}_L) \tag{6.1}$$

and calculated based on a graph Laplacian $\mathbf{G}_L \in \mathbb{R}^{N_d \times N_d}$, with inter-dipole connectivity information containing the neighboring dipoles, and ω, a positive constant value that determines the smoothness of the current distribution or spatial extent of the activated regions [114]. The graph Laplacian $\mathbf{G}_L$ is calculated using an adjacency matrix corresponding with the vertices and faces provided by the cortical surface mesh.

As such, each column of $\mathbf{Q}_G$ corresponds with a cortical patch and has a bell shape, with a full width half maximum depending on the neighboring dipoles and the smoothing factor ω which is equal to 0.6 in the SPM software. The centers of these patches correspond to the original set of dipoles used to form the lead field matrix.

6.2.1.1 Extension to multiple sparse volumetric priors (MSVP)

In the construction process of the surface patches, a cortical mesh is used to calculate the adjacency matrix using the faces and vertices of the cortical mesh. This way, the connections between the sulci of gray matter are taken into account. In order to incorporate the shape of the cortical layer based on the segmented gray matter, we propose a technique to construct volumetric sparse regions using a region growing approach.

Assume a source space of distributed dipoles located inside the segmented gray matter. For each dipole in the source space, a volumetric region is determined based on region growing within the segmented gray matter. The region growing approach starts from a dipole and is characterized by a certain maximum distance to the dipole. As such, the neighboring dipoles for each dipole of the source space can be determined as the dipoles located within the corresponding region of each dipole. An example of the approach in 2D is given in Fig. 6.1. In this example, we assume that we have a slice of a cubic 3D volumetric head model ($1 \times 1 \times 1$ mm resolution) with dipoles in the segmented gray matter equidistant to each other, with a 3mm spacing.

With the information of the neighboring dipoles within the region of each dipole, the adjacency matrix, graph laplacian and Green's function

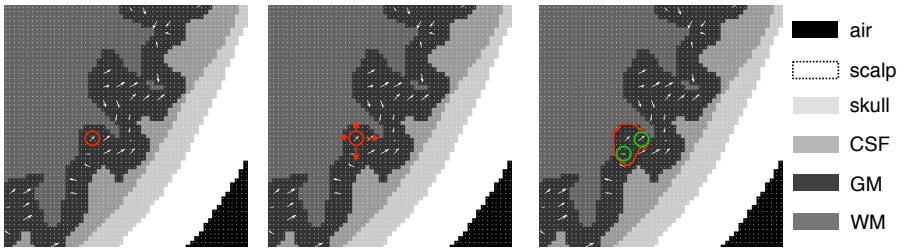

Figure 6.1: An example of the used region growing approach in 2D. The original dipole from which the region growing starts is depicted by the red circle on the left. The maximum distance to the original dipole is 5 mm (i.e. 5 voxels). Based on this restriction, the original dipole has 2 neighboring dipoles depicted by the green circles on the right. CSF = cerebrospinal fluid, GM = gray matter, WM = white matter

can be calculated. Each column of the Green's function Q_G represents a volumetric region and has a bell shape, with a full width half maximum depending on the maximum distance to the original dipole used in the region growing approach and the smoothing factor ω.

6.2.2 Illustration on realistic data

To illustrate the proposed approach, we used ERP data and anatomical MR images in 12 subjects to which checkerboard stimuli were presented. In brief, twelve healthy individuals performed 80 trials of circular black-and-white checkerboard stimuli presented to one of the four quadrants of the visual field. The EEG data were collected from 62 electrodes using the BrainAmp MR+ system (BrainProducts, Gliching, Germany). To extract task-related ERPs, data were then segmented from -100 ms before until 500 ms after stimulus onset, and baseline corrected. Finally, the data were average referenced resulting in 12×4 different grand averaged ERP datasets corresponding with each condition: down left, down right, upper left or upper right. The whole data-acquisition process and preprocessing of the data is described in detail in [160].

In addition, full brain anatomical images were obtained with the magnetization prepared rapid gradient echo (MPRAGE) imaging sequence (230 coronal slices, time to echo [TE] = 4.6 ms, TR = 9.7 s) which we used to construct the subject specific head models.

6.2.2.1 Construction of head models

Because we used a volumetric finite difference method based on reciprocity (FDRM) (as described in section 3.2.4.3) to calculate the dipole field propagation, each of the considered head models was volumetric with a 3D, $1 \times 1 \times 1$ mm voxel resolution.

3-layered models
We followed the default approach implemented in the SPM software to construct subject specific 3-layered models based on the anatomical MR images of the subjects. Meshes representing the scalp, outer skull and inner skull were extracted from the subjects' MR images (see Fig. 6.2A). These meshes were subsequently converted to filled volumes in order to construct volumetric 3-layered head models. Isotropic conductivities of the brain, scalp layer and skull layer were set to 0.33 S/m, 0.33 S/m and 0.022 S/m [35] respectively. In Fig. 6.2B an example is given of a 3-layered volumetric model, denoted as 3lay. We coregistered the 62 electrode positions, corresponding with our realistic EEG data, to the scalp surface and embedded them inside the boundary of the scalp.

4-layered models
Using the anatomical MR images of the subjects, we segmented gray matter, white matter and CSF using SPM8 segmentation techniques [27]. Based on these segmentations and the 3-layered models, 4-layered head models were constructed including a brain and CSF compartment. The conductivity of the CSF was set to 1.79 S/m [136] and 0.33 S/m for the brain layer. In Fig. 6.2C an example is given of a 4-layered volumetric model, denoted as 4lay. We coregistered the 62 electrode positions, corresponding with our realistic EEG data, to the scalp surface and embedded them inside the boundary of the scalp.

6.2.2.2 Construction of dipole source spaces

Cortical surface mesh
For each subject, the source space was constructed using a canonical cortical mesh, defined in a standard stereotactic space. This mesh was warped, in a nonlinear fashion, to match the subjects' anatomy [137]. This resulted in 8196 dipoles distributed on the nodes of the warped cortical surface mesh, with fixed orientations orthogonal to the mesh.

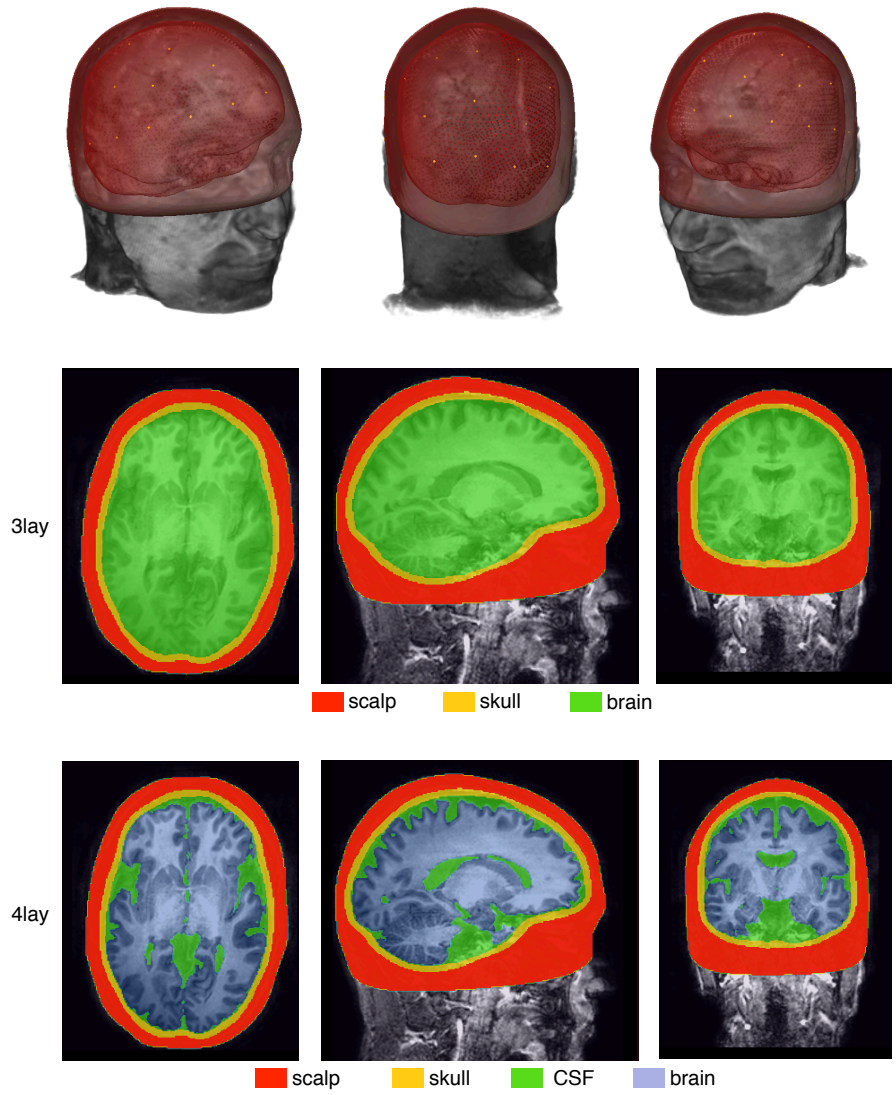

Figure 6.2: Example of the subject specific head models constructed based on an anatomical MR image. The subject specific anatomical MR image is depicted in gray. The electrodes are depicted in yellow. In the first row, the surface meshes used to construct the 3-layered models in SPM are shown in red. The inner mesh corresponding with the red dots corresponds with the inner skull surface. The second row depicts 3 orthogonal slices of the 3-layered volumetric model denoted as 3lay. The third row depicts 3 orthogonal slices of the 4-layered volumetric model including CSF denoted as 4lay.

Volumetric
For each of the models the source space was constructed based on the segmented gray matter. Dipoles were assumed inside gray matter on a cubic grid equidistant to each other with a spacing of 3 mm. Because the dipole model in the FDRM method extends over 3 nodes of the voxel elements in the x, y and z direction [50], we ensured that at least 2 voxels of gray matter were between the central node of the dipole model and the boundaries with other tissues in the x, y and z direction. This resulted in approximately 10.000 dipoles for each of the models. The orientations of the dipoles were determined based on a method described in [161]. This method starts from the segmented white matter to calculate the orientations of the grid points in gray matter after smoothing and taking the gradient of the volume. An example is given in Fig. 6.3.

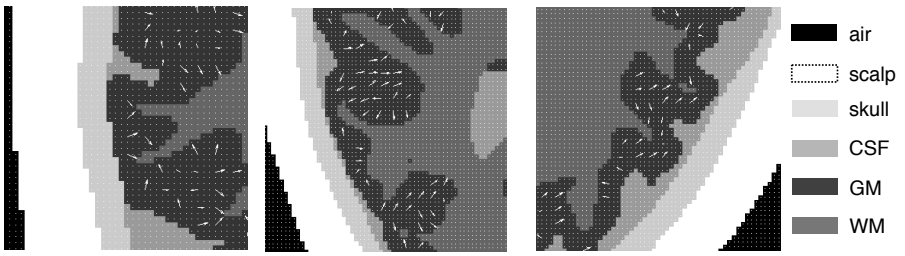

Figure 6.3: Example of the dipole orientations depicted by the white arrows shown in a detailed view corresponding with 3 orthogonal slices. The different colors in the slices correspond with different tissue types shown in the legend on the right. CSF = cerebrospinal fluid, GM = gray matter, WM = white matter.

6.2.2.3 Construction of the source priors

Cortical surface
We considered a subset of $N_p = 256$ source priors, sampled from the total set of priors (or columns of Q_G (see Eq. 4.18)), covering the entire cortical surface mesh. The size of each patch was approximately 1 cm^2 (dependent on the distance to the nearest dipoles). This type of source priors is denoted as Surf.

Volumetric
Again a set of $N_p = 256$ volumetric regions was considered covering the entire cortical layer. The maximum distance to the original dipole and

the smoothing factor ω were set to 5 mm and 0.6 respectively. The size of the regions was therefore approximately 1 cm^3. In order to compare with the default approach, we chose the centers of the 256 volumetric regions as close as possible to the centers of the 256 surface patches. All distances between the centers were below 9 mm. This type of source priors is denoted as Vol.

6.2.2.4 Bayesian model comparison based on free energy

In order to compare the different models we applied Bayesian model selection based on free energy for group studies [124, 125]. For all the comparisons reported in this chapter, we used the free energy values corresponding with the reconstructions of the full ERP time window, this means from 100 ms before stimulus to 500 ms after stimulus. This resulted in 3 different free energy values for each of the 12 subjects and each of the stimulus conditions. Bayesian model selection was used to identify the best model using 4 measures: the log group Bayes factor, the expected posterior model frequencies, the exceedance probability and the Bayesian omnibus risk (BOR) that were introduced in section 4.4.2.4. To compare the considered models, the free energy of the reconstructions were grouped over stimulus conditions, meaning that we compared 48 free energy values for each of the models.

6.2.2.5 Comparison of the reconstructed activity

To check the validity of the reconstructions based on the different models, we compared the evoked energy of the ERP reconstructed activity corresponding with the P1-peak. We used time windows of 16 ms centered around the peak. In Fig. 6.4 an example is given of the ERP waveforms in each of the stimulus conditions for one of the subjects on a left and right lateral occipital channel. The time windows for which we calculated the evoked energy are depicted by the different colors.

For the volumetric approaches, the subject specific volumetric source activity was transformed to MNI space, based on a spatial normalization transformation used to normalize the MR images to the MNI template in SPM8 [162]. Because a canonical cortical mesh in MNI space was used warped to the subject's anatomy to construct the cortical patches, each source of the mesh in subject space was directly corresponding with a location in MNI space [137]. As such, we generated 3D images corresponding with the P1-activity in MNI space. We averaged the resulting

images over subjects for each condition to compare the mean evoked P1 energy for each of the models. Moreover, equivalent to the approach in the previous chapter, we performed a statistical analysis based on the 3D images to see the main effect over subjects, i.e. at the group level, corresponding with each of the stimulus conditions.

From previous studies with similar ERP waveforms, we know that P1-activity is mainly generated contralateral to the stimulus, located around the calcarine sulcus, in the fusiform gyrus and lingual gyrus (see [163] and [160]). These findings are used to compare the reconstructed activity based on the different models and for the different stimulus conditions.

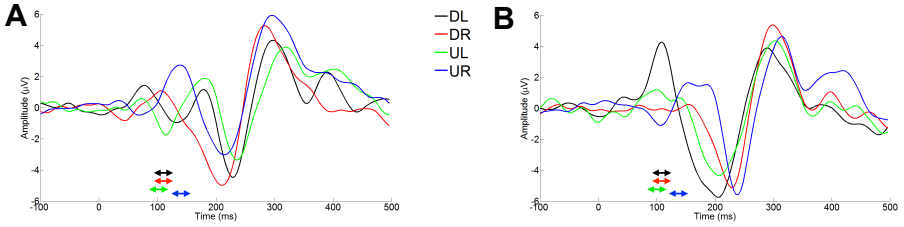

Figure 6.4: ERP data averaged over trials of one of the subjects for a (A) left lateral occipital and a (B) right lateral occipital channel. DL = down left stimuli, DR = down right stimuli, UL = upper left stimuli, UR = upper right stimuli. The arrows depict the time windows in which we calculated the mean evoked energy across subjects, 100 - 116 ms for DL stimuli, 100 - 116 ms for DR stimuli, 92 - 108 ms for UL stimuli and 132 - 158 ms for UR stimuli.

6.3 Results

6.3.1 Bayesian model comparison

In Fig. 6.5, the log Bayes factors are shown, computed as differences in free energy (F) corresponding with the reconstructions based on the considered models for each stimulus condition and every subject. In the first row, we compared the 3-layered models assuming volumetric regions, $\text{Vol}_{3\text{lay}}$, with the 3-layered models assuming cortical surface patches, $\text{Surf}_{3\text{lay}}$. In the second row, the 4-layered models assuming volumetric regions, $\text{Vol}_{4\text{lay}}$ were compared with the $\text{Surf}_{3\text{lay}}$ models. The $\text{Vol}_{4\text{lay}}$ models were compared versus the $\text{Vol}_{3\text{lay}}$ models in the last row. We can notice a trend in favor of the $\text{Vol}_{4\text{lay}}$ models compared to both 3-layered models and of the $\text{Vol}_{3\text{lay}}$ modes in favor of the $\text{Sur}_{3\text{lay}}$ models.

To verify these trends statistically over subjects and stimulus conditions, we performed Bayesian model selection for group studies. We performed two analysis resulting in summary statistics for model comparison. In the first analysis we compared the $\text{Surf}_{3\text{lay}}$ and $\text{Vol}_{3\text{lay}}$ models. The results are presented in the left panel of Fig. 6.6. In the first row, the log group Bayes factor is shown calculated versus the 3-layered volumetric models. It is clear it is considerably lower than -3, which corresponds with strong evidence in favor of the model assuming volumetric regions. The expected posterior model frequency and exceedance probability confirm this with an exceedance probability of the volumetric models equal to 0.99. The BOR for this comparison is equal to 0.018, which is below 0.25 and suggests that we can be very confident about the results of the exceedance probability.

In the second analysis we also included the $\text{Vol}_{4\text{lay}}$ models. The results are shown in Fig. 6.6 on the right panel. The first row shows the log group Bayes factor calculated versus the 4-layered volumetric models. Both 3-layered models have log group Bayes factors much lower than -3, which corresponds with strong evidence in favor of the 4-layered volumetric model. The exceedance probability of the 4-layered model is equal to 0.99. With a BOR of 0.001 we found very clear evidence in favor of the 4-layered volumetric model.

6.3.2 Comparison of the reconstructed activity

In the first row of Fig. 6.7, maximum intensity projections are shown of the 99th percentile mean evoked energy across subjects corresponding with the P1 peak for the down left stimulus condition shown in different columns for the $\text{Surf}_{3\text{lay}}$, $\text{Vol}_{3\text{lay}}$ and $\text{Vol}_{4\text{lay}}$ model. To enhance interpretation of the location of the reconstructed activity, the second row depicts the 99th percentile mean evoked energy rendered on the canonical cortical mesh in 2 views.

For the reconstructions based on the $\text{Surf}_{3\text{lay}}$ models, the activity is spread above the right calcarine sulcus, right lingual gyrus and right cuneus. Assuming both volumetric models, we found clear focal activity above the right calcarine sulcus and in the lingual gyri.

For both volumetric models, the P1 reconstructed activity agrees very well with the P1-activation found in a previous EEG/fMRI study using the same ERP data based on a jointICA decomposition (see [160] for more details). The late P1-activity that was found is included in the

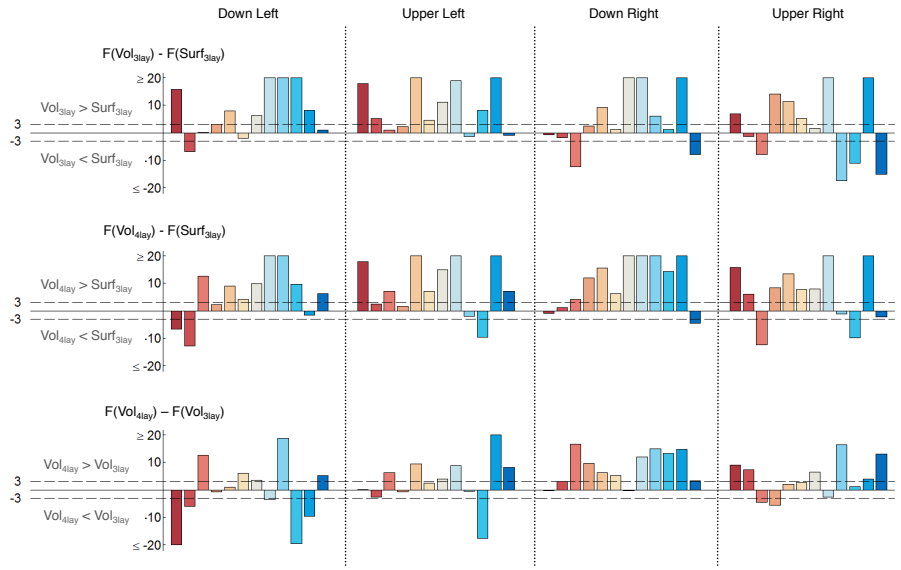

Figure 6.5: log Bayes factors computed as differences in free energy (F) to compare the considered models across subjects and stimulus conditions: $\text{Surf}_{3\text{lay}}$, for the 3-layered surface based models, $\text{Vol}_{3\text{lay}}$, for the 3-layered volumetric models and $\text{Vol}_{4\text{lay}}$ for the 4-layered volumetric models. The different subjects are represented by the different colors and each column represents a different stimulus condition. We used the $<$ and $>$ signs when there were differences bigger than 3 to denote evidence in favor of a one of the models. When comparing $\text{Vol}_{3\text{lay}}$ versus $\text{Surf}_{3\text{lay}}$ for example, a difference bigger than 3 corresponds with strong evidence in favor of the $\text{Vol}_{3\text{lay}}$ model, indicated as $\text{Vol}_{3\text{lay}} > \text{Surf}_{3\text{lay}}$ on the left side of the bar graph. We restricted the y-axis to differences bigger than 20 to increase the interpretation of smaller differences.

third row depicted in 3 orthogonal slices. The correspondence for the reconstructions based on the $\text{Surf}_{3\text{lay}}$ models was less pronounced.

The results of the group level statistical analysis for the down left stimuli are presented in Fig. 6.8. The activity with the highest significance is depicted by the red arrow for each of the considered models. The most significant area for $\text{Surf}_{3\text{lay}}$ was located in the center of the brain. For both $\text{Vol}_{3\text{lay}}$ and $\text{Vol}_{4\text{lay}}$ we found the same location of the most significant activity around the right calcarine sulcus.

The maximum intensity projections for the other stimulus conditions are shown in Fig. 6.9. For the down right stimuli, the reconstructed activity based on $\text{Surf}_{3\text{lay}}$ was mainly located in the left lingual gyrus,

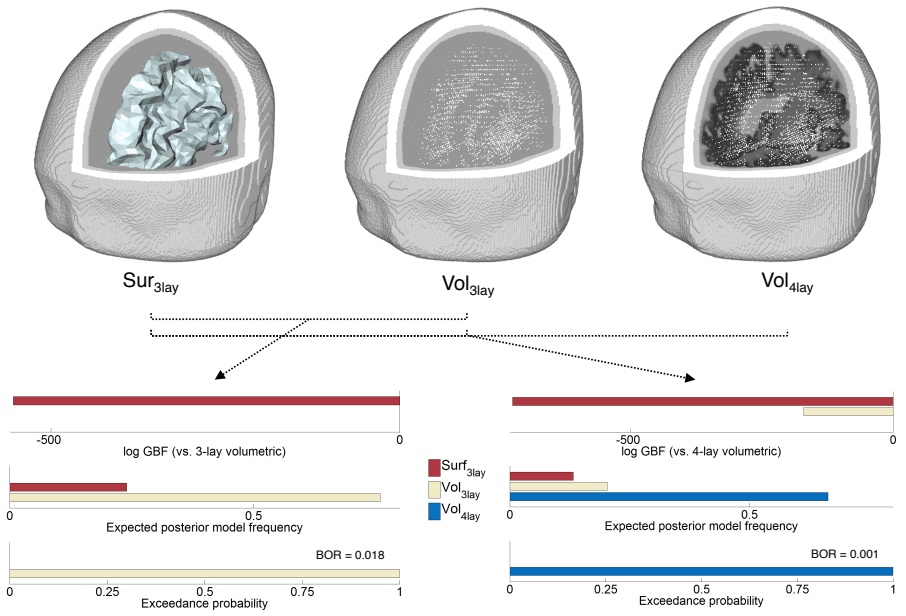

Figure 6.6: Bayesian model comparison results of the different models we assumed for reconstructing the ERP data: $\text{Surf}_{3\text{lay}}$, $\text{Vol}_{3\text{lay}}$ and $\text{Vol}_{4\text{lay}}$. On the left, the comparison results are shown between the 3-layered models. On the right, the comparison results are shown for both the 3-layered models and the 4-layered volumetric models. For both comparisons, we show the log group Bayes factor (log GBF), the expected posterior model frequency and the exceedance probability. The different models we used for reconstruction are depicted by the different colors shown in the legend. The log GBF is calculated versus $\text{Vol}_{3\text{lay}}$ for the comparison on the left and versus $\text{Vol}_{4\text{lay}}$ for comparison on the right. We also show the Bayesian omnibus risk (BOR). If the BOR is smaller than 0.25, then we can be confident in choosing the best model based on the results of the exceedance probability.

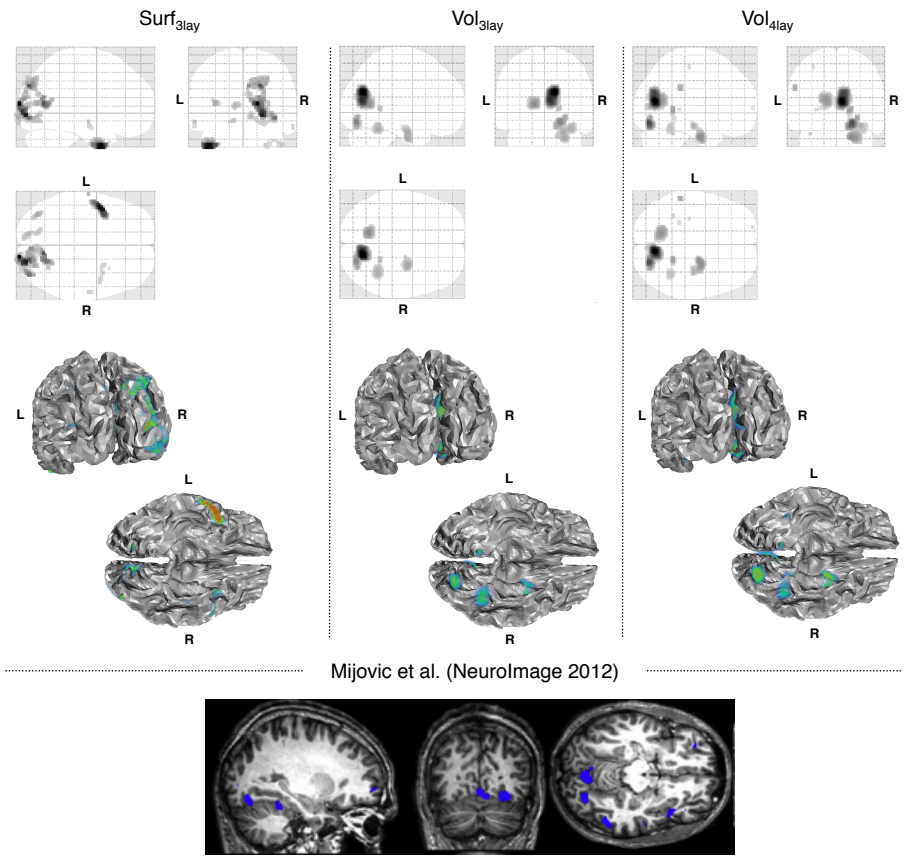

Figure 6.7: Maximum intensity projections of the 99th percentile of the mean evoked energy across subjects for the MSP inversions corresponding with the P1-peak (see Section 6.2.2.5) assuming $\text{Surf}_{3\text{lay}}$, $\text{Vol}_{3\text{lay}}$ or $\text{Vol}_{4\text{lay}}$ depicted in the different columns. In the second row, 2 views are shown of the 99th percentile mean evoked energy rendered on the canonical cortical mesh. In the third row, the late P1-activity is shown from a jointICA EEG/fMRI decomposition reprinted from NeuroImage, [160], Copyright 2012, with permission from Elsevier.

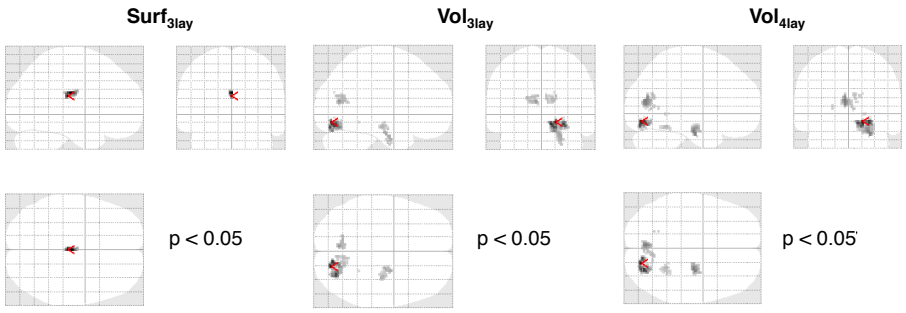

Figure 6.8: Statistical analysis of the reconstructed activity for the DL stimuli over subjects. The main effect is shown of a t-test for a p-value < 0.05. The activity with the highest significance is depicted by the red arrow.

left inferior occipital gyrus, left midcingulate cortex, right precuneus and right fusiform region. Assuming $\text{Vol}_{3\text{lay}}$ the reconstructed activity was less lateralized. We found a strong activation in the right parahippocampal region. The reconstructed activity based on $\text{Vol}_{4\text{lay}}$ was located above the left calcarine sulcus, left lingual gyrus and left fusiform gyrus. The results of the group level statistical analysis are presented in Fig. 6.10. The most significant area for $\text{Surf}_{3\text{lay}}$ was located in the center of the brain. For $\text{Vol}_{3\text{lay}}$ we found the most significant area located in the right fusiform gyrus. For $\text{Vol}_{4\text{lay}}$, the most significant area was located above the left calcarine sulcus.

For the upper left stimuli, the reconstructed activity based on $\text{Surf}_{3\text{lay}}$ was mainly located in the right inferior occipital and temporal gyrus and the left inferior temporal gyrus. For $\text{Vol}_{3\text{lay}}$ the reconstructed activity was less lateralized with strong activation around the left calcarine sulcus. The reconstructed activity based on $\text{Vol}_{4\text{lay}}$ was mainly located in the right lingual and right fusiform gyrus. The results of the group level statistical analysis are presented in Fig. 6.11. The most significant area for $\text{Surf}_{3\text{lay}}$ was located in the center of the brain. For $\text{Vol}_{3\text{lay}}$ and $\text{Vol}_{4\text{lay}}$ we found the most significant area located above the left calcarine sulcus.

For the upper right stimuli, the reconstructed activity based on $\text{Vol}_{4\text{lay}}$ and $\text{Vol}_{3\text{lay}}$ was mainly located around the left calcarine sulcus. The reconstructed activity based on $\text{Surf}_{3\text{lay}}$ was more widespread with the strongest activation located in the left cuneus. The results of the group level statistical analysis are presented in Fig. 6.12. Again the most significant area for $\text{Surf}_{3\text{lay}}$ was located in the center of the brain. For

Vol_{3lay} and Vol_{4lay} we found the most significant area located above the left calcarine sulcus.

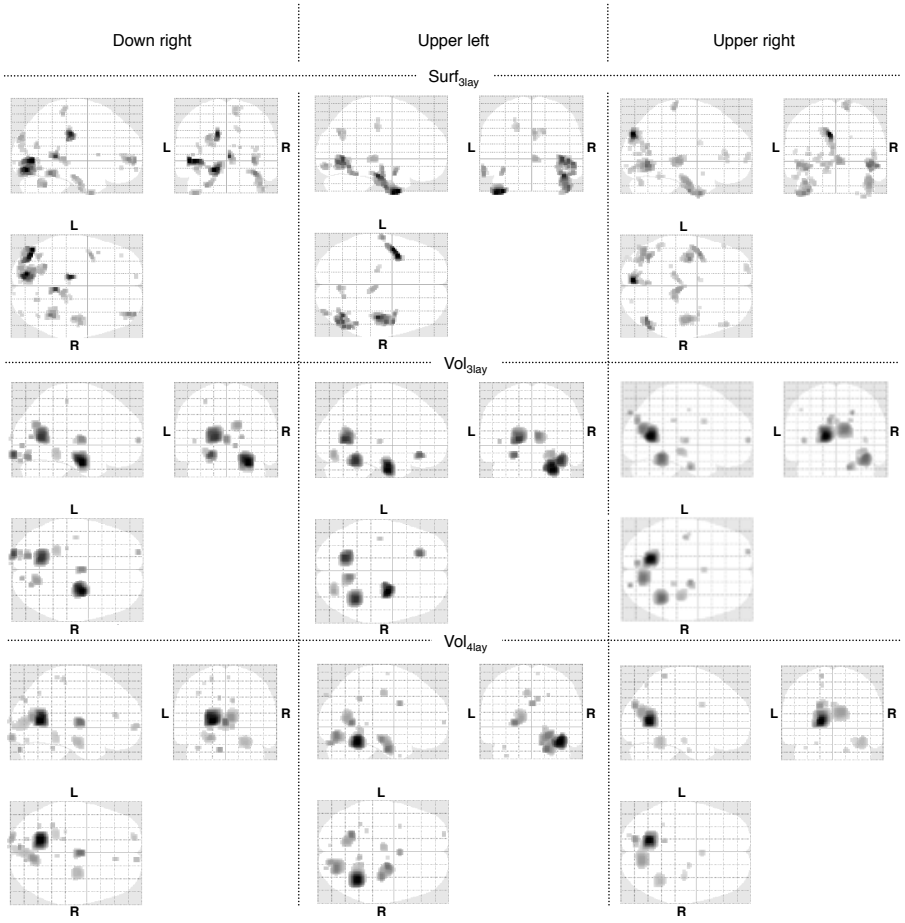

Figure 6.9: Maximum intensity projections of the 99th percentile of the mean evoked energy across subjects for the MSP inversions of the P1-peak (see Section 6.2.2.5) assuming $Surf_{3lay}$, Vol_{3lay} or Vol_{4lay}. The columns correspond with the different stimulus conditions

6.4 Discussion

In this chapter, we have extended the current application of the multiple sparse priors algorithm [114] from sparse surface based priors to multiple

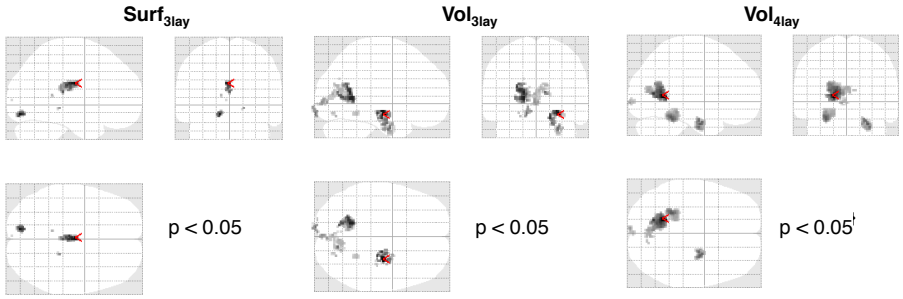

Figure 6.10: Statistical analysis of the reconstructed activity for the DR stimuli over subjects. The main effect is shown of a t-test for a p-value < 0.05. The activity with the highest significance is depicted by the red arrow.

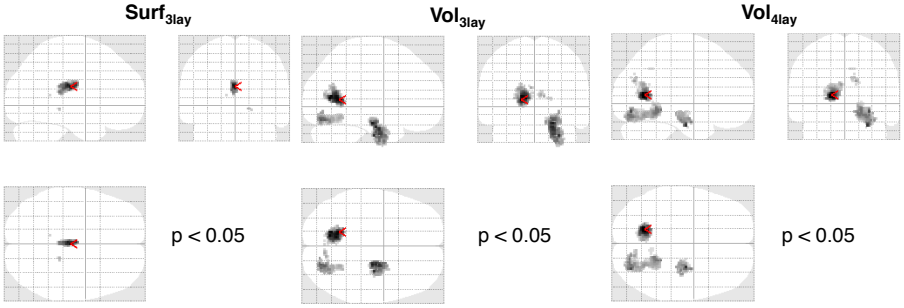

Figure 6.11: Statistical analysis of the reconstructed activity for the UL stimuli over subjects. The main effect is shown of a t-test for a p-value < 0.05. The activity with the highest significance is depicted by the red arrow.

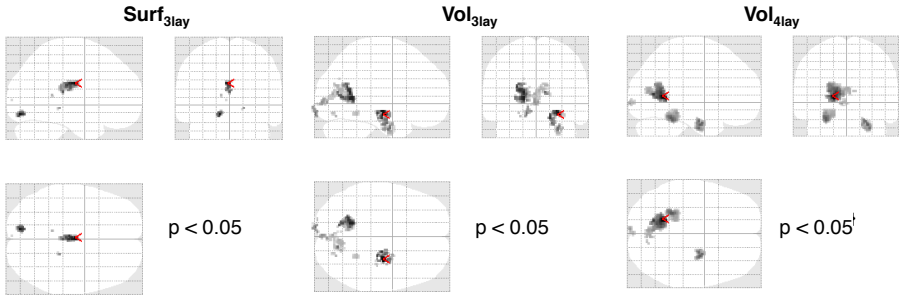

Figure 6.12: Statistical analysis of the reconstructed activity for the UR stimuli over subjects. The main effect is shown of a t-test for a p-value < 0.05. The activity with the highest significance is depicted by the red arrow.

sparse volumetric regions. This extension provides the ability to use the MSP algorithm to reconstruct brain structures besides the cortical surface and opens up the ability to introduce more advanced volumetric head models based on volumetric forward modeling approaches using finite differences [49], finite elements [164] or finite volume modelling [165]. Both the Bayesian model selection analysis and the comparison of the reconstructed P1 activity demonstrated the value of the extension compared to the currently used approach.

Because we could not rely on a ground truth, we could not explain the differences in reconstructed activity quantitatively. However, we did find clear differences between the reconstructed activity assuming each of the models. By using maximum intensity projections of the P1 reconstructed activity for down left stimuli and showing this activity on the canonical cortical surface mesh we showed a high correspondence of the reconstructions based on the volumetric models with the findings of previous studies for down left stimuli [160, 163]. This was less pronounced assuming the surface based models. Also the reconstructions for the other stimulus conditions showed clear differences assuming each of the considered models. In general, the reconstructed activity assuming $\mathrm{Vol}_{4\mathrm{lay}}$ was consequently focused in occipital regions contralateral to the stimulus which is congruent with previous studies in literature. This was less expressed for the reconstructions based on the 3-layered models. Notice that we would expect the activity for the upper stimuli to be more focused below the calcarine sulcus contralateral to the stimulus. Because the P1-components for the upper stimuli were not as highly expressed across subjects compared to the down stimuli we found deviations from the expected retinotopic locations in each of the models. Also the results of the statistical analysis at the group level showed clear differences assuming each of the 3 considered forward models for which the $\mathrm{Vol}_{4\mathrm{lay}}$ results provided the most consistent results with previous findings. Assuming $\mathrm{Sur}_{3\mathrm{lay}}$, the most significant activity was always found in the center of the brain.

We did not compare the considered models with the currently used approach based on cortical patches and assuming a 4-layered head model including CSF because of the fact that the dipoles are located on the boundary between the CSF and brain compartment. Because we used a finite difference approach with a dipole model extending over 3 nodes of each voxel (the outer nodes have opposite currents (monopoles) in x, y or z direction, see section 3.2.4.3), the dipoles placed onto the CSF-brain boundary will have one side of the dipole source feeding directly

to the CSF which is physically wrong and may have a large effect. We therefore had to ensure that at least 2 voxels of gray matter were between the central node of the dipole model and the boundaries with other tissues in the x, y and z direction, in order to have a proper source model. To construct such a model based on the cortical surface mesh is very difficult because the mesh would need to be resampled, inflated or deflated to ensure no dipoles were modeled inside the CSF. With the extension proposed in this work, we can avoid this.

Note that we found evidence in favor of the $\text{Vol}_{3\text{lay}}$ models compared to the $\text{Surf}_{3\text{lay}}$ models, although the same number of priors was used and these were at approximately the same cortical locations. The modeling of the volumetric regions was however closer to the actual anatomy of the subjects. They were constructed based on the actual segmented gray matter using the subject's anatomical MR image. For the construction of the cortical surface patches, a canonical cortical surface mesh was used which was warped to the subject's anatomy. This warping process is not faultlessly and the resulting cortical surface does not necessarily fully overlap with the actual cortical surface itself. Therefore also the orientations of the considered dipoles were different. For the dipoles located inside the gray matter layer, the orientations were determined based on the curvature of the segmented white matter and interpolating for gray matter. For the dipoles located on the cortical surface mesh, the orientations were set orthogonal to the surface. We could have used an approach in which we determined the individual cortical surfaces for each of the subjects based on subject's anatomical MRI. This is however not how it is done in the present implementation and the construction of these cortical surfaces often requires manual intervention [127].

Clearly, there are many issues that we have not addressed. There are for example a lot of different other possibilities to construct the volumetric regions by introducing fMRI prior regions, anatomical priors, different smoothing functions, etc. Also other parameters can be optimized. These include the spacing of the dipoles, the optimal number of regions, the spacing of the regions, the smoothness of the regions, the dipole orientations, etc. The question of which set of priors will work best in practice depends on the data, and the Bayesian framework is a useful tool to evaluate different sets of priors in future work.

We think that the use of realistic volumetric regions using advanced volumetric forward models can further improve PEB-EEG source imaging. In future studies, volumetric brain activity could be reconstructed

based on volumetric regions including more anatomical or functional information. For example using cortical parcellation information [166]. Also future studies including more realistic head models should be introduced in the framework. For example, with accurate modeling of the skull including compact bone and spongy bone [36] or tissue anisotropy [54].

6.5 Conclusion

In this chapter we revisited the multiple sparse priors (MSP) algorithm implemented in the statistical parametric mapping software (SPM) for distributed EEG source imaging. We presented a technique to construct volumetric cortical regions to introduce as source priors by restricting the dipole source space to a segmented gray matter layer and using a region growing approach. This extension allows to reconstruct brain structures besides the cortical surface and facilitates the use of more realistic volumetric head models including more layers, such as cerebrospinal fluid (CSF), compared to the standard 3-layered scalp-skull-brain head models. We illustrated the technique with ERP data and anatomical MR images in 12 subjects. Based on the segmented gray matter for each of the subjects, cortical regions were created and introduced as source priors for MSP-inversion assuming two types of head models. The standard 3-layered scalp-skull-brain head models and extended 4-layered head models including CSF. We compared with the current implementation by assessing the free energy corresponding with each of the reconstructions using Bayesian model selection for group studies. Strong evidence was found in favor of the volumetric MSP approach compared to the MSP approach based on cortical patches for both types of head models. Overall, the strongest evidence was found in favor of the volumetric MSP reconstructions based on the extended head models including CSF. These results were verified by comparing the reconstructed activity. The use of volumetric cortical regions as source priors is a useful complement to the present implementation as it allows to introduce more complex head models and volumetric source priors in future studies.

6.6 Original Contributions

The main idea to introduce volumetric regions as source priors was first presented at the 19th annual meeting of the organization for human

brain mapping [167]. An extension of this study was presented at the international conference on basic and clinical multimodal imaging [168]. The results that are presented in this chapter are published in the A1-journal NeuroImage [169].

Chapter 7

ESI of interictal spikes in patients with refractory epilepsy

"My brain is in a tangle"
Atoms For Peace - Stuck Together Pieces

7.1 Introduction

In this chapter we present a clinical application of the techniques that were presented in the previous chapter. We suggest to use the multiple sparse volumetric priors (MSVP) approach to localize the sources that are generating interictal epileptiform spikes. Interictal spikes are characterized by a large amplitude rapid component lasting 50 - 100 ms that is usually followed by a slow wave, 200 - 500 ms in duration [170], see Fig 2.20. The generation of interictal spikes is a complex phenomenon, and propagation of activity from the source to remote cortical regions can occur within milliseconds [92, 171, 172].

A problem to estimate the activity in these approaches is the selection of the time points or time periods of the spike to localize the origin of the epileptic activity. It has been shown in previous studies that the early component of the spike is likely to represent the location and field of the source, and the peak of the epileptiform discharge actually reflects propagated activity [173–175]. As such, modeling of the spike peak could be misleading. However, the early component of the spike is of much

smaller amplitude than the peak so accurate modeling is complicated by high noise contamination [62].

In this chapter, we compared different sets of MSVPs to localize the generating sources of interictal spikes recorded in 6 patients with refractory focal epilepsy that were successfully treated with surgery. We estimated the activity of the sources over the the time course of the spike, in order to obtain a high spatiotemporal resolution of the interictal epileptiform activity. Three different windows were chosen: (i) a window starting before the spike till 50% of the spike peak during the rising phase of the spike, (ii) a window starting before the spike till the spike peak and (iii) a window starting before the spike till 230 ms after the spike. For each of the three windows, multiple sets of MSVPs were introduced for reconstruction, and we obtained the most likely set of priors using Bayesian model comparison. Based on the time course of the intensity of the estimated sources, the maximum energy of the sources from the beginning of the spike till 50% of the peak during the rising phase of the spike was used to identify the primary interictal spike source from propagated sources. This way no additional information of the time samples or time periods to estimate the sources was required.

We compared different sets of MSVPs to localize the generating sources of interictal spikes recorded in six patients with refractory focal epilepsy who were successfully treated with surgery and showed no interictal spikes after surgery in routine EEG registrations of 1 hour. As such there was evidence that the generator of the epileptic activity was removed. For verification, we furthermore compared the performance of the MSVP introduced approach with the results obtained with the LORETA approach implemented in the CARTOOL software, commonly used for spike localization [40, 176]. Also an equivalent current dipole (ECD) approach was used. We compared the distances of the estimated interictal source maxima to the border of the resected area for each of the approaches.

7.2 Patient data

We retrospectively selected interictal spike data in six patients with refractory focal epilepsy who were treated with surgery using the following inclusion criteria: (i) the patient was seizure free (i.e. Engel class I) after surgery, with minimum follow up of 1.5 years, (ii) the electrode positions were known and (iii) the seizures and interictal spikes showed the same

lateralization in the EEG recordings, i.e. over the left or right hemisphere, (iv) there were no spikes observed in routine EEG registrations after resection. An overview of the patient data is given in tables 7.1 and 7.2. All patients had temporal lobe epilepsy.

Three patients had 27 channel EEG recordings and 3 patients had 64 channel EEG recordings. The recorded interictal EEG data was first filtered between 0.5 and 40 Hz with a Butterworth zero phase filter and a 50 Hz notch filter implemented in the Brain Vision Analyzer software (Brainproducts, Munich). Spike selection was visually performed by expert electrophysiologists (AM and EC) experienced in reading clinical EEG. All patients had one dominant spike type with an invariable morphology and maximal amplitude at the same electrode. The spikes were marked at the time point with the highest amplitude, i.e. the peak of the spike, on the same channel. The spikes were subsequently segmented from -50 ms to 230 ms around the peak, in order to include the large amplitude rapid component followed by a slow wave for inversion. The spikes were subsequently averaged. Some electrodes were removed in the analysis due to bad signal quality. In Figs. 7.1 and 7.2, the averaged spikes for the 64 channel and 27 channel recordings are shown, respectively. The electrode for spike selection and the number of averaged spikes are depicted for each patient. For each of the patients the topography corresponding with the spike peak and at 50% of the peak is also shown. The spikes were finally referenced to the average before ESI.

For all patients pre-surgical and post-surgical anatomical MR images were available. We manually segmented the resected zone from the post-surgical anatomical MR images to determine the volume of the resection and to compare the ESI approaches considered in this study. In order to construct the patient specific forward models, the electrode positions were extracted from CT images of the patient (with scalp electrodes attached) for the 27 channel recordings and Polhemus recordings (by Polhemus Inc., USA) for the 64 channel EEG..

7.2.1 Construction of patient specific forward models

In the CARTOOL software, patient-specific spherical forward models were constructed for all patients (see also section 3.2.4.2). For the ECD and MSVP inversions we constructed 5-layered patient-specific FDRM models.

patient	**1**	**2**	**3**
sex	F	F	F
date-of-birth	1993/09/08	1986/03/24	1974/06/08
age (surgery)	18	25	39
epilepsy type	TLE	TLE	TLE
#electrodes	62 (64)	62 (64)	63 (64)
elec. pos.	Digitizer	Digitizer	Digitizer
removed elec.	FC1, FC2, C3	FC1, FC2, C3	P1 , C3
samping freq.	1023.87 Hz	1023.87 Hz	1023.87 Hz
visual inspection scalp EEG	right frontotemporal IED + ictal discharges over right hemisphere	left frontotemporal IED + ictal discharges over left hemisphere	right frontotemporal IED + ictal discharges over the right frontotemporal region
#spikes (avg)	15	12	31
abundance spikes	100% Right	100% Left (anterior, posterior)	>90% Right
phase rev.	T8	T7	F8
MRI	right hippocampal sclerosis	left hippocampal sclerosis	right hippocampal sclerosis
surgery	right selective amygdalohippocampectomy	left selective amygdalohippocampectomy	right anterior 2/3 temporal lobectomy incl. hypocampectomy
resection vol.	2.7 cm^3	5.3 cm^3	27.7 cm^3
follow up	3 years	3.5 years	1.5 year
Engel class	Class 1	Class 1 (1 aura)	Class 1 (aura's)
IED post-op routine EEG	no	no	no

Table 7.1: Overview of the patient data we used in this study. F = Female, TLE = Temporal Lobe Epilepsy, phase rev. = phase reversal, elec. pos. = electrode positions, sampling freq. = sampling frequency, resection vol. = resection volume, post-op = post operative.

patient	**4**	**5**	**6**
sex	F	F	F
date-of-birth	1969/06/30	1984/07/17	1946/03/27
age (surgery)	41	26	64
epilepsy type	TLE	TLE	TLE
#electrodes	27	26 (27)	27
elec. pos.	CT	CT	CT
removed elec.	/	O1	/
samping freq.	128 Hz	256 Hz	128 Hz
visual inspection scalp EEG	left frontotemporal IED + ictal discharges over the left frontotemporal region	right frontotemporal IED + bilateral frontotemporal ictal discharges	left frontotemporal IED + ictal discharges over the left frontotemporal region
#spikes (avg)	35	41	14
abundance spikes	100 % Left	> 90% right	100% Left
phase rev.	F7	F8	F7
MRI	left hippocampal sclerosis	dysplastic lesion in right gyrus temporalis inferior	lesion in amygdala gyrus parahippocampalis
surgery	left selective amygdalolohypocampectomy	right anterior 2/3 temporal lobectomy	left selective amygdalohippocampectomy
resection vol.	4.7 cm^3	32.7 cm^3	6.1 cm^3
follow up	3 years	4 years	4 years
Engel class	Class 1	Class 1	Class 1
IED post-op routine EEG	no	1 (on 10 routine EEGs)	no

Table 7.2: Overview of the patient data we used in this study. F = Female, TLE = Temporal Lobe Epilepsy, phase rev. = phase reversal, elec. pos. = electrode positions, sampling freq. = sampling frequency, resection vol. = resection volume, post-op = post operative.

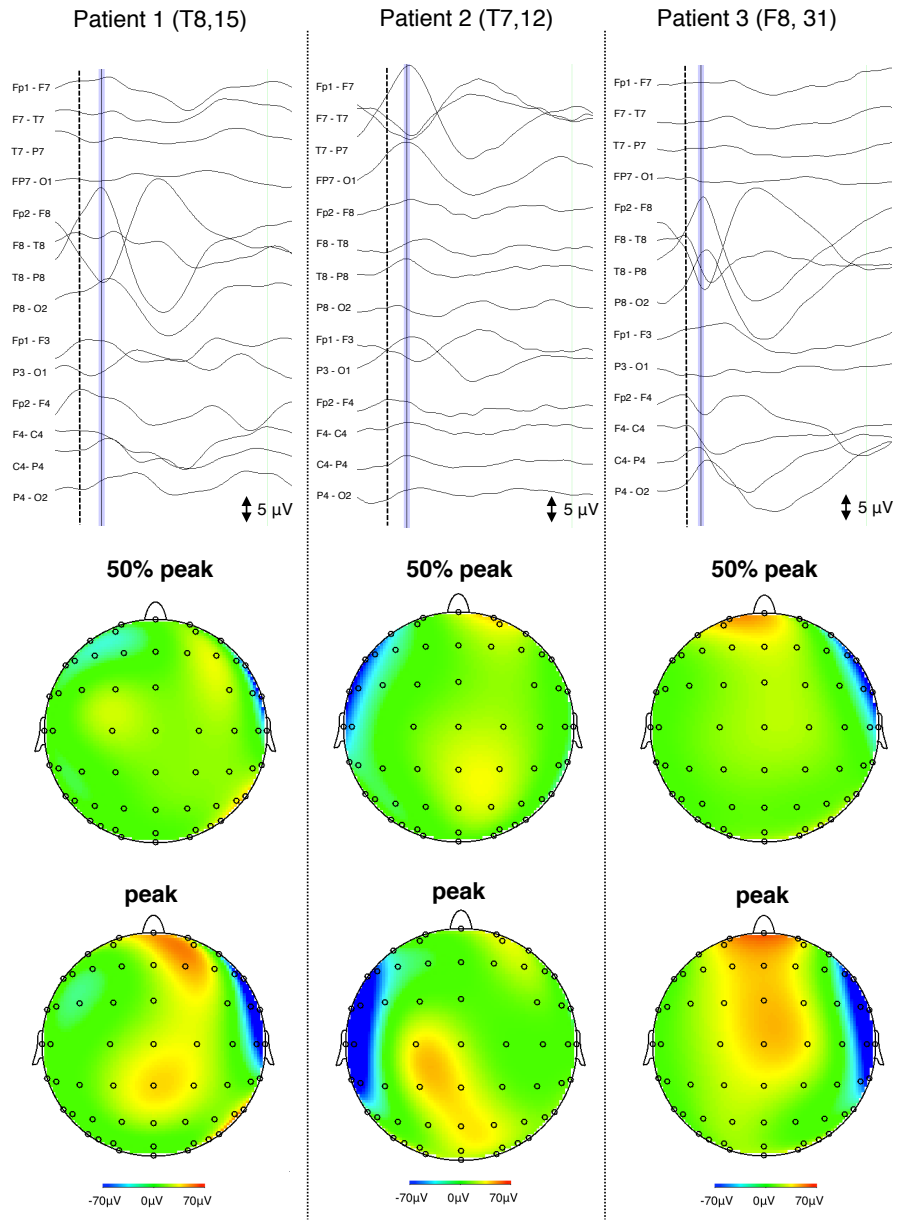

Figure 7.1: The averaged spikes and topographies corresponding with the spike peak and at 50% of the spike peak for the 64 channel recordings in patient 1 to 3. The vertical blue lines correspond with the spike peaks. The vertical dashed lines correspond with 50% of the spike peak during the rising phase of the peak. The channel to select the peak of the spike and the number of spikes that were averaged are given for each patient.

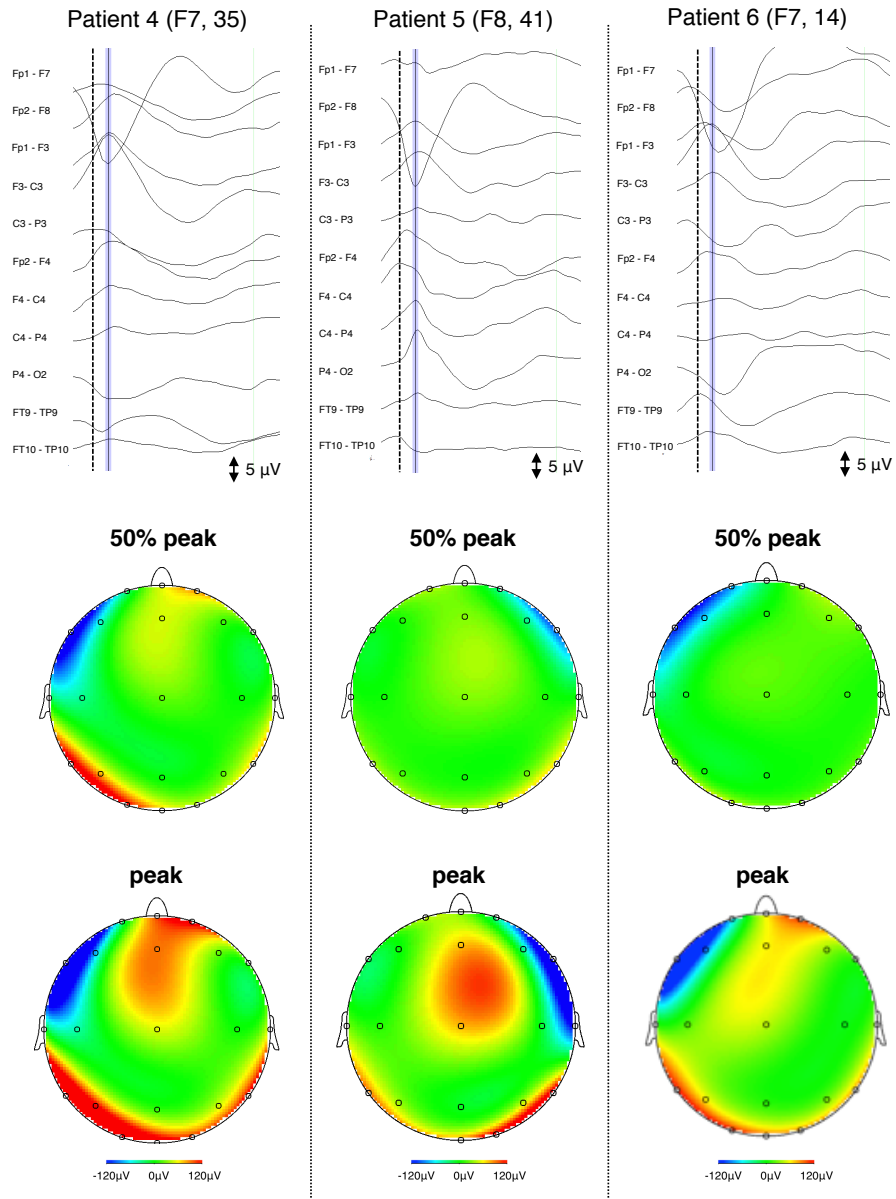

Figure 7.2: The averaged spikes and topographies corresponding with the spike peak and at 50% of the spike peak for the 27 channels recordings in patient 4 to 6. The vertical dashed lines correspond with 50% of the spike peak during the rising phase of the peak. The channel to select the peak of the spike and the number of spikes that were averaged are given for each patient.

7.2.1.1 Multi-layer spherical forward models

In the CARTOOL software, multi-layer spherical head models were constructed taken into account the anatomical pre-surgical MR images of the patients. This approach is known as the Locally Spherical Model with Anatomical Constraints, or LSMAC model [40, 176]. In this approach an adaptive local spherical model is used at each electrode. To do so, the thicknesses of the scalp, skull and brain are estimated from the MR images of the patients. These thicknesses are then used in a 3-shell spherical model with the local radiuses, allowing the real geometry between the dipole solution points. Around 5000 dipole solution points were distributed with equal distances inside the brain surface for each patient. The lead field matrices in x, y and z direction were subsequently computed for each electrode using the known analytical solutions for a three-shell spherical head model [177].

7.2.1.2 Forward models using the finite difference method

For each patient, FDRM head models were constructed based on the pre-surgical anatomical MR images. Meshes representing the scalp, outer skull and inner skull were extracted from the MR images in SPM. These meshes were subsequently converted to filled volumes. We segmented gray matter, white matter and CSF using Freesurfer segmentation techniques [28]. Based on these segmentations and the volumes that were built from the surface meshes, 5-layered head models were constructed including scalp, skull, gray and white matter and CSF layers. The conductivity of the CSF was set to 1.79 S/m [136], 0.33 S/m for gray matter, 0.14 S/m for white matter, 0.022 S/m and 0.33 S/m for the skull and scalp, respectively [36, 37]. In Fig. 7.3 the 5-layered volumetric model for patient 4 is shown. The electrodes were extracted from a CT image of the patient and we coregistered the electrode positions, corresponding with our realistic EEG data, to the scalp surface and embedded them inside the boundary of the scalp. The resulting volumetric head models were resampled to $1 \times 1 \times 1$ mm voxel resolution.

Construction of dipolar source spaces

For each of the head models, the source space was constructed based on the segmented gray matter. For the ECD approach, the dipoles were assumed inside the gray matter (excluding the cerebellum) on a cubic grid equidistant to each other with a 1mm spacing. We ensured that at

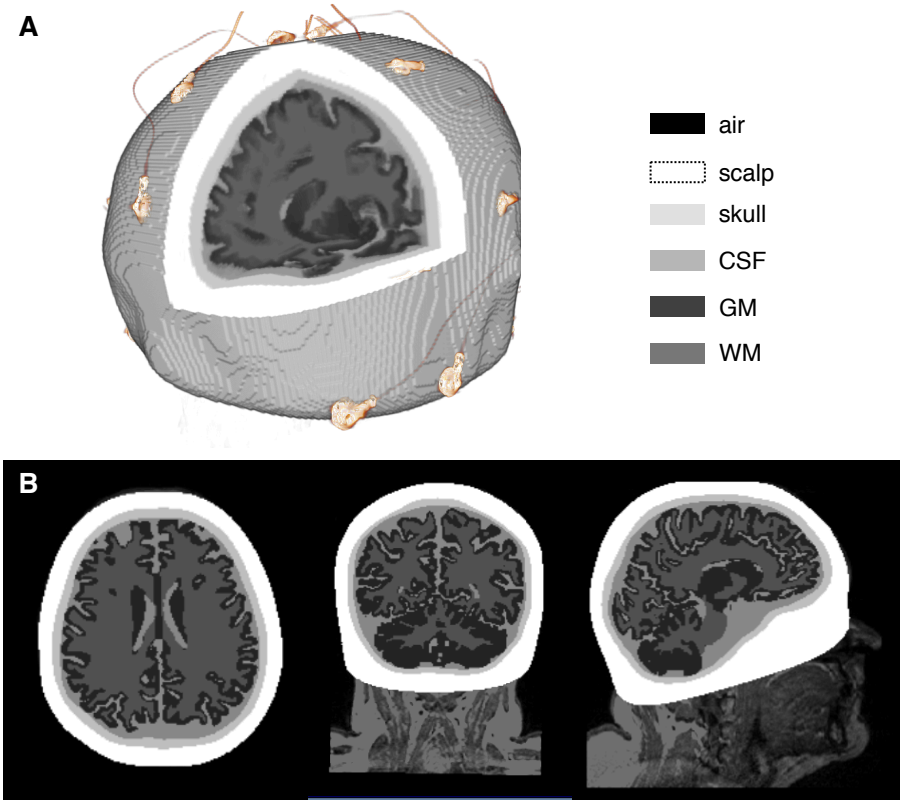

Figure 7.3: Example of a 5-layered patient specific head model. A: 3D representation of the head model. The electrodes were extracted from a CT image of the patient, depicted in yellow. CSF = cerebrospinal fluid, GM = gray matter, WM = white matter. B: The head model shown on top of the anatomical MR image of the patient in 3 orthogonal slices

least 2 voxels of gray matter were between the central node of the dipole model and the boundaries with other tissues in the x, y and z direction. This resulted in approximately 10,000 dipoles inside the gray matter for each of the models. The orientations of the dipoles were determined based on Eq. (3.25). For the MSVP approach, we used a subsampled dipolar source space with a spacing of 3 mm resulting in approximately 2,000 dipoles inside the gray matter for each of the models. The orientations of these dipoles were determined with the technique introduced in section 6.2.2.1.

7.2.2 EEG source imaging of the interictal spikes

For the multi-layer spherical models, ESI was performed using the LORETA approach. For the 5-layered patient specific FDRM forward models both an ECD approach was used and the MSVP approach that was introduced in chapter 6.

7.2.2.1 LORETA

For the multi-layer spherical models, source estimation was performed in the CARTOOL software using the low resolution electromagnetic tomography algorithm known as LORETA (see section 3.3.3). We localized the distributed sources at 50% of the spike peaks during the rising phase of the spike and on the spike peaks for each of the 6 patients.

7.2.2.2 Equivalent current dipole solutions

We localized ECDs at the spike peaks and at 50% of the spike peaks during the rising phase of the spikes for each of the 6 patients. We solved Eq. 3.26 (see section 3.3.2.1) with the Nelder-Maede simplex optimization method considering each dipole assumed in the source space of the patient.

7.2.2.3 Multiple sparse volumetric priors (MSVP)

We applied an equivalent approach to the approach presented in chapter 6 for the MSVP inversions. We assumed the same amount of prior variance on all electrodes, $\mathbf{C}_{\boldsymbol{\epsilon}} = \lambda_1^{(1)}\mathbf{I}_{N_c}$. Based on the dipolar source space in each patient, we constructed 100 possible sets of $N_p = 256$ sparse volumetric regions. For each set of volumetric regions, we assured

global gray matter coverage by randomly selecting 256 region locations, from 256 fixed regions covering the full gray matter. Each of the regions was constructed based on region growing inside the gray matter of the patient based on the methodology that was presented in section 6.2.2.3. The maximum distance to the original dipole and the smoothing factor ω were set to 5 mm and 0.6, respectively. Each of the regions were subsequently introduced as a single predefined covariance matrices $\mathbf{Q}_i^{(2)}$ ($i = 1, \ldots, 256$) in Eq. (4.17). As such, 256 covariance matrices were introduced as priors for inversion and the hyperparameters $\lambda_i^{(2)}$ were estimated in the variational Bayesian scheme by optimizing the free energy. The most likely set of volumetric regions was subsequently selected using Bayesian model comparison using the free energy values corresponding with each of inversions. We estimated the time courses of all the dipoles corresponding with tree different windows: (i) a window starting before the spike till 50% of the spike peak during the rising phase of the spike, (ii) a window starting before the spike till the spike peak and (iii) a window starting before the spike till 230 ms after the spike. Subsequently we calculated the energy of the dipoles from -50 ms to 50% of the spike peak during the rising phase of the spike.

7.2.3 Comparison of the ESI approaches

For all the ESI approaches considered in this study, we calculated the distances to the resected zone (d_r), defined as the closest distance of the estimated activity to the resection border. For the LORETA approach we calculated the d_r based on the dipole source with the maximum estimated activity corresponding with the spike peak and at 50% of the spike peak. For the ECD approach, we calculated the d_r for the dipole source corresponding with the spike peak and at 50% of the spike peak. For the MSVP approach, the source with the maximum estimated energy from -50 ms to 50% of the spike peak during the rising phase of the spike was selected and d_r was calculated for each of the different time windows.

7.3 Results

7.3.1 Overall results

The d_r values for each method are shown in Fig. 7.4. Overall, the mean and standard deviation of 3.8 mm $\pm$ 5.1 mm for the d_r based on the

proposed MSVP method using the full spike time course were the lowest distances to the border of the resection. For the MSVP method using smaller time windows, i.e. from -50 ms to 50% of the spike peak and from -50ms to the spike peak, we found 10.8 mm ± 9.3 mm and 14.1 mm ± 11.2 mm, respectively. The mean and standard deviation of d_r based on the CARTOOL software were 12.5 mm ± 11.0 mm at 50% of the spike peak and 7.1 mm ± 6.0 mm at the spike peak. For the ECD solutions we found 10.2 mm ± 6.6 mm at 50% of the spike peak, and 8.5 mm ± 6.4 mm at the spike peak.

In three patients, the proposed MSVP method using the full spike time course estimated the maximum activity inside the resected zone, compared to two patients using the MSVP method based on a window cropped to the rising phase of the spike. With the CARTOOL approach the maximum activity was estimated inside the resected zone for one patient at 50% of the spike and for two patients at the spike peak. For the ECD approach the activity was estimated inside the resected zone for one patient at 50% of the spike peak and at the spike peak.

The overall maximum distance to the resection of the MSVP approach using the full spike time course was 12 mm compared to 29.4 mm, 14 mm, 17 mm, 15 mm, 23 mm and 28 mm for the CARTOOL solution at 50% of the spike peak, the CARTOOL solution at the spike peak, the ECD solution at 50% of the spike peak, the ECD solution on the spike peak, and the MSVP approaches based on a window cropped to the rising phase of the spike, respectively.

7.3.2 Individual patient results

The results for patient 1 are presented in Fig. 7.5. In the first row, we show the resected zone based on the post-operative MR image of the patient in three orthogonal slices. In the second row, the results based on the CARTOOL software at the spike peak and the ECD solutions are presented. For the CARTOOL solution, the 95% percentile of the activity is shown in three orthogonal slices on top of the post-operative MR image. Also the locations of the estimated ECDs corresponding with the spike peak and at 50% of the spike peak are shown on top of the post-operative MR image. In panel A, a histogram depicts the number of reconstructions, corresponding with a certain free energy value, for different sets of MSVPs. We selected the set of volumetric regions corresponding with the highest free energy for further analysis in panel B. In panel B, we show the evoked energy (from -50 ms to 50% of the

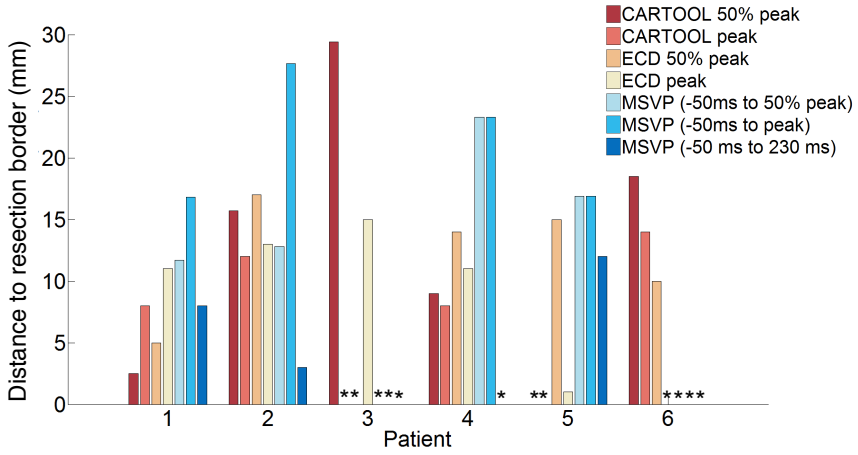

	Distance to resection border (mm)						
	CARTOOL 50% peak	CARTOOL peak	ECD 50% peak	ECD peak	MSVP (-50 ms to 50% peak)	MSVP (-50 ms to peak)	MSVP (-50 ms to 230ms)
mean	12.5	7.1	10.2	8.5	10.8	14.1	3.8
std	11.0	6.0	6.6	6.4	9.3	11.2	5.1

Figure 7.4: The distance to the resection border, d_r (in mm) for each of the patients (P1 to P6) and for the different methods. In the table below, the means, standard deviations and maximum distances to the resection of each method are given. The stars denote the situations in which the activity was correctly estimated inside the resected area

spike peak) for the estimated time courses of the estimated dipoles. The sources with the highest energy are depicted by S1, S2, S3 and S4. In panel C, the time courses of the sources are shown. The dipole with the highest energy is depicted by S1 and its location is shown on top of the post-operative MR image in Panel D. We presented the results for the five other patients considered in this study in the same fashion in Fig. 7.6, 7.7, 7.8, 7.9 and 7.10.

7.4 Discussion

To the best of our knowledge, this chapter demonstrates the first ESI application including a Bayesian multiple sparse priors inversion approach that uses the maximum energy of the estimated dipole intensities to depict the generator of the interictal spikes. Using the PEB framework,

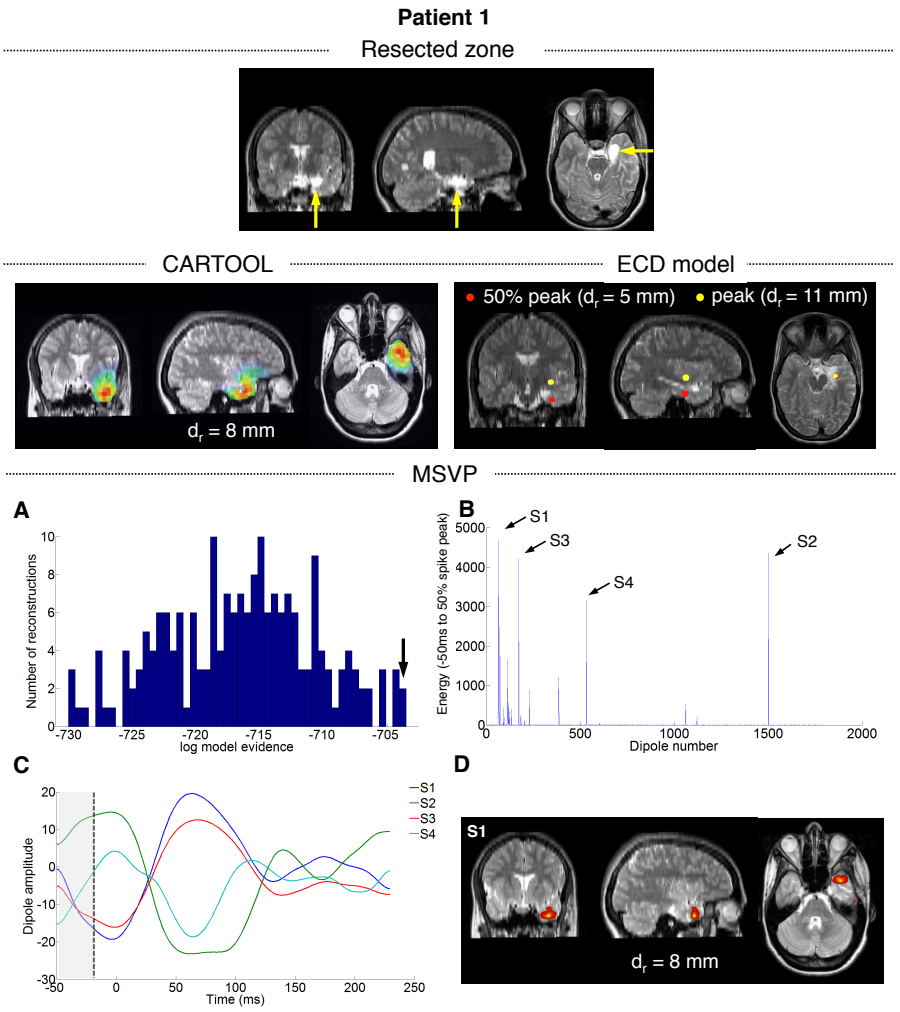

Figure 7.5: First row: the resected zone of patient 1. Second row: the CARTOOL solution at the spike peak and the ECD locations corresponding with the spike peak and at 50 % of the peak shown in yellow and red. Panel A: histogram of the free energy values corresponding with the MSVP inversions. Panel B: energy of the dipole intensities based on the MSVP solution. The dipoles with the maximum energy are depicted by S1, S2, S3 and S4. Panel C: the time courses of S1, S2, S3 and S4. Panel D: the location of volumetric region corresponding with S1.

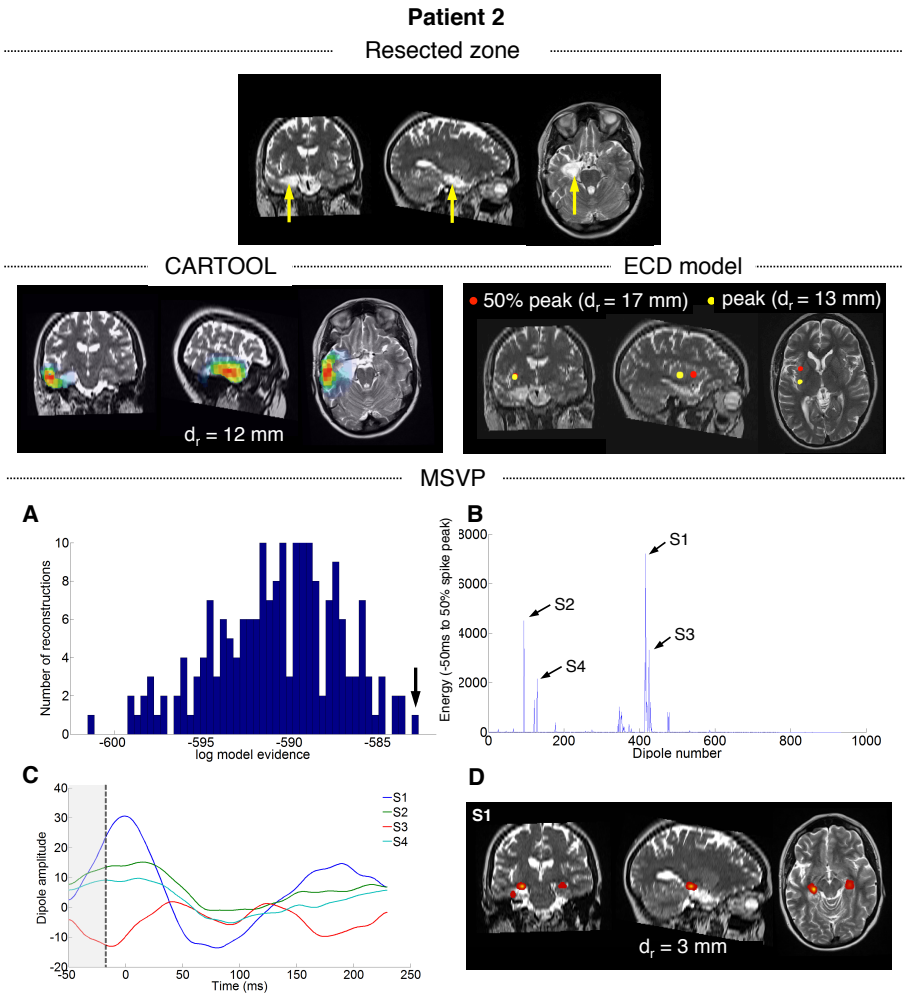

Figure 7.6: First row: the resected zone of patient 2. Second row: the CARTOOL solution at the spike peak and the ECD locations corresponding with the spike peak and at 50 % of the peak shown in yellow and red. Panel A: histogram of the free energy values corresponding with the MSVP inversions. Panel B: energy of the dipole intensities based on the MSVP solution. The dipoles with the maximum energy are depicted by S1, S2, S3 and S4. Panel C: the time courses of S1, S2 and S3. Panel D: the location of volumetric region corresponding with S1.

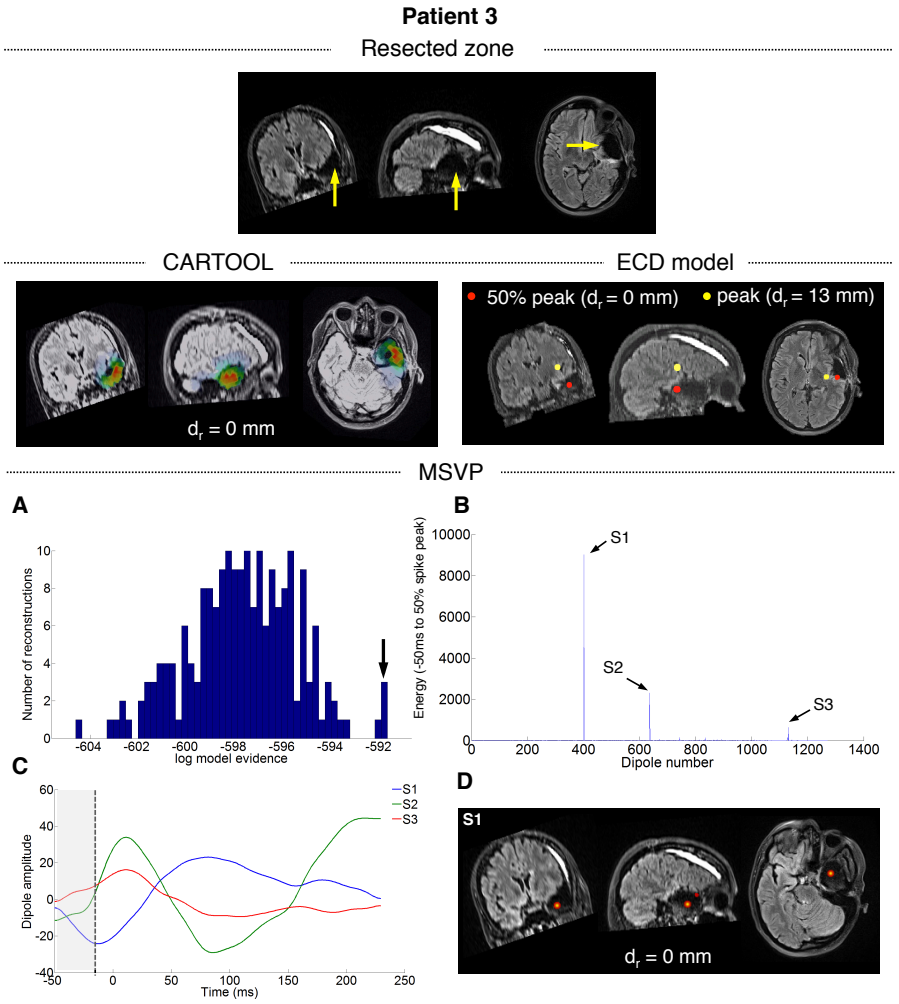

Figure 7.7: First row: the resected zone of patient 3. Second row: the CARTOOL solution at the spike peak and the ECD locations corresponding with the spike peak and at 50 % of the peak shown in yellow and red. Panel A: histogram of the free energy values corresponding with the with the MSVP inversions. Panel B: energy of the dipole intensities based on the MSVP solution. The dipoles with the maximum energy are depicted by S1, S2 and S3. Panel C: the time courses of S1, S2 and S3. Panel D: the location of volumetric region corresponding with S1.

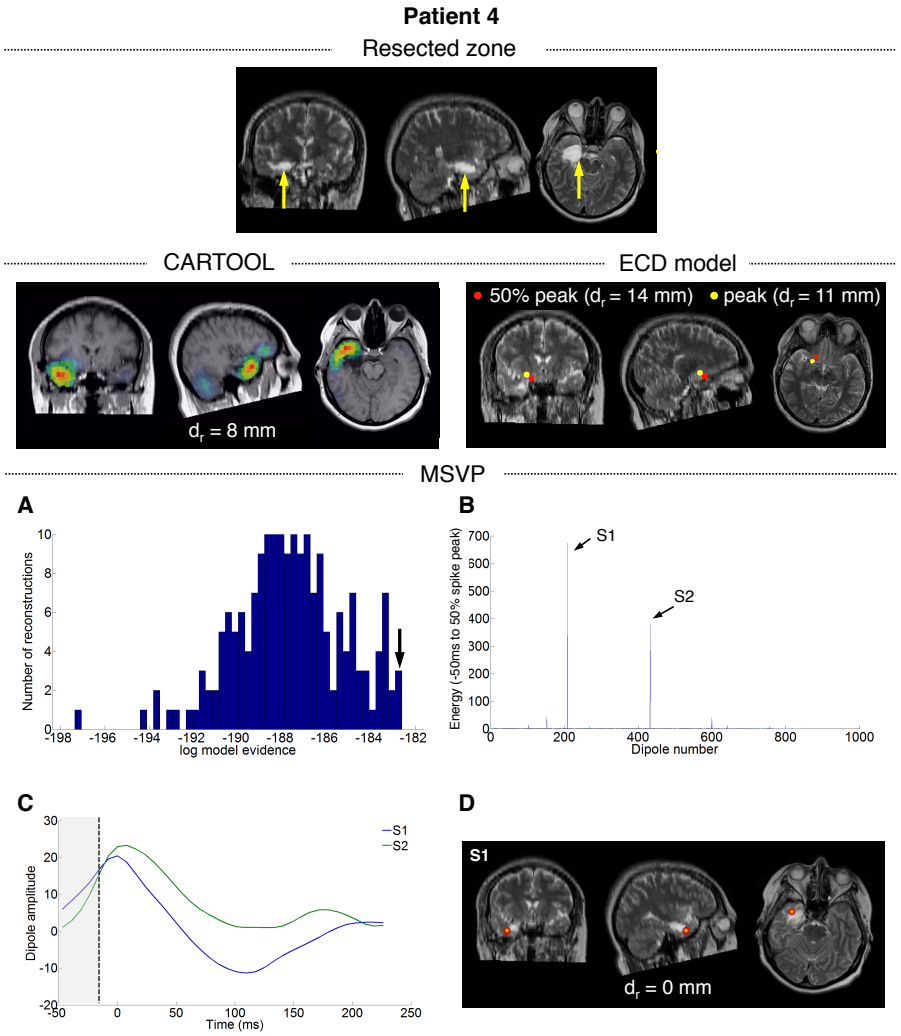

Figure 7.8: First row: the resected zone of patient 4. Second row: the CARTOOL solution at the spike peak and the ECD locations corresponding with the spike peak and at 50 % of the peak shown in yellow and red. Panel A: histogram of the free energy values corresponding with the MSVP inversions. Panel B: energy of the dipole intensities based on the MSVP solution. The dipoles with the maximum energy are depicted by S1 and S2. Panel C: the time courses of S1 and S2. Panel D: the location of volumetric region corresponding with S1.

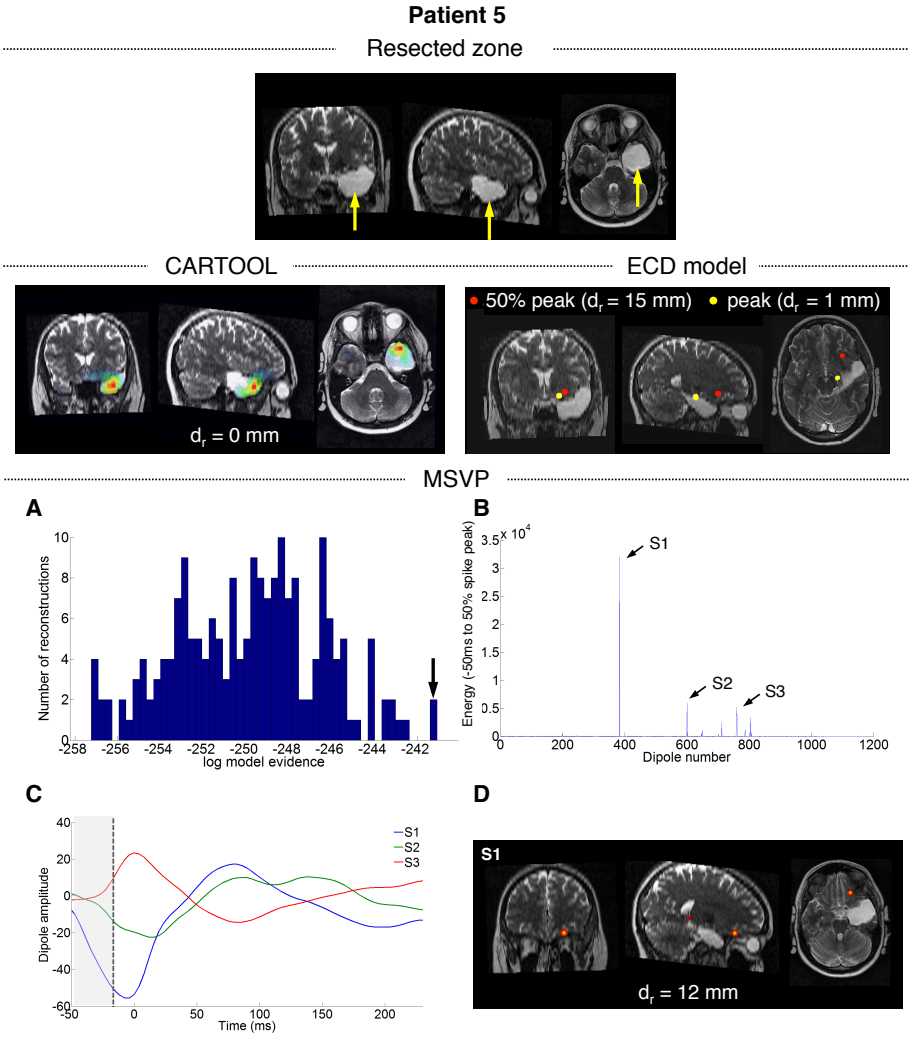

Figure 7.9: First row: the resected zone of patient 5. Second row: the CARTOOL solution at the spike peak and the ECD locations corresponding with the spike peak and at 50 % of the peak shown in yellow and red. Panel A: histogram of the free energy values corresponding with the MSVP inversions. Panel B: energy of the dipole intensities based on the MSVP solution. The dipole with the maximum energy is depicted by S1, S2 and S3. Panel C: the time course of S1, S2 and S3. Panel D: the location of volumetric region corresponding with S1.

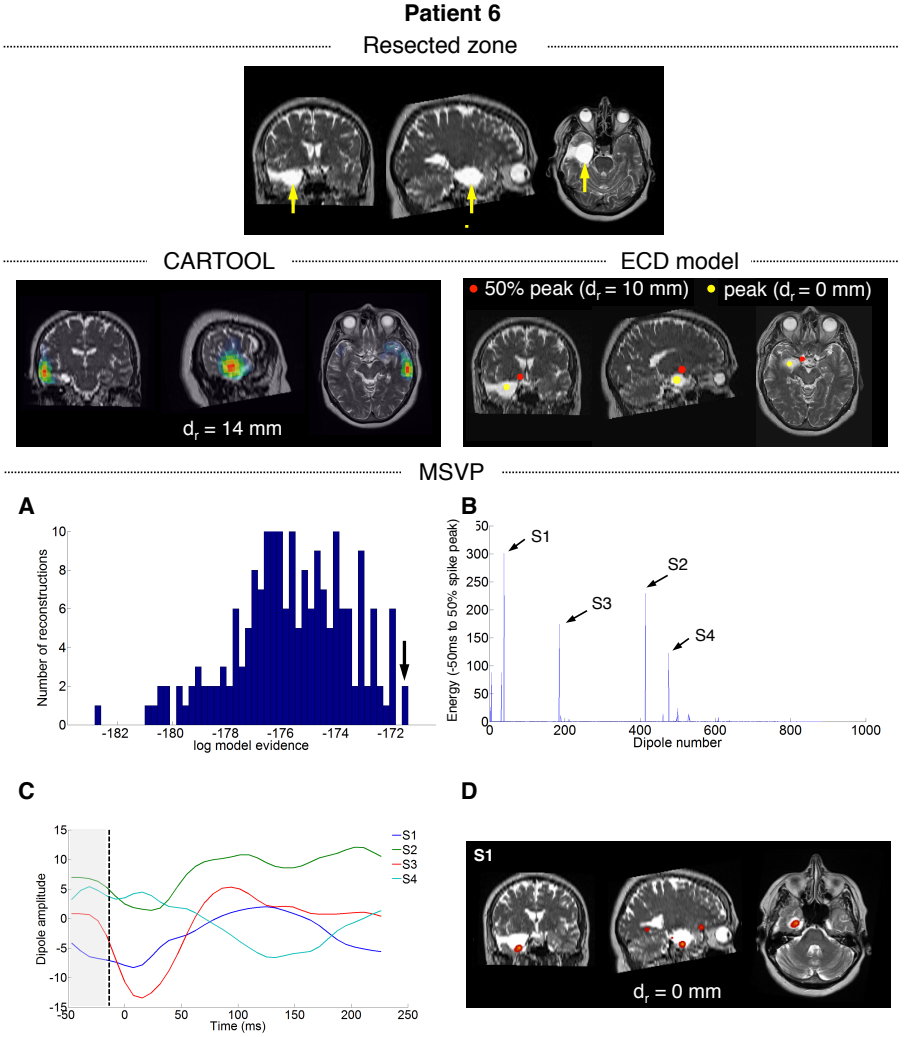

Figure 7.10: First row: the resected zone of patient 6. Second row: the CARTOOL solution at the spike peak and the ECD locations corresponding with the spike peak and at 50 % of the peak shown in yellow and red. Panel A: histogram of the free energy values corresponding with the MSVP inversions. Panel B: energy of the dipole intensities based on the MSVP solution. The dipoles with the maximum energy are depicted by S1, S2, S3 and S4. Panel C: the time courses of S1, S2, S3 and S4. Panel D: the location of volumetric region corresponding with S1.

we compared 100 sets of 256 volumetric priors for inversion and determined the most likely set of priors based on Bayesian model comparison [111, 178]. The localization results clearly corresponded to the resected zone in all patients. The proposed approach was compared with the results of the CARTOOL software and the ECD modeling technique. We found equally good or smaller distances to the resection, with robust results for all patients.

Note that patients 1, 2, 4 and 6 had a left or right selective amygdalolohypocampectomy. Discharges in the hippocampus or amygdala are assumed to produce no observable scalp EEG rhythms [179–181]. Because we did not observe interictal activity in the routine EEG registrations after surgery we can assume that the interictal activity observed in the EEG registration was caused by adjacent regions in the temporal cortex. Typically these regions are activated because of spreading from the hippocampus or amygdala. We therefore have to be careful to use the resection border to evaluate the different methods. Patients 3 and 5 had a 2/3 temporal lobectomy. In these patients the resected zone was larger. For patients 3, all the approaches estimated the activity inside the resected zone except the CARTOOL approach at 50% of the spike peak and the ECD approach at the peak of the spike. For patient 5, only the CARTOOL approach estimated the activity inside the resected zone, both at 50% of the spike peak and at the spike peak. In order to estimate the irritative zone (see section 3.4.1) more precisely, simultaneous intracranial recordings are necessary. These were however not available in the patients. Typically also the specificity and sensitivity of the ESI techniques are reported [91, 176, 182]. Because we only used 6 patients and the irritative zone wasn't clearly defined, these measures are not relevant in this study.

The choice to use the whole time window for spike inversion using the MSVP approach is similar to other studies [183, 184]. In addition to that we evaluated the influence of using smaller time windows before the spike. For each of the approaches, the noise was assumed to be independent in each sensor. The reason to use smaller time windows before the spike is that the high-amplitude spike activity is eliminated so the ESI scheme will not focus on reducing the error for reconstructing the peak activity and therefore might ignore the activity of interest. The choice of the time window effects the location of the region with the highest energy, which is a similar to the findings reported in [173]. In order to investigate this more in depth, more patients are needed.

Note that we only selected the solution with the highest free energy to compare the reconstructed activity. In some cases there were models with similar free energy values near the highest free energy value, i.e. in a range less than 3. For these solutions we calculated the Bayesian Model Average (BMA) in an interval of 3 from the highest free energy [185, 186]. The BMA approach did however not influence the selection of the source location with the maximum activity and therefore did not influence the findings based on the results corresponding with the maximum free energy.

So far many studies for EEG source imaging used ECD models [83, 187–189]. The ECD model is limited because it does not allow to investigate the spatial extend of the sources corresponding with the interictal activity. The technique that was presented here is especially suited to investigate the spatial extend of the epileptic activity, since it allows to introduce regions with a different spatial spread, i.e. by varying the parameters of the region growing and the smoothing factor. Another advantage of the approach is that any shape of the volumetric regions can be introduced as prior. For example, regions constructed based on (f)MRI prior knowledge, clinical results from PET or SPECT studies of the patients, prior knowledge based on the ECD solutions, etc. Whether the results improve with additional prior knowledge can be evaluated using Bayesian model selection. In this study, a set of volumetric priors was constructed by randomly selecting 256 dipole locations from 256 different fixed regions in the gray matter of the patient to cover the whole gray matter layer. Different numbers could also have been evaluated but we do not expect much differences in the results. A smaller number of volumetric regions would result in smaller sampling of the gray matter and higher numbers would increase the complexity of the problem. Each of the priors is weighted based on the data by estimating the hyperparameters, so the most relevant priors are selected for any set of priors.

An important factor influencing the ESI results is the forward modeling approaches we used to for the ECD, CARTOOL and MSVP technique. In this work we used both multi-spherical and 5-layered patient specific head models including scalp, skull, cerebrospinal fluid, white and gray matter segmented from the anatomical MR images of the patients. Moreover, we used both free orientations and fixed orientations of the dipoles. Because we used the resected zone to verify the ESI results, we could however evaluate different approaches for different forward models. Although the work of [176] suggests there is no need for highly sophisticated head models in clinical applications, we think the more realistic

the forward model is constructed, the more accurate the results could potentially be. In order to investigate this, more patients are needed and the results should be verified with intracranial EEG recordings to clearly delineate the irritative zone.

There are some issues that we did not address in this paper. For example the time window around the spike peak we used for inversion, i.e. -50 ms to 230 ms, could be chosen differently. In general, it is important to include the rising phase (from -50 ms to the peak) of the spike in order to include the origin of the epileptic activity [173–175]. Moreover, we did not evaluate the spatial spread of the source of the spike activity in detail using the CARTOOL software and for the ECD solutions. Only the results corresponding with the peaks of the spikes and at 50% of the peaks were reported. More time points could have been shown but we did not include this in the study because of small localization differences or higher RRE percentages due to increasing noise levels in the beginning of the rising phase of the spike. Moreover, we only evaluated averaged spikes for inversion because the RRE values of the ECD solutions were too high due to an increased noise level for single spikes. Furthermore, we analyzed both 27 channel and 64 channel EEG data but did not evaluate the effect of using a different number of electrodes because of the small patient group and the small differences we found between the distance to the resection. Finally, we did not investigate propagation effects based on the estimate time courses of the dipole sources. Also using the LORETA approach in the CARTOOL software, the dipole activity could have been estimated for the whole spike time window to study the network of the activity.

There are many opportunities for future work. First of all the network effects can be studied based on the estimated time courses of the dipoles. This can be investigated in future studies using different techniques to estimate connectivity patters between the sources, for example using dynamical causal modeling [190] or functional connectivity approaches [191]. Moreover, it is important in future studies to evaluate the applicability of ESI techniques in order to localize seizure activity. In this context, it is also important to focus on the network aspects of the estimated activity of the sources in order to localize the origin of the activity [192, 193].

7.5 Conclusion

In this chapter, we presented an ESI technique to localize interictal spike activity based on patient specific head models and by introducing multiple volumetric sparse regions in a parametric empirical Bayesian framework for distributed sources. The technique uses the whole time-window of the interictal spike activity to localize the generating sources and allows to study propagation effects. Based on averaged interictal spike data of 6 patients, the findings suggest that our approach is potentially useful to delineate the irritative zone in addition to other distributed approaches such as those implemented in the CARTOOL software and ECD modeling techniques.

7.6 Original Contributions

The work performed in this chapter was presented at the 18th international conference on biomagnetism [194] and the international conference on basic and clinical multimodal imaging [195]. The results that are presented in this chapter are currently in preparation for submission to the A1-journal NeuroImage [196] and will be presented at 17th Update@Kempenhaeghe.nl and the 20th annual meeting of the organization for human brain mapping.

Chapter 8

General conclusions and future research

"The words go, the word goes, The words go"
David August - innervisions #50

In this final chapter we give a general overview of the main contributions of the work that was performed in this dissertation. For each chapter, the results are summarized followed by the conclusions that can be drawn from them. Based on the overall presented work we discuss some future research directions and close with a final conclusion.

8.1 Summary

The purpose of this dissertation was to show that more accurate and realistic forward models improve EEG source imaging results. This was shown in this dissertation for several forward models, by testing them using real data, rather than the more traditional simulated data from an assumed true forward model as shown in various previous studies. We made use of a Bayesian framework to invert the forward model based on a distributed source model. This provided us an alternative way of testing forward models, using real data, based on the model evidence corresponding with a certain forward model. This way, we evaluated forward modeling choices using realistic EEG data in 32 subjects and 6 patients.

In chapter 2, the principles of electroencephalography (EEG) were described. We presented a brief history of the first EEG recordings. To un-

derstand the origin of the measured EEG activity, the subsequent section described the anatomy and function of the brain with the focus on the mechanisms of neural activity. This allowed us to elaborate on the origin of electrical brain activity at different spatial scales, going from electrical signals measurable at the microscopic level to signals that are measurable on top of the scalp. Next, we looked at the modern EEG recording techniques and described methods to visualize the recorded data. Various types of brain activity that can be observed in an EEG recording were also presented. The different types of artifacts often present in the EEG recordings, and some techniques to remove them were described subsequently. Finally, a number of applications were presented.

The techniques to estimate the sources that generate the measured EEG activity, a process called EEG source imaging (ESI) were introduced in chapter 3. EEG source imaging is characterized by a generative model or forward model of the EEG data and an inverse technique to find a unique solution. We started the chapter focusing on the forward model of the EEG data. First a brain source model of the sources generating the EEG data was described. We then introduced the head model. Several techniques to construct the head model using structural images of the head were introduced. Next, the algebraic representation of the forward model of the EEG data was introduced. Based on that, we explained how the field propagation of the sources through the various tissues in the human head can be modeled using a technique based on finite differences. After introducing the forward modeling part of the EEG data, several inverse techniques that were developed over the last 20 years were discussed. Also an overview was given of the features of EEG source imaging related to other functional neuroimaging techniques. We concluded the chapter by presenting an application of multimodal neuroimaging.

In chapter 4, we presented the Bayesian framework we used to invert the forward model. To draw the context of probability calculus we started the chapter with an explanation of Bayes' theorem. Subsequently the hierarchical Bayesian formulation of the inverse problem was described based on a distributed source model. Next, we explained the framework that allows to introduce multiple source priors for EEG source imaging. Also the Bayesian interpretation of the classic methods was discussed. A generalized cost function was derived, i.e. the free energy, that is optimized to find a unique solution using the Restricted Maximum Likelihood (ReML) algorithm. Most important for the subsequent chapters, we described how the framework can be used to compare

different forward models depending on the measured EEG data.

In chapter 5, the parametric empirical Bayesian (PEB) framework for distributed source imaging in EEG/MEG implemented in the Statistical Parametric Mapping software was introduced for forward models constructed based on finite differences. We introduced volumetric template head models based on the Colin27 template. FDM head models were constructed equivalent to the BEM model (used by default in the SPM software) and we constructed an extended FDM model including cerebrospinal fluid. These models were compared within the context of three different types of source priors related to the type of inversion used in the PEB framework: independent and identically distributed (IID) sources, equivalent to classical minimum norm approaches, coherence (COH) priors similar to methods such as LORETA, and multiple sparse priors (MSP). The resulting models were compared based on ERP data of 20 subjects. In brief, they performed trials of faces, houses, inverted faces and words stimuli resulting in 4 types of Event Related Potentials (ERP) for each subject. Using Bayesian model selection for group studies the different models were evaluated. The reconstructed activity was also compared with the findings of previous studies using functional magnetic resonance imaging. We found strong evidence in favor of the extended FDM head model with CSF and assuming MSP. These results suggest that the use of realistic volumetric forward models can improve PEB EEG source imaging.

In chapter 6, we revisited the MSP algorithm implemented in the SPM software for distributed EEG source imaging. In the present implementation, multiple cortical patches are introduced as source priors based on a dipole source space restricted to a cortical surface mesh. We presented a technique to construct volumetric cortical regions to introduce as source priors by restricting the dipole source space to a segmented gray matter layer and using a region growing approach. We called this technique the Multiple Sparse Volumetric Priors (MSVP) approach. This extension allowed us to reconstruct brain structures besides the cortical surface and facilitated the use of more realistic volumetric head models including more layers, such as cerebrospinal fluid (CSF), compared to the default 3-layered scalp-skull-brain head models in the SPM software. We illustrated the technique with ERP data and anatomical MR images in 12 subjects. In brief, the subjects performed 80 trials of circular black-and-white checkerboard stimuli presented to one of the four quadrants of the visual field resulting in 4 types of Event Related Potentials (ERP) for each subject. Based on the segmented gray matter

for each of the subjects, cortical regions were created and introduced as source priors for MSP-inversion assuming two types of head models. The standard 3-layered scalp-skull-brain head models and extended 4-layered head models including CSF. We compared these models with the current implementation by assessing the free energy corresponding with each of the reconstructions using Bayesian model selection for group studies. Strong evidence was found in favor of the MSVP approach compared to the MSP approach based on cortical patches for both types of head models. Overall, the strongest evidence was found in favor of the MSVP reconstructions based on the extended head models including CSF. These results were verified by comparing the reconstructed activity.

In chapter 7, we compared different sets of MSVPs to localize the generating sources of interictal spikes observed in EEG recordings of patients with refractory focal epilepsy. Based on the extensions of the MSP algorithm in chapter 6, an ESI technique was described to estimate the activity of multiple distributed sources corresponding with the full time course of the spikes. We suggested to identify the origin of the activity based on the source with the maximum energy during the rising phase of the spike. Our approach consisted of introducing multiple sets of sparse volumetric priors in the PEB framework and evaluating the effect of the priors based on the model evidence. We illustrated the technique using averaged interictal epileptic spikes in 6 patients with refractory focal epilepsy that were treated with surgery. Based on pre-surgical anatomical MR images and the electrode positions that were available for each patient, patient specific 5-layered head models were constructed. We modeled 100 different sets of 256 volumetric regions with locations that were maximally spread inside the gray matter of the patient. Each set of regions was introduced as priors for inversion, and we obtained the most likely set of priors using Bayesian model selection. The resected zone in each of the patients, extracted from post-operative MR images, was used to evaluate the proposed approach. We compared with a LORETA approach implemented in the CARTOOL software and an equivalent current dipole (ECD) approach at the spike peaks and at 50% of the peaks during the rising phase of the spike. We found equally good or smaller distances to the border of resection, i.e. < 15 mm, with robust results for all the patients. The results we obtained are promising because the approach allows to identify the spatial spread of the sources, and allows incorporating prior knowledge from other clinical investigations such as Positron Emission Tomography (PET) and functional Magnetic Resonance Imaging (fMRI).

8.2 Future research possibilities

Future research is still required for several aspects of EEG source imaging. It is a very slow moving field because of computational limitations in the past and the inherent challenge to validate the ESI techniques thoroughly. This is a consequence of the fact that EEG source imaging depends on a whole sequence of recording and pre-processing factors that could influence the results. Assuming that the recording equipment is functioning perfectly and the electrodes are placed well, we present some of the limiting factors below categorized as factors on the electrode level, for the forward model and validation aspects. A couple of research opportunities that are relevant to the research methodology presented in this dissertation are subsequently discussed.

1. At the electrode level the main limiting factor is the external noise in the recordings besides the brain activity being studied.
2. For the forward model we distinguished:
    - the quality and resolution of the anatomical images, i.e. the anatomical MR images or CT images, of the head to construct the forward model,
    - the segmentation techniques of the MR images that are used to model the different tissues in the head model,
    - the choice of the number of tissues that should be modeled in the head model,
    - the unknown conductivities of the tissues modeled in the head model,
    - whether modeling of the electrodes is possible based on additional measurements.
3. For ESI validation the main limiting factors are:
    - the lack of a ground truth,
    - and the different sensitivity of ESI to different areas in the brain, i.e. the detection of brain activity in deeper areas in the brain is less likely than activity close to the scalp surface.

It is moreover important to realize the fact that these limitations depend on the brain activity being studied. For example, the modeling choices

of an ESI technique for source imaging of interictal epileptic spikes will be different than localizing the sources generating an ERP component.

In order to improve the robustness to noise in the EEG recordings, the Bayesian framework that was introduced in this dissertation allows to incorporate prior information about the noise inserted as prior covariance components. The noise can be measured in single recording before the experiment.

For the forward model, the main opportunity is to cope with the problem of the conductivities of the tissues. Typically conductivity values are used that are reported in literature from in vivo measurement. In reality this is however an approximation because the conductivity of the tissues can vary from subject to subject, is dependent on the age, time, etc. Initiatives are taken to calibrate the conductivities in the brain using an evoked source inside the brain that comes from a well-known somatosensory experiment. These data can be measured in a single run before acquisition of the brain activity of interest. Also techniques such as Electrical Impedance Tomography (EIT) and Magnetic Resonance Electrical Impedance Tomography can provide alternative ways to measure the conductivity of the tissues in the human head. The Bayesian framework could offer an elegant opportunity to determine the conductivity empirically, by assessing the free energy values corresponding with reconstructions assuming head models with different conductivity values. Forward modeling choices such as the accurate modeling of the electrodes and different segmentations technique can be evaluated using the framework and the extensions that were proposed in this dissertation.

To validate ESI techniques, the most rigorous way is to use simultaneously recorded scalp EEG data and intracranially recorded EEG data, i.e. brain activity monitored inside the brain. This is of course not straightforward in humans because it requires a very invasive procedure to place the intracranial electrodes. Worldwide initiatives are however taken to provide datasets registered in monkeys in order to validate ESI techniques in depth. Often epileptic patients are monitored with intracranial electrodes in order to determine the epileptic focus. Datasets of simultaneously recorded EEG and intracranial EEG provide the most straightforward way to validate the techniques for ESI of epileptic events recorded in the EEG.

In order to validate ESI for a specific type of brain activity, large datasets are necessary to determine the accuracy and uncertainty on the localized sources. Such studies are currently lacking. Once a specific

technique for ESI is chosen for an experiment to localize the sources that are generating the EEG data, the uncertainty on the locations should also be quantified. The PEB framework provides an optimal statistical framework in that context.

8.3 Final conclusions

Several EEG source imaging techniques have been proposed to identify the generating neuronal sources of electrical activity measured on the scalp. The solution of these techniques depends directly on the accuracy of the forward model that is inverted. In this dissertation several forward models were compared based on realistic data in 32 subjects. We introduced advanced forward models in a parametric empirical Bayesian framework in order to compare the models based on an approximation of the model evidence. The results we obtained in this work suggest that the use of realistic volumetric forward models improve EEG source imaging. We furthermore showed that the use of volumetric cortical regions as source priors is a useful complement to the present implementation in the Bayesian framework as it allows to introduce more complex head models and volumetric source priors in future studies. In the final chapter we presented a new ESI technique to localize interictal spike activity based on patient specific head models and by introducing multiple sparse volumetric priors in the Bayesian framework for distributed sources. Based on data of 6 patients, the findings suggest that our approach is potentially useful to delineate the irritative zone in addition to the currently used techniques. The results are promising but need verification in a larger patient group and need to be compared with intracranial recordings.

Appendix

Appendix A

The reciprocity principle for EEG forward modeling

We could use Eq. (3.23) to compute the lead fields for every dipole we consider inside the head model. Typically about 10.000 to 100.000 dipoles are considered as possible sources so this would take a lot of computation time. Based on a reciprocal approach, we can limit the number of computations to the number of electrodes.

A.1 The general idea of reciprocity

Consider a circuit with two clamps A and B representing a pair of scalp electrodes, and two clamps on a location described by index r measuring a dipolar source in the brain region illustrated in Fig. A.1.

First a current I_r at clamps r is introduced. This source will generate a potential $V_{AB}(I_r)$ at AB as illustrated in Fig. A.1A. Next a current I_{AB} is introduced at clamps A and B. This will give rise to a potential difference $U_r(I_{AB})$ at r as illustrated in Fig. A.1B. The reciprocity theorem in circuit analysis states [198]:

$$V_{AB}\ I_{AB} = U_r\ I_r \tag{A.1}$$

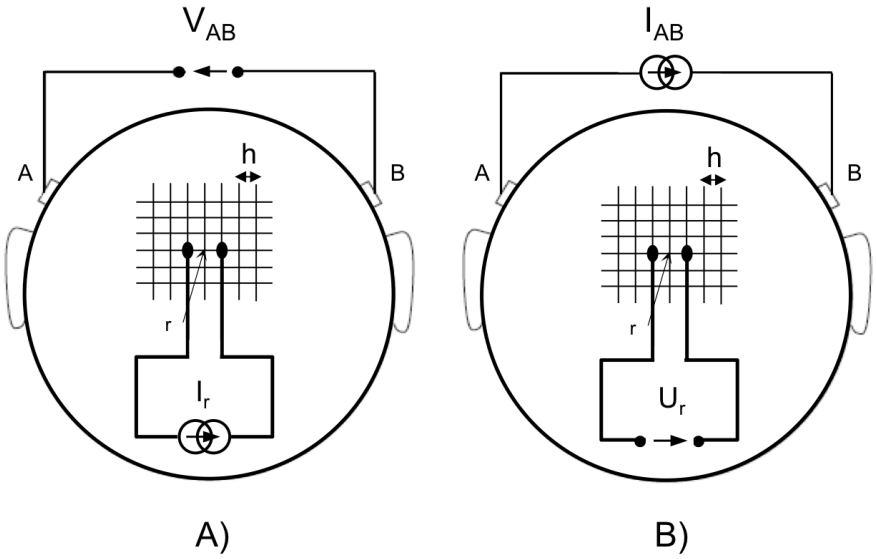

Figure A.1: A schematic representation of the reciprocity theorem. A network where a current source is introduced in the brain and a potential difference is measured at an electrode pair, and visa versa: (a) a current source I_r is introduced and the potential V_{AB} is measured, and (b) a current source I_{AB} is introduced and a potential U_r is measured. Figure adapted from [197].

A.2 Application of reciprocity to compute EEG lead fields using finite differences

Considering Eq. (A.1). We assume a dipole oriented in the x-direction at a location described by index r of the computational grid. The dipole is represented by two current monopoles, a current source and sink, providing I_r and $-I_r$, on opposite nodes along the x-direction separated by a distance $2h_x$, with h_x the spacing of the nodes in the x-direction. The dipole is oriented from the negative to the positive current monopole and the centre node with index r of the two monopoles is the dipole position. the magnitude of the dipole moment is then $2h_xI_r$. Because the scalp electrodes are located sufficiently far from the sources compared with the distance $2h_x$ between the sources we can assume a dipolar field. Equation (A.1) can be rewritten as:

$$V_{AB} = \frac{U_r\ I_r}{I_{AB}}. \tag{A.2}$$

To explicitly include the orientation of the dipole in x,y or z direction in Eq. (A.2), we describe a dipole based on its location $\mathbf{r} = [ih_x, jh_y, kh_z]$ in the 3D computational grid, with h_x, h_y and h_z the spacing of the nodes in the x,y or z-direction and the indices i, j, k the number of nodes along the x,y and z direction. Rewriting Eq. (A.2) with $d_x = 2h_x I_r$ and

$$\frac{\partial U}{\partial x}(\mathbf{r}) \approx \frac{[U(\mathbf{r} + h_x\mathbf{e}_x) - U(\mathbf{r} - h_x\mathbf{e}_x)]}{2h_x},$$

with $\mathbf{e}_x$ the unit vector in the x-direction, gives:

$$V_{AB} = \frac{d_x(\mathbf{r})\frac{\partial U}{\partial x}(\mathbf{r})}{I_{AB}}, \tag{A.3}$$

meaning that the potential V_{AB} can be calculated for a dipole oriented along the x-axis on location $\mathbf{r}$ given $\frac{\partial U}{\partial x}(\mathbf{r})$. In a similar way, V_{AB} can be calculated for a dipole located at $\mathbf{r}$ oriented along the y-axis and the z-axis. Consider a dipole at position $\mathbf{r}$ and with dipole components $\mathbf{d} = (d_x, d_y, d_z)^T \in \mathbb{R}^{3\times 1}$. The potential V_{AB} reads:

$$V_{AB}(\mathbf{r}, \mathbf{d}) = \frac{\mathbf{d}^T \cdot \nabla U(\mathbf{r})}{I_{AB}}, \tag{A.4}$$

with $\nabla U(\mathbf{r}) = (\partial U(\mathbf{r})/\partial x, \partial U(\mathbf{r})/\partial y, \partial U(\mathbf{r})/\partial z)^T \in \mathbb{R}^{3\times 1}$.

Based on Eq. (A.4), the approach based on reciprocity to calculate the EEG lead fields goes as follows for 2 electrodes considered on the scalp surface:

- A fictive current $I_{AB} = 1$, with unit amplitude is assumed, which enters the head at electrode A and leaves the head at electrode B.
- Utilizing the FDM equation (3.23), the potentials $U(ih_x, jh_y, kh_z)$ can be calculated for every position. Fig. A.2 illustrates the equipotential lines and current density vectors $\mathbf{J} = -\sigma\nabla U$ in the brain region, with $\nabla U = (\partial U/\partial x, \partial U/\partial y, \partial U/\partial z)^T$. The partial derivative $\partial U/\partial x$ is approximated by $[U((i+1)h_x, jh_y, kh_z) - U((i-1)h_x, jh_y, kh_z)]/2h_x$. The partial derivatives $\partial U/\partial y, \partial U/\partial z$ are obtained in a similar way.
- V_{AB} the potential difference between the scalp electrodes A and B generated by the dipole at position $\mathbf{r}$ and dipole moment $\mathbf{d}$ is obtained by applying Eq. (A.4).

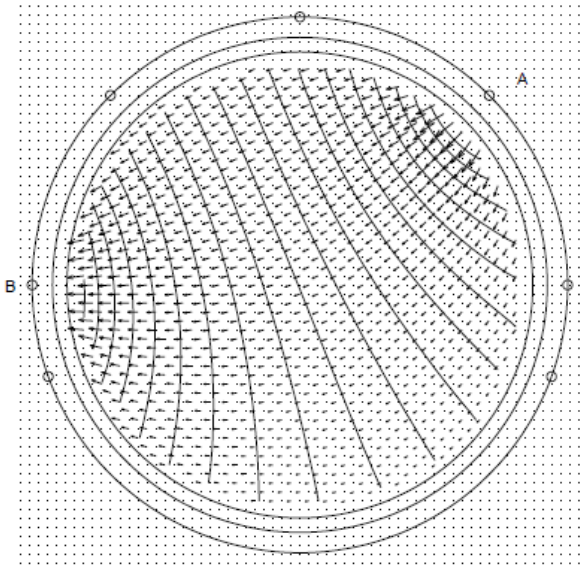

Figure A.2: Potential field calculated using the finite difference modeling approach for a current introduced between two electrodes A and B on the scalp. Figure adapted from [197].

If N scalp electrodes are used to measure the EEG, $N-1$ electrode pairs can be found with linear independent potential differences. For each electrode pair, Eq. (A.4) can be used to calculate the V_{AB} for each position $\mathbf{r}$ in the brain. Therefore $N-1$ numerical forward calculations are performed and the $N-1$ potential differences at the $N-1$ electrode pairs are subsequently transformed in N average referenced potentials at the N electrodes to calculate the lead fields in each direction [50]. As explained in section 3.2.4.2, if we subsequently assume that the dipolar sources have unit amplitudes in 3 orthogonal directions for each location $\mathbf{r}$ the resulting potentials $\mathbf{V}_u$ represent the lead field $\mathbf{L}$ in 3-directions for each location $\mathbf{r}$. Note that the leadfields computed based on the reciprocal approach will differ a factor of $2h_x$, $2h_y$ and $2h_z$ in each direction compared to the direct computation used in Eq. (3.23). This is important if different forward modeling techniques are compared to have a consistent comparison.

Appendix B

The derivation of $p(\mathbf{V}_m, \boldsymbol{\lambda})$

In this appendix we work out $p(\mathbf{V}_m, \boldsymbol{\lambda})$:

$$= \int p(\mathbf{V}_m|\mathbf{J})p(\mathbf{J}|\boldsymbol{\lambda})p(\boldsymbol{\lambda})d\mathbf{J}$$

$$\propto \int \exp\Big(-\tfrac{1}{2}tr((\mathbf{V}_m - \mathbf{L}\mathbf{J})^T\mathbf{C}_{\boldsymbol{\epsilon}}^{-1}(\mathbf{V}_m - \mathbf{L}\mathbf{J}))\Big)\exp\Big(-\tfrac{1}{2}tr(\mathbf{J}^T\mathbf{C}_{\mathbf{J}}^{-1}\mathbf{J})\Big)d\mathbf{J}$$

$$\propto \int \exp\Big(-\tfrac{1}{2}tr(((\mathbf{V}_m - \mathbf{L}\mathbf{J})^T\mathbf{C}_{\boldsymbol{\epsilon}}^{-1}(\mathbf{V}_m - \mathbf{L}\mathbf{J}) + \mathbf{J}^T\mathbf{C}_{\mathbf{J}}^{-1}\mathbf{J}))\Big)d\mathbf{J}$$

$$\propto \int \exp\Big(-\tfrac{1}{2}tr(\mathbf{V}_m^T\mathbf{C}_{\boldsymbol{\epsilon}}^{-1}\mathbf{V}_m - \mathbf{V}_m^T\mathbf{C}_{\boldsymbol{\epsilon}}^{-1}\mathbf{L}\mathbf{J} - \mathbf{J}^T\mathbf{L}^T\mathbf{C}_{\boldsymbol{\epsilon}}^{-1}\mathbf{V}_m + \mathbf{J}^T\mathbf{L}^T\mathbf{C}_{\boldsymbol{\epsilon}}^{-1}\mathbf{L}\mathbf{J} + \mathbf{J}^T\mathbf{C}_{\mathbf{J}}^{-1}\mathbf{J})\Big)d\mathbf{J}$$

$$\propto \exp\Big(-\tfrac{1}{2}tr(\mathbf{V}_m^T\mathbf{C}_{\boldsymbol{\epsilon}}^{-1}\mathbf{V}_m)\Big)\int \exp\Big(-\tfrac{1}{2}tr(\mathbf{J}^T(\mathbf{L}^T\mathbf{C}_{\boldsymbol{\epsilon}}^{-1}\mathbf{L} + \mathbf{C}_{\mathbf{J}}^{-1})\mathbf{J} - \mathbf{V}_m^T\mathbf{C}_{\boldsymbol{\epsilon}}^{-1}\mathbf{L}\mathbf{J} - \mathbf{J}^T\mathbf{L}^T\mathbf{C}_{\boldsymbol{\epsilon}}^{-1}\mathbf{V}_m)\Big)d\mathbf{J}$$

$$\propto \exp\Big(-\tfrac{1}{2}tr(\mathbf{V}_m^T\mathbf{C}_{\boldsymbol{\epsilon}}^{-1}\mathbf{V}_m)\Big)\int \exp\Big(-\tfrac{1}{2}tr(\mathbf{J}^T(\boldsymbol{\Sigma}_{\mathbf{J}}^{-1})\mathbf{J} - \mathbf{V}_m^T\mathbf{C}_{\boldsymbol{\epsilon}}^{-1}\mathbf{L}\mathbf{J} - \mathbf{J}^T\mathbf{L}^T\mathbf{C}_{\boldsymbol{\epsilon}}^{-1}\mathbf{V}_m)\Big)d\mathbf{J}$$

with $\boldsymbol{\Sigma}_{\mathbf{J}}^{-1} = \mathbf{L}^T\mathbf{C}_{\boldsymbol{\epsilon}}^{-1}\mathbf{L} + \mathbf{C}_{\mathbf{J}}^{-1}$

$$\propto \exp\Big(-\tfrac{1}{2}tr(\mathbf{V}_m^T\mathbf{C}_{\boldsymbol{\epsilon}}^{-1}\mathbf{V}_m)\Big)\int \exp\Big(-\tfrac{1}{2}tr(\mathbf{J}^T\boldsymbol{\Sigma}_{\mathbf{J}}^{-1}\mathbf{J} - 2\mathbf{V}_m^T\mathbf{C}_{\boldsymbol{\epsilon}}^{-1}\mathbf{L}\mathbf{J})\Big)d\mathbf{J}$$

$$\propto \exp\Big(-\tfrac{1}{2}tr(\mathbf{V}_m^T\mathbf{C}_{\boldsymbol{\epsilon}}^{-1}\mathbf{V}_m)\Big)\int \exp\Big(-\tfrac{1}{2}tr((\mathbf{J}^T\mathbf{J} - 2\mathbf{V}_m^T\mathbf{C}_{\boldsymbol{\epsilon}}^{-1}\boldsymbol{\Sigma}_{\mathbf{J}}\mathbf{J})\boldsymbol{\Sigma}_{\mathbf{J}}^{-1})\Big)d\mathbf{J}$$

For solving this integral it is necessary to apply the following solution for a Gaussian integral:

$$\int_{-\infty}^{+\infty} \exp\Big(-\frac{x^2}{a^2} - bx\Big)dx = 2|a|\sqrt{\pi}\exp(b^2/4) \tag{B.1}$$

resulting in $p(\mathbf{V}_m, \boldsymbol{\lambda})$:

$$\propto \exp\Big(-\tfrac{1}{2}tr(\mathbf{V}_m^T\mathbf{C}_{\boldsymbol{\epsilon}}^{-1}\mathbf{V}_m)\Big) \times \Big(2\sqrt{|\Sigma_{\mathbf{J}}|}\sqrt{\pi}\exp\Big(\tfrac{1}{2}tr(\mathbf{V}_m^T\mathbf{C}_{\boldsymbol{\epsilon}}^{-1}\mathbf{L}\Sigma_{\mathbf{J}}\mathbf{L}^T\mathbf{C}_{\boldsymbol{\epsilon}}^{-1}\mathbf{V}_m)\Big)\Big)$$

$$\propto \exp\Big(-\tfrac{1}{2}tr(\mathbf{V}_m^T\mathbf{C}_{\boldsymbol{\epsilon}}^{-1}\mathbf{V}_m - \mathbf{V}_m^T\mathbf{C}_{\boldsymbol{\epsilon}}^{-1}\mathbf{L}\Sigma_{\mathbf{J}}\mathbf{L}^T\mathbf{C}_{\boldsymbol{\epsilon}}^{-1}\mathbf{V}_m)\Big)$$

$$\propto \exp\Big(-\tfrac{1}{2}tr(\mathbf{V}_m^T\mathbf{C}_{\boldsymbol{\epsilon}}^{-1}\mathbf{V}_m - \mathbf{V}_m^T\mathbf{C}_{\boldsymbol{\epsilon}}^{-1}\mathbf{L}(\mathbf{L}^T\mathbf{C}_{\boldsymbol{\epsilon}}^{-1}\mathbf{L} + \mathbf{C}_{\mathbf{J}}^{-1})^{-1}\mathbf{L}^T\mathbf{C}_{\boldsymbol{\epsilon}}^{-1}\mathbf{V}_m)\Big)$$

$$\propto \exp\big(-\tfrac{1}{2}tr(\mathbf{V}_m^T(\mathbf{C}_{\boldsymbol{\epsilon}} + \mathbf{L}\mathbf{C}_{\mathbf{J}}\mathbf{L}^T)^{-1}\mathbf{V}_m)\big)$$

$$\propto \exp\Big(-\tfrac{1}{2}tr(\mathbf{V}_m^T\boldsymbol{\Sigma}_V^{-1}\mathbf{V}_m)\Big), \text{ with } \boldsymbol{\Sigma}_V = \mathbf{C}_{\boldsymbol{\epsilon}} + \mathbf{L}\mathbf{C}_{\mathbf{J}}\mathbf{L}^T.$$

References

[1] Bronzino JD. *Biomedical engineering handbook*, vol. 2. CRC press. 1999.

[2] Berger H. Über das elektrenkephalogramm des menschen. *European Archives of Psychiatry and Clinical Neuroscience*. 1929; 87(1):527–570.

[3] Azevedo FA, Carvalho LR, Grinberg LT, Farfel JM, Ferretti RE, Leite RE, Lent R, Herculano-Houzel S, et al. Equal numbers of neuronal and nonneuronal cells make the human brain an isometrically scaled-up primate brain. *Journal of Comparative Neurology*. 2009;513(5):532–541.

[4] Van Hoey G. *Detectie en bronlokalisatie van epileptische hersenactiviteit met behulp van EEG-signalen*. Univesiteit Gent. 2000.

[5] Michel CM. *Electrical neuroimaging*. Cambridge University Press. 2009.

[6] Carter R. *The human brain book*. Penguin. 2014.

[7] Brodmann K, Garey LJ. *Brodmann's: Localisation in the Cerebral Cortex*. Springer. 2007.

[8] Hjorth B. The physical significance of time domain descriptors in EEG analysis. *Electroencephalography and clinical neurophysiology*. 1973;34(3):321–325.

[9] Steriade M, McCormick DA, Sejnowski TJ. Thalamocortical oscillations in the sleeping and aroused brain. *Science*. 1993; 262(5134):679–685.

[10] Nunez PL. *Neocortical dynamics and human EEG rhythms*. Oxford University Press, USA. 1995.

[11] JASPER HH. The ten twenty electrode system of the international federation. *Electroencephalography and clinical neurophysiology*. 1958;10:371–375.

[12] Braisby N, Gellatly A. *Cognitive psychology*. Oxford University Press. 2012.

[13] Sörnmo L, Laguna P. *Bioelectrical signal processing in cardiac and neurological applications*. Academic Press. 2005.

[14] Tallon-Baudry C, Bertrand O. Oscillatory gamma activity in humans and its role in object representation. *Trends in cognitive sciences*. 1999;3(4):151–162.

[15] Repovš G. Dealing with noise in EEG recording and data analysis. *Inform Medica Sloven*. 2010;15(1):18–25.

[16] Lins OG, Picton TW, Berg P, Scherg M. Ocular artifacts in EEG and event-related potentials I: Scalp topography. *Brain topography*. 1993;6(1):51–63.

[17] Hyvärinen A, Oja E. Independent component analysis: algorithms and applications. *Neural networks*. 2000;13(4):411–430.

[18] Jung TP, Makeig S, Humphries C, Lee TW, Mckeown MJ, Iragui V, Sejnowski TJ. Removing electroencephalographic artifacts by blind source separation. *Psychophysiology*. 2000;37(02):163–178.

[19] Jung TP, Makeig S, Westerfield M, Townsend J, Courchesne E, Sejnowski TJ. Removal of eye activity artifacts from visual event-related potentials in normal and clinical subjects. *Clinical Neurophysiology*. 2000;111(10):1745–1758.

[20] Delorme A, Sejnowski T, Makeig S. Enhanced detection of artifacts in EEG data using higher-order statistics and independent component analysis. *Neuroimage*. 2007;34(4):1443–1449.

[21] Strobbe G, Van de Vaerd R. Geschiktheidsstudie van connectiviteitsmaten in het. *Universiteit Gent*. 2010;.

[22] Fisher CE, Chin L, Klitzman R. Defining neuromarketing: Practices and professional challenges. *Harvard review of psychiatry*. 2010;18(4):230–237.

[23] Roth VA. The Potential of Neuromarketing as a Marketing Tool. *University of Twente*. 2014;.

[24] Baillet S, Mosher JC, Leahy RM. Electromagnetic brain mapping. *Signal Processing Magazine, IEEE*. 2001;18(6):14–30.

[25] De Munck J, Van Dijk B, Spekreijse H. Mathematical dipoles are adequate to describe realistic generators of human brain activity. *Biomedical Engineering, IEEE Transactions on*. 1988;35(11):960–966.

[26] De Munck J, Peters MJ. A fast method to compute the potential in the multisphere model. *IEEE transactions on biomedical engineering*. 1993;40(11):1166–1174.

[27] Frackowiak R, Friston K, Frith C, Dolan R, Friston K, Price C, Zeki S, Ashburner J, Penny W, eds. *Image segmentation*. Academic Press, 2nd ed. 2003.

[28] Fischl B. FreeSurfer. *Neuroimage*. 2012;62(2):774–781.

[29] Jenkinson M, Beckmann CF, Behrens TEJ, Woolrich MW, Smith SM. FSL. *NeuroImage*. 2012;62:782–790.

[30] Tadel F, Baillet S, Mosher JC, Pantazis D, Leahy RM. Brainstorm: a user-friendly application for MEG/EEG analysis. *Computational intelligence and neuroscience*. 2011;2011:8.

[31] Mazziotta J, Toga A, Evans A, Fox P, Lancaster J, Zilles K, Woods R, Paus T, Simpson G, Pike B, Holmes C, Collins L, Thompson P, Macdonald D, Iacoboni M, Schormann T, Amunts K, Palomero-gallagher N, Geyer S, Boomsma D, Cannon T, Kawashima R, Mazoyer B. A probabilistic atlas and reference system for the human brain : International Consortium for Brain Mapping (ICBM). *Philos T Roy Soc B*. 2001;pp. 1293–1322.

[32] Marin G, Guerin C, Baillet S, Garnero L, Meunier G. Influence of skull anisotropy for the forward and inverse problem in EEG: simulation studies using FEM on realistic head models. *Human brain mapping*. 1998;6(4):250–269.

[33] Huiskamp G, Vroeijenstijn M, van Dijk R, Wieneke G, van Huffelen AC. The need for correct realistic geometry in the inverse EEG problem. *Biomedical Engineering, IEEE Transactions on*. 1999; 46(11):1281–1287.

[34] Oostenveld R, Fries P, Maris E, Schoffelen JM. FieldTrip: Open source software for advanced analysis of MEG, EEG, and invasive electrophysiological data. *Comput Intell Neurosci.* 2011; 2011:156869.

[35] Oostendorp TF, Delbeke J, Stegeman DF. The conductivity of the human skull: results of in vivo and in vitro measurements. *IEEE Trans Biomed Eng.* 2000;47(11):1487–92.

[36] Montes-Restrepo V, van Mierlo P, Strobbe G, Staelens S, Vandenberghe S, Hallez H. Influence of skull modeling approaches on EEG source localization. *Brain topography.* 2014;27(1):95–111.

[37] Vorwerk J, Cho JH, Rampp S, Hamer H, Knösche TR, Wolters CH. A guideline for head volume conductor modeling in EEG and MEG. *NeuroImage.* 2014;100:590–607.

[38] Nunez P. *Electric fields of the brain, 1981.* Oxford University Press, New York. 1981.

[39] He S. Frequency series expansion of an explicit solution for a dipole inside a conducting sphere at low frequency. *Biomedical Engineering, IEEE Transactions on.* 1998;45(10):1249–1258.

[40] Brunet D, Murray MM, Michel CM. Spatiotemporal analysis of multichannel EEG: CARTOOL. *Computational intelligence and neuroscience.* 2011;2011:2.

[41] Chari MV, Silvester PPP. *Finite elements in electrical and magnetic field problems.* John Wiley & Sons Incorporated. 1980.

[42] Van den Broeh S, Zhou H, Peters M. Computation of neuromagnetic fields using finite-element method and Biot-Savart law. *Medical and Biological Engineering and Computing.* 1996;34(1):21–26.

[43] Awada KA, Jackson DR, Williams JT, Wilton DR, Baumann SB, Papanicolaou AC. Computational aspects of finite element modeling in EEG source localization. *Biomedical Engineering, IEEE Transactions on.* 1997;44(8):736–752.

[44] Buchner H, Knoll G, Fuchs M, Rienäcker A, Beckmann R, Wagner M, Silny J, Pesch J. Inverse localization of electric dipole current sources in finite element models of the human head. *Electroencephalography and clinical Neurophysiology.* 1997;102(4):267–278.

[45] Wolters C, Kuhn M, Anwander A, Reitzinger S. A parallel algebraic multigrid solver for finite element method based source localization in the human brain. *Computing and visualization in science*. 2002;5(3):165–177.

[46] Rosenfeld M, Tanami R, Abboud S. Numerical solution of the potential due to dipole sources in volume conductors with arbitrary geometry and conductivity. *Biomedical Engineering, IEEE Transactions on*. 1996;43(7):679–689.

[47] Saleheen HI, Ng KT. New finite difference formulations for general inhomogeneous anisotropic bioelectric problems. *Biomedical Engineering, IEEE Transactions on*. 1997;44(9):800–809.

[48] Saleheen HI, Ng KT. A new three-dimensional finite-difference bidomain formulation for inhomogeneous anisotropic cardiac tissues. *Biomedical Engineering, IEEE Transactions on*. 1998; 45(1):15–25.

[49] Vanrumste B, Van Hoey G, Van de Walle R, Michel RD, Lemahieu IA, Boon PA. The validation of the finite difference method and reciprocity for solving the inverse problem in EEG dipole source analysis. *Brain topography*. 2001;14(2):83–92.

[50] Hallez H, Vanrumste B, Van Hese P, D'Asseler Y, Lemahieu I, Van de Walle R. A finite difference method with reciprocity used to incorporate anisotropy in electroencephalogram dipole source localization. *Physics in medicine and biology*. 2005;50(16):3787.

[51] Becker AA. *The boundary element method in engineering: a complete course*. McGraw-Hill Companies. 1992.

[52] Ferguson AS, Stroink G. Factors affecting the accuracy of the boundary element method in the forward problem. I. Calculating surface potentials. *Biomedical Engineering, IEEE Transactions on*. 1997;44(11):1139–1155.

[53] Mosher JC, Leahy RM, Lewis PS. EEG and MEG: forward solutions for inverse methods. *Biomedical Engineering, IEEE Transactions on*. 1999;46(3):245–259.

[54] Hallez H, Vanrumste B, Grech R, Muscat J, De Clercq W, Vergult A, D'Asseler Y, Camilleri KP, Fabri SG, Van Huffel S, et al. Review

on solving the forward problem in EEG source analysis. *Journal of neuroengineering and rehabilitation*. 2007;4(1):46.

[55] Gramfort A, Papadopoulo T, Olivi E, Clerc M. OpenMEEG : opensource software for quasistatic bioelectromagnetics. *BioMed Eng Online*. 2010;pp. 1–20.

[56] Litvak V, Mattout J, Kiebel S, Phillips C, Henson R, Kilner J, Barnes G, Oostenveld R, Daunizeau J, Flandin G, Penny W, Friston K. EEG and MEG Data Analysis in SPM8. *Comput Intell Neurosci*. 2011;2011:1–32.

[57] Fingberg J, Berti G, Hartmann U, Basermann A, Zimmermann F, Wolters C, Anwander A, McCARTHY A, Woods S. Bio-numerical simulations with SimBio. *NEC Research and Development*. 2003; 44(1):140–145.

[58] Vanrumste B, Van Hoey G, Van de Walle R, D'HAVE M, Lemahieu I, Boon P. The validation of the finite difference method and reciprocity for solving the inverse problem in EEG dipole source analysis. *Brain Topogr*. 2001;14(2):83–92.

[59] Hallez H, Vanrumste B, Van Hese P, D'Asseler Y, Lemahieu I, Van de Walle R. A finite difference method with reciprocity used to incorporate anisotropy in electroencephalogram dipole source localization. *Phys Med Biol*. 2005;50(16):3787–3806.

[60] Malmivuo J, Plonsey R. *Bioelectromagnetism: principles and applications of bioelectric and biomagnetic fields*. Oxford University Press. 1995.

[61] Panizo M, Castellanos A, Rivas J. Finite-difference operators in inhomogeneous anisotropic media. *Journal of Applied Physics*. 1977; 48(3):1054–1057.

[62] Scherg M, Bast T, Berg P. Multiple source analysis of interictal spikes: goals, requirements, and clinical value. *Journal of Clinical Neurophysiology*. 1999;16(3):214–224.

[63] Aine C, Huang M, Stephen J, Christner R. Multistart algorithms for MEG empirical data analysis reliably characterize locations and time courses of multiple sources. *NeuroImage*. 2000;12(2):159–172.

[64] Hämäläinen MS, Ilmoniemi R. Interpreting magnetic fields of the brain: minimum norm estimates. *Medical & biological engineering & computing*. 1994;32(1):35–42.

[65] Pascual-Marqui RD, Lehmann D, Koenig T, Kochi K, Merlo MC, Hell D, Koukkou M. Low resolution brain electromagnetic tomography (LORETA) functional imaging in acute, neuroleptic-naive, first-episode, productive schizophrenia. *Psychiatry Research: Neuroimaging*. 1999;90(3):169–179.

[66] Uutela K, Hämäläinen M, Somersalo E. Visualization of magnetoencephalographic data using minimum current estimates. *NeuroImage*. 1999;10(2):173–180.

[67] Baillet S. Forward and Inverse Problems of MEG/EEG. In: *Encyclopedia of Computational Neuroscience*, pp. 1–8. Springer. 2014; .

[68] Waldorp LJ, Huizenga HM, Nehorai A, Grasman RP, Molenaar PC. Model selection in spatio-temporal electromagnetic source analysis. *Biomedical Engineering, IEEE Transactions on*. 2005; 52(3):414–420.

[69] Mosher JC, Lewis PS, Leahy RM. Multiple dipole modeling and localization from spatio-temporal MEG data. *Biomedical Engineering, IEEE Transactions on*. 1992;39(6):541–557.

[70] Scherg M. Fundamentals of dipole source potential analysis. *Auditory evoked magnetic fields and electric potentials Advances in audiology*. 1990;6:40–69.

[71] Moon YM, Lee TH, Park YP. Development of an automotive joint model using an analytically based formulation. *Journal of sound and vibration*. 1999;220(4):625–640.

[72] Nelder JA, Mead R. A simplex method for function minimization. *The computer journal*. 1965;7(4):308–313.

[73] Xu XL, Xu B, He B. An alternative subspace approach to EEG dipole source localization. *Physics in medicine and biology*. 2004; 49(2):327.

[74] Grech R, Cassar T, Muscat J, Camilleri KP, Fabri SG, Zervakis M, Xanthopoulos P, Sakkalis V, Vanrumste B. Review on solving

the inverse problem in EEG source analysis. *Journal of neuroengineering and rehabilitation*. 2008;5(1):25.

[75] Tikhonov AN, Arsenin VY. *Solutions of ill-posed problems*. Winston. 1977.

[76] Hansen PC. Analysis of discrete ill-posed problems by means of the L-curve. *SIAM review*. 1992;34(4):561–580.

[77] Pascual-Marqui RD, Michel CM, Lehmann D. Low resolution electromagnetic tomography: a new method for localizing electrical activity in the brain. *International Journal of psychophysiology*. 1994;18(1):49–65.

[78] Pascual-Marqui RD. Review of methods for solving the EEG inverse problem. *International journal of bioelectromagnetism*. 1999; 1(1):75–86.

[79] Van Veen BD, Buckley KM. Beamforming: A versatile approach to spatial filtering. *IEEE assp magazine*. 1988;5(2):4–24.

[80] Sekihara K, Nagarajan SS, Poeppel D, Marantz A, Miyashita Y. Reconstructing spatio-temporal activities of neural sources using an MEG vector beamformer technique. *Biomedical Engineering, IEEE Transactions on*. 2001;48(7):760–771.

[81] Barnes GR, Hillebrand A. Statistical flattening of MEG beamformer images. *Human brain mapping*. 2003;18(1):1–12.

[82] Boon P, Vandekerckhove T, Achten E, Thiery E, Goossens L, Vonck K, D'Have M, Van Hoey G, Vanrumste B, Legros B, et al. Epilepsy surgery in Belgium, the experience in Gent. *Acta Neurologica Belgica*. 1999;99(4):256–265.

[83] Boon P, D'Havé M, Adam C, Vonck K, Baulac M, Vandekerckhove T, De Reuck J. Dipole modeling in epilepsy surgery candidates. *Epilepsia*. 1997;38(2):208–18.

[84] Boon P, D'Havé M, Vandekerckhove T, Achten E, Adam C, Clemenceau S, Baulac M, Goossens L, Calliauw L, De Reuck J. Dipole modelling and intracranial EEG recording: correlation between dipole and ictal onset zone. *Acta neurochirurgica*. 1997; 139(7):643–52.

[85] Boon P, D'havé M, Van Hoey G, Vanrumste B, Vonck K, Adam C, Vandekerckhove T, Michielsen G, Baulac M, De Reuck J. Source localization in refractory partial epilepsy. *Revue neurologique*. 1999; 155(6-7):499–508.

[86] Michel CM, de Peralta RG, Lantz G, Andino SG, Spinelli L, Blanke O, Landis T, Seeck M. Spatiotemporal EEG analysis and distributed source estimation in presurgical epilepsy evaluation. *Journal of clinical neurophysiology*. 1999;16(3):239–266.

[87] Boon P, D'Havé M, Vanrumste B, Van Hoey G, Vonck K, Van Walleghem P, Caemaert J, Achten E, De Reuck J. Ictal source localization in presurgical patients with refractory epilepsy. *Journal of Clinical Neurophysiology*. 2002;19(5):461–468.

[88] Plummer C, Litewka L, Farish S, Harvey A, Cook M. Clinical utility of current-generation dipole modelling of scalp EEG. *Clinical Neurophysiology*. 2007;118(11):2344–2361.

[89] Oliva M, Meckes-Ferber S, Roten A, Desmond P, Hicks RJ, OÕBrien TJ. EEG dipole source localization of interictal spikes in non-lesional TLE with and without hippocampal sclerosis. *Epilepsy research*. 2010;92(2):183–190.

[90] Brodbeck V, Spinelli L, Lascano AM, Pollo C, Schaller K, Vargas MI, Wissmeyer M, Michel CM, Seeck M. Electrical source imaging for presurgical focus localization in epilepsy patients with normal MRI. *Epilepsia*. 2010;51(4):583–591.

[91] Brodbeck V, Spinelli L, Lascano AM, Wissmeier M, Vargas MI, Vulliemoz S, Pollo C, Schaller K, Michel CM, Seeck M. Electroencephalographic source imaging: a prospective study of 152 operated epileptic patients. *Brain*. 2011;134(10):2887–2897.

[92] Kaiboriboon K, Lüders HO, Hamaneh M, Turnbull J, Lhatoo SD. EEG source imaging in epilepsy - practicalities and pitfalls. *Nature Reviews Neurology*. 2012;8(9):498–507.

[93] Di Russo F, Martínez A, Hillyard SA. Source analysis of event-related cortical activity during visuo-spatial attention. *Cerebral cortex*. 2003;13(5):486–499.

[94] Strobbe G, Santens S, Van Mierlo P, Hallez H, Van Opstal F, Rosseel Y, Verguts T, Vandenberghe S. Comparison of fMRI

activation and EEG source localization using beamformers during motor response in the Stroop task: Preliminary results. In: *Noninvasive Functional Source Imaging of the Brain and Heart & 2011 8th International Conference on Bioelectromagnetism (NFSI & ICBEM), 2011 8th International Symposium on*. IEEE. 2011; pp. 98–102.

[95] Van Veen BD, van Drongelen W, Yuchtman M, Suzuki A. Localization of brain electrical activity via linearly constrained minimum variance spatial filtering. *Biomedical Engineering, IEEE Transactions on*. 1997;44(9):867–880.

[96] Qin L, Ding L, He B. Motor imagery classification by means of source analysis for brain–computer interface applications. *Journal of Neural Engineering*. 2004;1(3):135.

[97] Grosse-Wentrup M, Liefhold C, Gramann K, Buss M. Beamforming in noninvasive brain–computer interfaces. *Biomedical Engineering, IEEE Transactions on*. 2009;56(4):1209–1219.

[98] Gutiérrez D. Designing a spatial filter to improve SNR in two-class discrimination problems for BCI applications. In: *Signals, Systems and Computers, 2008 42nd Asilomar Conference on*. IEEE. 2008; pp. 372–377.

[99] Staljanssens W, Strobbe G, van Mierlo P, Van Holen R, Vandenberghe S. EEG beamforming to extract better features of motor imagery in a two-class real-time BCI. In: *International conference on basic and clinical multimodal imaging*, vol. 20. SAGE. 2013; pp. 108–109.

[100] van Mierlo P. Epileptic focus localization using functional brain connectivity. Ph.D. thesis, Ghent University. 2013.

[101] Goldman RI, Stern JM, Engel Jr J, Cohen MS. Simultaneous EEG and fMRI of the alpha rhythm. *Neuroreport*. 2002;13(18):2487.

[102] Laufs H, Kleinschmidt A, Beyerle A, Eger E, Salek-Haddadi A, Preibisch C, Krakow K. EEG-correlated fMRI of human alpha activity. *Neuroimage*. 2003;19(4):1463–1476.

[103] Rosa M, Daunizeau J, Friston K. EEG-fMRI integration: a critical review of biophysical modeling and data analysis approaches. *Journal of integrative neuroscience*. 2010;9(04):453–476.

[104] Dale AM, Sereno MI. Improved localizadon of cortical activity by combining eeg and meg with mri cortical surface reconstruction: A linear approach. *Journal of cognitive neuroscience*. 1993;5(2):162–176.

[105] Henson RN, Mouchlianitis E, Friston KJ. MEG and EEG data fusion: simultaneous localisation of face-evoked responses. *Neuroimage*. 2009;47(2):581–589.

[106] Dubarry AS, Badier JM, Trébuchon-Da Fonseca A, Gavaret M, Carron R, Bartolomei F, Liégeois-Chauvel C, Régis J, Chauvel P, Alario F, et al. Simultaneous recording of MEG, EEG and intracerebral EEG during visual stimulation: From feasibility to single-trial analysis. *NeuroImage*. 2014;.

[107] Penny WD, Friston KJ, Ashburner JT, Kiebel SJ, Nichols TE. *Statistical Parametric Mapping: The Analysis of Functional Brain Images: The Analysis of Functional Brain Images*. Academic Press. 2011.

[108] Kolmogorov AN. Foundations of the Theory of Probability. *Chelsea Publishing Co*. 1950;.

[109] Phillips C, Mattout J, Rugg MD, Maquet P, Friston KJ. An empirical Bayesian solution to the source reconstruction problem in EEG. *NeuroImage*. 2005;24:997–1011.

[110] Liu AK, Dale AM, Belliveau JW. Monte Carlo simulation studies of EEG and MEG localization accuracy. *Human brain mapping*. 2002;16(1):47–62.

[111] Henson RN, Wakeman DG, V, Friston KJ, Trujillo-barreto NJ. A parametric empirical Bayesian framework for the EEG / MEG inverse problem : generative models for multi-subject and multimodal integration. *Front Hum Neurosci*. 2011;5(August):1–16.

[112] López J, Litvak V, Espinosa J, Friston K, Barnes GR. Algorithmic procedures for Bayesian MEG/EEG source reconstruction in SPM. *NeuroImage*. 2014;84:476–487.

[113] Harrison L, Penny W, Ashburner J, Trujillo-Barreto N, Friston K. Diffusion-based spatial priors for imaging. *NeuroImage*. 2007; 38(4):677–695.

[114] Friston K, Harrison L, Daunizeau J, Kiebel S, Phillips C, Trujillo-Barreto N, Henson R, Flandin G, Mattout J. Multiple sparse priors for the M/EEG inverse problem. *NeuroImage*. 2008;39(3):1104–1120.

[115] Jaynes ET. Information theory and statistical mechanics. *Physical review*. 1957;106(4):620.

[116] Friston K, Mattout J, Trujillo-Barreto N, Ashburner J, Penny W. Variational free energy and the Laplace approximation. *NeuroImage*. 2007;34(1):220–34.

[117] López J, Penny WD, Espinosa J, Barnes GR. A general Bayesian treatment for MEG source reconstruction incorporating lead field uncertainty. *Neuroimage*. 2012;60(2):1194–1204.

[118] Blumer A, Ehrenfeucht A, Haussler D, Warmuth MK. Occam's razor. *Information processing letters*. 1987;24(6):377–380.

[119] Phillips C, Mattout J, Rugg MD, Maquet P, Friston KJ. An empirical Bayesian solution to the source reconstruction problem in EEG. *NeuroImage*. 2005;24(4):997–1011.

[120] Friston K, Mattout J, Trujillo-Barreto N, Ashburner J, Penny W. Variational free energy and the Laplace approximation. *NeuroImage*. 2007;34(1):220–234.

[121] Wipf D, Nagarajan S. A unified Bayesian framework for MEG/EEG source imaging. *Neuroimage*. 2009;44(3):947–966.

[122] Kass RE, Raftery A. Bayes Factors. *J Am Stat Assoc*. 1995; 90(430):773–795.

[123] Penny WD, Stephan KE, Mechelli a, Friston KJ. Comparing dynamic causal models. *NeuroImage*. 2004;22(3):1157–72.

[124] Stephan KE, Penny WD, Daunizeau J, Moran RJ, Friston KJ. Bayesian model selection for group studies. *NeuroImage*. 2009; 46(4):1004–17.

[125] Rigoux L, Stephan KE, Friston KJ, Daunizeau J. Bayesian model selection for group studies - Revisited. *NeuroImage*. 2013;84C:971–985.

[126] Penny WD. Comparing Dynamic Causal Models using AIC , BIC and Free Energy. *NeuroImage*. 2011;59(1).

[127] Henson RN, Mattout J, Phillips C, Friston KJ. Selecting forward models for MEG source-reconstruction using model-evidence. *NeuroImage*. 2009;46(1):168–176.

[128] Lew S, Sliva DD, Choe Ms, Grant PE, Okada Y, Wolters CH, Hämäläinen MS. Effects of sutures and fontanels on MEG and EEG source analysis in a realistic infant head model. *NeuroImage*. 2013;76:282–93.

[129] Rice JK, Rorden C, Little JS, Parra LC. Subject position affects EEG magnitudes. *NeuroImage*. 2013;64:476–84.

[130] Vanrumste B, Van Hoey G, Van de Walle R, D'Havé M, Lemahieu I, Boon P. Dipole location errors in electroencephalogram source analysis due to volume conductor model errors. *Med Biol Eng Comput*. 2000;38(5):528–34.

[131] Ramon C, Schimpf P, Haueisen J, Holmes M, Ishimaru a. Role of soft bone, CSF and gray matter in EEG simulations. *Brain Topogr*. 2004;16(4):245–8.

[132] Ramon C, Schimpf PH, Haueisen J. Influence of head models on EEG simulations and inverse source localizations. *BioMed Eng Online*. 2006;5:10.

[133] Vorwerk J, Clerc M, Burger M, Wolters CH. Comparison of boundary element and finite element approaches to the EEG forward problem. *Biomed Tech*. 2012;57 Suppl 1:795–798.

[134] Stenroos M, Sarvas J. Bioelectromagnetic forward problem: isolated source approach revis(it)ed. *Phys Med Biol*. 2012; 57(11):3517–35.

[135] Stenroos M, Nenonen J. On the accuracy of collocation and Galerkin BEM in the EEG / MEG forward problem. *Int J Bioelectromagn*. 2012;14(1):29–33.

[136] Baumann SB, Wozny DR, Kelly SK, Meno FM. The Electrical Conductivity of Human Cerebrospinal Fluid at Body Temperature. *IEEE Trans Biomed Eng*. 1997;44(3):220–223.

[137] Mattout J, Henson RN, Friston KJ. Canonical Source Reconstruction for MEG. *Comput Intell Neurosci*. 2007;2007.

[138] De Vos M, Thorne JD, Yovel G, Debener S. Let's face it, from trial to trial: Comparing procedures for N170 single-trial estimation. *NeuroImage*. 2012;63(3):1196–1202.

[139] Daunizeau J, Adams V, Rigoux L. VBA: a probabilistic treatment of nonlinear models for neurobilogical and behavioural data. *Plos Comp Biol*. in press;.

[140] Kanwisher N, McDermott J, Chun MM. The fusiform face area: a module in human extrastriate cortex specialized for face perception. *J Neurosci*. 1997;17(11):4302–11.

[141] Kanwisher N, Yovel G. The fusiform face area: a cortical region specialized for the perception of faces. *Philos T Roy Soc B*. 2006; 361(1476):2109–28.

[142] Pitcher D, Walsh V, Yovel G, Duchaine B. TMS evidence for the involvement of the right occipital face area in early face processing. *Curr Biol*. 2007;17(18):1568–73.

[143] Deffke I, Sander T, Heidenreich J, Sommer W, Curio G, Trahms L, Lueschow A. MEG / EEG sources of the 170-ms response to faces are co-localized in the fusiform gyrus. *NeuroImage*. 2007;35:1495 – 1501.

[144] Haxby JV, Ungerleider LG, Clark VP, Schouten JL, Hoffman Ea, Martin a. The effect of face inversion on activity in human neural systems for face and object perception. *Neuron*. 1999;22(1):189–99.

[145] Yovel G, Kanwisher N. The neural basis of the behavioral face-inversion effect. *Curr Biol*. 2005;15(24):2256–62.

[146] Epstein Ra, Higgins JS, Parker W, Aguirre GK, Cooperman S. Cortical correlates of face and scene inversion: a comparison. *Neuropsychologia*. 2006;44(7):1145–58.

[147] Price CJ, Devlin JT. The myth of the visual word form area. *NeuroImage*. 2003;19(3):473–481.

[148] McCandliss BD, Cohen L, Dehaene S. The visual word form area: expertise for reading in the fusiform gyrus. *Trends in Cogn Sci*. 2003;7(7):293–299.

[149] Grill-Spector K, Knouf N, Kanwisher N. The fusiform face area subserves face perception, not generic within-category identification. *Nat Neurosci.* 2004;7(5):555–62.

[150] Park, S and Chun, M M. Different roles of the parahippocampal place area (PPA) and retrosplenial cortex (RSC) in panoramic scene perception. *NeuroImage.* 2009;47(4):1747–1756.

[151] Cohen L, Dehaene S, Naccache L, Lehéricy S, Dehaene-Lambertz G, Hénaff Ma, Michel F. The visual word form area: spatial and temporal characterization of an initial stage of reading in normal subjects and posterior split-brain patients. *Brain.* 2000;123 (Pt 2):291–307.

[152] Lanfer B, Paul-Jordanov I, Scherg M, Wolters CH. Influence of interior cerebrospinal fluid compartments on EEG source analysis. *Biomed Tech.* 2012;57:623–626.

[153] Akalin Acar Z, Makeig S. Effects of forward model errors on EEG source localization. *Brain Topogr.* 2013;26(3):378–96.

[154] Oostenveld R, Oostendorp TF. Validating the boundary element method for forward and inverse EEG computations in the presence of a hole in the skull. *Hum Brain Mapp.* 2002;17(3):179–92.

[155] Dannhauer M, Lanfer B, Wolters CH, Knösche TR. Modeling of the human skull in EEG source analysis. *Human Brain mapp.* 2011; 32(9):1383–99.

[156] Litvak V, Friston K. Electromagnetic source reconstruction for group studies. *Neuroimage.* 2008;42(4):1490–1498.

[157] Strobbe G, Lopez J, Montes V, van Mierlo P, Hallez H, Vandenberghe S. Comparing Finite Difference Forward Models Using Free Energy based on Multiple Sparse Priors. In: *18th Annual Meeting of the Organization for Human Brain Mapping.* OHBM. 2012; pp. 181–181.

[158] Strobbe G, Lopez JD, van Mierlo P, Vanderperren K, Mijovic B, De Vos M, Van Huffel S, Hallez H, Vandenberghe S. Comparison of BEM and FDM head modeling in SPM for EEG source reconstruction based on free energy. In: *18th International Conference on Biomagnetism (BIOMAG-2012)*, online. BIOMAG. 2012; pp. 240–241.

[159] Strobbe G, van Mierlo P, De Vos M, Mijović B, Hallez H, Van Huffel S, López JD, Vandenberghe S. Bayesian model selection of template forward models for EEG source reconstruction. *NeuroImage*. 2014;93:11–22.

[160] Mijović B, Vanderperren K, Novitskiy N, Vanrumste B, Stiers P, Van Den Bergh B, Lagae L, Sunaert S, Wagemans J, Van Huffel S, De Vos M. The "why" and "how" of JointICA: Results from a visual detection task. *NeuroImage*. 2012;60(2):1171–1185.

[161] Phillips C, Rugg MD, Friston KJ. Anatomically Informed Basis Functions for EEG Source Localization: Combining Functional and Anatomical Constraints. *NeuroImage*. 2002;16(3):678–695.

[162] Friston KJ, Ashburner J, Frith CD, Poline J, Heather JD, Frackowiak RSJ. Spatial Registration and Normalization of Images. *Hum Brain Mapp*. 1996;189(1995).

[163] Novitskiy N, Ramautar JR, Vanderperren K, De Vos M, Mennes M, Mijovic B, Vanrumste B, Stiers P, Van den Bergh B, Lagae L, Sunaert S, Van Huffel S, Wagemeans J. The BOLD correlates of the visual P1 and N1 in single-trial analysis of simultaneous EEG-fMRI recordings during a spatial detection task. *NeuroImage*. 2011; 54(2):824–835.

[164] Wolters CH, Kuhn M, Anwander A, Reitzinger S. A parallel algebraic multigrid solver for finite element method based source localization in the human brain. *Comp Vis Sci*. 2002;5(3):165–177.

[165] Pruist GW, Gilding GH, Peters MJ. A comparison of different numerical methods for solving the forward problem in EEG and MEG. *Physiol Meas*. 1993;14:A1–A9.

[166] Knösche TR, Gräser M, Anwander A. Prior knowledge on cortex organization in the reconstruction of source current densities from EEG. *NeuroImage*. 2013;67:7–24.

[167] Strobbe G, van Mierlo P, Lopez JD, Vandenberghe S. Volumetric sparse priors for the EEG inverse problem. In: *19th Annual Meeting of the Organization for Human Brain Mapping*. 2013; p. 1.

[168] Strobbe G, van Mierlo P, Vandenberghe S. Bayesian distributed EEG source reconstruction using realistic finite difference forward

models. In: *International conference on basic and clinical multimodal imaging*. 2013; p. 1.

[169] Strobbe G, van Mierlo P, De Vos M, Mijović B, Hallez H, Van Huffel S, López JD, Vandenberghe S. Multiple sparse volumetric priors for distributed EEG source reconstruction. *NeuroImage*. 2014; 100:715–724.

[170] de Curtis M, Jefferys JG, Avoli M. Interictal Epileptiform Discharges in Partial Epilepsy. *Jasper's Basic Mechanisms of the Epilepsies*. 2012;80:213.

[171] Alarcon G, Guy C, Binnie C, Walker S, Elwes R, Polkey C. Intracerebral propagation of interictal activity in partial epilepsy: implications for source localisation. *Journal of Neurology, Neurosurgery & Psychiatry*. 1994;57(4):435–449.

[172] Wennberg R, Valiante T, Cheyne D. EEG and MEG in mesial temporal lobe epilepsy: where do the spikes really come from? *Clinical neurophysiology*. 2011;122(7):1295–1313.

[173] Lantz G, Spinelli L, Seeck M, de Peralta Menendez RG, Sottas CC, Michel CM. Propagation of interictal epileptiform activity can lead to erroneous source localizations: a 128-channel EEG mapping study. *Journal of clinical neurophysiology*. 2003;20(5):311–319.

[174] Rose S, Ebersole JS. Advances in spike localization with EEG dipole modeling. *Clinical EEG and neuroscience*. 2009;40(4):281–287.

[175] Plummer C, Harvey AS, Cook M. EEG source localization in focal epilepsy: where are we now? *Epilepsia*. 2008;49(2):201–218.

[176] Birot G, Spinelli L, Vulliémoz S, Mégevand P, Brunet D, Seeck M, Michel CM. Head model and electrical source imaging: A study of 38 epileptic patients. *NeuroImage: Clinical*. 2014;5:77–83.

[177] Ary JP, Klein SA, Fender DH. Location of sources of evoked scalp potentials: corrections for skull and scalp thicknesses. *Biomedical Engineering*. 1981;28:447–52.

[178] Maziero D, Castillanos AL, Salmon CEG, Velasco TR. Comparison between Different ESI Methods of Refractory Epilepsy Shows a High Sensitivity for Bayesian Model Averaging. *Journal of Biomedical Science and Engineering*. 2014;7(09):662.

[179] Pacia SV, Ebersole JS. Intracranial EEG substrates of scalp ictal patterns from temporal lobe foci. *Epilepsia*. 1997;38(6):642–654.

[180] Jan MM, Sadler M, Rahey SR. Electroencephalographic features of temporal lobe epilepsy. *The Canadian Journal of Neurological Sciences*. 2010;37(04):439–448.

[181] Yamazaki M, Tucker DM, Fujimoto A, Yamazoe T, Okanishi T, Yokota T, Enoki H, Yamamoto T. Comparison of dense array EEG with simultaneous intracranial EEG for interictal spike detection and localization. *Epilepsy research*. 2012;98(2):166–173.

[182] Mégevand P, Spinelli L, Genetti M, Brodbeck V, Momjian S, Schaller K, Michel CM, Vulliemoz S, Seeck M. Electric source imaging of interictal activity accurately localises the seizure onset zone. *Journal of Neurology, Neurosurgery & Psychiatry*. 2014; 85(1):38–43.

[183] Heers M, Chowdhury RA, Hedrich T, Dubeau F, Hall JA, Lina JM, Grova C, Kobayashi E. Localization Accuracy of Distributed Inverse Solutions for Electric and Magnetic Source Imaging of Interictal Epileptic Discharges in Patients with Focal Epilepsy. *Brain Topography*. 2015;pp. 1–20.

[184] Heers M, Hedrich T, An D, Dubeau F, Gotman J, Grova C, Kobayashi E. Spatial correlation of hemodynamic changes related to interictal epileptic discharges with electric and magnetic source imaging. *Human brain mapping*. 2014;35(9):4396–4414.

[185] Trujillo-Barreto NJ, Aubert-Vázquez E, Valdés-Sosa PA. Bayesian model averaging in EEG/MEG imaging. *NeuroImage*. 2004; 21(4):1300–1319.

[186] Lopez JD, Espinosa JJ, Barnes GR. Random location of Multiple Sparse Priors for solving the MEG/EEG inverse problem. In: *Engineering in Medicine and Biology Society (EMBC), 2012 Annual International Conference of the IEEE*. IEEE. 2012; pp. 1534–1537.

[187] Ebersole JS. Noninvasive localization of epileptogenic foci by EEG source modeling. *Epilepsia*. 2000;41(s3):S24–S33.

[188] Ebersole JS, Ebersole SM. Combining MEG and EEG source modeling in epilepsy evaluations. *Journal of Clinical Neurophysiology*. 2010;27(6):360–371.

[189] Wennberg R, Cheyne D. EEG source imaging of anterior temporal lobe spikes: validity and reliability. *Clinical Neurophysiology*. 2014; 125(5):886–902.

[190] Lemieux L, Daunizeau J, Walker MC. Concepts of connectivity and human epileptic activity. *Frontiers in systems neuroscience*. 2011;5.

[191] Van Mierlo P, Carrette E, Hallez H, Vonck K, Van Roost D, Boon P, Staelens S. Accurate epileptogenic focus localization through time-variant functional connectivity analysis of intracranial electroencephalographic signals. *Neuroimage*. 2011;56(3):1122–1133.

[192] Ding L, Worrell GA, Lagerlund TD, He B. Ictal source analysis: localization and imaging of causal interactions in humans. *Neuroimage*. 2007;34(2):575–586.

[193] Lu Y, Yang L, Worrell GA, He B. Seizure source imaging by means of FINE spatio-temporal dipole localization and directed transfer function in partial epilepsy patients. *Clinical Neurophysiology*. 2012;123(7):1275–1283.

[194] van Mierlo P, Strobbe G, Hallez H, Staelens S, et al. Added value of connectivity analysis on brain waveforms in EEG source reconstruction to detect the epileptic driver during seizures. In: *18th International Conference on Biomagnetism (BIOMAG-2012)*. BIOMAG. 2012; pp. 98–99.

[195] Strobbe G, David CP, Montes Restrepo VE, van Mierlo P, Vandenberghe S. Selecting volume conductor models for EEG source localization of epileptic spikes: preliminary results based on 4 operated epileptic patients. In: *International conference on basic and clinical multimodal imaging*. 2013; p. 1.

[196] Strobbe G, Carrette E, López J, Van Roost D, Meurs E, Vonck K, Boon P, Vandenberghe S, van Mierlo P. EEG source imaging of interictal spikes in patients with refractory focal epilepsy through Bayesian multiple dipole modeling. *NeuroImage*. Submitted;.

[197] Bart V. EEG dipole source analysis in a realistic head model. Ph.D. thesis, Ghent University. 2002.

[198] Rush S, Driscoll DA. EEG electrode sensitivity-an application of reciprocity. *Biomedical Engineering, IEEE Transactions on*. 1969; 1(1):15–22.

List of Publications

Journal papers

[1] **Strobbe, G.**, Carrette, E., López, J.D., Van Roost , D., Meurs, E., Vonck, K., Boon, P., Vandenberghe, S., van Mierlo, P. (2015). EEG source imaging of interictal spikes using multiple sparse volumetric priors for presurgical focus localization. *NeuroImage*, In preparation for submission.

[2] Vanhoutte, S, **Strobbe, G.**, van Mierlo, P., Cosyns, M., Batens, K., Corthals, P. , De Letter, M., Van Borstel, J., Santens, P. (2014). Early lexico-semantic modulation of motor related areas during action and non-action verb processing . *Journal of Neurolinguistics*, accepted (doi: 10.1016/j.jneuroling.2015.01.001)

[3] **Strobbe, G.**, van Mierlo, P., De Vos, M., Mijovic , B., Hallez, H., Van Huffel, S., Lopez, J. D., Vandenberghe, S (2014). Multiple sparse volumetric priors for distributed EEG source reconstruction. *NeuroImage*, 100, 715-724.

[4] **Strobbe, G.**, van Mierlo, P., De Vos, M., Mijovic , B., Hallez, H., Van Huffel, S., Lopez, J. D., Vandenberghe, S (2014). Bayesian model selection of template forward models for EEG source reconstruction. *NeuroImage*, 93, 11-22.

[5] Montes-Restrepo, V., van Mierlo, P., **Strobbe, G.**, Staelens, S., Vandenberghe, S., Hallez, H. (2014). Influence of skull modeling approaches on EEG source localization. *Brain topography*, 27(1), 95-111.

Conference proceedings

[1] **Strobbe, G.**, Santens, S., van Mierlo, P., Hallez, H., Van Opstal, F., Rosseel, Y., Verguts, T., Vandenberghe, S. (2011). Comparison of fMRI activation and EEG source localization using beamformers during motor response in the Stroop task: preliminary results. *Proceedings of the 8th International Symposium on Noninvasive Functional Source Imaging of the Brain and Heart and the 2011 8th International Conference on Bioelectromagnetism (NFSI and ICBEM)*, 98-102.

Conference abstracts

[1] **Strobbe, G.**, Carrette, E., López, J.D., Van Roost , D., Meurs, E., Vonck, K., Boon, P., Vandenberghe, S., van Mierlo, P. (2015). EEG source imaging of interictal spikes using multiple sparse volumetric priors for presurgical focus localization. *Update @ Kempenhaeghe*

[2] **Strobbe, G.**, Carrette, E., López, J.D., Van Roost , D., Meurs, E., Vonck, K., Boon, P., Vandenberghe, S., van Mierlo, P. (2015). EEG source imaging of interictal spikes through Bayesian multiple dipole modeling. *21th Annual Meeting of the Organization for Human Brain Mapping*

[3] Van Mierlo, P., Coito, A., Birot, G., **Strobbe, G.**, Staljanssens, W., Michel, C., Seeck, M., Vuilliémoz, S. (2015). Functional connectivity helps to localize the ictal onset zone from ictal scalp EEG recordings. *21th Annual Meeting of the Organization for Human Brain Mapping*

[4] Staljanssens, W. **Strobbe, G.**, De Taeye, L., Van Roost , D., Vonck, K., Raedt, R., Van Holen, R., Vandenberghe, S., van Mierlo, P. (2014). EEG Source reconstruction of the P3 event-related potential can help to understand the mechanism of action of VNS. *FEA Research Symposium 2014*

[5] Staljanssens, W. **Strobbe, G.**, De Taeye, L., Van Roost , D., Vonck, K., Raedt, R., Van Holen, R., Vandenberghe, S., van Mierlo, P. (2014). Source reconstruction of the P300 event-related potential as a biomarker for the efficacy of vagus nerve stimula-

tion in patients with epilepsy. *13th Belgian Day on Biomedical Engineering Ð joint meeting with IEEE EMBS Benelux Chapter*

[6] Staljanssens, W. **Strobbe, G.**, De Taeye, L., Van Roost , D., Vonck, K., Raedt, R., Van Holen, R., Vandenberghe, S., van Mierlo, P. (2014). Source reconstruction of the P300 event-related potential as a biomarker for the efficacy of vagus nerve stimulation in patients with epilepsy. *19th International Conference on Biomagnetism*

[7] Aerts, A., **Strobbe, G.**, van Mierlo, P., Hartsuiker, R., Santens, P., De Letter, M. (2013). Interplay between auditory and motor areas during phoneme and word processing investigated on a millisecond time basis. *SNL Annual meeting*

[8] **Strobbe, G.**, van Mierlo, P., Lopez, J. D., Vandenberghe, S. (2013). Volumetric sparse priors for the EEG inverse problem. *19th Annual meeting of the Organization for human brain mapping*

[9] **Strobbe, G.**, van Mierlo, P., Vandenberghe, S. (2013). Bayesian distributed EEG source reconstruction using realistic finite difference forward models. *International Conference on Basic and Clinical Multimodal Imaging*

[10] **Strobbe, G.**, David, C. P., Montes Restrepo, V. E., van Mierlo, P., Vandenberghe, S. (2013). Selecting volume conductor models for EEG source localization of epileptic spikes: preliminary results based on 4 operated epileptic patients. *International Conference on Basic and Clinical Multimodal Imaging*

[11] Staljanssens, W., **Strobbe, G.**, van Mierlo, P., Van Holen, R., Vandenberghe, S. (2013). EEG beamforming to extract better features of motor imagery in a two-class real-time BCI. *International Conference on Basic and Clinical Multimodal Imaging*

[12] Vanhoutte, Sarah, De Letter, M., Cosyns, M., van Mierlo, P., **Strobbe, G.**, Corthals, P., Van Borsel, J., et al. (2013). Neurophysiological dysfunctions in adults who stutter during a perception task. *34e VVL-congres*

[13] Montes Restrepo, V. E., **Strobbe, G.**, van Mierlo, P., Vandenberghe, S. (2013). Effects of conductivity perturbations of the

tri-layered skull on EEG source analysis. *International Conference on Basic and Clinical Multimodal Imaging*

[14] **Strobbe, G.**, Lopez, J., Montes Restrepo, V. E., van Mierlo, P., Hallez, H., Vandenberghe, S. (2012). Comparing finite difference forward models using free energy based on multiple sparse priors. *18th Annual Meeting of the Organization for Human Brain Mapping*

[15] Vanhoutte, S., De Letter, M., Cosyns, M., van Mierlo, P., **Strobbe, G.**, Corthals, P., Santens, P., Van Borsel, J. (2012). Neurofysiologische afwijkingen bij volwassenen met ontwikkelingsstotteren tijdens een perceptietaak. *Nederlandse Vereniging voor Stem-, Spraak- en Taalpathologie Jaarcongres 2012?: Huidige ontwikkelingen in de stem-, spraak-, taal-pathologie*

[16] **Strobbe, G.**, Lopez, J. D., van Mierlo, P., Vanderperren, K., Mijovic, B., De Vos, M., Van Huffel, S., Vandenberghe, S. (2012). Comparison of BEM and FDM head modeling in SPM for EEG source reconstruction based on free energy. *18th International Conference on Biomagnetism*

[17] van Mierlo, P., **Strobbe, G.**, Montes restreo, V., Hallez, H., Lopez, J. david, Staelens, S. (2012). Added value of connectivity analysis on brain waveforms in EEG source reconstruction to detect the epileptic driver during seizures. *18th International Conference on Biomagnetism*

[18] **Strobbe, G.** (2010). Multimodal integration of simultaneous acquired EEG and fMRI data to study cognitive processes. *11th UGent-FirW Doctoraatssymposium*